

DISS. ETH NO. 29186

Process Modelling of Diamond Wire Sawing

A thesis submitted to attain the degree of

DOCTOR OF SCIENCES

(Dr. sc. ETH Zurich)

presented by

Stefan Süßmaier

M. Sc. RWTH, RWTH Aachen University

born on *10.02.1989*

accepted on the recommendation of

Prof. Dr.-Ing. Dr. hc. Konrad Wegener

Prof. Dr.-Ing. Shreyes Melkote

2023

Abstract

Photovoltaic technology plays an important role in the efforts to reduce greenhouse gas emissions during energy generation. The growth in total installed capacity has been remarkable in recent years, but if energy production is to be emission-free by 2050, the energy generated by solar power must grow by 24% annually. The demand for silicon wafers, on which the most widespread technology is based, is correspondingly high. To produce wafers, silicon monocrystals are cut into hundreds of wafers at a time on diamond wire saws using a $< 100 \mu\text{m}$ thick wire impregnated with diamonds. Efforts to maximise material utilisation are leading to the use of thinner wires to produce larger and thinner wafers. These efforts present challenges in terms of weakening and deformation of the wafers. The weakening results from the brittle material behaviour during cutting. Under certain conditions, the hard and brittle silicon can be cut in a ductile manner, resulting in a less damaged surface. Plastic flow is only possible under atmospheric conditions by pressure-induced phase transformations, which, however, can lead to amorphisation of the material on the surface, thus to volume change and potentially to deformation-inducing stresses. In this study, a contribution to the state of the art is made by systematically investigating the relationship of the pressure induced by the cut with normal forces and indentation depth in single grain scratch tests. The scratch and ploughing hardness, friction coefficient and cutting-to-normal force ratio are determined. The influence of grain shape on phase change at high cutting speeds is discussed. The results are applied to diamond wire sawing. A model for the description of the wire bow due to acting forces is presented. Based on this, a correlation between forces, cutting speed, wire topography and the achieved material removal rate is derived. Verification experiments are carried out on a specially developed wire sawing machine.

Zusammenfassung

Die Photovoltaiktechnik nimmt bei den Bestrebungen, den Treibhausgasausstoss während der Energieerzeugung zu reduzieren, einen wichtigen Stellenwert ein. Der Zuwachs der installierten Gesamtleistung ist seit Jahren beachtlich. Wenn die Energieerzeugung jedoch bis 2050 emissionsfrei sein soll, muss die durch Solarstrom erzeugte Energie jährlich um 24% wachsen. Entsprechend hoch ist der Bedarf an Siliziumwafern, auf denen die verbreitetste Technologie beruht. Zur Herstellung von Wafern werden Siliziumeinkristalle auf Diamantdrahtsägen durch einen $< 100 \mu\text{m}$ dicken, mit Diamanten belegten Draht in hunderte Wafer gleichzeitig getrennt. Bestrebungen die Materialausnutzung zu maximieren führen zur Verwendung immer dünnerer Drähte um grössere Wafer mit immer geringerer Dicke zu erzeugen. Diese Bestrebungen bringen Herausforderungen mit sich, die sich durch Schwächung und Verformung der Wafer äussern. Die Schwächung resultiert aus dem spröden Materialverhalten beim Schnitt. Das sprödharte Silizium kann unter bestimmten Voraussetzungen duktil geschnitten werden, was zu einer weniger stark geschädigten Oberfläche führt. Das plastische Fliessen ist unter atmosphärischen Bedingungen nur durch druckinduzierte Phasenumwandlungen möglich, die jedoch zu Amorphisierung des Materials auf der Oberfläche, somit zu Volumenänderung und potenziell zu verformungsinduzierenden Spannungen führen können. In dieser Arbeit wird ein Beitrag zum Stand des Wissens geleistet, indem der Zusammenhang des durch den Schnitt induzierten Druck mit Normalkräften und Eindringtiefe in Einzelkornkratzversuchen systematisch untersucht wird. Dabei werden Kratz- und Pflüghärte, Reibkoeffizient und Schnitt-zu-Normalkraft Verhältnis bestimmt. Der Einfluss der Kornform auf die Phasenveränderung bei hoher Schnittgeschwindigkeit wird diskutiert. Die Ergebnisse werden auf das Diamantdrahtsägen übertragen. Es wird ein Modell zur Beschreibung des Drahtbogens aufgrund wirkender Kräfte vorgestellt. Darauf aufbauend wird ein Zusammenhang zwischen Kräften, Schnittgeschwindigkeit, Drahttopografie und die erreichte Abtrage rate erarbeitet. Verifikationsexperimente werden auf einer eigens entwickelten Drahtsägemaschine durchgeführt.

Acknowledgements

This dissertation sums up the most important findings resulting from my work as a research assistant at the Institute of Machine Tools and Manufacturing (IWF) of the ETH Zürich. I would like to thank the people who accompanied and supported me throughout the years.

First and foremost, my appreciation is directed towards Prof. Konrad Wegener, who gave me the opportunity, freedom and trust to conduct this research. Your knowledge in and enthusiasm for various topics related with manufacturing and production engineering was always an inspiration and lead to finding solutions for problems that seemed like dead-ends more than once. I have always appreciated the goal-oriented and non-judgmental approach to challenges arising and hope to maintain this attitude myself in the future.

I would like to thank Prof. Shreyes Melkote of the Georgia Tech Manufacturing Institute for the co-examination, the review of my thesis and the friendly and helpful discussions. It was a pleasure receiving constructive critics from someone as prestigious in the field.

I am grateful for the guidance and exchange with my group leaders, who made sure I never ran out of work but also had my back at all times. Dr. Fredy Kuster's creativity and assurance in roughly the first half of my employment certainly shaped my personal and professional development in a very positive way. Dr. Michal Kuffa's constructive feedback helped to focus my work especially towards the end of my work. I very much appreciated the honest exchange and your confidence shown in me.

This work was primarily funded through the Swiss National Science Foundation project 200021_162611. Some devices acquired through the SNF project 200020_197361 were also used. My later employment at IWF was in parts financed through the Innosuisse projects 46047.1 and 51074.1. I am grateful for the support and the opportunity.

I have always wondered why it is called "philosophiae doctor". Throughout the years of sharing an office with Uygur, I have certainly got to

understand why. Your mentorship and the multifaceted atmosphere in our office and endeavours made science fun.

To all my colleagues (mentioned by name or not) with whom I have worked on projects, in lectures, events, publications and project applications... thank you very much, you are the main reason I have always enjoyed going to work. Special thanks to Jens Boos who brought me to IWF and to my JAR friends Christian, Varun, Lukas, Martina and Fabian who kept motivation and standards high - your part in this work is invaluable. An honourable mention to Hagen for all his support, ideas, the fruitful discussions (at work or after) and for showing me my topics in a different light. Nanyuan, Lucas, Mert, Adrian, Jona - you are among the few people with whom I could discuss my work in detail, thank you for challenging my ideas and contributing to my work! To Albert, Josef, Sandro, Mark, Athina and Miriam for not just doing your job but actually always being there when things were on fire without me being able to offer much in return. Those of you with whom I did not work on any particular problem but who just enjoyed spending your free time with me - Andreas, Mamzi, Matthias, Moritz, Norbert and Stefan - thank you for the good times!

I want to express my gratitude to the more than 20 Students who placed their trust in my coaching for their thesis and have contributed significantly to my work; foremost to Ariely, who spent a whole year at IWF and showed a rare enthusiasm for the topic. I hope you all enjoyed and learned as much from working with me as I have from working with you.

I would like to thank my room-mate and friend Norbert for spending his free-time with meticulously reviewing my dissertation and providing invaluable insights.

My thanks also go out to my friends and family who have encouraged and motivated me throughout all these years and made me who I am. I would like to express my gratefulness to Catarina, who stood by my side when we started together in Zürich and who especially motivated and helped me through the first Corona year. Lastly I want to thank Milena for her love and support which made the many weekends and evenings spent to finalise the thesis pleasant and who helped me shut off after work and disperse my mind.

Contents

Abstract	i
Zusammenfassung	iii
Acknowledgements	v
Nomenclature and Abbreviations	xi
1 Introduction	1
1.1 Photovoltaic and Solar Industry	1
1.2 Diamond Wire Sawing	2
1.3 Motivation: Current Research Areas	4
2 Literature Review	7
2.1 Workpiece and Tool Material	7
2.1.1 Workpiece Material Silicon	7
2.1.2 Tool Material Diamond	12
2.2 Material Removal	13

2.2.1	Scratch Tests as a Means of Analysing Material Removal and Hardness	15
2.2.2	Phenomena of Material Removal in Silicon	25
2.2.3	Friction	35
2.3	Analysis and Modelling of the Diamond Wire Sawing Process	39
2.3.1	Modelling of the Wire Bow	40
2.3.2	Analysis of the Removal Rate in Diamond Wire Sawing	41
2.3.3	Kinematic Process Modelling	45
2.3.4	Conclusion: Kinetics of Diamond Wire Sawing . . .	47
3	Research Objectives	49
4	Material Removal Mechanism of Silicon	53
4.1	Motivation: Material Interaction Modelling	53
4.2	Material and Experimental Procedure	56
4.2.1	Test Rig: Single Grain Scratching Set-up	56
4.2.2	Workpiece: Silicon Disk	57
4.2.3	Tools: Diamond Indenters	58
4.2.4	Experimental Procedure	59
4.3	Analysis and Modelling	60
4.3.1	Measurement and Analysis of the Scratch Topography	60
4.3.2	Generation of the Contact Geometry	67
4.3.3	Analysis of Forces	71
4.3.4	Determination of the Penetration Depth and Rate of Recovery	75
4.3.5	Analysis of the Crystallographic Composition	76

4.4	Results and Discussion	79
4.4.1	Surface Appearance	80
4.4.2	Rate of Depth Recovery	81
4.4.3	Scratch and Ploughing Hardness of Si	85
4.4.4	Load-bearing Area when Scratching with Vickers Face First Orientation	92
4.4.5	Determination of the Coefficient of Friction between Si and Diamond	97
4.4.6	Force Ratio	103
4.4.7	Crystallography Composition	105
4.5	Conclusions: Material Removal Mechanism of Si	111
5	Process Modelling of DWS	115
5.1	Motivation: Kinematic Modelling	115
5.2	Chapter Outline	116
5.3	Experimental Materials and Methods	116
5.3.1	Test Rig: Endless Wire Saw	118
5.3.2	Workpiece: Silicon Bricks	122
5.3.3	Tool: Stranded Diamond Wire	123
5.4	Model for the Description of the Wire Bow	124
5.4.1	General Process Kinematics	124
5.4.2	Wire Deflection Model	125
5.4.3	Verification of the Wire Bow Differential Equation by FEM modelling	135
5.4.4	Experimental Verification of the Wire Bow Model	138
5.4.5	Parameter Analysis of the Wire Bow in Equilibrium	149

5.4.6	Dynamic Bow Creation	154
5.4.7	Conclusion: Wire Bow Model	157
5.5	Discussion of the Force Ratio	158
5.5.1	Effects of Process Parameters	159
5.5.2	Effects of Wear	162
5.5.3	Conclusion: Force Ratio in DWS	165
5.6	Material Removal Rate Model	166
5.6.1	Analytical Description of the Removal on Grain Level	166
5.6.2	Description of the Removal on Topography Level . .	169
5.6.3	Verification of the Material Removal Model	182
5.6.4	Results and Discussion	191
5.7	Conclusions: Process Modelling of DWS	202
6	Summary and Outlook	205
	Appendix	211
	A - Scratch and Ploughing Hardness - Plots	211
	B - FEM User Constraint	221
	Bibliography	xix
	Curriculum Vitae	xxxix

Nomenclature and Abbreviations

Greek Letters

α	wire bow angle	[°]
β	parameter accounting for stiffness deviations	[-]
ΔV	removed material volume	[$\mu\text{m}^3/\text{min}$]
ϵ	geometric constant related to indenter geometry	[-]
η	viscosity	[Pa s]
$\hat{\mu}$	cutting-to-normal-force ratio	[-]
κ	material constant for determining critical depth of cut for ductile-to-brittle transition	[-]
λ	thermal conductivity at 300 K	[W K/m]
\mathcal{O}	higher order terms	[-]
μ	friction coefficient	[-]
ν	Possion's ratio	[-]
ν	Raman shift	[1/cm]
ν_a	Raman shift at peak centre for amorphous peaks	[1/cm]
ν_c	Raman shift at peak centre for crystalline peaks	[1/cm]
ϕ	angle that spans the scratched arc	[°]
ρ	density	[g/cm ³]
ρ_g	grain density	[-]

σ	principal stress	[GPa]
σ_f	fracture strength	[GPa]
σ_n	normal stress	[GPa]
σ_y	compressive yield strength	[GPa]
σ_{yield}	yield stress	[GPa]
φ	angular position of a grain on the wire	[°]
φ	half included indenter angle	[°]
φ	local deflection angle	[°]
ζ_0	constant in threshold load function	[–]
ζ_L	constant in limiting crack function	[–]

Capital Latin Letters

\tilde{F}_c	cutting force corrected for friction	[N]
\tilde{N}	number of active grains or active wire sections	[–]
A	constant related with the relative length of cracks	[–]
A_0	nominal contact area	[mm ²]
A_{ref}	reference area	[mm ²]
A_c	area projected into the plane orthogonal to the cutting direction	[mm ²]
A_n	area projected into the plane orthogonal to the normal direction	[mm ²]
A_r	true contact area	[mm ²]
A_t	area projected into the plane orthogonal to the tangential direction	[mm ²]
A_{LB}	load bearing area	[mm ²]
A_p	projected wire area	[mm ²]
A_s	contact surface	[mm ²]
C_1	USUI wear coefficient	[mm/N]
C_2	USUI temperature coefficient	[K]
$C_{25^\circ\text{C}}$	solid heat capacity at 25 °C	[J K/mol]
E	Young's modulus	[GPa]
E_s	specific cutting energy (= H_p)	[GPa]
E_{eff}	effective elastic modulus	[GPa]

F_0	threshold load	[N]
F_c	cutting force	[N]
F_f	feed force	[N]
F_n	normal force	[N]
F_p	passive (radial) force	[N]
F_r	friction force	[N]
F_s	wire tension in the empty run	[N]
F_t	tangential force	[N]
F_{sa}	wire tension in the load run	[N]
H	hardness	[GPa]
H_c	static indentation hardness	[GPa]
H_p	ploughing hardness	[GPa]
H_s	scratch hardness	[GPa]
H_V	Vickers hardness	[GPa]
I	moment of inertia	[m ⁴]
I_a	Raman intensity of the amorphous phase	[a.u.]
I_c	Raman intensity of the crystalline phase	[a.u.]
$I_{\alpha\text{-Si}_{475}}$	Raman intensity of the amorphous phase at a Raman shift around 475 1/cm	[a.u.]
$I_{\text{Si-IV}}$	Raman intensity of the Si-IV phase at a Raman shift around 510 1/cm	[a.u.]
$I_{\text{Si-I}}$	Raman intensity of the Si-I phase at a Raman shift around 521 1/cm	[a.u.]
K_c	fracture toughness	[MN/m ^{2/3}]
L	pulley distance	[mm]
L_w	length of the wire loop	[mm]
M	bending moment	[N m]
M_p	melting point	[K]
N	number of grains or wire sections	[–]
P	cumulative probability density	[–]
P	hydrostatic pressure	[GPa]

P	local normal force	[N]
Q	local tangential force	[N]
S	unloading stiffness	[GPa]
T	temperature	[K]
V	shear force	[N]
W_e	cumulated cutting energy	[kJ]
W_u	cumulated wear proportionality coefficient derived from the USUI wear model	[N/nm]

Miniscule Latin Letters

\hat{p}	distributed normal force	[N/mm]
\hat{q}	distributed cutting force	[N/mm]
\tilde{h}_f	mean residual depth	[μm]
\tilde{h}	mean penetration of active grains	[μm]
\tilde{s}	characteristic wire length, spacing parameter of currently active grains	[μm]
a	indenter radius	[μm]
a_e	average depth of cut	[μm]
b	coefficient in Sneddon's load-displacement function	[N/ μm]
b_a	half-power bandwidth of the Gaussian distribution representing amorphous phases	[1/cm]
b_c	half-power bandwidth of the Lorentz distribution representing crystalline phases	[1/cm]
c	circle cord length	[mm]
c^L	limiting crack function	[—]
c_l	crack length	[μm]
c_p	half width of the plastic zone	[μm]
d_a	thickness of the amorphous layer	[nm]
d_g	grain size	[μm]
d_n	removed depth	[μm]
d_w	wire core diameter	[μm]
dL	sliding distance	[mm]

dW	worn volume	[mm ³]
f	feed distance per wire pass	[mm]
f	ratio of local interfacial shear strength	[—]
f_b	load bearing factor	[—]
h	sawn height (height of the workpiece)	[mm]
h	total indentation depth	[μm]
h_a	height of the Gaussian distribution representing amorphous phases	[a.u.]
h_c	contact depth	[μm]
h_c	height of the Lorentz distribution representing crystalline phases	[a.u.]
h_e	recovered depth	[μm]
h_f	final (residual) depth	[μm]
h_g	grain protrusion	[μm]
h_p	depth of the plastic zone	[μm]
h_s	grain penetration due to spacing and feed-rate-to-cutting-speed ratio	[μm]
h_s	sink-in depth	[μm]
$h_{cu,crit}$	critical chipping thickness	[μm]
$h_{cu,eff}$	effective chipping thickness	[μm]
h_{max}	maximum indentation depth	[μm]
h_{cp}	contact depth considering the pile-up	[μm]
h_{cu}	undeformed chipping thickness	[μm]
h_{ec}	recovered contact depth	[μm]
h_{fp}	final (residual) height on the ridge	[μm]
$k_{n,f}$	scratch hardness coefficient (final depth)	[mN/μm ³]
k_n	cutting ability of the wire	[—]
k_n	scratch hardness coefficient (penetrated depth)	[mN/μm ³]
k_p	Preston coefficient	[mm ² /min]
l	contact length	[mm]
l	workpiece width (approx. contact length)	[mm]
l_{meas}	measured wire length	[mm]
m	exponent in SNEDDON's load-displacement function	[—]

Nomenclature and Abbreviations

$m_{n,f}$	scratch hardness exponent (final depth)	[–]
m_n	scratch hardness exponent (penetrated depth)	[–]
n	force distribution exponent	[–]
n	number of pass	[–]
p	lapping pressure	[N/mm ²]
r	Raman intensity ratio	[–]
r	pulley radius	[mm]
r	radial distance on the workpiece surface	[–]
r_e	ratio of depth recovery	[–]
r_k	kerf radius	[μ m]
r_r	removal rate	[mm/min]
r_s	rate of sink-in	[–]
r_s	scratch radius	[mm]
r_w	wire core radius	[μ m]
$r_{\alpha-IV}$	Raman intensity ratio between amorphous Si and Si-IV	[–]
$r_{\alpha-I}$	Raman intensity ratio between amorphous Si and Si-I	[–]
r_{I-IV}	Raman intensity ratio between Si-I and Si-IV	[–]
s	scratch length	[mm]
s_f	scratch length determined from the force signal	[mm]
s_i	gap between two active grains	[μ m]
s_p	gap between wire and ingot	[μ m]
s_s	scratch length determined from the surface topography	[mm]
s_{in}	horizontal distance of wire entry into the workpiece	[mm]
s_{out}	horizontal distance of wire exit from the workpiece	[mm]
t	time	[s]
t_p	bearing ratio	[–]
t_{cut}	cutting duration	[s]
v_c	cutting speed	[m/s]
v_f	feed rate in normal direction	[mm/min]
v_p	feed rate in passive direction	[mm/min]
w	width	[μ m]

w	wire deflection	[mm]
w'	wire slope	[mm]
w''	wire curvature	[mm]
w_{max}	maximum wire deflection	[mm]
y_n	load-bearing width	[μm]
z	profile height	[μm]
z_{max}	maximum profile height	[μm]

Abbreviations

α -Si	amorphous silicon
ANOVA	analysis of variance
DOF	degrees of freedom
DWS	diamond wire sawing
erf	Gaussian error function
FEM	finite element method
HSK	hollow shank taper (German: Hohlschaftkegel)
LAS	lose-abrasive sawing
PID	proportional-integrative-derivative (controller)
POI	point of interest
PV	photo-voltaic
Si	silicon
Si-#	silicon in the crystalline phase #, # representing a Roman number
SiC	silicon carbide
SPH	smooth-particle hydrodynamics
USB	universal serial bus

Chapter 1

Introduction

1.1 Photovoltaic and Solar Industry

The ever increasing need for energy and pro-environmental policy pressure researchers to develop sources of sustainable and renewable energies. One of the most important sources of renewable energy lies in the solar energy. The most efficient and common way of harnessing solar energy is through photovoltaic (PV) cells. The amount of energy generated with PV increased by 23% in 2020, but the annual increase needs to rise to 24% per year between 2020 and 2030 to achieve the Net Zero Emission by 2050 Scenario [72]. With a market share of 95%, PV technology based on single- or multi-crystalline silicon (Si) wafers as substrates is the most important technology. High cell efficiency of up to 26.7% in the laboratory has been achieved [138]. The technology is sustainable: in Europe, the time for amortisation of the energy required for production of a PV system is lower than 1.2 years [138]. An impediment to widespread adoptions of PV as an alternative to traditional energy sources is the high cost of solar cells. 35% of the cost of a module produced at a 600 MW assembly centre in Australia is attributed to the wafer: approximately 0.1 USD/Wp [38]. A large lever to produce cheaper solar cells is reducing the cost of wafers: low-cost, thin wafers with high surface quality are needed [94].

In recent years, the global production capacity for PV modules exceeded demand, however, each preceding manufacturing stage provided a bottle neck: module manufacturing capacity was larger than cell capacity, which was larger than wafer capacity, which finally exceeded polysilicon production capacity [73]. The latest report on Photovoltaic Applications trends by the International Energy Agency [114] indicates that reducing polysilicon usage has led to a decrease in the thickness of 158.75 to 166 mm diameter wafers from 175 to 180 μm to 160 μm between 2020 and 2021. At the same time, the share of larger 182 to 210 mm wafers increased from 4.5% to 45%, also accompanied with a wafer thickness reduction. Further polysilicon yield increase is expected due to the ongoing efforts of improving the wafering process.

1.2 Diamond Wire Sawing

In the last decade, diamond wire sawing (DWS) has emerged as the main technology to cut hard and brittle materials and is most commonly used in manufacturing Si wafers for PV industry. Diamond-wire-sawn single-crystal Si wafers have proven to show high mechanical strength which enables the production of thinner wafers thus increasing yield [188]. The schematics of the process is illustrated in Fig. 1.1.

The ingot is fed onto a wire web that is created by winding the wire around guiding rollers with 600-800 parallel grooves. The wire moves in one direction for a couple of 100 m before it is decelerated and accelerated in the opposite direction. The backwards movement is shorter than the initial direction, hence new wire sections are introduced in each cycle [119]. Wire speeds reach up to 35 m/s on modern machines, with machine producers aiming for even higher speeds.

In DWS, abrasive grains are attached to a cold-drawn steel wire body with electroplating or resin bonding. For the purpose of cutting solar wafers or wafers for other semiconductor applications, electroplated wires are most commonly employed, where the diamond grains are held by a metal filler (nickel - or nickel-cobalt alloy), see Figure 1.2a. Wire core diameters

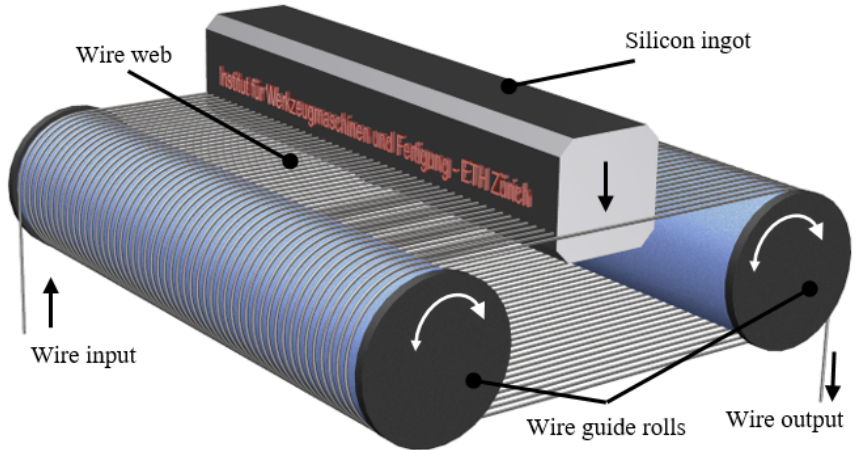


Figure 1.1: Schematic of the multi-wire sawing process.

are in the range of $60 - 140 \mu\text{m}$ with typical abrasive grain sizes in the range of $8 - 25 \mu\text{m}$. A scanning electron microscope (SEM) image of an electroplated diamond wire is presented in Figure 1.2b. The surface of the unworn wire and the diamond grains are completely or partly covered with the Ni-filler material that wears off as the wire wear propagates leading to exposure of cutting edges of diamond grains.

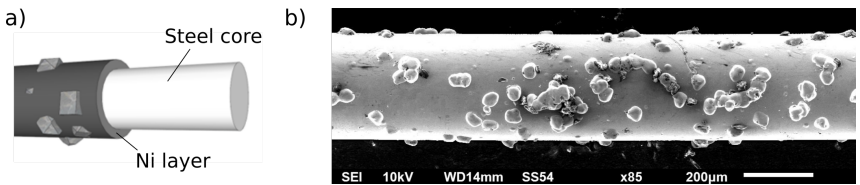


Figure 1.2: a) Steel core and Ni-filler layer of an electroplated diamond wire, b) SEM image of an unworn electroplated diamond wire, from [132].

The efficiency of the wire sawing process is determined by the output rate that can be defined as the number of fault-free wafers produced per Si-ingot and unit time. A significant amount of material is lost due to the cutting kerf and post-conditioning of the sawn surfaces [26]. Reduction of kerf loss by reducing the wire diameter has been of interest to reduce

the material consumption. Furthermore, the efficiency can be increased with decreasing wafer thickness, since a higher number of wafers can be produced from one ingot [119]. A general lower bound for the wafer thickness due to its brittle characteristics has been determined to be 80 μm [142]. Thinner wafers have advantages when being used for PV cells: with improved light-trapping techniques, wafers as thin as 50 μm made of low-quality Si have the potential of outperforming thicker wafers [6].

1.3 Motivation: Current Research Areas

Thinner wafers and wires increase the process complexity, as both become more prone to failure and decrease the size of the process window. In order to being able to approach the theoretical limits, a sound understanding of the interaction between tool and workpiece is necessary.

On the grain-workpiece interaction level, the process of cutting Si is extremely complex: the generally brittle material can be cut with ductile material removal mode, if a certain critical penetration depth is not exceeded. This depth in turn depends on the geometry of the tool, the crystallographic direction, the cutting speed and the temperature. While ductile removal is generally favoured since no cracks are generated that propagate into the surface and lower the fracture strength of the wafer, ductile removal requires a transition of the brittle Si-I phase to the metallic and meta-stable Si-II phase. This phase transition is problematic as it sets off a suit of phase transitions when the load is taken from the material and eventually leads to amorphisation of the silicon on the surface. Phase changes are accompanied by volumetric changes that lead to residual stress in the wafer, which may lead to undesired deformation of the wafer. In recent years, efforts to understand the mechanisms of the ductile-to-brittle transition as well as the effect of process parameters on phase transitions, have intensified.

In the field of these fundamental aspects of material removal, the present study aims at understanding the effect of grain shape, depth of cut and corresponding process forces on pressure exerted onto the workpiece ma-

terial. The pressure triggers phase transition. The analysis is built upon the theory of scratch and ploughing hardness. The empiric data-basis is derived from scratch tests with hardness indentation tools made of diamond, with a contact length of up to 30 mm and cutting speed of 25 m/s.

On a macroscopic perspective, the process is far from trivial as well: Since the wire provides a compliant support for the grains, the shape of the tool and thus the trajectory of the grains depends on process forces. The bow of the wire in stationary process condition is mainly determined by on wire speed, ingot feed speed and wire tension. These process parameters lead to a distribution of normal- and cutting forces acting on the wire through the individual grains. The pressure the grains exert onto the silicon determine the material removal mode as well as the removal rate. Investigating the process is inhibited by high material and tool cost when using industrial machines, as well as challenging accessibility of the processing zone. Laboratory-scale wire saws typically do not reach the wire speeds of industrial machines. While parameter studies evaluating roughness and subsurface damage, as well as resulting process forces are abundantly available, a generic transfer function linking wire properties and kinetic parameters with the removal rate is currently unknown. The ratio of cutting to normal forces is insufficiently described. Few studies investigated the effect of phase transitions on wafer warp.

The DWS process is addressed with a model of the wire bow that results from prescribed process parameters and the compliant tool. A discussion of the ratio between cutting and feed force acting in the process sheds light onto the importance of process parameters and wear on the cutting ability of the wire. A model for the material removal rate is derived from applied process parameters and tools. The validation is done via experiments on an endless-wire-saw designed and built specifically for this purpose.

Chapter 2

Literature Review

This chapter presents the state of the art of silicon-ingot DWS. It provides the necessary theoretical framework for the thesis and serves as a baseline to develop the research question and hypothesis. The chapter is structured in three parts: First, important material properties of silicon and diamond are introduced. Next follows a section about material removal, which introduces scratch tests as a way of material testing and the concept of scratch and ploughing hardness, phenomena of brittle and ductile removal and friction between silicon and diamond. The chapter closes with a section about the kinetics of a diamond wire saw.

2.1 Workpiece and Tool Material

In this section, fundamental material properties and behaviour of the workpiece material Si and the tool material diamond are summarised.

2.1.1 Workpiece Material Silicon

Si is the second-most-common element in the crust of the earth. Due to its abundant availability and electrical properties, it is commonly used as

a semiconductor in various electrical components. It is a semi-metallic element found in the fourth group of the periodic table. At room temperature, Si crystallises in the cubic-diamond lattice structure Si-I. The elementary cell consists of 18 Si atoms, see Fig. 2.1. Other crystalline forms of Si are metastable at atmospheric conditions. Especially the compositions Si-II and Si-IV are relevant in the machining of Si and will be discussed later on.

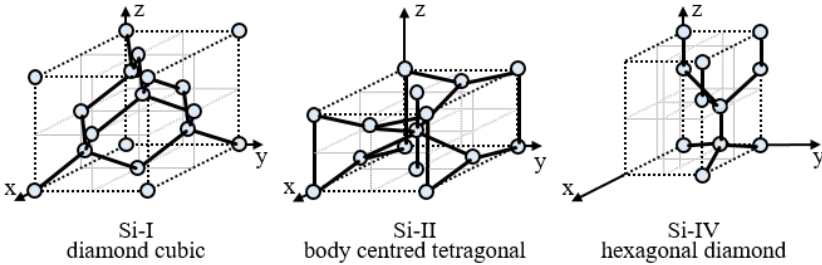


Figure 2.1: Lattice structure of Si crystals: stable composition at room temperature Si-I and metastable metallic structures Si-II and Si-IV, after [9, 31].

In crystalline form, Si shows strong anisotropy, meaning that the material properties depend on the lattice orientation. Commercial Si ingots are typically drawn along the $[111]$ -axis or $[100]$ -axis [128], while the latter is typically used for PV cells and the earlier for other semiconductor applications.

Some of the properties of single crystalline Si are given in Tab. 2.1. At atmospheric pressure the lattice does not transform with temperature changes until melting at 1683 K [140]. Due to the covalent bonds, the electron movement is aggravated at room temperature, the fracture stress is reached without substantial creep or flow at room temperature. Plastic flow can occur at temperatures above 800 °C [128].

While dislocation movement is impeded, the Si lattice changes its structure under pressure. According to PAGE et al. [130] the dislocation nucleation in silicon upon indentation is determined by whether the critical

Table 2.1: Properties of Si-I single crystalline silicon [103, 128, 190].

Crystal structure	diamond cubic
Young's modulus E [GPa]	$E_{[100]} = 131$, $E_{[110]} = 169$, $E_{[111]} = 187$
Vickers hardness H_V [GPa]	10.0
Fracture toughness K_c [$\text{MN m}^{-2/3}$]	0.6
Fracture strength σ_f [GPa] (load direction $\langle 100 \rangle$, surface orientation (100))	5.31 ± 1.26 [4]
Poisson's ratio ν	0.27
Density ρ [g/cm^3]	2.33
Melting point M_p [K]	1685 ± 2
Solid heat capacity $C_{25^\circ\text{C}}$ [$\text{J}/(\text{mol K})$]	20.007 [39]
Thermal conductivity at 300 K λ [$\text{W}/(\text{m K})$]	156 [71]

shear stress for the dislocation movement is reached before a critical hydrostatic pressure for densification (10 – 20 GPa) is reached. This suggests a dependence on contact scale, load and geometry. Indentations at around 350 nm loaded depth lead to structural rearrangement and amorphisation as well as dislocation structures, while indentations at 250 nm show a densification transformation but only little dislocation nucleation.

At room temperature, the cubic diamond structure of Si-I subsists up to a pressure of $\sim 9 - 16$ GPa. Upon exceeding the threshold, an allotropic change is initiated to the denser β -tin structure Si-II. Also Si-IV can be formed immediately from Si-I, prior to the transformation to Si-II [79], which was however mainly observed in hot indentation tests [37]. Eleven more crystalline phases of Si have been identified [41, 71], along with an amorphous phase (α -Si). Upon release of pressure, and with sufficient annealing time or temperature, the material transitions back to Si-I, however not necessarily immediately but via other phases as Fig. 2.2 shows. The order of phase transitions furthermore depends on the rapidity of pressure release.

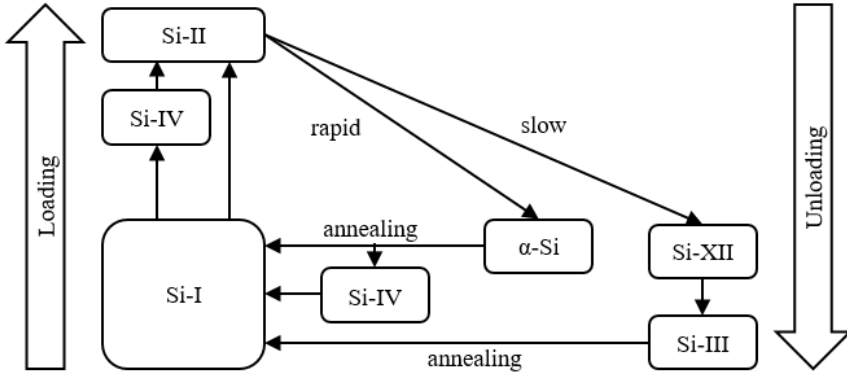


Figure 2.2: Phase transitions in silicon under static contact loading and subsequent annealing, from [79].

Withdrawing the indenter at rates faster than 1 mm/min during unloading implies no sufficient time for the reconstruction of the Si lattice, leading to the formation of amorphous material, instead of the kinetically controlled Si-II to Si-XII phase transformation [79]. This agrees with the observations made in scratching experiments with low scratching speeds of 1 – 10 $\mu\text{m/s}$, where the sequence for slow static contact unloading was observed, with the only difference being a transition back to Si-XII after reaching Si-III [190]. In the m/s-range however, mainly Si-IV and α -Si were reported [164], suggesting that the unloading rate is not the only decisive factor.

Tab. 2.2 summarises the different phases of Si along with their conditions. A common method of determining the presence of crystalline phases is Raman backscattering [78]. The wave-numbers associated with the phases are also indicated in the table and taken from measurements in scratched grooves excited with a 488 nm laser [92, 164]. The Raman shift depends also on the strain in the material, therefore the values are indicative. An annealing temperature of 500 $^{\circ}\text{C}$ is sufficient to transform all phase changed material induced by scratching back to Si-I [27].

Hydrostatic pressure values indicated in Tab. 2.2 refer to the transition to the phase mentioned in the table from the corresponding phase as in-

Table 2.2: Phases of silicon after [41, 71], Raman shift from [92, 164].

Label	Lattice structure	Hydrostatic pressure GPa	Raman shift 1/cm	Primary source
Si-I	diamond cubic	0.1 – 12.5	520	[22, 68]
Si-II	body centred tetragonal (β -tin)	8.8 – 16	n.a.	[67, 68, 74, 125]
Si-III	body-centred cubic	2.1	166, 432, 464	[1, 67, 68, 80]
Si-IV	hexagonal diamond	from Si-I at 450 – 650 °C	290, 497 – 510	[141]
Si-V	primitive hexagonal (zinc-blende)	14 – 35	n.a.	[68, 125]
Si-VI	(undefined)	34 – 40	n.a.	[44, 125]
Si-VII	hexagonal closest packed	40 – 78	n.a.	[44, 67, 125]
Si-VIII	tetragonal	14.8 \rightarrow 0.1	n.a.	[191]
Si-IX	tetragonal	12 \rightarrow 0.1	n.a.	[191]
Si-X	face centred cubic	78 – 230	n.a.	[43, 44]
Si-XI	body centred orthorhombic	13 – 15	n.a.	[117]
Si-XII	trigonal	2	350, 384	[36, 79, 139]
Si-XIII	diamond cubic	0.1	n.a.	[21, 32, 79, 130]
α -Si	amorphous	0.1	150, 300, 475 (all broad)	[164]

dicated in Fig. 2.2 where applicable. Si-I to Si-II transition happens at 9 – 16 GPa under near-hydrostatic stress [67, 68, 74, 125]. The transition is not reversible since Si-II transforms into other metastable phases depending on how the pressure is released. Upon slow pressure release, Si-XII forms at 10 – 12 GPa [36, 139], followed by a partial transformation to Si-III. Some Si-II remains present until reaching ambient pressure [41]. The generation of the Si-IX phase from Si-I to Si-II phase upon rapid pressure release from 12GPa has been reported [36, 191], although not in indentation tests [41]. It is believed that the formation of Si-IX precedes the formation of amorphous silicon at fast unloading rates [41] since its structure is the closest to amorphous silicon [76].

When pressure is induced by a sharp and pointy indenter, very high stress at the tip is quickly reached. Upon unloading, the transformation reverts, recovering parts of the indenters displacement by a non-elastic process [65]. This implies that shape recovery after indentation is not only due to the elastic response of the material but also due to plasticity in the phase transition. The non-elastic deformation stems at least in part from volume change due to density differences of the phases. It was found that $\rho_{\text{Si-XII}} > \rho_{\text{Si-III}} > \rho_{\text{Si-I}} \sim \rho_{\text{Si-IV}} > \rho_{\text{a-Si}}$ [41].

The Si-I to Si-II transformation results in $\sim 20\%$ densification. Upon slow decompression, transition from Si-II to Si-XII leads to $\sim 9\%$ volume expansion, with $\sim 2\%$ recovered from the Si-XII to Si-III transformation at low pressures, since the equilibrium Si-III structure was found to be $\sim 9\%$ denser than Si-I and $\sim 2\%$ less dense than Si-XII. Finally, the hexagonal diamond Si-IV phase has an atomic volume identical to that of Si-I. [41]

2.1.2 Tool Material Diamond

Diamond wire is made up of cold-drawn steel wires with diamond splinters held in a nickel matrix electroplated onto them. In the following paragraphs, important properties of diamond are presented.

Diamond is an allotrope of carbon, crystallised in cubic diamond structure, the same as Si-I. Diamond is metastable at room temperature and atmospheric pressure, but conversion to the stable form of carbon, graphite, is very slow. It is the hardest material known and therefore suitable for abrasive tools. It moreover exhibits further favourable properties such as high thermal conductivity and high chemical inertness. From a chemical perspective, synthetic and natural diamonds are identical and feature the same mechanical properties. Some properties of diamond are recapitulated in Tab. 2.3

Since diamond is metastable, high temperature or stress may accelerate graphitisation. The decomposition further depends on the atmosphere. Diamond graphitises at 1973 K in vacuum after less than 15 min [66] and at around 900 K in air [52]. It was calculated that diamond may undergo graphitisation at shear stresses of 95 GPa, it was noted that the effect

Table 2.3: Properties of diamond [147] apud [53].

Crystal structure	face-centred (diamond) cubic
Young's modulus E [GPa]	1141
Shear modulus G [GPa]	553
Bulk modulus E [GPa]	442
Poisson's ratio ν	0.07
Density ρ [g/cm ³]	3.52
Compressive yield strength σ_y [GPa]	130-140 [45]
Thermal conductivity λ [W/(m K)]	900-2320 [170], 2000-2200 [118]

is anisotropic [24]. Traces of graphite were found on diamonds used for sawing of Si [180]. Diamond starts to oxidise at lower temperatures of around 625 °C [185]. Diamond can form carbides with Si (SiC) at higher temperatures and pressures [185], which was also observed when cutting Si [192].

2.2 Material Removal

Material separation through abrasion of chips is the consequence of a typically harder tool body (in this case diamond, section 2.1.2) penetrating a softer workpiece body (in this case Si, section 2.1.1), thereby inducing plastic and elastic deformation and eventually material separation and fracture. According to DIN 8580 [46] manufacturing processes that separate material are classified in 5 groups, of which the group 2, chipping with a geometrically defined cutting edge such as turning, and group 3, chipping with geometrically undefined cutting edges such as grinding or honing, are of particular interest in the context of this work. Material separation happens if the shear stress surpasses the material strength, either through fatigue or exceeding the ultimate strength.

Depending on the direction and amplitude of load, a ductile or brittle material response can be achieved. When the applied stress exceeds certain

limits, a transition from elastic to plastic behaviour or material failure may be observed. Ductile and brittle material removal are illustrated in Fig. 2.3.

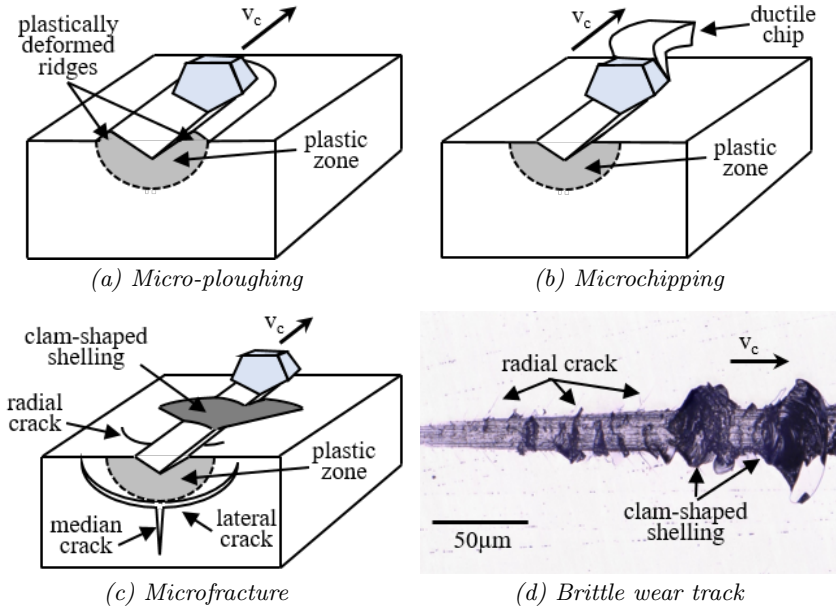


Figure 2.3: Different abrasive material removal modes: ductile modes a) micro-ploughing, b) micro-chipping and brittle mode c) microfracture, d) micrograph of a wear track in Si in the range of the ductile-to-brittle transition.

In either removal mode, a plastically condensed zone forms under the wear track. When the stresses are not sufficient to form a chip, the abrasive grain ploughs through the material and generates plastically deformed pile-ups, ridges, on the sides of the wear track, as shown in Fig. 2.3a. If a successive grain passes near the ridges, the material may fracture due to fatigue and be removed. In the case of machining through ductile chip removal, as depicted in Fig. 2.3b, the formation of a chip is associated with plastic flow and exceeding the fracture strength locally. Brittle material removal shows failure with no or little plastic deformation and propagation

of cracks. The different crack systems are shown in Fig. 2.3c. Large material volumes that have not been subjected to excessive stress may be removed if cracks grow to the surface. The micrograph shown in Fig. 2.3d shows the onset of fracture on a wear track in Si, with clam-shaped shelling of material where the cracks intersect. The mechanics of the two material removal regimes and their necessary conditions is discussed in the following sections.

2.2.1 Scratch Tests as a Means of Analysing Material Removal and Hardness

Scratch tests with a single diamond tip on a monocrystalline Si surface have been developed to study the material removal mechanism for the fixed abrasive sawing process. Because of the size distribution of the diamond particles on the wire, the forces and indentation depth vary throughout the process, leading to changes in the material removal mode. Therefore, it is important to know the influence of process parameters on the surface quality. Under normal sawing conditions, the size distribution will also change due to wear or pull-outs which changes the total forces [132, 133]. There is considerable interest focused on the machining of Si and process parameters prediction. GOGOTSI et al. [60] affirmed that prediction of the conditions for ductile regime machining of brittle materials from scratch tests is possible for diamond wire sawing.

Scratch tests are often used to analyse material removal at small scales, at penetration depths in the nano- or micrometer range. In-situ process parameters such as forces and temperatures, as well as residual properties such as wear, removed volume, edge zone damage or phase change can be measured.

Test rig designs for scratch tests

Many different setups are reported on in literature. Often, scratch tests are carried out in atomic force measurement devices, which is convenient but limited to very small scales and speeds. An overview of scratch test designs is presented in [131]. Limitations to the speed range of scratch-

ing experiments are typically due to the high engagement frequencies in rotatory setups which excite the force dynamometers or the short contact lengths. Linear setups are limited by the acceleration and final velocity of the axis. Some relevant setups are presented here.

MELKOTE et al. performed several studies on scratched Si [93, 95, 96, 164, 167, 172, 173]. They used a set-up consisting of a vacuum chuck or other holder mounted to a force dynamometer on a x-y-z-stage. A disk holding an indenter eccentrically is attached to a spindle mounted above the vacuum chuck. By fixing a piece of a polished wafer on the vacuum chuck and moving it sideways while the spindle is rotating, a series of quasi-parallel scratches with a depth adjusted via the z-stage is achieved. Cutting speeds of up to 25 m/s were achieved. Linear scribing was performed by mounting the indenter above the vacuum chuck directly without a spindle and using the x-y-stage to displace the wafer at speeds of up to 100 mm/min [93, 95, 172, 173]. In a similar way, diamond wire can be clamped instead of the indenter and used as a scratching tool [96].

PALA et al. used a setup in which a Si workpiece is clamped to the spindle of a machine tool, rotated and moved sideways across a diamond wire bent around a sharp tip with an isolated grain on top, thereby achieving sections of circular scratches with lengths of up to 40 mm at cutting speeds of up to 20 m/s. The tool is mounted on a dynamometer and a pyrometer fibre is pointed at the diamond, allowing for measurement of forces and temperature [87, 131, 134].

Indentation hardness, scratch hardness and ploughing hardness

Hardness is a material property, which is a measure of the resistance of a material to penetration by a body. In classic indentation hardness tests, such as Vickers, Rockwell, Brinell or Knoop hardness tests, a geometrically defined body is penetrated into another one with controlled force, velocity and/or distance. Another way of determining hardness is to evaluate the ability of one material to abrade or scratch another material [171]. Even though the tests for determining the scratch hardness have not been formalised to the same degree, they have been used

from early on and one of the earliest hardness scale is that developed by MOHS in 1824 [120]. In the following paragraphs, after shortly pointing to established hardness measurement methods, concepts of hardness measurement by indentation put forth by OLIVER AND PHARR [126, 127] are introduced to set a framework before elaborating on analytical models of scratch hardness as described by WILLIAMS [171].

In Rockwell measurement, a spherical indenter tip is pushed into the work-piece with a defined force and duration and the hardness is derived from the penetration depth [49]. In Brinell hardness measurement, it is calculated from the applied force and the diameter of the residual imprint left by a sphere [48]. The Vickers method uses a pyramidal indenter but is otherwise identical to the Brinell method: the hardness is evaluated on the basis of the indentation force and the area of the imprint left on the surface [50]. The Knoop hardness test is a variation of the Vickers test, where a rhombic indenter is used [51]. The methods have different areas of application and are chosen on the basis of hardness of the test material, scale as well as layer thickness and distance of the test location from the specimen edge.

In summary, indentation hardness measurement methods use some kind of load-displacement relationship. OLIVER AND PHARR analysed the load-displacement curves of different ductile and brittle materials and derived a measurement methodology [126] and later refined and elaborated upon it [127]. Earlier, SNEDDON had shown that for any indenter, the relationship between load F_n , displacement h and contact area is given by the function of a solid of revolution of a smooth function [150]. For simple geometries, the load-displacement function can be described by a power law of the form

$$F_n = bh^m \tag{2.1}$$

where b is a constant depending on the material properties and the indenter shape and m is a constant depending on the indenter shape only. The constants can be determined analytically. The exponent is given as $m = 1$ for a flat cylinder, $m = 2$ for a conical shape, $m = 1.5$ for spheres

at small displacements and a paraboloid of revolution, and $m = 1.38$ for a Berkovich indenter [136]. OLIVER AND PHARR's analysis starts from the assumption, that the behaviour of conical or paraboloid of revolution-shaped indenter as resolved by SNEDDON approximates the behaviour of other indenter geometries well. The conical indenter accounts for a geometrical singularity of the tip and represents Berkovich or Vickers pyramids in that way, and the area of the cross section varies with the square of the depth of contact [126]. The paraboloid of revolution features no such singularity and therefore accounts for some rounding of the tip. Another assumption is that the elastic unloading of a flat, semi-infinite half space is the same as that of a real indented surface [126].

The geometry of a hardness indentation test and corresponding schematic loading and unloading curves are depicted in Fig. 2.4 and show most parameters necessary for the analysis.

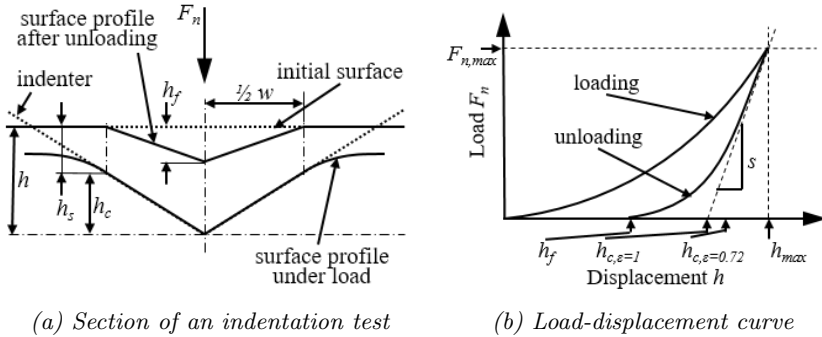


Figure 2.4: Schematics of an indentation test: a) cross section of the surface during and after loading with quantities, b) load-displacement curve with graphical interpretation of the contact depth h_c , after [126]

Fig. 2.4a shows a schematic of a cross section of an indentation test with the trace of the surface before, during and after loading with a pointy indenter. The total displacement while any load is applied h is

$$h = h_c + h_s \quad (2.2)$$

where h_c is the contact depth and h_s is the depth at which the indenter loses contact with the material as the surface at the perimeter of the contact is displaced. At maximum load $F_{n,max}$, the total displacement reaches h_{max} , as seen in Fig. 2.4b. The radius of the contact is $\frac{1}{2}w$, half the width in the cross section. When the load is removed, some of the displacement is elastically recovered, leaving an impression with the residual depth h_f , while the width of the imprint is as large as the width of the contact at maximum displacement.

As seen in Fig. 2.4b, the stiffness in the beginning of the unloading state $S = dF_n/dh$ can be determined experimentally and can be determined as

$$S = \frac{dF_n}{dh} = \beta \frac{2}{\sqrt{\pi}} E_{eff} \sqrt{A_n} \quad (2.3)$$

with the effective elastic modulus E_{eff} that takes compliance of both the specimen and the indenter into account

$$\frac{1}{E_{eff}} = \frac{1 - \nu_s^2}{E_s} + \frac{1 - \nu_i^2}{E_i} \quad (2.4)$$

E_s and ν_s being the Young's modulus and Poisson's ratio of the specimen and the indenter, and A_n the normally projected area of the elastic contact [126]. The geometrical shape of pyramidal indenters cannot be parametrised as a solid of revolution of a smooth function. The resulting stiffness deviations can be corrected by applying a dimensionless parameter β [127], that is approximated on the basis of the half included indenter angle φ and the Poisson's ratio of the specimen ν_s [63]

$$\beta = \pi \frac{\left[\frac{\pi}{4} + 0.155 \cot(\varphi) \frac{1-2\nu_s}{4(1-\nu_s)} \right]}{\left[\frac{\pi}{2} - 0.831 \cot(\varphi) \frac{1-2\nu_s}{4(1-\nu_s)} \right]^2} \quad (2.5)$$

Equation (2.3) holds for any indenter of the shape of revolution of a smooth function [137], and is reasonably correct for Vickers and Berkovich indenters [19, 86].

A_n is a function of the contact depth h_c and can be determined from the indenter geometry by measurement. The contact depth h_c is also determined from experimental data as

$$h_c = h_{max} - h_s \quad (2.6)$$

and the elastic deflection of the surface follows from SNEDDON's analysis [150] for a conical indenter

$$h_s = \frac{\pi - 2}{\pi}(h - h_f) \quad (2.7)$$

Consideration of (2.7) limits the applicability of the model to cases where pile-up is negligible. The effect of pile-up is discussed in [127]. The force-displacement analysis furthermore gives

$$(h - h_f) = 2 \frac{F_n}{S} \quad (2.8)$$

When considering peak load, (2.7) and (2.8) yield

$$h_s = \epsilon \frac{F_{n,max}}{S} \quad (2.9)$$

with the geometric constant ϵ . For a conical indenter $\epsilon = \frac{2}{\pi}(\pi - 2) \approx 0.72$. For a flat punch, $\epsilon = 1$, for a paraboloid of revolution $\epsilon = 0.75$ and for a Berkovich indenter $\epsilon = 0.76$ [136]. In the graphical representation of the unloading curve in Fig. 2.4b, the effect of different values of ϵ is indicated, while only the case of the flat punch is correctly represented by the linear-elastic behaviour of the initial unloading curve and other indenters reach higher contact depths [126]. Besides the modulus, the static indentation hardness H_c is defined as

$$H_c = \frac{F_{n,max}}{A_n} \quad (2.10)$$

OLIVER AND PHARR [127] pointed out, that by this definition of hardness as contact area under load, it diverges from the traditional method of measuring a residual imprint, and the derived hardness deviates especially if large elastic recovery is observed. BOLSHAKOV AND PHARR [13] noted, that when the proportion of the residual depth from total indentation depth exceeds $\frac{h_f}{h_{max}} > 0.7$, the method overestimates hardness significantly. It is therefore important to note, that this measure of hardness is not a material property but a process quantity.

If the indenter is moved sideways during the indentation, that is applying an additional tangential load F_t , the load-bearing area is reduced as the indenter forms a wear track and the rear faces on a Vickers and Berkovich indenter or rear half in case of a conical indenter do not support the normal load any more [171]. A schematic of the scratching indenter is shown in Fig. 2.5a, the corresponding load-bearing areas for pyramidal and conic indenters in normal and tangential direction are depicted in Fig. 2.5b.

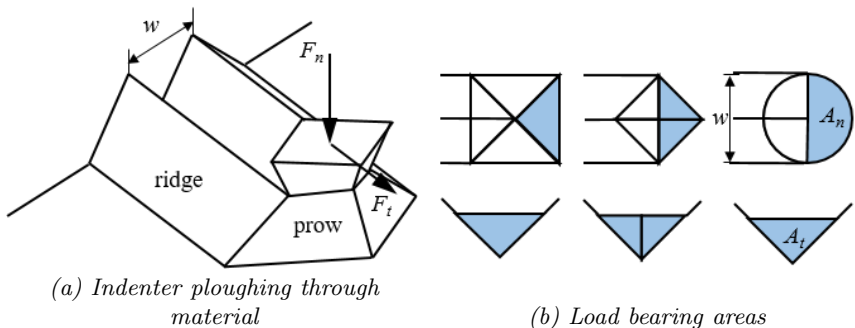


Figure 2.5: Schematics of a scratch test: a) indenter ploughing through material, pushing a proW and leaving ridges on the side of the scratch, b) top row: load-bearing areas in normal direction A_n during scratching (pyramidal indenter face first and edge first orientation and conical indenter), bottom row load-bearing areas in tangential direction A_t , after [171]

As a result, the indenter will sink in further in comparison with the static indentation test. A proW will form in front and ridges on the side of the indenter, adding some support and lifting it out of the material again.

The two effects will partially compensate each other in a steady state, where plastic deformation is also constant [171]. Scratch hardness H_s can be defined as the static indentation hardness

$$H_s = \frac{F_n}{A_n} \quad (2.11)$$

while the load bearing area is now that which is supported by material during scratching. In the same way, the hardness can be evaluated in tangential direction, leading to the definition of the ploughing hardness H_p

$$H_p = \frac{F_t}{A_t} \quad (2.12)$$

The load bearing areas A_n and A_t in (2.11) and (2.12) are the areas of the indenters supported by material projected into the vertical plane normal to the direction of the normal load and the sliding direction, respectively, as indicated in Fig. 2.5b.

It was shown that scratch hardness differs from indentation hardness using identical indenters [17, 20], which is associated with different rates of material displacement, work-hardening and variations in the measurement of the topography of the residual surfaces. Since scratch hardness measurements vary significantly with crystallographic anisotropy and their control is crucial, comparing independent investigations is challenging [17]. This underlines again, that measures of hardness that relate an area with an applied load are specific process forces rather than quantities describing a material parameter.

When scratching brittle materials, hydrostatic compression forms under the indenter, leading to a plastic zone surrounding the area of impression (see Fig. 2.3c) and to plastic deformation and/or ductile removal and inhibiting brittle fracture. As the penetration depth h increases, cracks may develop. The local plasticity moves the concentration further into the material below the indenter, where median cracks nucleates. As the indenter moves forward, lateral and radial cracks develop with release of

the load, behind the indenter. Consideration of an energy balance shows a scale effect [171]: elastic strain energy released in cracking has to equal the surface energy of the cracks generated. The released elastic energy depends on the volume of a cube with a characteristic length in which the elastic strain energy is confined. The surface energy of the generated crack depends on its length squared. Therefore, the smaller the indentation, the larger is the shear stress required to produce cracking.

An additional scale effect stems from the consideration of defects in the bulk material, for instance dislocations. When these are present, the stress necessary to initiate plastic deformation is much smaller than in a perfect crystal, where dislocations have to be generated. At small scales of micro scratching experiments, at depth between 1 nm to $\sim 10 \mu\text{m}$, it may be assumed that the crystal is defect-free [171]. Note that in mono-crystalline Si, the bulk material may be assumed to be defect free, but cracking will occur before reaching depths of more than $\sim 2 \mu\text{m}$ or less depending on the crystallographic orientation. Furthermore, phase transformation due to high load is likely to happen before to dislocation nucleation [55]. The scale effect was shown in molecular-dynamics simulations, where the specific energy per area displaced increases with decreasing depth of cut [8], see Fig. 2.6. This specific energy corresponds to the ploughing hardness.

CHAVOSI et al. [27] reported observing strain hardening when scratching Si with Berkovich indenters in different configurations at higher speeds of $10 \mu\text{m/s}$ as opposed to $1 \mu\text{m/s}$: The scratch hardness increased by more than 35% at room temperature and more than 20% at 500°C . The observation of increasing scratch hardness with increasing speed was confirmed on the nanoscale for speed ranges between 10 and $100 \mu\text{m/s}$; the scratch hardness then remained approximately constant up to the highest tested speed of $300 \mu\text{m/s}$ [149]. In that same study, the scratch hardness values when scratching with Berkovich face first were consistently higher than when scratching with edge first.

TSYBENKO et al. [156] performed scratch hardness measurements in different ductile and brittle materials and stated, that the scratch hardness in softer materials decreases with increasing depth, while it increases for harder materials, such as Si.

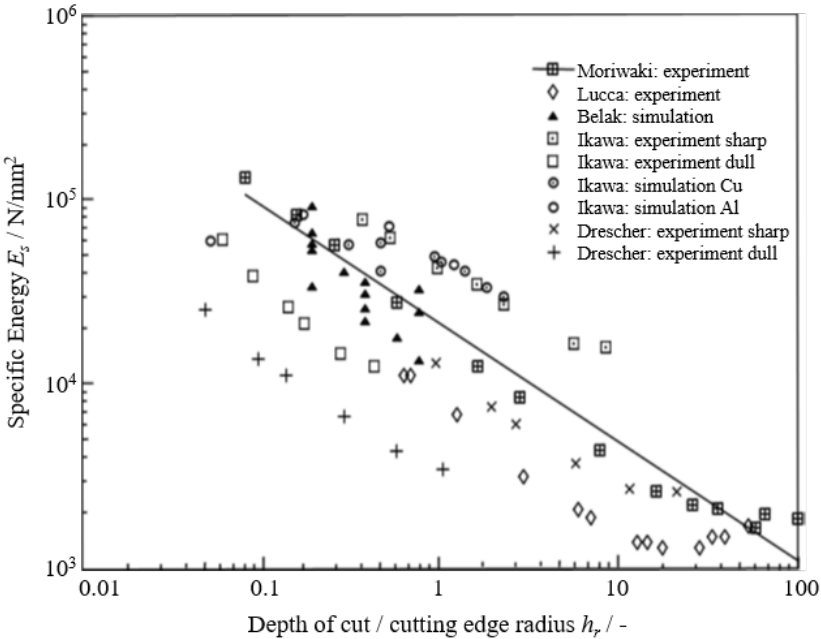


Figure 2.6: Curated experimentally and simulatively acquired data illustrating the scaling effect of specific energy with diminishing depth of cut normalized with the cutting edge radius. The observed proportionality of specific energy E_s with depth of cut h is $E_s \sim h^{-0.6}$, from [8].

Conclusion: Scratch tests, scratch hardness

Scratch tests are an established means to analyse material removal behaviour and to derive material characteristics. Scratch and ploughing hardness, which essentially describe the force necessary to deform the material in normal and tangential direction and constitute a process quantity, scale significantly with the penetration depth. Furthermore, when deviating from the idealised shape of an indenter that is described by a axisymmetric body, e.g. Vickers and Berkovich indenters that do not feature axial symmetry and more importantly arbitrary abrasive grits, the analytic solution is less accurate. WILLIAMS states, that Vickers indenter in face first orientation is supported on only a quarter of its projected

area (see Fig. 2.5b) [171], which neglects the effect of elastically recovering material on the flanks of the indenter and which does not agree with observations made when simulating the behaviour of Si scratched with a geometrically undefined grain [87]. The scratch and ploughing hardness of Si when using different indenter geometries have not been comprehensively determined, comparison of values determined in independent studies is problematic [17]. No studies on scratch hardness determined at speeds as high as in diamond wire sawing have been found.

2.2.2 Phenomena of Material Removal in Silicon

The following paragraphs deal with phenomena that occur in or are related to material removal when cutting Si with diamond, namely ductile and brittle removal modes as well as the transition between the two, and occurring phase transitions.

Brittle Material Removal

Brittle materials show a fracture strength that is lower than or similar to their yield strength. The abrasive material removal is governed by a sequence of crack initiation, crack growth and minor plastic deformation. As cracks grow to the surface of the workpiece or intersect, larger volumes of material are removed due to spalling. Three kinds of cracks can be distinguished as shown in Fig. 2.3c: axial or median, radial [100] and lateral cracks [113]. The mechanics of the formation of these cracks will be discussed in the following paragraphs.

Axial and lateral cracks are the result of stress field exceeding fracture strength caused by the indentation of a harder body into the specimen surface. A commonly-used configuration of the Hertzian contact theory used for the analysis of indentation applies an indenter assumed to be ideally rigid while the specimen is considered to be an ideally elastic and brittle flat half-space. The elastic stress field in this case is well defined until fracture occurs [98].

According to GRIFFITH'S theory of "*the phenomena of rupture and flow in solids*" fracture occurs at the position of greatest stress, while stress

is greatly intensified at flaws, and propagates in agreement with energetic equilibrium states [61]. The application of a pointy indenter leads to a singularity in the elastic stress field at the tip resulting in plastic flow. The indentation stress field always contains a tensile component; consequently crack initiation arises in brittle materials upon exceeding of the yield strength. Once a crack is initiated at a position of dominant flaw, it propagates in the material in an orientation that maximizes the mechanical-energy-release rate in an isotropic solid [98]. The formation of cracks during an indentation test of a brittle material with a pointy indenter is shown in Fig. 2.7.

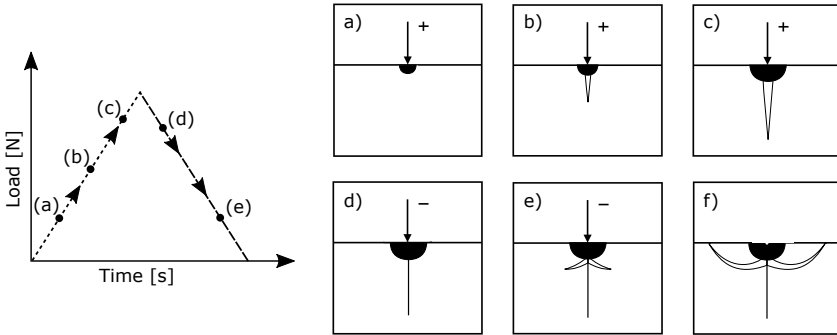


Figure 2.7: Load curve and schematic of crack formation in a brittle material upon indentation, [131] after [98].

According to Lawn et al. [98], the sequence for the development of the median-lateral-crack system is as follows: Upon contact, the indenter generates a zone of plastic deformation (a). With increasing load a median crack is initiated at the position of the dominant flaw, which in an idealised surface and isotropic material is at the tip of the indenter (b). As the load increases further, the median crack propagates stably (c). Upon unloading, the median crack closes (d). Further reduction of the load triggers the development of lateral cracks starting from the interface of the zone of plastic deformation and the lateral crack (e). As the load is removed completely, lateral cracks continue extending sideways and may grow to the surface, leading to chipping (f).

The radial cracks indicated in Fig. 2.3c (p. 14) are a consequence of a sliding movement of the indenter including friction. HAMILTON AND GOODMAN [62] derived an analytic solution for the determination of stress fields generated by a circular sliding contact on the basis of Hertzian contact theory. Radial cracks are a result of failure due to tensile stresses behind the indenter and their shape can be determined analytically. LAWN [99] further shows that the shape and extension of the cracks can be estimated by analysis of the principal stresses at the relative distance from the centre of the indenter along the crack path. He discusses that the stress trajectories indicate the shape of partial cone cracks well for crack lengths c in the magnitude of the indenter radius a , since σ_1 is always the greatest principal stress. However for crack length $c \gg a$, with increasing distance from the contact area, the principal stress σ_2 can become as large or larger as σ_1 , especially for large friction coefficients. In this case, the crack may deviate from its well defined path and description of the geometry becomes more difficult. LAWN [99] argues furthermore that in reality, the assumptions of the theory (Hertzian elastic theory with purely elastic respectively elastic-brittle indenter and specimen and idealised sliding motion free of stick-slip) are hardly met. Experiments performed by ZHANG et al.[190] indicate that Hertzian elastic contact theory is indeed not suitable to describe the behaviour for scratching Si with a Berkovich indenter.

In case of brittle material fracture during indentation, a model developed by MARSHALL et al. [113] accommodates spalling of material due to brittle fracture. The geometry of the lateral crack system, as well as the dimensions of the plastic zone are shown in Fig. 2.8.

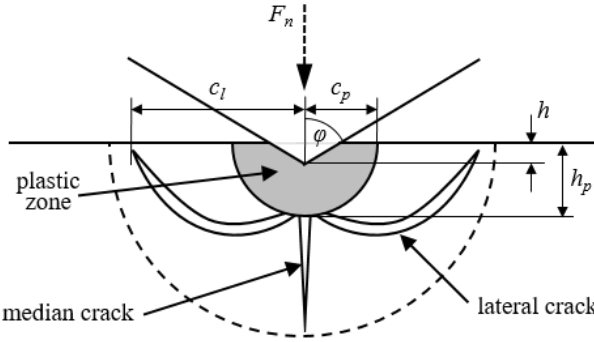


Figure 2.8: Schematics of the geometry of the lateral crack system in an indentation test with a sharp indenter and a brittle solid, upon release of the load F_n , from [113].

When material is removed due to the propagation of lateral cracks to the surface [122], the depth of the material removed equals the depth of the plastic zone where the cracks start [113]. The plastic zone extends equally in half width c_p and depth h_p [100] and equals the residual, measured depth, while the length of the lateral cracks c_l equals half of the measured width of the residual scratch. The displacement depth h can be determined with [113]

$$h = F_n \frac{Ac_l^2}{Eh_p^3} \quad (2.13)$$

where F_n is the peak point load applied onto the indenter, E stands for the Young's modulus of the indented material, and A depends on the relative sizes of lateral and median cracks. A is approximated as $A = 3(1-\nu^2)/4\pi$ for a full-plate approximation and $A = 0.75$ for a quarter-plate approximation, ν denoting the Poisson's ratio. The latter quarter-plate approximation implies that lateral cracks are shorter than median cracks, the earlier implies the opposite. In case of a sliding indenter, radial cracks develop additionally to median and lateral cracks and are approximately as long as the median cracks [100]. Since radial cracks are

visible upon close observation and often extend beyond the chipped-off width assumed to equal the length of the lateral cracks, the quarter-plate assumption is reasonable in this case.

The size of the plastic zone is derived from analysis of the elastic field and varies with [113]

$$h_p \sim c_p \sim \left[\left(\frac{E}{H} \right)^{1/2} (\cot\varphi)^{1/3} \left(\frac{F_n}{H} \right)^{1/2} \right] \quad (2.14)$$

with Young's modulus E , hardness H and half included indenter angle φ . Furthermore, the length of the lateral cracks c_l can be expressed as a function of material properties E , H , and the fracture toughness K_c , the applied load F_n and φ according to MARSHALL et al. [113]:

$$c_l = c^L \left[1 - \left(\frac{F_0}{F_n} \right)^{1/4} \right]^{1/2} \quad (2.15)$$

where c^L is called the limiting crack function and F_0 is the apparent threshold load. The limiting crack function is:

$$c^L = \left\{ \left(\frac{\zeta_L}{A^{1/2}} \right) (\cot\varphi)^{5/6} \left[\left(\frac{E}{H} \right)^{3/4} / K_c H^{1/4} \right] \right\}^{1/2} F_n^{5/8} \quad (2.16)$$

where ζ_L is a dimensionless constant independent of the material pair and is given as $\zeta_L = 0.025$, A is the same as in (2.13).

The threshold load has been defined by MARSHALL et al. and is not to be confused with the critical load for the onset of cracking:

$$F_0 = \frac{\zeta_0}{A^{1/2}} (\cot\varphi)^{-2/3} \frac{K_c^4 E}{H^3 H} \quad (2.17)$$

where $\zeta_0 = 1200$ for all cases.

Ductile Material Removal

Ductile removal is typically a mixture of plastic deformation and chip removal, visualised in Figs. 2.3a and 2.3b (p. 14).

In ploughing, no material is actually removed, instead the material is displaced by the indenter and pushed sideways. The plastically deformed ridges are strained and if deformed again by a following cutting edge may chip off due to fatigue. This mode is favoured when the active rake face (which may be on the rounding of the cutting edge for shallow depth of cut) features a large negative rake angle. As the negative rake angle becomes smaller (as in closer to zero), the shear stress in the prow of the indenter will eventually exceed the ultimate strength of the material and lead to material separation and chip formation.

Since perfect plasticity, in which the trace left by the indenter would have the exact shape of the indenter, does not exist in Si (and in metals, ceramics and most polymers in general), plastic deformation is always accompanied by elastic deformation. The extent of elastic deformation is defined by the elastic limit and the Young's modulus of the material. Elastic deformation is fully recovered after unloading.

In Si, according to HUANG et al. [70], the ratio of elastic recovery r_e over the penetration depth h decreases with increasing penetration depth and grain size. They proposed a semi-analytic model to derive the recovered depth for scratching with spherical bodies on the basis of the work of OLIVER AND PHARR [126]. Their grinding experiments with Si showed that rate of elastic recovery approaches 1 at very shallow penetration depth and follows a power law with a negative exponent. The rate of recovery decreases with increasing speed, grain size and tip or cutting edge radius [69, 70]. Purely elastic behaviour up to a penetration depth of approximately 250 nm when scratching a Si (001) wafer with a blunt Berkovich tip at 2 $\mu\text{m/s}$ velocity was observed by GASSILLOUD et al. [55].

Whenever plastic deformation occurs in a crystal, dislocations are nucleated, migrate or multiply. At room temperature, dislocation slip in Si is largely inhibited and is only eased at temperatures above 750 $^{\circ}\text{C}$ [103], which is more than 60% of the melting temperature. As the ultimate strength of Si decreases with increasing temperature, chip formation is

favoured at higher temperatures. Thermal softening and increased plasticity was reported when scratching wafers heated to 500 °C [27]. Extremely high flash temperatures exceeding 1500 K have been reported when scratching Si with diamond [134], suggesting that dislocation slip may actually play a role in ductile removal of Si. It is however not clear whether the material in the shear zone reaches such high temperatures, as the thermal conductivity of diamond is up to 14 times higher than that of Si (compare Tabs. 2.1 and 2.3 in sections 2.1.1 and 2.1.2). GASSILLOUD et al. [55] furthermore suggested that the stress needed for activating dislocation slip is higher than that which leads to a phase transition in Si.

Ductile-to-Brittle Transition

Balancing crack nucleation and growth, dislocation migration and phase transitions decides on whether Si is removed in ductile or brittle mode, meaning that a transition between the two modes happens.

Established models on the transition of ductile-to-brittle material removal regimes consider the critical penetration depth and material properties. Most prominent is a model proposed by BIFANO et al. [10]

$$h_{cu,crit} = \kappa \left(\frac{E}{H} \right) \left(\frac{K_c}{H} \right)^2 \quad (2.18)$$

where $h_{cu,crit}$ is the critical depth of cut for transition from ductile to brittle removal regime, E and H denote Young's modulus and Hardness as before, K_c is the fracture toughness, and κ is the material constant identified as $\kappa = 0.15$ for many brittle materials including Si.

Although several studies suggest that the transition is further dependent on parameters such as tool geometry [12, 60, 96], cutting speed [124, 164], crystallographic orientation [96, 172, 176], or lubrication [181] there are no established models defining the interconnection of such properties. Work on the topic is mainly limited to experimental research and more recent studies focus on finite element models. WANG et al. [167] published an extended finite-element-based model that accurately predicts the critical depth of cut. Deviations of the simulation from the experiments were

accounted to differences in the simulated and real tool geometry and the anisotropy of the fracture properties of silicon.

ZHANG et al. performed scratching experiments with Berkovich indenters [190]. Keeping the load constant, they scratched a polished silicon surface and measured the resultant cutting depth and investigated the topography of the scratch and phase transitions of the material. The effect of scratching speeds between 1 and 10 $\mu\text{m/s}$ was found to not have a significant effect on the maximum depth of cut and depth of the plastic zone. Plastic flow resulting from shear in the direction of the scratch was observed. Plastic deformation in the form of pile up at the edge of the scratches. No cracks (purely ductile material removal) were induced at loads of 10, 20 and 40 mN, lateral cracks were observed at loads of 60 and 80 mN and shelling occurred at loads of 100 mN.

The effect of crystallographic orientation on the ductile to brittle transition was thoroughly investigated by Wu and Melkote, who scratched Si wafers in the (111), (110) and (001) plane in different directions [173]. It was found that the ductile to brittle transition happens at lowest depths in the (001) plane, followed by (110) and (111) where the critical depth of cut varies significantly with the direction scratched. The critical depth of cut varies between 0.11 and 1.27 μm .

It was furthermore shown that the cutting force decreases with the appearance of first cracks [29].

Phase Transition and Analysis of the Crystallography

GOGOTSI et al. [59] demonstrated that phase transformations occur in a variety of silicon machining operations, including slicing, dicing and grinding. To study the effect, phase transitions in Si were experimentally induced by indentation or scratching, which is elaborated upon in the following paragraphs.

Phase transitions during indentation tests in Si have frequently been reported on, e.g. in [40, 42, 189]. A so-called pop-in and pop-out in the loading and unloading curves respectively is attributed to changing phases. The observations led to the development of a new constitutive material

model that accounts for several of the transitions and points out that they manifest in material hardening and volumetric change [161].

In indentation tests, a pop-in was observed at a penetration of around 210 nm, with loading of 10 GPa of pressure, which corresponds to approximately 30 mN load with a spherical indenter. A pop-out was observed upon unloading at ~ 200 nm and 15 mN load [161]. From the same experimental series, the formation of a metallic phase followed by the appearance of planar defects under the transformation zone, that was however transformed to an amorphous phase upon unloading was reported [189]. By modelling this transition from Si-I to the metallic Si-II phase and then to α -Si with an extended Drucker-Prager constitutive model, WANG et al. [167] were able to predict the ductile-to-brittle transition with an error of only 3% in an XFEM-model, which underlines the significance of the phase transition for ductile material behaviour.

GOGOTSI AT AL. [59] discussed the formation of a Si-II phase that is formed during scratching in the compression zone under the indenter and that this metallic phase can be removed in ductile mode, however it is transformed into Si-XII and Si-II behind the indenter immediately after the compression is removed. They further found that more amorphous Si is produced at lower depth of cut. In a different study they evaluated the effect of the indenter geometry on the residual phase in scratching and found similar behaviour for sharp and blunt tools with regards to the phase transition, even though the material removal behaviour varied [60].

YAN et al. [178] proposed the use of the Raman intensity ratio r to quantify the relative significance of two phases for the analysis of the Raman spectrum of Si. The thickness of the amorphous layer d_a is proportional to the ratio r of the intensities I_a of the α -Si peak with that of the Si-I peak I_c :

$$r = \frac{I_a}{I_c} \quad (2.19)$$

I_a and I_c are the integrals over the amorphous and crystalline peaks, respectively. A Gaussian distribution $f_{Ga}(\nu)$ is fitted to the broad amorphous

ous peak and a Lorentz distribution $f_{Lc}(\nu)$ to the sharp crystalline peak.

$$f_{Ga}(\nu) = h_a \exp\left(-\frac{(\nu - \nu_a)^2}{b_a^2}\right) \quad (2.20)$$

and

$$f_{Lc}(\nu) = \frac{h_c}{1 + (\nu - \nu_c)^2/b_c^2} \quad (2.21)$$

ν is the Raman shift, h is the height and b is the half-power bandwidth, with indices a and c indicating amorphous or crystalline phases. Integrating (2.20) and (2.21) and substituting in (2.19) yields

$$r = \frac{\int f_{Ga}(\nu)d\nu}{\int f_{Lc}(\nu)d\nu} = \frac{h_a b_a \sqrt{\pi}}{h_c b_c \pi} = \frac{1}{\sqrt{\pi}} \frac{h_a b_a}{h_c b_c} \quad (2.22)$$

YAN et al. [178] identified a strong, locally linear correlation between the logarithm (base 10) of the Raman intensity ratio $r_{\alpha-I}$ of α -Si to Si-I and the thickness of the amorphous layer d_a as shown Fig. 2.9a.

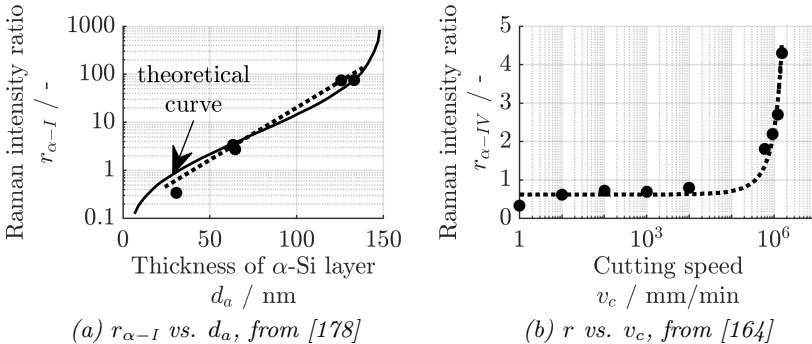


Figure 2.9: Dependencies of the Raman intensity ratio: (a) relation between the Raman intensity ratio $r_{\alpha-I}$ of α -Si to Si-I and the thickness of the amorphous layer and (b) change of the Raman intensity ratio $r_{\alpha-IV}$ of α -Si to Si-IV with increasing cutting speed v_c .

The effect of scratching speed on phase transformation in high-speed scratching of monocrystalline Si was studied by WANG et al. [164]. With variable loading/unloading rates different phases of Si are formed. The study also shows that with cutting speed up to 1 mm/min, the unloading rate is not high enough to produce amorphous silicon but only Si-III and Si-XII – those phases were not produced on cutting speeds higher than 1 mm/min where only Si-IV and α -Si were observed. WANG et al. furthermore evaluated the Raman intensity ratio of α -Si to Si-IV and found a strong dependency on the scratching speed as shown in Fig. 2.9b. A significantly larger amount of α -Si is produced at higher scratching speeds.

Conclusion: Material Removal in Si

The material removal behaviour of Si is a complex and highly researched topic. The greatest challenge is to transfer the observations in the micro and nano range to the dimensions that exist in the wire sawing process. Here, a need for research on the effect of high cutting speeds and different grain geometries on the material removal mode and, when ductile removal is concerned, the phase change in the material is identified. In addition, due to the challenging experimental parameter range, the development of constitutive material models is interesting, which can represent the high shear rates during cutting and phase changes.

2.2.3 Friction

Fundamental Aspects of Friction

Friction describes the restrictive reaction when one body is moved or attempted to be moved tangentially to another one [23]. The classic friction laws were put forward by AMONTONS in 1666 (friction is proportional to the normal force applied $F_r \propto F_n$, and friction is independent of the nominal contact area A_0) and DE COULOMB (sliding friction is not dependent on the relative velocity of the bodies v). AMONTONS' first law can be used to quantify the reactive friction force F_r in terms of the acting normal force F_n by introducing a proportionality coefficient of friction μ :

$$F_r = \mu F_n \tag{2.23}$$

μ depends mainly on the materials of the contact bodies. It was later shown that friction is proportional to the true contact area A_r due to roughness on the micro-scale which leads to adhesion on the individual contact spots [15]. Since the size and amount of contacts making up the true contact area are proportional to the normal load, the same holds for the friction force according to Amonton's first law. For that reason, the true contact area being smaller for a harder contact pair subjected to the same load, friction is generally lower for harder materials than softer ones, albeit the hardness having only a minor influence on friction [121]. It was shown that the coefficient of friction remains constant over a very large range of normal forces ranging from 10^{-5} to 10^4 N in case of rubbing of steel against poly-tetrafluoroethylene (PTFE) [146].

These laws have proven useful on the macroscopic scale and for dry, unlubricated friction which describes a wide range of engineering applications. On the atomic scale, frictional phenomena are more complex, as experiments with atomic force microscopes [64, 187] and by means of molecular dynamics simulation [7] showed temperature dependence as well as load dependence of the coefficient of friction. Energy is dissipated in friction due to the stick-slip movements of individual atoms [64], which also leads to wear of the contacting bodies.

The Effect of Friction on Material Removal

Regarding the effect of friction in ductile material removal processes, KLOCKE AND KÖNIG state that the effective chipping thickness $h_{cu,eff}$ increases with increasing friction as shown in Fig. 2.10 [88].

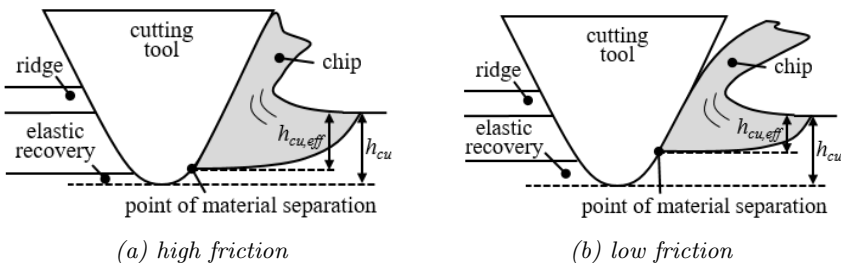


Figure 2.10: Influence of friction on the chipping thickness, after [88].

Due to the upwards shift of the material separation point in front of the cutting edge, it can be assumed that fewer cracks propagate into the bulk material when cutting brittle materials at a depth of cut near the critical depth of cut by decreasing the friction between workpiece and tool.

Considering a sliding indenter incurring friction, HAMILTON et al. [62] modelled the tangential load as a Cerruti Problem and have shown that increasing the tangential load by increasing friction, the locus of maximum yield stress moves towards contact surface and that another region of high local yield stress appears at the rear end of the indenter. Considering more relevant tensile stresses which lead to crack development and growth in case of brittle material behaviour, they further showed that increasing friction leads to increasing tensile, radially acting stress near the rear end of the indenter as well.

Friction Between Si and Diamond

Friction between diamond and Si is a comparatively sparsely investigated topic. Few studies on the coefficient of friction as in Coulomb friction are available, when limiting the search to macroscopic scales and omitting studies on an atomic scale:

- The coefficient of friction shows anisotropic behaviour when rubbing Si against Si in different crystallographic directions within a crystallographic plane. The same behaviour was much less pronounced when rubbing Si probes coated with diamond-like carbon against Si and was not observed when using a diamond tip. The coefficient of friction varies slightly when rubbing on different crystallographic planes with a normal force $F_n = 100 \mu\text{N}$ and a scratch length $s = 6 \mu\text{m}$. Values of $\mu \approx 0.08$ in the $\{100\}$ plane and $\mu \approx 0.12$ in the $\{001\}$ and $\{111\}$ planes were determined. The difference was deemed insignificant and it was concluded that the coefficient of friction between diamond and Si was independent of the lattice orientation and direction of movement. [56]
- It was shown that friction in the $\{111\}$ plane is lower than in the $\{100\}$ plane when rubbing metallic and ceramic balls against Si

wafers (diamond was not tested) at forces ranging from $F_n = 10$ to 80 mN, which was attributed to the lower surface energy and higher in-plane strength. For a rough Si wafer, an effect of crystallography-influenced anisotropy was not observed, which is attributed to the presence of a third body (rubbed-off particles) in the contact. [151]

- In a tribometer test using a {111} wafer and a sphero-conical diamond indenter with a nominal radius of 11.9 μm applying loads of up to 10 mN and a sliding distance of 50 μm resulted in a coefficient of friction $\mu = 0.097$. Only elastic indentation behaviour was observed under these conditions. [18]
- It was shown that the presence of an oxidised layer at the interface reduces the coefficient of friction [121]. In tests evaluating friction of Si against Si and silicon dioxide SiO_2 against SiO_2 , it was shown that the final coefficient of friction does not differ significantly for the two material pairs, however it was shown that the atmosphere, ambient in comparison with dry nitrogen, has a significant influence with the coefficient of friction being much higher when oxygen is present. [160]

Coefficient of Friction and Force Ratio

It should be noted that the term "coefficient of friction" and letter " μ " are often used synonymous with the ratio of tangential force and normal force $\hat{\mu} = \frac{F_t}{F_n}$ and not to be confused with the definition as the proportionality constant μ as defined in 2.23. The difference stems from the fact that in material removal processes the tangential force F_t (often defined as the cutting force F_c) includes also forces resulting in material separation and plastic deformation along with frictional forces. Notable work on the consideration of the force ratio $\hat{\mu}$ as the coefficient of friction in material removing processes has been put forth by CHALLEN AND OXLEY [25, 129] and then been elaborated on by BACK et al. [11], where the parameter f was defined as the ratio of local inter-facial shear strength of a lubricating film and yield shear strength of the deforming material. Three different models for the removal modes *wave formation*, *wave removal* and *chip formation* have been introduced. According to the models, the forces F_t

and F_n can be determined by analysing the slip-line field defined by the geometry of the indenter and the resulting material deformation when knowing f [25]. This shows that $\hat{\mu}$ defines the mode of material removal for certain wedge angles (or indenter included angles) and values of f . The models agree with Atmoutons' laws of friction.

Conclusion: Friction

The literature review shows that friction plays an important role resulting in different stress fields. The stress fields define the material separation point in case of ductile removal and the location and length of cracks in brittle removal. While cutting speed, acting normal force and crystallographic orientation appear to have low or no influence on the coefficient of friction between Si and diamond, rubbed-off particles present in the contact zone lower the coefficient of friction. No tests considering the long contact length, high sliding velocity and high pressure as present in diamond wire sawing are available for the material pair. Due to the above mentioned considerations, a coefficient of friction of maximum $\mu \approx 0.08 - 0.12$ can be expected for the diamond wire sawing process, but since cutting speed and contact length are extrapolated and debris is present, this assumption has to be verified.

2.3 Analysis and Modelling of the Diamond Wire Sawing Process

In DWS, the path of individual diamond grains is defined by the current shape of the wire, which provides a compliant support. As such, the forces acting on individual grains or, more general, segments of the wire, have a direct influence on the path of the grains, therefore on the depth of cut of the grains. This in return influences the material removal mode, which again affects process forces. Overall, the kinetics are a complex and interdependent aspect of the process. In this section, an overview of literature findings that deal with the kinetics of the process and the origin of the process forces is presented.

2.3.1 Modelling of the Wire Bow

The wire bow is a result of forces acting upon the flexible tool body. Studies on the bow of slurry diamond wire sawing (lose-abrasive sawing - LAS) process are more numerous than on the fixed abrasive process. While the basic reaction of the wire due to forces is the same, the distribution of the forces and the ratio of cutting to normal forces differ and cannot assumed to be the same for both processes.

A simplifying assumption is that the wire bow in the cutting area has the shape of a circular arc. This assumption has been made by YANG et al. [179] for the slurry based process, who used it to calculate reaction forces depending on the angle of the contact zone, leading to results similar to the capstan equation for belt friction. Furthermore a finite element model was applied to analyse the effect of bending stiffness. Later, TURCHETTA et al. [157] used the same assumption for the determination of forces acting on diamond beads on diamond saws used to cut blocks of rock in quarries.

LIEDKE [109] derived a differential equation for wire bow deflection based on forces acting on an infinitesimal wire segment for the slurry process. Forces are shown to be the result of lapping pressure distributions. The model is able to accurately capture an asymmetric wire bow and describe the effect of pulley distance, workpiece position, ingot size as well as friction for a steady state cut. Bending stiffness and the creation of the bow in a none stationary process state are not considered. The same differential equation has been derived by KONYUKHOV [91] from the generalized capstan equation for ropes clinging to arbitrary surfaces applying the principle of virtual work. PALATHRA et al. [135] included bending stiffness and the dynamic generation of the bow by calculating the bow incrementally using an Euler finite difference scheme. Their solution for the wire bow is symmetrical since they neglected cutting forces acting on the wire. A very detailed process model for the slurry process has been presented by LORENZ [112], who applied the Hamilton's principle and FEM. The solution comprises the dynamic creation of the bow while considering vibration and contact mechanics.

TEOMETE [154] used a rope model for the fixed abrasive process, describing the deflection of the wire in and orthogonal to the working plane, on the basis of an acting force distribution. Balancing oblique cutting energy with work done by the wire tension leads to an energy balance that drifts the wire back into the cutting plane. If the work done by wire tension is lower than the work done by free standing wire, representing an upper bound for wire deflection, the wire may drift out of the cutting plane which leads to waviness, high-frequency roughness in the ingot centre and tapered edges.

A general model of the asymmetric wire bow was developed and used to discuss loss in cutting power and stiffness in the wire web by QIU et al. [145]. An effort is made at discussing the relationship between removal rate and cutting power which is however limited to a description of the observed effects.

2.3.2 Analysis of the Removal Rate in Diamond Wire Sawing

In LAS, which is essentially a lapping process, the Preston equation [143] governs the material removal rate r_r

$$r_r = k_p p v_c \quad (2.24)$$

with k_p being the Preston coefficient, a material-pair-dependent constant, lapping pressure p and relative velocity between tool and workpiece v_c . This relationship was used to derive a functional relationship between process forces and removal rate for LAS [109]. In DWS however, where both ductile and brittle removal can be present, a linear relationship between feed force and removal rate is not obvious.

Very recently, WALLBURG et al. [163] published a parameter range for k_p in diamond wire sawing. The value is derived from FEM simulations considering phase transitions through the application of an Extended-Drucker-Prager-Cap constitutive material model (detailed in [162]). The

case considered is scratching with a Vickers indenter, the removed volume is determined by the length and depth of the lateral crack calculated in the finite element analysis. They gave $k_p = 125.5 \mu\text{m}^2/\text{N}$ as an upper bound and stated that, with wire wear, the value may decrease by as much as 50%. The dependence of the coefficient on the wear state indicates a strong dependence on the shape of the abrasive grits.

More generally, the removal rate in diamond wire sawing is governed by the sum of the amount of material removed by the individual grains. Each grain subjected to load penetrates into the workpiece, performs a scratching motion and removes material according to the mechanisms described in section 2.2. Effects of process parameters on material removal as well as modelling approaches are described in this section. In the static process state, when the bow is fully developed, the removal rate is equal to the feed rate.

KIM et al. [84, 102] studied the cutting ability of electroplated diamond wire in two studies. In the later one [84] they introduced a method to derive the removed depth d_n of a pass with the length l :

$$d_n = \sum k_n F_n l \quad (2.25)$$

with the constant k_n indicating the cutting ability of the wire and F_n being the feed force in normal direction. They proposed a simple equation for the normal load on the basis of wire tension F_s , maximum wire deflection w_{max} and pulley distance L

$$F_n = \frac{4F_s w_{max}}{L} \quad (2.26)$$

which neglects bending stiffness of the wire and asymmetry due to an acting cutting force. The feed distance of the ingot f per pass n is the sum of the removed depth d_n and the deflection w_{max}

$$f = \frac{w_{max} + d_n}{n} \quad (2.27)$$

The cutting ability of the wire k_n at a given pass can be obtained by evaluating (2.25), (2.26) and (2.27):

$$k_n = \frac{1}{F_n l} \left(n f - \frac{F_n L}{4 F_s} - \sum k_{n-1} F_{n-1} l \right) \quad (2.28)$$

In other words, the determination of the current removal rate from acting forces requires knowledge of the history of the cutting ability and current wire deflection. The cutting ability embodies several aspects when defined in this way, and while normal force and loaded length are factored explicitly, factors such as wear and cutting speed are implicit to the history and the definition of an initial k_0 .

A semi-empirical model for the derivation of the normal force acting on a wire with resin bonded diamond grains was put forth by LIU et al. [111], considering feed rate v_f , cutting speed v_c , contact length l and wire diameter D :

$$F_n = 0.141 \frac{v_f^{0.728}}{v_c^{0.656}} D^{1.017} l^{0.975} \quad (2.29)$$

The equation shows that the feed rate behaves proportionally to the feed force and the cutting speed and anti-proportionally to the wire diameter and the workpiece width.

The dependency of the removed depth per pass on different parameters is introduced mostly qualitatively in the following paragraphs.

Effect of Wire Tension and Normal Load

Increasing wire tension increases the normal load onto the grains, therefore leads to increased removal and consequently to a smaller wire bow [109, 154]. As the protrusion of grains is statistically distributed, more grains become kinematically active with increasing penetration and the total load-bearing area increases [83]. Consequently the force and penetration per grain decrease. The feed rate or normal force therefore has to be adapted to the load-bearing characteristics of the wire.

Effect of Wire Speed

Equation (2.29) shows that an increase in wire speed leads to a higher removal rate. This relationship has been analytically demonstrated by COSTA et al. [35], who argued that the average depth of cut a_e is a function of the sawn height h , the cutting time t_{cut} and the active wire length l

$$a_e = \frac{h}{t_{cut} v_c} l \quad (2.30)$$

Considering that the ratio between the sawn height and the cutting time is the effective removal rate r_r leads to

$$r_r = \frac{a_e}{l} v_c \quad (2.31)$$

which shows that the removal rate correlates directly with the average depth of cut per wire length and the cutting speed.

Effect of Grain Density

The load is distributed onto more grains when the density is higher. The removed material volume ΔV is proportional to the grain density ρ_g and the penetrated area projected into the plane normal to the cutting direction A_c [83]:

$$\Delta V \propto \rho_g A_c \quad (2.32)$$

Grain protrusion is limited by the contact of the bonding material and lifetime of the wires is shortened when the density is high [83], if the same feed rate is prescribed. When the grain density is too low, excessive load on individual grains may lead to rapid wear [83]. This suggests that the process parameters have to be adapted to the grain density in order to optimise removal rate and wear.

Effect of Wear

Aside from the effect of kinematically activating grains with loss of protru-

sion, the grain sharpness influences the removal rate. As the grains dull, the wire loses its cutting ability. LEE et al. [102] analysed the cutting ability of wires during their life-time and noted four phases: the cutting ability initially decreases during a "levelling" phase where the cut is dominated by few grains with large protrusion. The grains quickly wear off leading to increasing normal and decreasing cutting force. "Levelling" is followed by a "dressing" phase where the nickel layer rubs off and grains with sharp edges become exposed, leading to decreasing normal and stabilising cutting force. The cutting ability reaches its maximum, which slowly decreases during a following phase characterised by a stable condition. The grain protrusion decreases steadily, leading to slowly rising normal force. Dulling of the grains leads to decreasing cutting force. Towards the end of the life-time, the wire deteriorates rapidly, grains get pulled out, normal force rises quickly and cutting ability and cutting force drop sharply.

When prescribing a uniform feed rate, the normal force is larger on the used-wire side of the ingot than on the new-wire side if the amount of wire per wafer fed into the web is below a critical value, which may lead to non-uniform cutting behaviour over the ingot length [85]. Moreover, the ratio of cutting to normal force increases with increasing wire wear [85].

Higher normal force leads to greater wear [82], resulting in turn in lower penetration per grain.

2.3.3 Kinematic Process Modelling

Kinematic models are becoming increasingly popular to analyse and simulate machining processes. Searching the web service `app.dimensions.ai` for publications with the keywords "kinematic model" and "grinding" in the field of "manufacturing engineering" reveals, that the number of publications per year on the topic increased from 206 to 301 between 2016 and 2021 [148]. Their popularity is due to their ability to accurately capture and describe the main effects and therefore they provide an alternative to otherwise complicated and expensive experimental analysis.

According to BRINKSMEIER et al. [16] kinematic models are based on the geometric interaction between tool and workpiece. A detailed model of the tool topography is required. Sophisticated models consider the interaction of individual grains and therefore require high computational power. Typically, idealised material removal without plastic or elastic deformation is assumed, however more advanced models considering deformation, material pile-up or thermo-mechanical aspects have been reported. They offer high flexibility for different grinding processes and tools and can be extended with models for forces, temperature and surface damage. Because of their detailed description and the consideration of physical process behaviour, they are deemed to have high potential for application in the industry. While the initial effort to set up a simple model is considered to be low, they require profound knowledge of the underlying process in order to derive meaningful results. The results themselves are transparent and can therefore be interpreted easily and used as a decision-making tool. The current limitation of the models in general lays in the material behaviour at high cutting speeds and simulation of temperatures to predict surface damage.

Several approaches at modelling the diamond wire sawing process by means of kinematic simulation have been reported on in literature, e.g. [30, 105, 107, 111, 166, 177, 182]. As their quality evolves rapidly, only a few notable and recent ones are presented:

LE AND TRAN [101] implemented a kinematic model where ductile removal is simplified to perfect micro chipping without elastic effects and brittle removal is modelled on the basis of [113] after transition determined by the critical depth of cut [10], as described in section 2.2.2. They pointed out that brittle removal in the kerf ground and ductile removal on the sides of the kerf are possible simultaneously, that a higher grain density leads to more material removed in ductile mode and that brittle removal is observed regardless of the grain density.

GE et al. [57] developed a kinematic model to predict the depth of sub-surface damage on the basis of the work of MARSHALL, LAWN AND EVANS [100, 113]. Their model includes the development of a wire bow, ductile and brittle removal and, according to the authors, is able to predict

the damage with a maximum relative error of 5.26%.

An extensive kinematic model was published by QIU et al. [144]. The wire bow is derived from the equation of a hanging rope and extended to account for distributed process forces, considering the effect of pilgrim and wire torsion due to the pitch of the grooves on the guide rolls. However, only ductile removal is considered. The model is primarily used to discuss the origin and extend of saw marks.

LI et al. [104] introduced a model that combines stress field modelling (see also [2, 106, 186]) with kinematic modelling and used it to analyse subsurface damage of sawn wafers. They determined that high wire speed in combination with a low feed rate can reduce the damage depth but increases the amount of cracks. Both damage depth and crack amount increase with increasing abrasive density. While the average abrasive size has no significant effect on subsurface damage and crack count, a smaller abrasive size variation range leads to lower subsurface damage and an increased crack count.

2.3.4 Conclusion: Kinetics of Diamond Wire Sawing

At the beginning of the research work leading to the present dissertation, the wire deflection in DWS had not been formalised as for loose abrasive sawing. In the meantime, several solutions for the wire bow have been published, however a universal link describing the dependence of the removal rate on process parameters such as the Preston equation is yet to be delineated: no general model to describe the removal rate of the diamond wire sawing process in terms of prescribed normal force, cutting speed, wire, workpiece and machine geometry and wire topography has been introduced.

Most kinematic models consider analytical force and removal models which provide a universal and well theoretically secured basis. A draw-back is that they typically consider idealised conditions. Also, scaling effects are often not considered, e.g. the fundamental analysis is based upon different sizes or loading rates. The processes therefore have to be simplified which

forcedly leads to deviations between the experimental observations and the simulated results. To account for the errors, empiric constants are introduced. Their validity is however also limited to the parameter range tested and extrapolation leads to uncertainty. Therefore, a need for experimental analysis at identical scales and otherwise realistic parameters is identified.

Chapter 3

Research Objectives

The literature review shows that the application of fundamental material removal models to DWS remains a frequently investigated topic. The following conclusions are drawn and research objectives derived:

1. Specific process forces:

On the aspects of fundamental material removal, no comprehensive study on the scratch hardness of Si, that explores conditions similar to those present in diamond wire sawing, is available. The interaction of grains with the material is typically studied by means of scratching experiments, however the relative velocity typically falls short of that applied in the industrial wire sawing processes. Scratch hardness relates geometric parameters with forces and can serve as a specific feed force, while the ploughing hardness provides a model for the specific cutting force, both of which are useful for the evaluation of kinematic models of machining processes. Specifically in DWS, the process kinematics depends on acting forces due to the compliant support of the grains, making force models necessary for accurate kinematic modelling.

- Empiric functions for the calculation of specific process forces are to be derived from single-grain experiments at high speed and long contact length.

- The transferability of the relations to the DWS process must be established.

2. Ductile-to-brittle transition:

It has furthermore been shown, that the description of the ductile-to-brittle material behaviour on the basis of BIFANO's work alone is not sufficiently accurate. The critical depth of cut ultimately depends on stress and strain acting on the material and phenomena such as phase changes and plastification in the immediate contact zone. The stress has to be sufficiently high to enable phase transition to a metallic phase, which allows for plastic deformation.

- A more general model for the transition between ductile and brittle removal is to be derived. The focus is not laid on the conditions that lead to the appearance of first cracks, but rather on conditions that lead to a residual surface whose state is predominantly determined by ductile traces or brittle fracture.
- The residual depth of cut after elastic recovery, volumetric change due to phase transition and removal due to fracture has to be derived on the basis of tool shape, acting stress and penetrated depth.

3. Surface integrity:

Most studies analysing the residual crystalline phase on the machined surface use only one grain geometry. Comparative studies investigating the effect of the grain shape on the amorphisation of the Si surface at scratching speeds in the metre-per-second range are not known. Different Si phases exhibit different specific densities. Depending on the composition, thickness and regularity of the surface layer, different residual stress states may result. Especially on thin and large wafers, they potentially lead to considerable deformation.

- The effect of different tool geometries on the residual surface crystallography when scribing in the high-speed range must be determined.

4. Friction:

Only one value for the coefficient for dry friction is available in literature. This parameter is frequently used as an input in process simulations based on for example FEM and SPH.

- A value for the coefficient of friction between Si and diamond under macroscopic contact conditions must be determined. These conditions are characterised by high contact pressure and elastic deformation of the surface rather than phenomena acting on molecular level.

5. Cutting-to-normal-force ratio:

In DWS, the ratio between cutting and feed force is not constant and the derivation of the ratio from process parameters is not trivial. Most published work is limited to an empirical description of the ratio based on experimental data derived from limited parameter space. The comprehensive cause-effect relationship of the process parameters on the force ratio is not yet established.

- The cutting-to-normal-force ratio must be explored on the basis of the fundamental interaction between tool and workpiece for different contact geometries and transferred to DWS.
- The effect of process parameters in DWS on the cutting-to-normal-force ratio must be experimentally analysed.

6. Material removal rate in DWS:

The material removal rate in DWS is not yet described as a function of the process parameters, the forces resulting from a prescribed feed rate can currently not be derived analytically. An expression such as the Preston equation for polishing and lapping, as used to describe the material removal rate in loose abrasive sawing, is not applicable for diamond wire sawing. The Preston coefficient is not sufficiently explanatory and appears to functionally depend on the process parameters. When modelling the removal rate with kinematic models, idealised grain shapes are assumed, while a discussion whether these represent the grains on wires with respect to load-bearing characteristics accurately has so far not been presented.

- An established macroscopic model for the wire bow that forms in LAS must be re-evaluated with the boundary conditions present in DWS. It must be evaluated, whether an extension of the available model to include effects of pulley guidance and wire stiffness is necessary.
- Expanding from the macroscopic process model, the grain-workpiece interaction must be formalised with the goal of deriving the relation between acting forces and cutting speed and the material removal.
- The wire topography has to be considered to derive fitting parameters for the material removal rate model. In this context, the load-bearing area of idealised grains and grains on diamond wires must be compared.

To achieve these goals, the work is divided into two parts:

In chapter 4, the fundamental material removal behaviour is investigated. Ductile material removal of a sliding indenter is modelled on the basis of hardness theory. The contact conditions derived from measured forces, scratch and indenter geometry are to be represented by the model. The Raman spectroscopy technique is used to quantify residuals of phase-changed material on the surface that was scratched by indenters of varying shapes. The results are then analysed in relation to the contact geometry. A cutting-to-normal force ratio and a friction coefficient are furthermore derived on the basis of the experiments.

In chapter 5, the fundamental aspects of material removal in silicon are applied to DWS. Initially the process kinetics is derived macroscopically; the wire bow is obtained from the acting forces. Based on microscopic, grain-level interactions between the tool and the workpiece, the material removal rate is theoretically derived. A representative grain shape is determined for the wire topography which is then used to deduce the penetration depth and removal behaviour based on the forces on the wire. The thereby derived removal rate model is compared with experimental findings. The dependence of the force ratio on process parameters and its evolution is experimentally investigated and discussed with the findings from single grain scratch tests.

Chapter 4

Material Removal Mechanism of Silicon

4.1 Motivation: Material Interaction Modelling in Diamond Wire Sawing

Diamond wire sawing is a complex process, in which microscopic, grain-level interactions between tool and workpiece inter-depend with macroscopic aspects of tool shape deviation. The phenomena happening on grain level determine the material removal mode, which leads to more surface damage and less phase-changed material on the surface and therefore residual stress in the subsurface in case of brittle material removal. On the other hand, ductile removal results in fewer cracks, extensive elastic spring-back, phase-transitioned material in the material zone affected by contact pressure and a pronounced residual stress field. The removal mode influences the removal rate. The material behaviour depends in particular on the stress state.

In kinematic modelling of material removal processes, process variables such as forces, temperature or removed material volume are often derived on the basis of the geometrical overlap between tool and workpiece. For

this reason, it is purposeful to describe the interaction behaviour, especially the forces, normalised with the contact area. Scratch and ploughing hardness are examples of such specific process forces, as the hardness is specified as load per load-bearing area.

In diamond wire sawing, the feed rate and cutting speed are typically specified and the forces develop according to the resulting wire arc. With the experimental setup discussed in the chapter 5, it is beneficial to prescribe a force and therefore a wire bow and evaluate the resulting material removal rate. In order to analyse the process, empirical functions describing the relation between hardness and residual depth h_f , contact depth h_c , and normal force F_n are to be derived by means of single-grain scratch tests on Si. Due to the scaling effect elaborated in the literature review, section 2.2.1, power-function type relationships describing the hardness are anticipated. Geometrically defined and standardised tools are used to assure reproducibility. Specifically, Berkovich and Vickers indenters in face-first and edge-first orientation are evaluated and a dependence of the hardness on different indenter shapes and orientations is expected. Furthermore, the material on the scratched surface is to be analysed by means of Raman spectroscopy to evaluate the crystallographic composition.

A flow-chart of the experimental analysis described in this chapter is presented in Fig. 4.1. In the analysis several quantities from multiple sources are combined to ultimately determine and relate scratch and ploughing hardness, crystallography of the scratched surface, friction and depth recovery (the ratio of recovered depth from total penetrated depth), which are edged in red.

Starting from an experiment in which a Si disk is scratched with geometrically defined diamond indenters, process forces and a scratch topography are obtained. Points of interest (POI) on the Si surface are optically identified along with their coordinates. POI are beginning and end of a scratch, intersection of the scratch with a reference mark on the surface, ductile-to-brittle transition zone and areas with well visible radial cracks. The length of the scratch traces is derived from the coordinates. The crystallographic composition of the scratched material can immediately be determined at

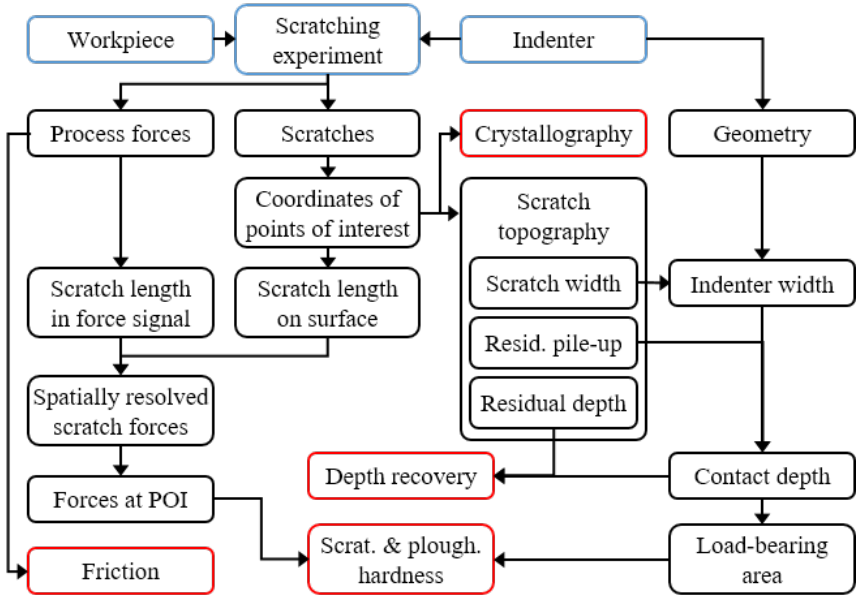


Figure 4.1: Flow chart showing the dependencies in the analysis of the material removal mechanisms in Si.

POI applying Raman spectroscopy. From the scratch topography at the POI the physical parameters scratch width, residual pile-up height and residual depth are determined. By intersecting the scratch topography with the optically measured geometry of the indenters prior to the experiment, the depth of the contact during the scratch can be determined. Since the width of the scratch is measured on top of the ridges next to the scratch, the contact depth has to be corrected by the height of the ridges, if one assumes that the pile-up does not significantly contribute to the load-bearing area, which can then be determined. By comparing contact depth and residual depth, the rate of recovered depth, consisting of an elastic component and a component stemming from the volumetric change due to phase transitions, is calculated. In order to spatially resolve the force signal, that is, determining the measured force at a given coordinate along the scratch, the duration of the contact from the force

signal is aligned with the length of the scratch measured on the surface. The instantaneous forces at the POI are therefore known. Scratch and ploughing hardness are determined from the corresponding forces and associated load-bearing surfaces. The coefficient of friction is determined from the force signal measured in experiments with spherical indenters that remove no material.

4.2 Material and Experimental Procedure

All experiments have been conducted on a novel experimental setup which is introduced in this section. In the next subsections, the experimental setup, the tools and material used, and the experimental procedure are introduced.

4.2.1 Test Rig: Single Grain Scratching Set-up

In order to achieve long scratch distances at varying cutting depth and high speed, the test rig introduced in [87, 131, 134] is adapted and improved. The basic kinematic applied is that of a face turning process with no overlapping traces: A stationary tool leaves a spiral-shaped trace on a rotating workpiece face. The Si workpiece is rotated and fed vertically into a stationary tool while being moved radially as shown in Fig. 4.2.

The 5-axis milling machine used is a Fehlmann Picomax Versa 825. The workpiece is mounted in a specially designed tool holder with a Hollow Shank Taper (HSK63) interface and fixed to the spindle. The machine and interface were chosen due to their high stiffness and good repeatability when re-clamping the tool into the spindle. The Fehlmann also allows for precise movement of the axes at high spindle speeds required to achieve the relevant cutting speed.

A diamond indenter is attached to a Kistler Type 9109AA three-component piezoelectric dynamometer and fixed on the machine table. The force measurement system further consists of a Kistler Type 5080A charge amplifier, a Kistler Type 5697A data acquisition system and a computer

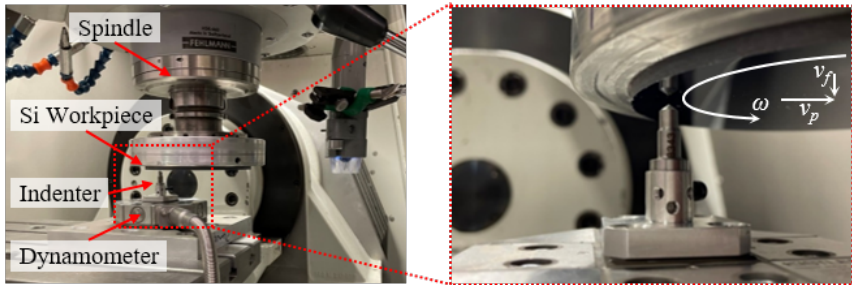


Figure 4.2: *Experimental setup: The diamond indenter is fixed to the dynamometer under the Si workpiece attached to the spindle. The motion of the workpiece is indicated in the magnification on the right: angular velocity ω , vertical feed v_f and horizontal feed v_p .*

running Kistler's "Dynoware" software. The signal is low-pass filtered at 1 kHz by the charge amplifier and digitalised at a sampling rate of 120 kHz.

4.2.2 Workpiece: Silicon Disk

The workpiece is a roughly 20 mm thick disk cut from a photovoltaic grade Si ingot. The rotational axis is aligned with the [001] axis of the ingot and the working plane is the (100) crystal plane, accordingly. A shoulder was machined onto the disk which is used to fix the workpiece in the HSK-holder. The workpiece face has a diameter of 100 mm. In order to achieve as good a perpendicularity of the surface with the kinematic axis of the machine as possible, the surface was machined in the fixation on the machine and by facing with a sharp polycrystalline diamond insert with rake angle of 0° and nose radius 4 mm at the lowest adjustable axial infeed $1 \mu\text{m}$, radial feed 5 mm/min and spindle rotation speed of 5000 min^{-1} . The surface was machined repeatedly until all traces of previous operations were removed and a relatively smooth and shiny surface was achieved. The holder with the disk was then removed and lapped externally to achieve a surface roughness of $R_z < 0.5 \mu\text{m}$. In a last step, the workpiece was balanced on the machine in one plane to an imbalance of $\sim 5 \text{ g mm}$.

4.2.3 Tools: Diamond Indenters

The tools used in the study are diamond indenters with the standardised hardness testing geometries Berkovich, Vickers and Rockwell, which were supplied by Eugen Buob AG, Switzerland. The geometries along with the tested orientations relative to the direction of scratching (face first and edge first for Berkovich and Vickers geometries) are shown in Fig. 4.3. The correct orientation is verified using a microscope aligned with the kinematic axis of the machine with an accuracy $< 0.2^\circ$.

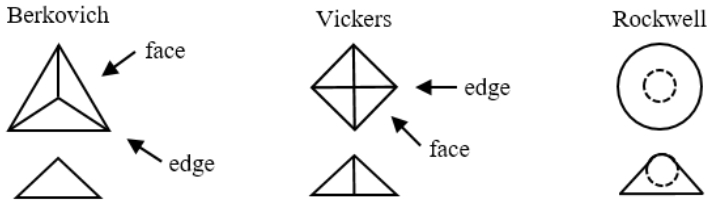


Figure 4.3: Sketch of the used indentation geometries with their orientation relative to the direction of cut.

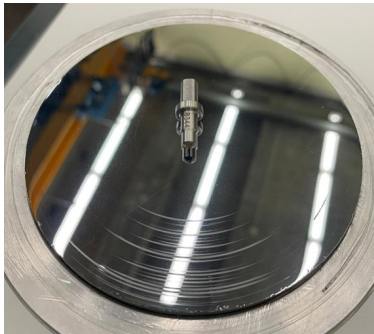
Each geometry and orientation is tested three times, of which each at least with one pristine indenter. Experiments with a Rockwell indenter and Berkovich indenter with edge first orientation have been repeated five respectively six times due to irregularities during the experiments or poor quality of the resulting scratches. Thus, a total of 19 experiments have been performed. Some indenters are used several times.

In order to be able to account for geometrical imperfections and wear, the indenter geometries are measured optically (Sensofar Neox, Focus Variation, 150x magnification) before and after each experiment. The indenter geometry is exported as a point cloud and processed in Matlab for the determination of the contact geometry. The processing procedure is introduced in section 4.3.2.

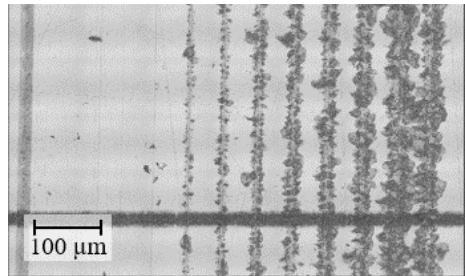
4.2.4 Experimental Procedure

One experiment generates a series of approximately 10 scratches. The contact point between the indenter and the workpiece is determined manually by slowly approaching the workpiece and observing the force signal. Once the spindle axis position at the contact is determined, the actual experiment is started. Using a program run on the CNC of the machine, the spindle is moved vertically downwards to the contact point, then radially by 0.5 mm and at the same time downwards by 1 μm . The spindle speed is chosen in such a way that the resulting initial cutting speed is 25 m/s. The change of the cutting speed due to the changing radius and the constant rotational speed is negligible. The radial feed rate v_p is chosen according to the rotational speed such that the workpiece performs 10 rotations while the radial motion of 0.5 mm is achieved. This motion should result in 10 scratches with a distance of 50 μm and with increasing depth.

The workpiece after all experiments have been performed is shown in Fig. 4.4a. Fig. 4.4b shows a microscopic image of the scratch series generated during one experiment.



(a) Workpiece after performing all scratch tests, with an indenter.



(b) Scratches resulting from one experiment and horizontal reference mark. The leftmost scratch stems from initially determining the contact point.

Figure 4.4: Workpiece and scratch series overview.

Due to a combination of workpiece shape deviation and kinematic error of the setup, the scratches are interrupted and have a length of up to

40 mm depending on the depth of cut and the radius. Because of the path interpolation of the CNC and the finite axis acceleration, the lateral movement is accelerated and decelerated in the beginning and end of the motion, leading to smaller distances between the first and last scratches and sometimes even overlapping scratches.

Cutting speeds other than $v_c = 25$ m/s are not considered in this study. The low observed effect of cutting speed on ductile-to-brittle transition, along with the extremely high heat conductivity of diamond in comparison with Si leads to the assumption that Si does not significantly soften due to higher temperatures that come along with higher shear rates (i.e. cutting speeds). Therefore it is expected that the observations from experiments at cutting speeds within the same order of magnitude do not differ significantly, aside from the known dependency of the Raman intensity ratio with sliding speed. $v_c = 25$ m/s was chosen as it is relatively close to the industrially applied cutting speed of $v_c = 35$ m/s in diamond wire sawing and as the corresponding rotational speed of the workpiece is within a range that does not excessively excite the machine structure due to imbalance.

4.3 Analysis and Modelling

The following section introduces the analysis and modelling methods applied. Starting with the measurement and analysis of the surface topography, it proceeds to the geometric measurement of the tools, the analysis of forces and the determination of the grain penetration depth. Finally the methodology of the analysis of the crystalline structure in the scratch ground is explained. The results are discussed in section 4.4.

4.3.1 Measurement and Analysis of the Scratch Topography

In order to facilitate the measurement of the workpiece topography, a mark in radial direction passing approximately through the centre of the

scratches was produced on the surface with a laser, as visible in Fig. 4.4b as the horizontal line.

The measurement of the workpiece topography was conducted with a Sensofar Neox S microscope using focus variation with 150x magnification. The vertical scan speed was kept on the lowest setting and each scan was repeated once.

The measurement procedure for each set of scratches of one experiment performed with a Berkovich or Vickers indenter was as follows:

1. The coordinates of the scratches and the touching-scratch at the laser mark are recorded. They will later be used to determine the length of the scratches and the relative position of the mark on the scratch.
2. A microscopic depth image of all scratches is generated. The image is approximately 0.7 mm by 0.5 mm large, the vertical scan rate is chosen according to the distance between the surface and the deepest scratch, typically around 3 μm .
3. The individual scratches are traced and the coordinates at their beginning and end are recorded.

For Rockwell indenters, only the overview image has been captured.

Determination of the Scratch Length from the Topography

The length of the scratches s_s on the surface can be determined immediately from the radius of the scratch r_s and the start and end point coordinates $(x_{start}|y_{start})$ and $(x_{end}|y_{end})$. The radius of the mark from touching is considered the most accurate, since no lateral motion of the machine tool was performed and therefore no path interpolation in radial direction was active. The radius of each scratch can be determined by measuring the radial distance along the laser mark. The angle θ that spans the arc is given as

$$\theta = 2 \arcsin \left(\frac{c}{2r_s} \right) \quad (4.1)$$

where c is the length of the circle chord defined by the start and end point coordinates:

$$c = \sqrt{(x_{start} - x_{end})^2 + (y_{start} - y_{end})^2} \quad (4.2)$$

The length of the scratch is then given by

$$s_s = r_s \theta \quad (4.3)$$

The surface scratch length is compared with the scratch length calculated from the force signal, as described in section 4.3.3, in order to be able to derive the acting force at a certain location ($x|y$).

Classification of Ductile and Brittle Scratches

It is important to note, that the classification aims at describing when the removal is characterised by predominantly ductile or brittle removal mechanisms. The goal is not the identification of a critical depth or stress at which the material first fails due to fracture.

The ductile-to-brittle transition is not sharp and locations determined merely indicate a range in which the transition is expected to happen. Often cracks and chipped of material are clearly visible on a scratch, followed by several hundreds of microns without any traces of brittle removal. In that case, the brittle behaviour may be attributed to pre-existing damage on the surface. Furthermore, several different brittle phenomena can be observed visually on the scratches, as exemplarily shown in Fig. 4.5.

Especially a new, unworn Berkovich indenter in face first orientation leaves a series of radial cracks on the scratch flanks, pointing in the direction of cut (top to bottom in Fig. 4.5). It can also be seen, in the detail in the left side of the image, that pitting appears at the bottom of the scratch when the tip is very sharp. It does not appear any more as the tip wears off slightly, even though greater depth of cut is achieved, as visible in the third scratch in the centre of the image. However, first chipping on the surface appears shortly after the first radial cracks are visible, see detail on the right of the image. Mainly radial cracks are visible, while median and lateral cracks become visible only once the material chips off and

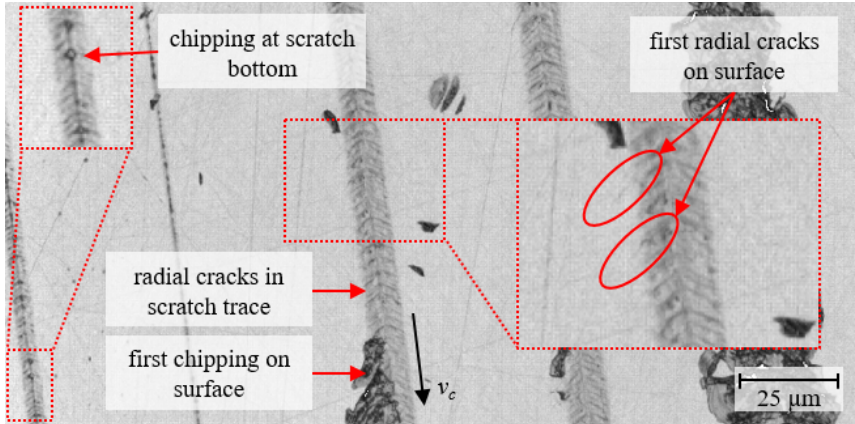


Figure 4.5: Details of brittle phenomena visible in the ductile-to-brittle transition zone (sharp Berkovich indenter, face first, scratching direction top to bottom).

constitute the limits of the chipped-off area.

All scratches are categorised into ductile (d), predominantly ductile (dt), predominantly brittle (tb) and brittle (b). This categorisation is somewhat arbitrary and subjective, as even scratches classified as ductile show radial cracks or occasional breakouts and therefore have been produced at least in parts in brittle regime with cracking on the surface. The reason for the categorisation is mainly to judge whether the residual stress field around the scratch will be dominated by phase-changed material or by stress relaxation due to frequent cracks. In that sense, a ductile scratch is expected to show residual phase-changed material with negligibly few stress relieved areas, while a brittle scratch will show barely any residual stress fields due to a phase transition. The intermediate categories will show a more or less well developed stress field. The exact categorisation is not important and is meant to be used for a qualitative comparison of the removal regime between the geometries and orientations.

Examples for the categorisation for the Berkovich and Vickers experiments are shown in Fig. 4.6. Scratches with the Rockwell indenters show no material removal and are therefore not classified.

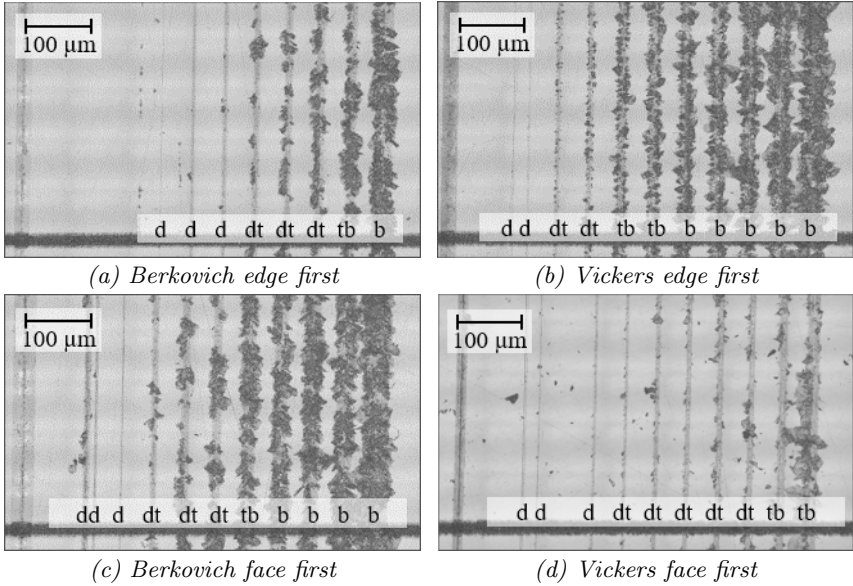


Figure 4.6: Examples for the categorisation of the scratch appearance for the different geometries and orientations: *d* = ductile, *dt* = transition mainly ductile, *tb* = transition mainly brittle, *b* = brittle.

Analysis of the Scratch Geometry

In order to apply the theory of scratch hardness presented in section 2.2.1, the penetration geometry has to be known. Values to be determined are the final, residual depth of the scratch h_f , the final height of the pile-up on the flanks of the scratch h_{fp} and the width of the scratch w . The derivation of the contact geometry from an overlap of measured tool and scratch cross-sections is presented in the following section 4.3.2.

Fig. 4.7 shows an example of how the values are measured from the captured workpiece topography.

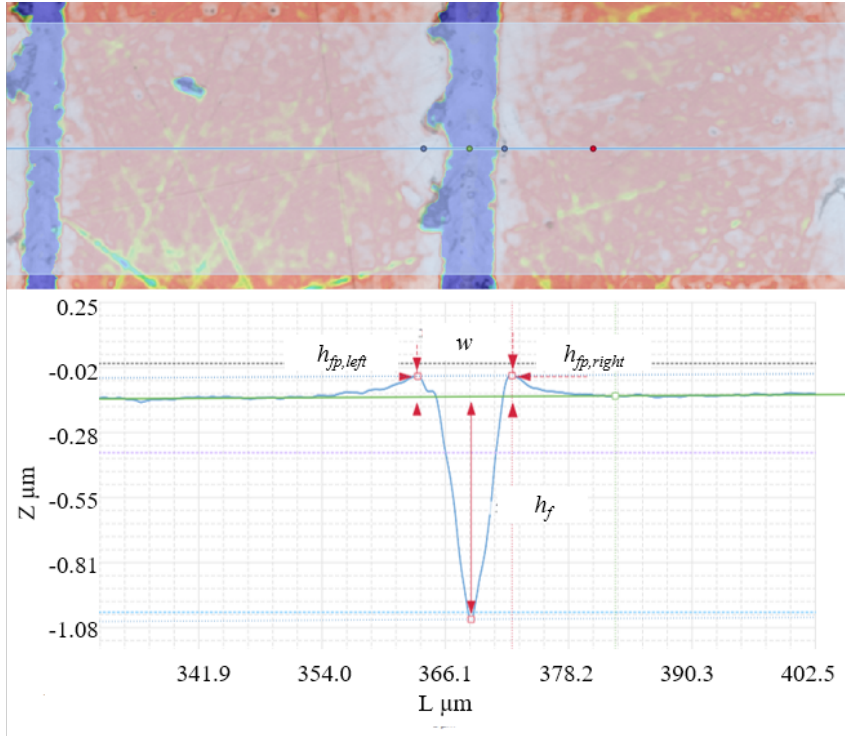


Figure 4.7: Example of the derivation of the scratch geometry in the Sensofar SensoVIEW 1.8.0 software, indicating the residual depth h_f , final height of the ridges h_{fp} and the width of the scratch w .

Depicted is a scratch in the region of the ductile-to-brittle transition, which features both ridges on the sides of the scratch as well as fracture on one side of the scratch. Analysing the profile is only possible in regions with at least partially ductile material removal: The scratch ground and at least one edge must be recognisable and not exclusively characterised by brittle fracture. A profile line is drawn perpendicularly across a representative position of the scratch. The profile trace is determined from a region spanning 5 to 50 μm along the scratch, shown as a shaded area around the profile line in the false-colour image on the top of Fig. 4.7. The profile trace plotted in the bottom of Fig. 4.7 is the mean profile gen-

erated from the shaded region and therefore averages the effect of pile-up and fracture on the left scratch flank.

Marked on the profile trace in the bottom of Fig. 4.7 are the scratch width w , the residual depth h_f determined as the vertical distance between the scratch ground and the unscratched surface, as well as the height of the ridges on the left and right of the scratch $h_{fp,left}$ and $h_{fp,right}$. The height of the ridges h_{fp} is determined as the mean height of the pile-up on the left and right side.

There are different possibilities to define the width w of the scratch. The effect of the choice was discussed thoroughly by TSYBENKO et al. [156]:

1. Using the width at the level of the undisturbed surface perpendicular to the scratch between the pile-up to calculate the contact depth shows the best agreement with the contact depth measured in-situ, during the cut.
2. Using the width between the peaks of the pile-ups considers the additional height of the ridges for the determination of the contact depth and signifies that the pile-up contributes to the load-bearing area.
3. Using the width between the points of maximum slope in the height profile indicates the width at which the indenter loses contact to the material and considers partial contribution of the pile-up to the load-bearing area.

The points of maximum slope are the most difficult to determine. In case of Si, volume change due to phase transition contributes to the recovery, which might affect the scratch flanks as well.

The width at surface level is very sensitive to the presence of brittle break-out at the scratch flanks. The profile trace in the bottom of Fig. 4.7 shows a step on the left ridge near the green line marking the surface level. The sensitivity can be illustrated from the shape of the ridge on the left: if the surface level was determined as little as $0.05\ \mu\text{m}$ higher, the step would be below the surface level and the scratch width determined at surface

level would be approximately $1\ \mu\text{m}$ wider, which is equal to the residual depth of the scratch and constitutes a large error. Furthermore, since large elastic recovery and pile-up of material is observed, the width at surface level does likely not represent the width of contact during scratching.

For these reasons, the width of the scratch is determined from the distance between the maxima of the ridges. It is easier to identify the maxima in comparison with the point of maximum slope. Brittle break-out affects the horizontal location of the maximum on the ridge less than on surface level.

As argued by TSYBENKO et al. [156], the pile-up contributes to the load bearing area if the width is determined from the maximum on the ridges. In case of scratching Si, simulations have shown, that the prow that builds in front of the tool and the ridges on the side do not significantly contribute to the load bearing area. The simulation result is shown later, see Fig. 4.28, left, section 4.4.4. A compensation is therefore suggested when deriving the contact depth from the measured scratch geometry.

4.3.2 Generation of the Contact Geometry

In order to derive the scratch and ploughing hardness from the experiments, the load-bearing areas in cutting and normal direction A_c and A_n have to be identified as a function of the contact depth h_c . This is achieved by overlaying the geometry of the indenter with the geometry of the residual scratch, as illustrated in Fig. 4.8. The underlying presumption is that the residual scratch width equals the width at the indenter at contact height. However, as described above, the width of the scratch is determined as the width of the maxima on the ridges, while the contact height of the pile-up is supposed to not contribute to the contact height.

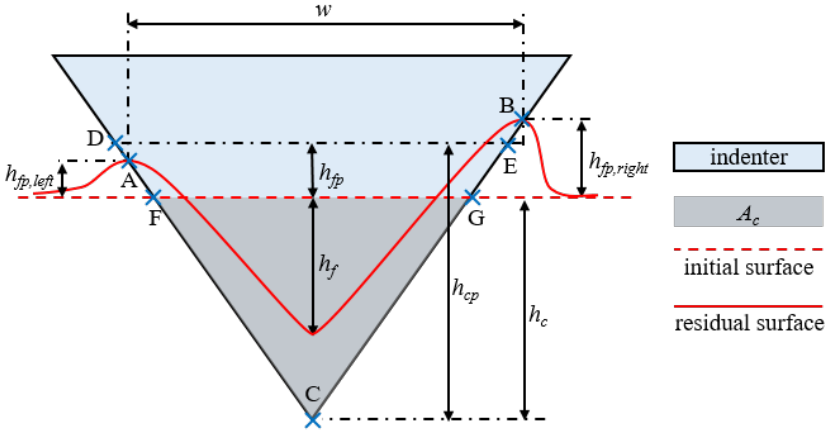


Figure 4.8: Illustration of the overlay of indenter and scratch geometries in a cross section normal to the cutting direction with the goal of determining the load-bearing area A_c .

Fig. 4.8 shows the profile of residual scratch after elastic recovery as a red solid line, with two ridges of height $h_{fp, left} < h_{fp, right}$. From the maxima on the ridges, points A and B, the width w is determined. The indenter of known shape, indicated in blue, is overlaid in such a way, that its edges intersect with the identified maxima. The area of the triangle $\triangle ABC$ corresponds to the load-bearing area when the ridges are taken into account. The triangle $\triangle CDE$, defined by the intersection points D and E of the indenter contour with a line shifted parallel from the original workpiece surface (red dashed line) by $h_{fp} = \frac{1}{2}(h_{fp, left} + h_{fp, right})$, has the same area. The height of the triangle $\triangle CDE$ is the contact depth with contribution of the pile-up h_{cp} . Since the pile-up is not to be considered, the contact height h_c is calculated as $h_c = h_{cp} - h_{fp}$. h_c is then the height of the triangle $\triangle CFG$, which represents the contact between the non-scratched surface and the indenter during scratching. The area of this triangle is the load-bearing area A_c without consideration of pile-up, shaded in grey in Fig. 4.8.

Thus, the contact depth h_c determined in this way is decisive for the derivation of the load-bearing areas A_n and A_c from the measured indenter

geometry. The automated processing of the point-cloud representing the indenter geometry is visualised on the example of a Berkovich indenter in face-first orientation in Fig. 4.9. The process is as follows:

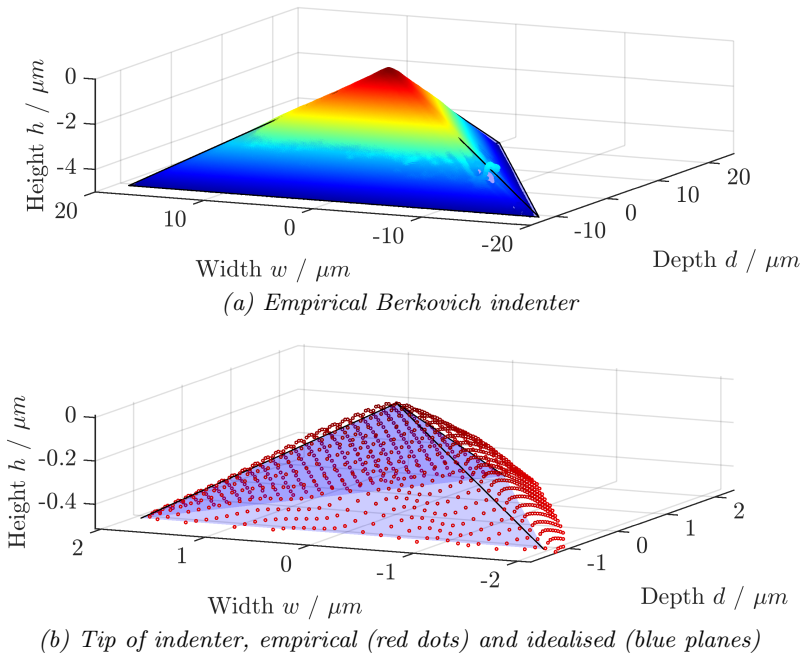


Figure 4.9: Example of the point-cloud processing of a Berkovich indenter: a) visualisation of the point cloud with color indicating height, b) detail of the tip, idealised Berkovich shape visible in blue.

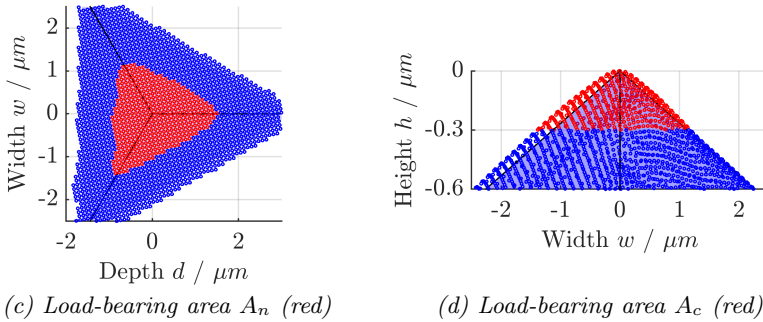


Figure 4.9: (cont.) view projected in the plane orthogonal to the direction of the applied normal load (c) and the plane orthogonal to the cutting direction (d), red data points are used for determination of A_n and A_c , respectively ($h_c = 0.3 \mu\text{m}$).

1. The highest point of the point cloud is determined. The point-cloud is cropped at $h = 5 \mu\text{m}$ so all lower data points are on the same level. The edges are determined and the dataset is oriented so the face facing in (face-first) or away from (edge-first) cutting direction (depth) is oriented parallel to the x-axis (width) as shown in Fig. 4.9a. The example shows a Berkovich indenter in face-first orientation, cutting motion is in negative depth-direction.
2. An idealised Berkovich indenter with a perfectly sharp tip is fitted into the point-cloud and shifted downwards so its tip is on the same height as the highest point of the point-cloud. This is done mainly to visualise the shape deviation, but by evaluating the idealised geometry, it is also possible to analyse the effect of wear. The shape deviation is visible in the detail in Fig. 4.9b.
3. Based on the width w of the analysed scratches, the contact height with pile-up h_{cp} at which the indenter is w wide is determined. The contact height is then corrected for the pile-up $h_c = h_{cp} - h_{fp}$. All data points with a height-value larger than the contact height are indexed, as visualised with red points in Figs. 4.9c and 4.9d. A polygon is fitted around the indexed data points projected in a plane orthogonal to the normal direction (A_n) or cutting direction

(A_c) using the MATLAB object *alphaShape* with an *alpharadius* of 0.5 to avoid holes [115]. The load-bearing area in either direction is determined as the area of the *alphaShape*-object.

4. Finally, a bearing-factor f_b is multiplied to the load-bearing area in normal direction to account for the lower material support in the rear of the indenter during scratching. The bearing-factor depends on the shape and orientation:

- Berkovich edge-first: $f_b = \frac{2}{3}$
- Berkovich face-first: $f_b = \frac{1}{3}$
- Vickers edge-first: $f_b = \frac{1}{2}$
- Vickers face-first: $f_b = \frac{1}{4}$ according to WILLIAMS [171];
 $f_b = \frac{3}{4}$ in the present study, see discussion
in section 4.4.4

4.3.3 Analysis of Forces

Signal Processing

The force-signal processing is automated in Matlab. The code reads the raw force signal and corrects drift and offset. The zero level is determined as the mean of the whole signal; the peaks are negligible as they make up less than 1% of the signal. Next, the peaks are identified in the signal of the normal force F_n , which has the best signal-to-noise ratio. The beginning and the end of the signal of a single scratch are determined as the crossing with the zero line. A data file containing the data points belonging to each scratch along with their timestamps is saved. The force signal of the passive force F_p (radial, passive direction), the cutting force F_c (tangential, cutting direction) and the normal force F_n are displayed as shown in Fig. 4.10.

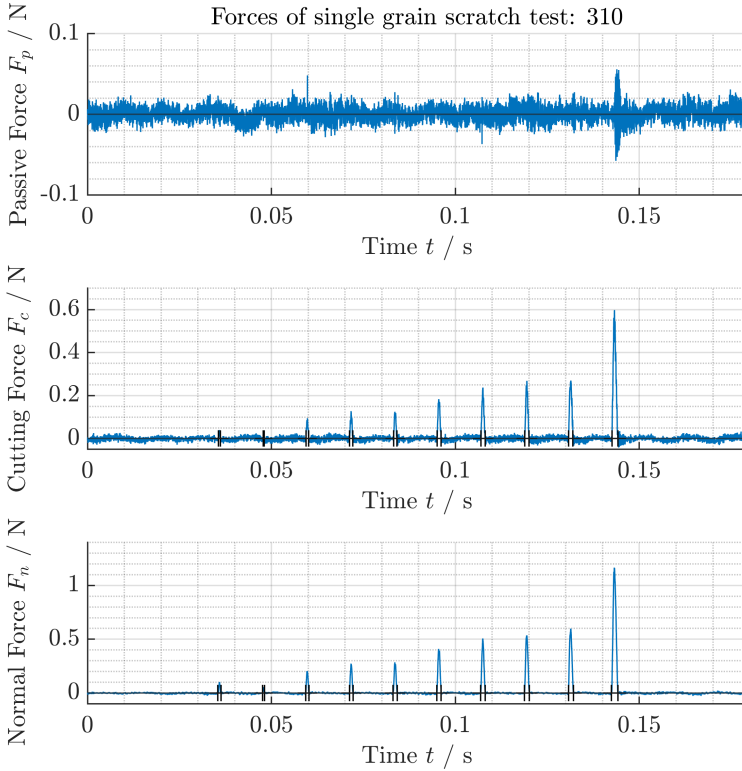


Figure 4.10: Example of the force signal generated from scratching Si with a Berkovich indenter, face first.

The passive force F_p , normal to the working plane kinematically defined by F_c and F_n is supposed to be near zero, as the radial feed rate is about three orders of magnitude smaller than the cutting speed and the indenters are symmetric to the cutting speed vector. Deviations from zero, such as the one seen at about 0.14s, are comparably small in amplitude and are possibly due to cross-talk or brittle fracture. They are significantly more pronounced in case of rubbing with a Rockwell indenter, which is ad-

dressed in section 4.4.5. Because of the high eigenfrequency of the Kistler Type 9109AA dynamometer and the light tool holder, no significant excitation in direction of the cutting or normal force despite the very short force impulses are captured.

Analysis of a Single Scratch Signal

When analysing the force signal of one single grain-workpiece interaction, the file containing all data points and timestamps belonging to the interaction are loaded and a polynomial of 5th order is fitted to the cutting and normal force signal. Ideally, the force peaks would have the shape of a sine-function. However, since the force signal represents only a small proportion of one period, fitting an odd polynomial is much easier to implement numerically and yields sufficiently accurate results. A 5th order polynomial is able to represent one period of a sine-wave accurately. As the passive force should be zero, it is represented with a line-fit for visual inspection, but not evaluated further. The plots of the force signals and the fits are exemplarily shown in Fig. 4.11.

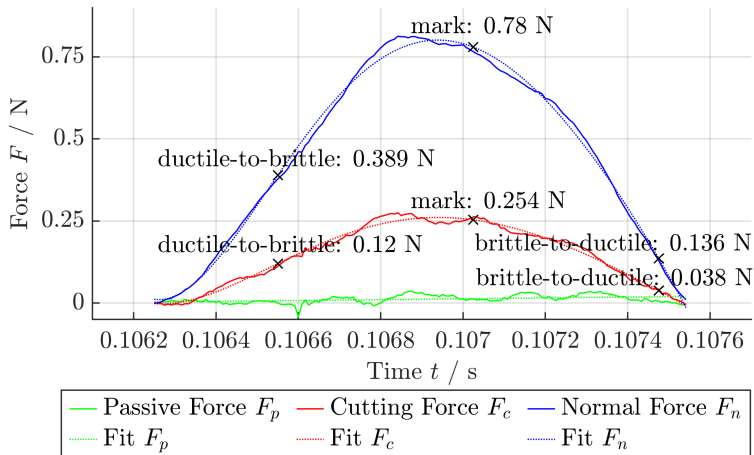


Figure 4.11: Force peak signal generated with a Vickers indenter, face first, with material removal mode transition points marked. The scratch appearance at the mark is brittle.

Spatial Resolution of the Force Signal

In order to identify the acting force at a certain position on the scratch (e.g. the ductile-to-brittle transition or at the reference mark), the force signal has to be aligned with the scratch geometry, which is done via the information of the scratch length. The scratch length s_f can be determined from the duration of contact Δt identified from the force peak and the known cutting speed v_c . The scratch length is

$$s_f = v_c \Delta t \tag{4.4}$$

By calculating the ratio of the surface scratch length with the force scratch length s_s/s_f for each scratch, it is possible to map forces measured at a certain time to a location on the scratch, given by its distance from the beginning or end of the scratch. The determined ratios for all scratches plotted over the radius over the scratches is shown in Fig. 4.12

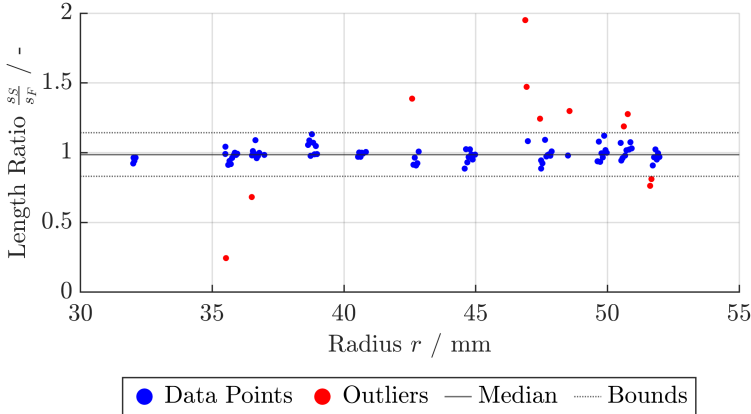


Figure 4.12: Ratio of scratch length on the surface s_s and in the force signals s_f .

Overall a ratio close to unity is achieved, signifying that measurement of the scratch length on the surface agrees well with the length determined

by the force signal. Nonetheless, some outliers are identified: a data set is considered an outlier, if the length ratio is further than three scaled median absolute deviations away from the median of all ratios, indicated as *bounds* in Fig. 4.12. Outliers typically originate from a wrong identification of the beginning of the scratch in the force signal due to noise. Furthermore, the manual recognition of the beginning or end of the scratch on the workpiece surface is a potential source of error. Identified outliers are not considered henceforth. In all further analysis, the exact ratio is used for each scratch.

4.3.4 Determination of the Penetration Depth and Rate of Recovery

With the width w of the scratch determined, the contact depth h_c can be derived from the measured indenter geometry as described in section 4.2.3. The penetration depth h at a given normal force, which is necessary to derive the elastic recovery rate, is based on (2.2) where the contact depth is derived as described above from experimental data, but the sink-in depth h_s is unknown. Using (2.9) [127], which assumes that pile-up is negligible, h_s can be estimated as follows:

$$h_s = \epsilon \frac{F_n}{S} \quad (4.5)$$

with the unknown elastic modulus of the unloading curve S and $\epsilon = 0.76$ for a Berkovich indenter [136]. Here, it is assumed that ϵ is the same for a Berkovich and a Vickers indenter. The potential for error due to this assumption is not large as argued by OLIVER AND PHARR, who recommend $\epsilon = 0.75$ if no better value can be reasoned for [127]. S is given by

$$S = \beta \frac{2}{\sqrt{\pi}} E_{eff} A_n \quad (4.6)$$

$E_{eff} = 126.16 \text{ N/mm}$ for the indenter-specimen pair of diamond and $\text{Si}_{[100]}$, A_n is derived from the scratch width and the indenter geometry with consideration of a load-bearing correction factor due to scratching as de-

scribed above. $\beta = 1.0742$ is calculated using 2.5 [63] with $\nu_{\text{Si}[100]} = 0.27$ and an equivalent indenter angle $\varphi = 70.32^\circ$. The consideration of an equivalent indenter angle instead of the half-included angle of the Vickers or Berkovich indenter is necessary, since β is derived applying SNEDDON's theory [150] which applies to axisymmetric punches only. In their representation by equations, the geometries of the Vickers and Berkovich indenters are therefore changed to that of a cone that has the same contact area to height function as a Berkovich indenter. Since Vickers and Berkovich geometries are the same in that aspect, $\varphi = 70.32^\circ$ applies to both of them.

With all quantities for the derivation of h according to (2.2) now known, the elastically recovered height h_e can be determined as

$$h_e = h - h_f \quad (4.7)$$

and the rate of the depth recovery r_e as

$$r_e = \frac{h_e}{h} \quad (4.8)$$

Experiments that show a negative rate of recovery are considered outliers and not considered for further analysis.

An alternative way of calculating elastic displacement is the determination of the elastic field in front of the indenter, as proposed by TAYEBI et al. [153]. The derivation of stress and strain in the elastic field is based on BOUSSINESQ's theory of potentials [14]. As it is expected that the final depth of a scratch in Si is not only determined by the elastic response of the material but also by volume changes due to phase transition, this approach is not pursued in this study.

4.3.5 Analysis of the Crystallographic Composition

The aim of analysing the crystallographic composition of the material after scribing is to identify phase-changed material and ideally quantify it.

Especially amorphous Si shows a lower density than Si-IV and its accumulation leads to volumetric expansion and residual stress. The dependence of the crystallographic composition on indenter shape and orientation, as well as penetrated depth is to be investigated. The necessary theoretical background is presented in the state of the art, sections 2.1.1 and 2.2.2.

Raman measurements were performed to evaluate the crystallography of the scratched material. Scratches to be measured were identified on the basis of their ductile appearance, since brittle regions show little to no signs of phase transition. The region measured is close to the reference mark on the surface to allow for correlation with force, scratch depth and determined scratch hardness. All measurement points lay in the bottom of the scratch, which was determined as the point where maximum signal intensity indicates vertical orientation of the light path to the surface. A line scan was performed across the scratch to determine this point of maximum intensity. Each scratch was measured at 3 to 5 different locations with a distance of approximately 20 μm from one another along the scratch.

A commercial Raman microscope Alpha CRM 200 from WiTec modified by the Nanometallurgy Group LMN of ETH Zürich was used. A laser of wavelength $\lambda = 532\text{ nm}$ was employed to excite the material through a 100x lens with a numerical aperture of $A_N = 0.8$. The resulting penetration depth in the pristine crystal is $\lambda/4\pi k \approx 814\text{ nm}$ (with extinction coefficient $k = 0.052$ [5]) and the estimated diffraction limited spot has a diameter of $\lambda/2A_N \approx 330\text{ nm}$. The integration time used was 10 s, 5 accumulations per measurement were averaged. The Raman data was exported using ProjectFour software. In the final step of the evaluation, the signals were smoothed, the Raman shift was corrected according to the location of the Rayleigh peak and consecutively evaluated on the basis of the intensity ratio proposed by YAN et al. [178] applying a MATLAB code.

Analogous to WANG et al. [165], mainly α -Si and Si-IV and occasionally Si-I are observed in the area of the scratch ground. The intensity ratio of measurements in the scratch ground between the peaks of Si-IV around 5101/cm and the adjacent α -Si peak around 4751/cm is evaluated, that

is $r_{\alpha\text{-IV}} = \frac{I_{\alpha\text{-Si}_{475}}}{I_{\text{Si-IV}}}$. While this intensity ratio does not provide a measure for the thickness of the phase-changed layer but only one for the relative amount of Si amorphised from crystalline forms of Si, it gives an important measure for the change of density and therefore the residual stress present after cutting: a high intensity ratio indicates a lot of material in the less-dense amorphised form and therefore higher compressive residual stress. The densities of Si-IV and Si-I are approximately equal [41].

To calculate the intensity ratio, the intensity of the Raman signal must be approximated by a sum of Lorentz and Gaussian distributions [178]. Only the distributions for the phases of Si-I, Si-IV at 510 1/cm as well as for α -Si around 150, 300 and 475 1/cm are fitted. These phases represent the overall spectrum reasonably well, even though sometimes additional smaller peaks corresponding to other Si phases are detected. A representative resulting peak separation is shown in Fig. 4.13.

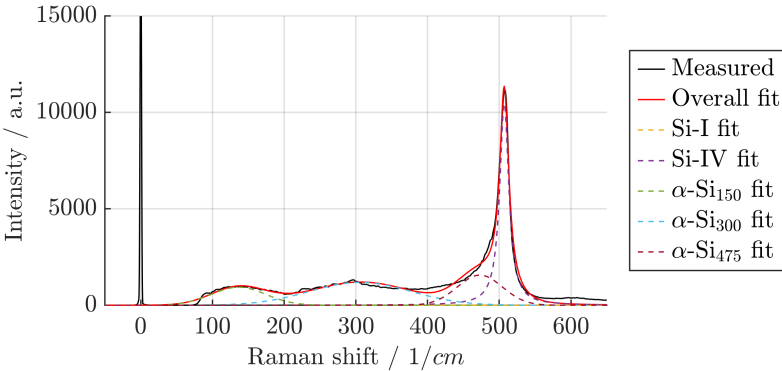


Figure 4.13: Peak separation of the measured Raman spectrum in order to identify the intensity of the Si-IV phase at 510 1/cm and the neighbouring α -Si peak at 475 1/cm. No Si-I is detected in this example.

In the example shown in Fig. 4.13, the measured intensity shows a small Si-IV peak at around 290 1/cm which does not affect the overlapping α -Si peak. No Si-I is fitted in this example, showing that the fitting of the two crystalline peaks at similar Raman shifts is parametrised to distinguish

between the two phases. If both a Si-I and a Si-IV peak are detected, the measurement is only taken into account if the intensity ratio of Si-IV and Si-I $\frac{I_{Si-IV}}{I_{Si-I}} > 4$.

The fitting algorithm is implemented in Matlab. The fit function is defined as the sum of the individual Lorentz and Gaussian distributions, described by their shift ν , amplitude h and width w , and fitted to the measured signal. In order to achieve reproducible results, the limits in which the peaks are fitted to all measured intensity curves are restricted as shown in Tab. 4.1.

Table 4.1: Fitting boundaries of the Lorentz and Gaussian distributions fit to the measured Raman shift.

	Raman shift ν			amplitude h			width b		
	initial	min	max	initial	min	max	initial	min	max
Lorentz distribution	$f_{Lc}(\nu) = \frac{h_c}{1+(\nu-\nu_c)^2/b_c^2}$								
Gaussian distribution	$f_{Ga}(\nu) = h_a \exp(-\frac{(\nu-\nu_a)^2}{b_a^2})$								
Si-I	521	516	526	500	0	60000	5	0	20
Si-IV	507	502	512	500	0	60000	8	0	24
α -Si ₁₅₀	150	145	155	500	0	60000	50	0	100
α -Si ₃₀₀	300	295	305	500	0	60000	50	0	100
α -Si ₄₇₅	475	470	480	500	0	60000	50	0	100

4.4 Results and Discussion

A total of 102 scratches show a force signal and a measurable scratch topography of which 83 are considered valid data points: 25 Berkovich edge (+3 outliers), 17 Berkovich face (+5 outliers), 21 Vickers edge (+7 outliers) and 20 Vickers face (+4 outliers). Furthermore, 47 scratches with a Rockwell indenter are analysed, of which 34 are used to determine the coefficient of friction.

All following analysis considers a load-bearing area $A_{LB} = \frac{3}{4}A_n$ (three-quarters of the contact area projected in a plane perpendicular to the

normal force) for a Vickers indenter in face first orientation (see discussion in sec. 4.4.4)

4.4.1 Surface Appearance

As explained in section 4.3.1, scratches are characterised qualitatively by the appearance of their surface and assigned a category "predominantly ductile", "ductile transition", "transition brittle" and "predominantly brittle". The aim is to achieve a notion of when material removal is defined rather by phenomena of ductile removal, such as elastic recovery and phase transition, or brittle removal with larger break-outs. With the indentation depth h determined, it is possible to compare the appearance with indentation depth for each indenter geometry and orientation. Fig. 4.14 shows this comparison.

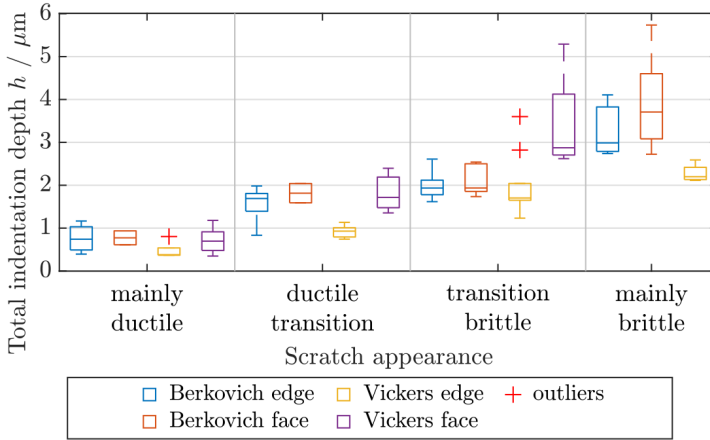


Figure 4.14: Box plots visualising the indentation depth h and corresponding scratch appearance for groups of indenter shape and orientation.

It is observed that increasing depth consistently leads to more brittle behaviour. However, for scratches made with Vickers indenters in face-first orientation, which exhibit predominantly brittle behaviour, it is not possible to determine the contact geometry, and therefore no data is presented

for this category. Additionally, scratching with Vickers edge-first results in more brittle behaviour and an earlier transition compared to other geometries. With Berkovich indenters, only a slight trend towards ductile removal in face-first orientation with increasing depth is observed compared to edge-first orientation. However, for Vickers indenters, this trend is clearly more pronounced, with scratches generated in face-first orientation showing some remaining ductility at higher depths and remaining in the "transition brittle" category, while scratches made with Berkovich indenters already exhibit mostly brittle removal at similar depths.

4.4.2 Rate of Depth Recovery

Fig. 4.15 shows the relative recovered depth r_e for all geometries scattered over the indentation depth h and the measured normal force F_n . This rate incorporates the effects of elastic recovery and reduction of residual depth due to volumetric expansion stemming from phase transitions.

The rate of recovery scatters significantly over all geometries but also within one geometry. It is higher at lower penetration depth and normal forces as expected and found by other researchers [3, 70]. Furthermore, scratching with a Vickers indenter face first produces the highest relative recovered depth. When scratching with a Berkovich indenter, more depth is recovered when scratching edge first than face first, agreeing with the theoretical analysis and experimental observation of GE et al. [58]. Scratching with Vickers oriented edge first produces more recovery than Berkovich face first but less than Berkovich edge first.

When investigating the scratch appearance in relation with the relative recovered depth, these observations are underlined as seen in Fig. 4.16. Vickers in face-first orientation shows the largest recovery especially in the mainly ductile range and its recovery is consistently higher in comparison with Berkovich in face-first orientation. Berkovich in edge-first orientation shows slightly higher recovery especially when partially brittle behaviour is observed and similar recovery in comparison with Vickers edge-first in all categories.

While it is not possible to separate elastic recovery from volumetric ex-

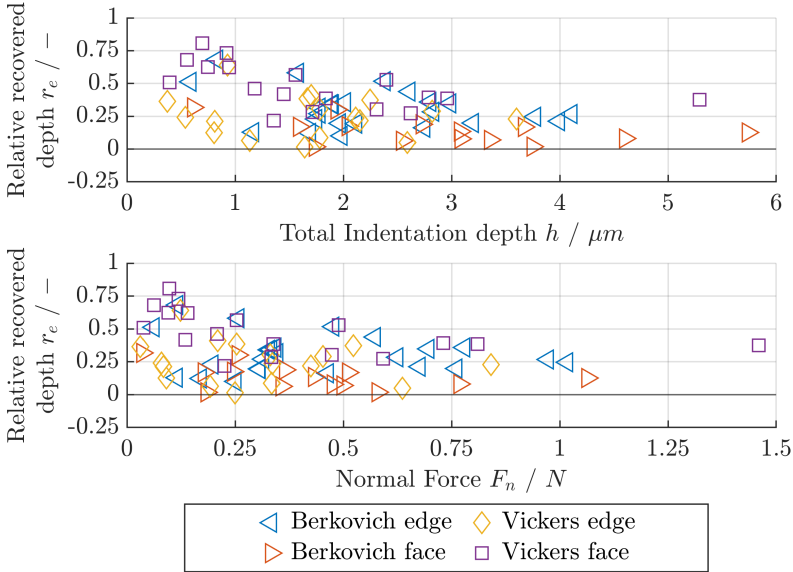


Figure 4.15: Rate of depth recovery r_e over all experiments versus the determined indentation depth h (top) and the measured normal force F_n (bottom).

pansion completely, it is possible to evaluate the rate of sink-in $r_s = \frac{h_s}{h}$, which is elastically recovered upon unloading. Fig. 4.17 shows the rate of sink-in plotted over the total indentation depth.

Sink-in is determined on the basis of an analytical solution by SNEDDON which considers the experimentally determined normal force and load-bearing area (see (2.9) and (4.6)). It is therefore reasonable, that the data can be fitted with a power function. Fig. 4.17 demonstrates that sink-in is more significant at low penetration depth and becomes less significant with higher indentation depth. The data would suggest that scratching with a depth of indentation of approximately $h < 100$ nm leads to no defined contact or purely elastic displacement, which is in line with other observations [55] where full recovery was observed up to $h = 200$ nm.

The depth recovery can be analysed further by subtracting the sink-in

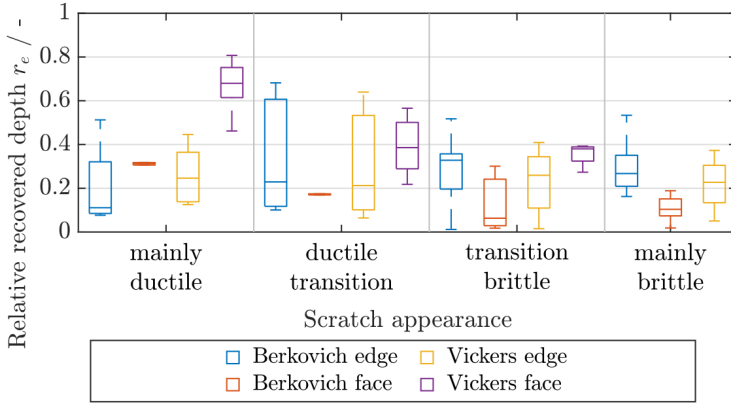


Figure 4.16: Box plots visualising relative recovery r_e and corresponding scratch appearance for groups of indenter shape and orientation.

depth h_s from the recovered depth h_e , which gives a value h_{ec} .

$$h_{ec} = h_e - h_s \quad (4.9)$$

or by elementary algebraic transformation of (2.2) and (4.7) and substitution in (4.9)

$$h_{ec} = h_c - h_f \quad (4.10)$$

This value represents the recovered depth that stems solely from the contact depth h_c , as illustrated in Fig. 4.18. Per (2.2), the total depth of indentation while the load is applied h consists of the sink-in depth h_s , indicating the elastic response of the material around the contact, and the contact depth h_c , which describes the depth in which the material touches the indenter. The residual depth h_f is the total depth h reduced by the total recovered depth h_e . All of h_s is recovered elastically and not by volume expansion due to phase transition. The rate of contact recovery r_{ec} is defined as the absolute contact recovery divided by the total

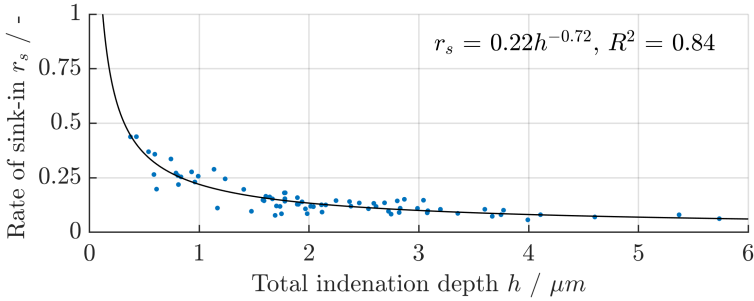


Figure 4.17: Rate of sink-in r_s versus indentation depth h .

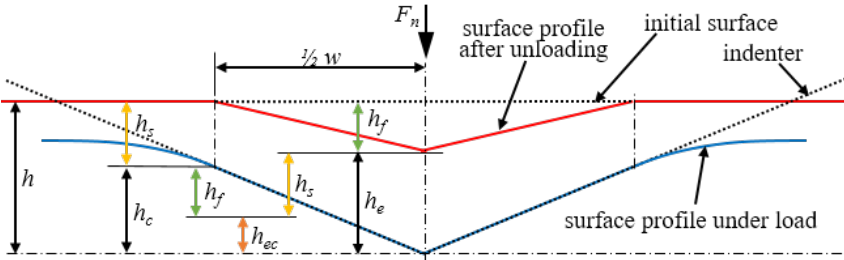


Figure 4.18: Schematic illustrating the different depth quantities accessible from the analysis of a static indentation test, notably the derivation of the recovered depth attributed to the contact depth h_{ec} in orange.

indentation depth

$$r_{ec} = \frac{h_{ec}}{h} \tag{4.11}$$

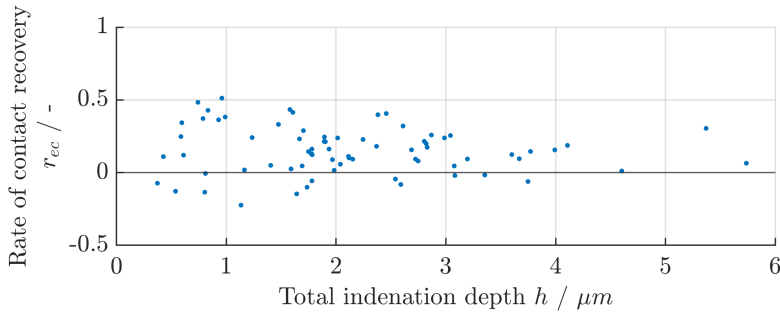


Figure 4.19: Rate of contact recovery r_{ec} versus indentation depth h .

Fig. 4.19 shows the rate of material recovery in the contact scattered over the indentation depth. Negative values for the rate of material recovery can stem from two circumstances: the sink-in depth is not fully recovered, which means that plastic deformation or residual stress suppress the elastic recovery; or the residual depth is greater than the contact depth, which is the case when additional material is removed, as happens during brittle removal.

Overall, the rate of recovery depends on the geometry and orientation of the indenter and decreases with increasing normal force and therefore indentation depth. No empiric function describing the recovery accurately on the basis of indenter geometry and penetration depth or normal force can be derived. Negative recovery, in other words additional removal, is sometimes observed in the contact zone over all penetration depths.

4.4.3 Scratch and Ploughing Hardness of Si

Scratch and ploughing hardness, as introduced in the state of the art in section 2.2.1, are to be understood as specific process forces rather than a material property. Scratch hardness relates the prescribed load in normal direction with the load-bearing area projected in a plane orthogonal to the direction of load, while ploughing hardness provides a specific cutting force which is defined as the force opposing the transversal motion divided by the area projected into a plane orthogonal to the cutting direction.

Scratch and ploughing hardness are evaluated for each geometry and orientation with regards to total penetration depth h , contact depth h_c , residual depth h_f and normal force F_n . A power function $y = bx^m$ is fitted to each set of data. The functions are amalgamated in Tab. 4.2, together with their R^2 -values showing the quality of fit and an indication of the respective figure. For reasons of readability, the plots for individual geometries are listed in appendix A from p. 211 onward. To exemplify the analysis, a plot of the hardness for each indenter geometry is presented in Fig. 4.20, followed by overviews with all data points and respective fit functions in Figs. 4.21 and 4.22.

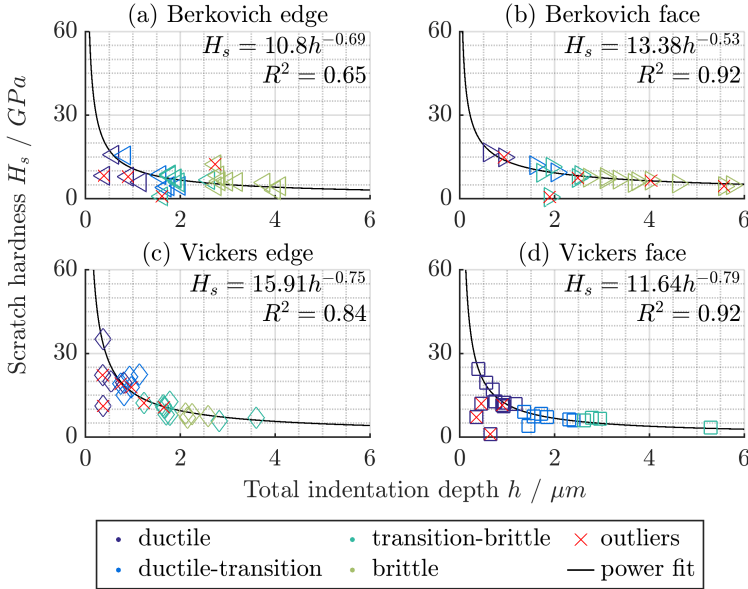


Figure 4.20: Scratch hardness H_s plotted against total indentation depth h for different geometries: (a) Berkovich edge, (b) Berkovich face, (c) Vickers edge and (d) Vickers face.

Fig. 4.20 shows scratch hardness for all geometries plotted over the total indentation depth. As expected, fitting a power function to the empiric

data yields a negative exponent and shows generally good agreement [8]. However, the quality of the fit changes significantly with different geometries and also with different categories of sets, as seen in Tab. 4.2 below. The fit quality of data generated from Berkovich edge first is often poorer in comparison with the other configurations, however no systematic cause is identified. Neglecting the data of the Berkovich indenter edge first from the overall fits does not lead to significant improvement of the fit quality.

The plots are also colour-coded based on the scratch appearance classification, as described on p. 62. It is observed that the hardness decreases as the scratch becomes increasingly brittle. Scratches are mostly ductile up to a depth of approximately $h \approx 2 \mu\text{m}$, and this value can be used as a threshold for determining the dominant removal mode. The corresponding scratch hardness falls within the range of $5 \text{ GPa} \leq H_s \leq 15 \text{ GPa}$. This pressure range is below or in the lower range of the range stated for the possible transition from Si-I to Si-II in Table 2.2, which is given as $8.8 - 16 \text{ GPa}$ under near-hydrostatic stress [67, 68, 74, 125]. However, this difference is acceptable since scratch hardness does not measure hydrostatic pressure, and the transition classification is subjectively based on the visual appearance of the scratched surface.

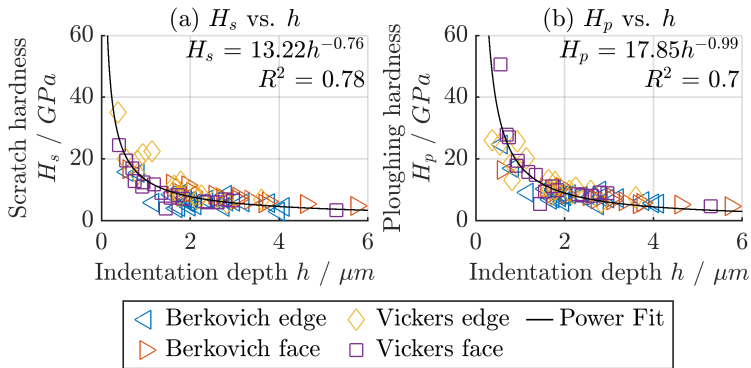


Figure 4.21: (a) Scratch hardness H_s and (b) ploughing hardness H_p plotted against total indentation depth h .

Fig. 4.21 shows that a fit function with reasonable quality can be derived even if all geometries are jointly considered. The quality of the fit is particularly positive when it is taken into account that the functions differ significantly for different geometries. Outliers accumulate at very low hardness values and small indentation depth, which suggests that either forces are underestimated when they are very small or that the load-bearing area is excessively overestimated. The latter is the case if the width of the scratch is poorly represented by the measured width on the peak of the ridges. Material recovery is large at low penetration depth and the ridges become increasingly pronounced if material is ploughed rather than removed, the relative contribution of the piled-up material to the load-bearing area is more pronounced for small scratch depths than for larger ones.

Fig. 4.22 shows the same kind of plots when deriving the hardness from a set of normal forces. The quality of the fit decreases, indicating that the errors in the measurement of the force affect the hardness more significantly than errors in the determination of the contact geometry.

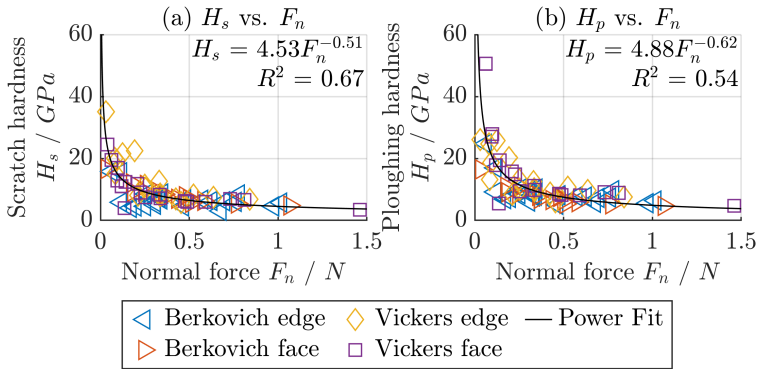


Figure 4.22: (a) Scratch hardness H_s and (b) ploughing hardness H_p plotted against normal force F_n .

Tab. 4.2 shows scratch and ploughing hardness functions for different sets: penetration depth, contact depth, residual depth and normal force. These

functional relations have special significance:

- The total penetration depth h is the parameter that is typically considered as the undeformed chip thickness h_{cu} . The load-bearing area derived from this parameter is often used to describe the geometric overlap of tool and workpiece in kinematic models.
- Contact depth h_c represents a more accurate estimation when deriving the load-bearing area, but requires knowledge of the contact conditions including sink-in and development of a burr in front of the tool (if the burr is considered to bear load).
- The residual depth h_f is the easiest quantity to determine after an experiment and represents the amount of material removed. Since the material height after the pass of a tool is the determining height that has to be removed by the next pass, it can be related directly with the feed rate.
- The normal force F_n is the determining factor when assuming that the total force is distributed onto grains following a given distribution. This is particularly relevant for processes with force-bound grains, such as honing or diamond wire sawing.

Table 4.2: Overview of all hardness functions with R^2 values and figure references.

	Scratch hardness H_s		Ploughing hardness H_p	
	Fit equation	R^2	Fit equation	R^2
Penetration depth h	Fig. A.1		Fig. A.5	
all geometries	$H_s = 13.22h^{-0.76}$	0.78	$H_p = 17.85h^{-0.99}$	0.7
Berkovich edge	$H_s = 10.8h^{-0.69}$	0.65	$H_p = 14.69h^{-0.8}$	0.83
Berkovich face	$H_s = 13.38h^{-0.53}$	0.92	$H_p = 12.91h^{-0.55}$	0.94
Vickers edge	$H_s = 15.91h^{-0.75}$	0.84	$H_p = 16.19h^{-0.58}$	0.76
Vickers face	$H_s = 11.64h^{-0.79}$	0.92	$H_p = 19.54h^{-1.43}$	0.96
Contact depth h_c	Fig. A.2		Fig. A.6	
all geometries	$H_s = 11.16h_c^{-0.64}$	0.82	$H_p = 14.43h_c^{-0.8}$	0.7
Berkovich edge	$H_s = 9.49h_c^{-0.63}$	0.71	$H_p = 12.57h_c^{-0.71}$	0.87
Berkovich face	$H_s = 12.23h_c^{-0.49}$	0.93	$H_p = 11.75h_c^{-0.52}$	0.95
Vickers edge	$H_s = 13.23h_c^{-0.61}$	0.86	$H_p = 14.02h_c^{-0.47}$	0.77
Vickers face	$H_s = 9.84h_c^{-0.65}$	0.94	$H_p = 14.96h_c^{-1.13}$	0.97
Residual depth h_f	Fig. A.3		Fig. A.7	
all geometries	$H_s = 9.62h_f^{-0.46}$	0.57	$H_p = 11.6h_f^{-0.68}$	0.65
Berkovich edge	$H_s = 7.75h_f^{-0.53}$	0.83	$H_p = 9.96h_f^{-0.54}$	0.82
Berkovich face	$H_s = 11.7h_f^{-0.46}$	0.93	$H_p = 11.21h_f^{-0.48}$	0.95
Vickers edge	$H_s = 12.49h_f^{-0.65}$	0.8	$H_p = 13.35h_f^{-0.53}$	0.78
Vickers face	$H_s = 7.61h_f^{-0.49}$	0.77	$H_p = 11.51h_f^{-0.73}$	0.58
Normal force F_n	Fig. A.4		Fig. A.8	
all geometries	$H_s = 4.53F_n^{-0.51}$	0.67	$H_p = 4.88F_n^{-0.62}$	0.54
Berkovich edge	$H_s = 4.48F_n^{-0.38}$	0.36	$H_p = 4.84F_n^{-0.51}$	0.62
Berkovich face	$H_s = 5.66F_n^{-0.34}$	0.88	$H_p = 5.24F_n^{-0.35}$	0.91
Vickers edge	$H_s = 5.55F_n^{-0.52}$	0.82	$H_p = 7.47F_n^{-0.38}$	0.65
Vickers face	$H_s = 4.06F_n^{-0.54}$	0.82	$H_p = 2.56F_n^{-1.03}$	0.92

The best overall fit is achieved when considering the contact depth h_c , the worst is acquired from the normal force F_n .

The quality of the fits for scratch hardness when considering all geometries

are overall slightly better than those for the ploughing hardness. The only exception are the fits based on residual depth. This may be due to the better signal-to-noise ratio of the ploughing hardness-determining normal force in comparison with the scratch-hardness determining cutting force, meaning that the scratch hardness is more prone to error. However, the average R^2 -value for all individual fits H_p and H_s : $\overline{R_{H_p}^2} = \overline{R_{H_s}^2} = 0.79$, meaning that on average, models built on the basis of the cutting force are as good as those derived from normal force. For that reason, this error source is considered insignificant.

Furthermore, the exponents in the ploughing hardness functions derived from Vickers face-first experiments are much smaller than those of other geometries, leading to a worse fit when all geometries are considered together. The exponent indicating the gradient of the slope when plotting a power function on double-logarithmic scale illustrates that a smaller exponent leads to a faster decrease in hardness with increasing force or penetration depth. That in turn means that the ploughing hardness, or mean specific cutting force, decreases more rapidly with higher depth when using a Vickers indenter in face-first orientation than other geometries and orientations. Moreover, experiments with Vickers face-first orientation stand out in terms of mostly higher multiplicative coefficients, which is addressed in the following section 4.4.4.

Hardness values underlay several potential sources of error:

- When determining the depth of the sink-in by (2.8), pile-up is neglected, even though pile-up is observed in the experiments. Furthermore, the method for calculation of the unloading stiffness was developed for static indentation with axisymmetric punches, while, here, it is applied to scratching with pyramidal indenters.
- The largest source of error is the derivation of the scratch width. The profile is averaged over a certain area, in which both brittle breakouts and irregular ridges occur. The height of the ridges is averaged, sometimes left and right deviate significantly and one side is twice as high as the other. It can be assumed that the error is normal distributed, so that it will be averaged out if enough data

points are considered. With only approximately 20 data points of each geometry available, the uncertainty is rather large.

- Some uncertainty stems from the force measurement, especially for the cutting force where the signal-to-noise ratio is lower. Noise affects mostly the determination of the beginning and the end of the scratch (zero crossing), but also the shape and amplitude of the force peak. The effect is considered minor but is proportionally larger for smaller forces than larger ones.
- The contact depth and consequently the load-bearing area are always derived from the indenter shape at the beginning of the experiment and do therefore not consider progressing wear. Wear is small but not zero. Later scratches at higher contact depth are affected more than earlier ones, implying that the error is larger for deep scratches. In turn, the topography measurement is more reliable at deep scratches due to relatively lower pile-up. For this reason the error potential due to wear is also considered minor.
- Errors from misalignment of the tool on the machine, relative to the direction of cut, would manifest as pervasive radial forces, which are not observed.
- As in most hardness measurement methods, the effect of friction is neglected. Measured forces always contain a friction component. A separation is only possible by the application of models and by measuring the friction separately. The effect of friction on scratch and ploughing harshness is assumed to be negligible, but has an influence especially in the Vickers face-first configuration where half of the contact area is subjected to rubbing only. This is discussed in connection with the friction coefficient in section 4.4.5.

4.4.4 Load-bearing Area when Scratching with Vickers Face First Orientation

The rate of recovery of material displaced during scratching of Si is significant, especially for small indentation depths, as pointed out in section 4.4.2.

Fig. 4.15 reveals that especially when scratching with a Vickers indenter in face first orientation, more than 50% of the total penetrated depth is recovered. Two faces of the indenter in this configuration are aligned with the direction of cut and exposed to friction. This leads to the question of whether the assumption of WILLIAMS, who suggested that 1/4th of the area projected into the plane normal to the direction of indentation A_n is bearing load during scratching [171], is reasonable.

The material recovery rate combines the effect of elastic recovery and volume expansion due to phase transition. The Si-I to Si-II transition leads to densification of the material, taking pressure away from the indenter if it doesn't lead to additional sink-in. The following phase transition towards α -Si is accompanied by volumetric expansion, which leads to a high recovery rate. However, the transition happens upon release of pressure, behind the indenter, and does not contribute to additional support on the side flanks of the indenter. Therefore, all contribution of the side faces of the Vickers indenter must be due to elastic displacement.

The contact between indenter and Si workpiece can be analysed within a numerical simulation model utilising the smoothed particle hydrodynamics (SPH). Within this simulation model the hydrodynamic stress distribution is evaluated below the indenter contact surfaces, which in the following is used to discuss load-bearing characteristics and is related with the derived scratch hardness. Scratch hardness, however, describes uniaxial contact stress in global normal direction and neither normal to the indenter face nor a three-dimensional stress state. While scratch hardness differs from hydrostatic pressure, it is expected to be proportional to it for particles in contact with the indenter.

The simulation of ductile removal of Si with grits of arbitrary shape SPH simulation with the Johnson-Cook flow stress model is described in [87]. Material model parameters for Si are taken from [159]. The Johnson-Cook flow stress model [77] evaluates the flow stress based on strain and strain rate hardening, as well as thermal softening. This model was developed for materials subjected to large strains, and high strain rates and temperatures as present in metal cutting operations and is typically applied to ductile materials.

However, the model has limitations regarding the applicability to brittle materials: Ductile materials undergo plastic deformation before failure, whilst brittle materials fail without significant plastic deformation due to cracking. Cracking as a failure mode is not represented in the Johnson-Cook flow stress model. Furthermore, in the specific case of Si, the model does not account for changes in mechanical and thermal properties due to phase transitions. The validity of the model is therefore limited to ductile behaviour and it has to be assumed that model parameters derived for Si in [159] consider the material properties of Si-II or Si-IV where plastic flow is possible. In [87] it was concluded that the model is partially useful for the representation of the ductile response of Si with regards to the modelled hydrostatic and contact stress but not for the prediction of the temperature. The majority of the deviations are attributed to a false assumption of the coefficient of friction and the unknown Taylor-Quinney coefficient. The coefficient of friction was assumed to be $\mu = 0.3$ in [87] but is determined as $\mu = 0.06$ in this work. The Taylor-Quinney coefficient describes the proportion of plastic work converted into heat. It is typically assumed to be around 90% for metals, although the exact value can depend on the material and the conditions of deformation. In the case of Si, some of the energy otherwise dissipated in heat is stored in phase transitions.

As shown in [87] on the example of a grain of arbitrary shape, sections in the rear and the side of the grain are in contact with material and support the grain. Applying the same methodology while using an idealised Vickers indenter instead of a geometrically undefined tool and the friction coefficient of $\mu = 0.06$ determined in section 4.4.5 enables the evaluation of hydrostatic stress in particles under the indenter as visualised in Fig. 4.23.

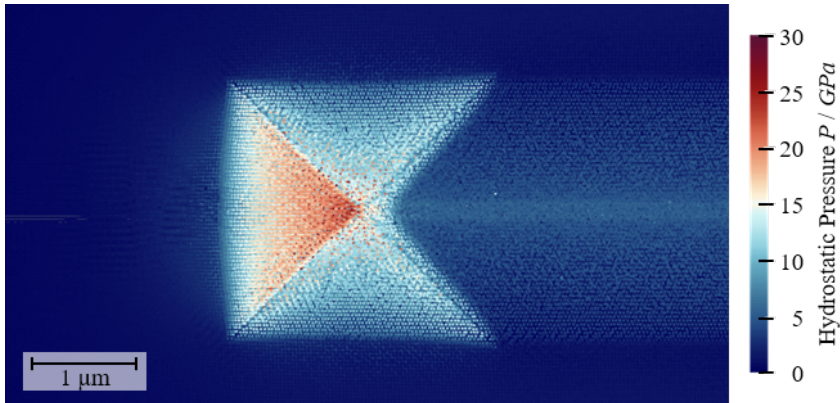


Figure 4.23: SPH simulation of a scratch test showing the resulting hydrostatic pressure: ideal Vickers indenter, face first, $v_c = 25$ m/s, $h = 0.5$ μm , movement direction of the indenter from right to left. The colour-map is capped at 0 and 30 GPa. Particles that are subjected to hydrostatic stresses outside this range are shown with the colour of the limits.

The simulated normal force, derived from the total stress in normal direction, is $F_n = 53$ mN. The projected area of the Vickers indenter in normal direction at a penetration depth $h = 0.5$ μm is $A_{p,n} = 6$ μm^2 . Assuming that the side flanks bear the same load in normal direction as the front face, the equally distributed pressure in normal direction is $P = F_n / \frac{3}{4} A_{p,n} = 11.8$ GPa. The result corresponds reasonably well with the simulated hydrostatic pressure. Obviously, the front face bears additional load due to the cutting force acting on it, this force does however act tangentially and increases the hydrostatic pressure.

To investigate the effect of a changed load-bearing factor assumption, the experimental data is evaluated with $f_b = \frac{1}{4}$ and $f_b = \frac{3}{4}$ in terms of scratch hardness. The results are shown in Fig. 4.24.

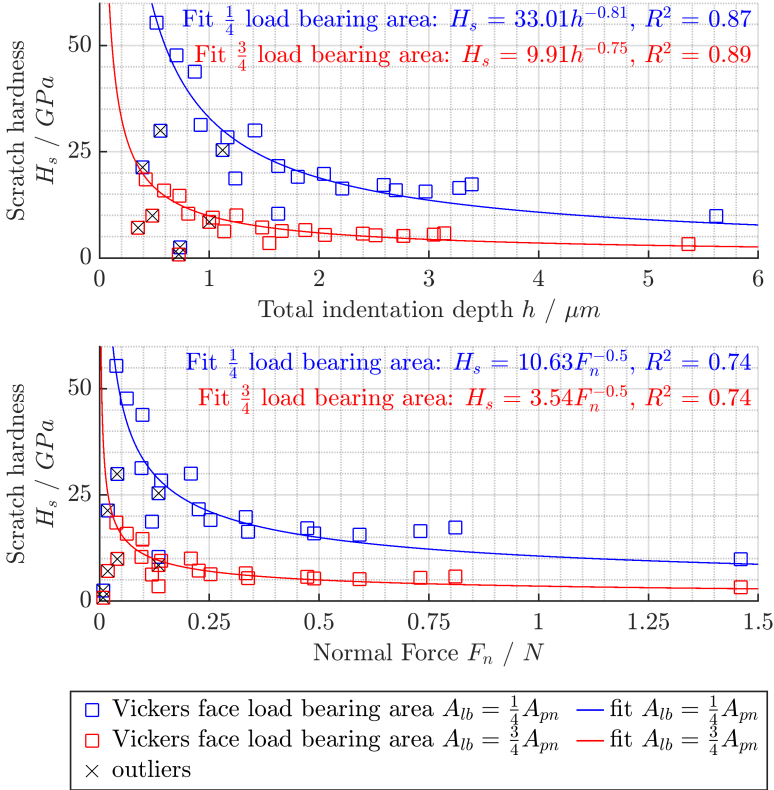


Figure 4.24: Comparison of scratch hardness for Vickers scratching face first assuming a load-bearing factor of 1/4 as assumed by WILLIAMS [171] and 3/4.

The scratch hardness predicted from the evaluation of the fit functions derived in Fig. 4.24 are $H_s = 16.7$ GPa when evaluated with the indentation depth at $h = 0.5 \mu\text{m}$ and $H_s = 15.4$ GPa when calculated from the simulated normal force at $F_n = 53$ mN. These results agree very well with the hydrostatic pressure at the flanks of the indenter shown in Fig. 4.23. Consideration of a load bearing area $A_n = \frac{1}{4}A_{p,n}$ as suggested by WILLIAMS would lead to unrealistically high values of $H_s = 57.9$ GPa (via the

penetrated depth) or $H_s = 46.2$ GPa (via the simulated normal force).

On the basis of this analysis, it is concluded that a load-bearing factor $f_b = \frac{3}{4}$ produces more consistent and accurate results for the determination of the scratch hardness of Si than a load-bearing factor $f_b = \frac{1}{4}$.

4.4.5 Determination of the Coefficient of Friction between Si and Diamond

The determination of the coefficient of friction is done on the basis of force data acquired from experiments with Rockwell indenters. No material was removed, but the cracks appeared on the surface when normal forces exceeded $F_n \approx 15$ N, as can be seen in the microscopic image of the residual surface after an experiment with a Rockwell indenter shown in Fig. 4.25.

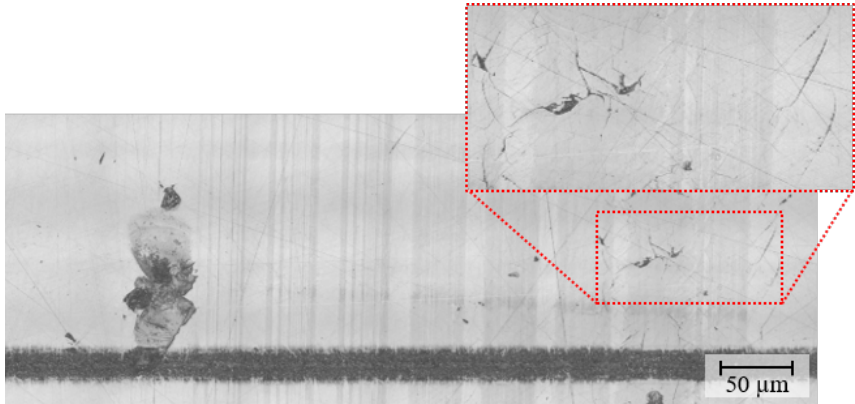


Figure 4.25: Examples of a surface generated by rubbing with a Rockwell indenter. Cracks are visible around the rightmost traces which were generated with a normal force of $F_n > 15$ N.

In order to determine the friction coefficient and whether it changes when the material cracks, the force ratio μ of the cutting and passive forces F_c and F_p with the normal force F_n is analysed. The passive force is

considered in this case, as it sometimes diverted significantly from zero in these experiments, and is also fitted with a polynomial of 5th order. The coefficient of friction is calculated as

$$\mu = \frac{\sqrt{F_c^2 + F_p^2}}{F_n} \tag{4.12}$$

using data points from the fits to the continuous force signals (see section 4.3.4) as shown in Fig. 4.26

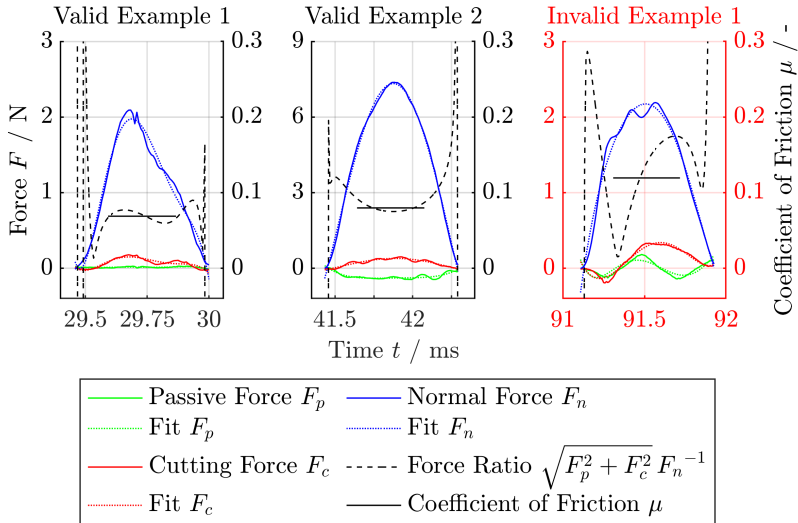


Figure 4.26: Examples of the determination of the coefficient of friction from the force signal, with an example of an outlier on the right with red axes.

The value of the coefficient of friction of one data set is its mean, calculated from the middle 50% of the data points. A data set is considered an outlier, if its mean coefficient of friction diverges more than three scaled median absolute deviations away from the median of all calculated coefficients of friction. Outliers show much higher values for the coefficient

of friction and significantly larger standard deviations. This can be attributed to the noisy passive and cutting forces, as seen in the rightmost plot of Fig. 4.26. The signal-to-noise ratio is small when forces are in the range of 0.025 N, which is about 10 times above the threshold of the dynamometer (< 0.002 N according to the data sheet). The signal in this range is dominated by a disturbance with a frequency slightly lower than 3000 Hz and an amplitude of ≈ 0.025 N, therefore in same range as the forces. This disturbance must be due to data processing as the signal is low pass-filtered at 1000 Hz.

An overview of the mean coefficients of friction and their standard deviations of all data sets generated with Rockwell indenters is shown in Fig. 4.27, with outliers marked in red.

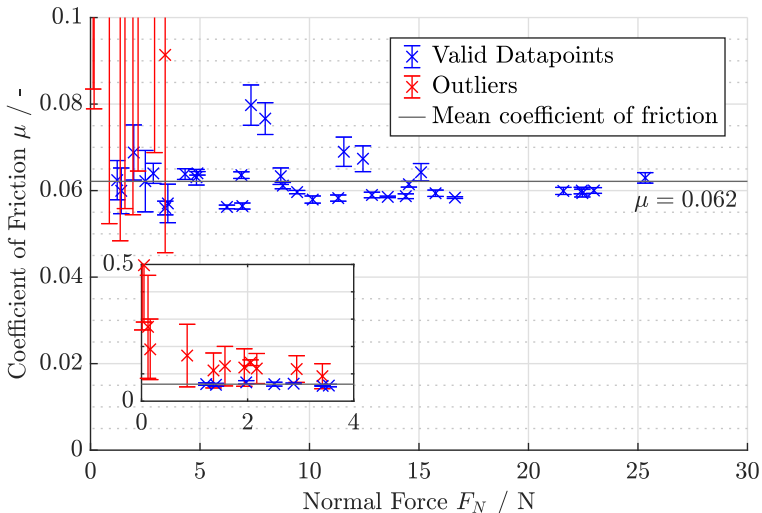


Figure 4.27: Determined values for the coefficient of friction μ and their standard deviations from all experiments with Rockwell indenters.

The coefficient of friction between Si and diamond is $\mu = 0.062$. The standard deviation from the mean of all valid data sets is $\sigma_\mu = 0.0053$. In agreement with theory, the analysis shows no dependence between the

friction coefficient and the acting normal force. It can also be seen, that the coefficient of friction does not change when cracks are induced. The standard deviation decreases with increasing normal force which is attributed to the better signal-to-noise ratio at higher force. This value for the coefficient of friction is slightly smaller than the value of $\mu = 0.08$ determined elsewhere [56]. An effect of crystallographic orientation was not observed in similar experiments [151], and is not expected for the here invested load spectrum either.

The importance of the coefficient becomes obvious when simulating the process in the SPH modelling environment as in [87] and as described in sec. 4.4.4. Neglecting friction ($\mu = 0$) shows 3% smaller normal and 32% smaller cutting forces as opposed to a simulation with $\mu = 0.062$. Increasing the friction to $\mu = 0.3$ changes not only forces and therefore contact pressure, but has the potential to also change the cutting mode. As shown in Fig. 4.28, the higher friction leads to the development of a prow and the onset of a ductile chip in front of the indenter, while the material only densifies with lower friction. It should be noted, that the underlying Johnson-Cook flow-stress model is not able to describe phase transitions that would happen in reality, so the example shown here is only illustrative and does not represent the actual removal mode well.

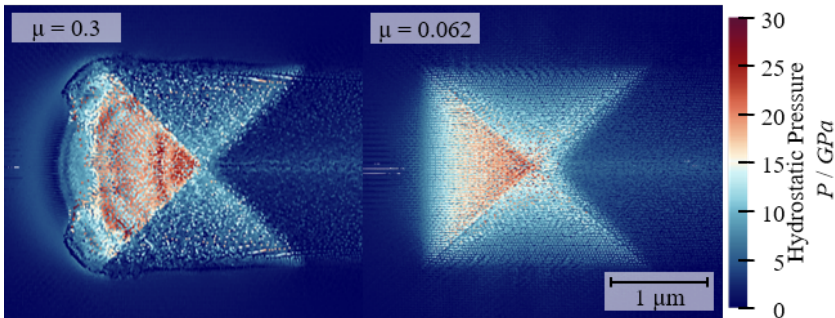


Figure 4.28: SPH simulation of a Vickers indenter moving from left to right at $h = 0.5 \mu\text{m}$ with $\mu = 0.3$ (left) and $\mu = 0.062$ (right), the scratched distance is the same in both images.

The question, whether friction is to be considered specifically in the development and parametrisation of force models such as the ploughing hardness model, arises and is discussed in the following.

The largest effect of friction is expected for the Vickers indenter in face first orientation. In this configuration, friction on the side faces, which according to the analysis above bear approximately two-thirds of the load in normal direction, might influence the ploughing hardness significantly. Without consideration of friction, the front-facing surface is subjected the full force acting in cutting direction, that is actual cutting force and the friction force. A considerable amount of the friction force does however not act on the front face, but on the two side faces. Accordingly, the cutting force acting on the front face has to be reduced by the friction force F_r acting on the side faces, which is

$$F_r = \frac{2}{3}F_n\mu \quad (4.13)$$

The force ratio $\frac{F_c}{F_n}$ for a Vickers indenter in this configuration is

$$\hat{\mu} = \frac{F_c}{F_n} = 0.2 \quad (4.14)$$

as derived from Fig. 4.29. Solving for F_n , substituting in (4.13) and setting $\mu = 0.06$ yields $F_r = 0.2F_c$. That means that around 20% of the measured tangential force acts as friction force on the side flanks of the indenter. Additional friction occurs on the front face, which is however not separated from force applied for material deformation and separation. Since in all other configurations the entire tangential and normal force acts on the friction surfaces and the frictional force is thus at least partially taken into account, the expected effect of separating friction from cutting force is significantly lower there. In addition, the exact analysis is complicated by the consideration of friction: part of the tangential force acts in the direction of the normal force due to friction on inclined surfaces, just as the normal force causes a frictional force. A division of the forces is not possible without the use of further models and, as explained above, is also

not sensible against a practical background.

In the case where friction is to be taken into account for a Vickers indenter in face first orientation, limited to the effect of friction on the side faces, this can be done by reducing the cutting force used to calculate the ploughing hardness by the amount of the friction force. The corrected cutting force \tilde{F}_c is then

$$\tilde{F}_c = F_c - \frac{2}{3}F_n\mu \tag{4.15}$$

Applying this equation and re-calculating the fit functions for the ploughing hardness leads to new fit equations as summarised in Tab. 4.3.

Table 4.3: Ploughing hardness functions for Vickers face-first orientation, corrected for friction.

	Ploughing hardness H_p	
	Fit equation	R^2
Penetration depth h		
all geometries	$H_p = 16.82h^{-0.98}$	0.72
Vickers face	$H_p = 16.21h^{-1.54}$	0.96
Contact depth h_c		
all geometries	$H_p = 13.62h_c^{-0.79}$	0.73
Vickers face	$H_p = 12.23h_c^{-1.21}$	0.97
Residual depth h_f		
all geometries	$H_p = 11.11h_f^{-0.65}$	0.63
Vickers face	$H_p = 9.5h_f^{-0.76}$	0.56
Normal force F_n		
all geometries	$H_p = 4.62F_n^{-0.62}$	0.57
Vickers face	$H_p = 1.8F_n^{-1.12}$	0.93

In comparison with the values from Tab. 4.2, a slight improvement of the fit quality for all geometries of at least 2% is achieved. This means that

by addressing friction in case of Vickers face-first, the results agree better with those of other geometries, albeit not by much. The fit functions for Vickers in face-first orientation still stand out by their large exponent. As argued above, the effect of consideration of friction is expected to be largest for this geometry. The fact that the improvement of the fit qualities for all geometries by consideration of friction is between 2 and 3% only shows, that the neglect of friction when determining the cutting force does not significantly worsen the model quality.

While the consideration of friction is significant when modelling the material removal process with methods such as SPH or FEM or to compare the work done by friction with the work done to separate the material, it is not necessary to consider frictional forces separately from the forces applied for material separation. Friction is always present in real manufacturing processes and the determination of scratch hardness should have friction integrated rather than be corrected for the effects of friction.

In summary, it is shown that the macroscopic friction coefficient between Si and diamond is $\mu = 0.062$, which is lower than the value found in the literature. Furthermore, the influence of friction on the ploughing hardness for the Vickers Indenter in face first orientation is discussed and optimised functions are determined.

4.4.6 Force Ratio

The force ratio $\hat{\mu}$ is derived from experiments with sharp indenter geometries and plotted over the contact depth h_c in Fig. 4.29.

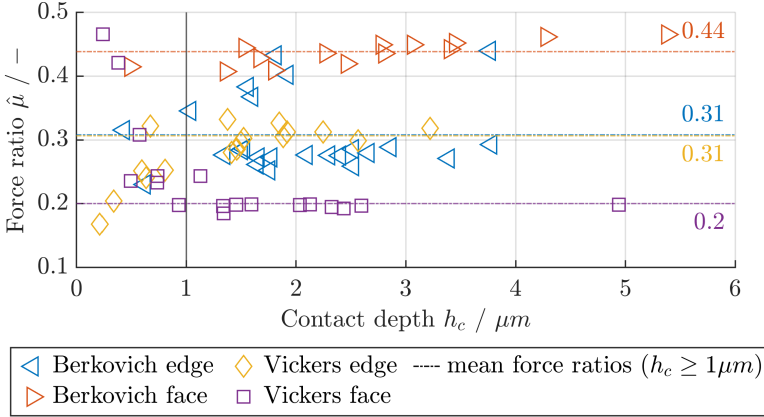


Figure 4.29: Force ratio $\hat{\mu}$ derived from experiments with sharp indenter geometries. Means are derived from data points where the contact depth $h_c \geq 1 \mu\text{m}$ to mitigate effects of the dull tip.

Fig. 4.29 shows the experimentally resolved force ratio $\hat{\mu} = \frac{F_c}{F_n}$ for each tested geometry, along with their mean indicated by the dash-dotted lines and the respective number. Inspecting data points belonging to experiments with Vickers indenters shows that force ratios at a penetration depth $h < 1 \mu\text{m}$ deviates strongly from the mean of data points at greater penetration depth, which may be attributed to the imperfect tip of the indenter. In micro-cutting, the effect of the cutting edge rounding has a significant impact on forces and material flow (see e.g. [175]). The rounding of the top dominates the behaviour at very low contact depth until the rake face is sufficiently determining the scratching process. For this reason, the means are derived from data points at contact depth $h_c \geq 1 \mu\text{m}$. The SPH simulation predicts a force ratio $\hat{\mu} = 0.225$ for a Vickers indenter with an ideally sharp tip in face-first alignment at an indentation depth $h = 0.5 \mu\text{m}$. This result agrees well with the experimentally determined average value for contact depths $h_c \geq 1 \mu\text{m}$, thus confirming the assumption that the error is mainly due to the rounding of the tip. Experiments with a Berkovich indenter in edge-first orientation scatter more than those with other geometries. The force ratio $\hat{\mu}$ depends on the geometry used

and is $0.2 \leq \hat{\mu} \leq 0.45$ for scratching Si with diamond.

4.4.7 Crystallography Composition

As pointed out in the literature review, ductile removal is thought to be possible only if Si metallises under high pressure and undergoes a phase transition from Si-I to Si-II. Si-II is metastable and transitions back to amorphous α -Si and finally back to Si-I when the pressure is released. The pressure range for the transition is given as 8.8 to 16 GPa. While the scratch hardness does not equal the contact pressure or the stress in the material under the indenter which ultimately determines the phase transition, it may be used to approximate the pressure in normal direction near the tip of the indenter. The scratch hardness functions determined in section 4.4.3 for all geometries can be used to estimate the depth of cut at which the pressure in normal direction is sufficiently high to activate the phase transition and allow for ductile material removal:

$$H_s = 15.4h^{-0.82} \quad (4.16)$$

Setting $H_s = 8.8 \dots 16$ GPa and solving for h yields $h \approx 0.95 \dots 1.95 \mu\text{m}$ as the range defining the upper bound in which ductile removal can happen. The pressure is high enough at depth lower than $0.95 \mu\text{m}$ and not sufficiently high at depth larger than $1.95 \mu\text{m}$. This means that up to contact depths in this range, amorphised silicon must be present. In spite of all shortcomings of this very simplified approach, the range agrees well with the observation of predominantly ductile scratch appearance up to $h \leq 2 \mu\text{m}$ described in section 4.4.3.

The crystallographic composition of the scratched material is analysed on the basis of the Raman intensity ratio between the peaks of Si-IV at $5101/\text{cm}$ and the adjacent α -Si peak around $4751/\text{cm}$ $r_{\alpha\text{-IV}} = \frac{I_{\alpha\text{-Si}475}}{I_{\text{Si-IV}}}$. It should be noted, that the presence of both phases indicates a preceding phase transition from Si-I to Si-II. Datasets where a Si-I-phase is detected and the intensity of that phase is more than 1/4th of the intensity of the Si-IV-phase are disregarded for reasons of consistency, as these data sets

show an intensity ratio $r_{\alpha\text{-IV}}$ that is orders of magnitude greater than when no Si-I phase is present. Still, the determined intensity ratios calculated for the same scratch at different locations in the scratch ground on a length of approximately $20\ \mu\text{m}$ scatter strongly as shown in Fig. 4.30.

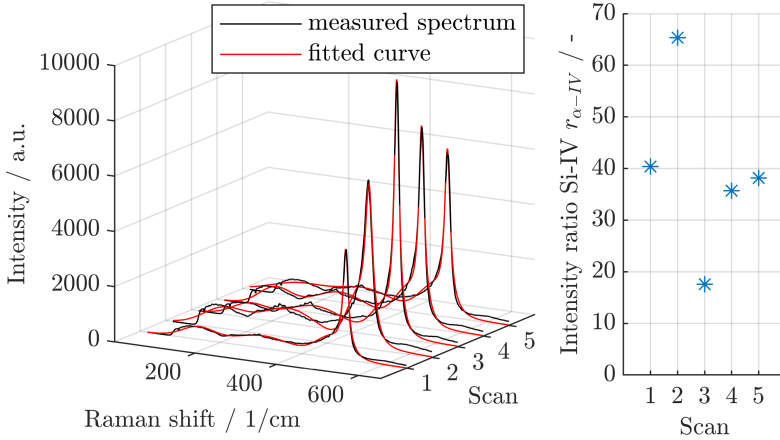


Figure 4.30: Raman spectra (left) and intensity ratios of the Si-IV-phase with the adjacent α -Si-peak (right) for a Vickers indenter in edge-first orientation.

Of 151 measured positions, 73 fulfil the above mentioned criteria and furthermore belong to scratches, that were not considered outliers in the hardness analysis. Seeing that many data points analysed showed Si-I indicates, that the response volume is larger than the volume affected by phase change. This is the case if either the material transitioned back to Si-I or the phase changed layer is thinner than the penetration depth of 935 nm and pristine crystalline regions beneath the phase changed layers are measured.

The data is grouped by indenter type and orientation analysed with respect to the total indentation depth, normal force, scratch hardness and ploughing hardness of the respective scratch. The results are shown as box-plots in Figs. 4.31 to 4.33, where each box represents the data points acquired from measurements within the same scratch. Box plots show the

median of the measured values inside the box. Further analysis showed that for almost all data sets, the median does not differ at a 5% significance level. Accordingly, further interpretation is subject to a high degree of uncertainty. However, most importantly, this signifies that the phase transition is not significantly influenced by indenter shape and orientation.

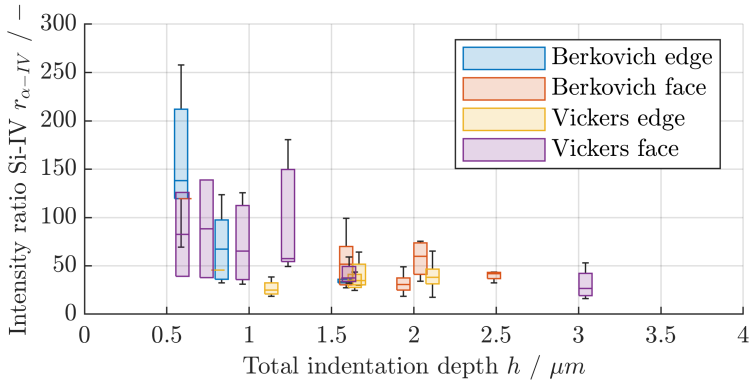


Figure 4.31: Box plot of the intensity ratio $r_{\alpha-IV}$ plotted over the total indentation depth h .

Fig. 4.31 shows a decreasing trend for the intensity ratio with increasing depth for all geometries, meaning that less amorphous α -Si is present when the penetration depth increases. This means either that more α -Si is changed back to crystalline Si or less material was phase-changed in the first place. Since there is no immediate reason for an improved annealing process, the latter phenomenon is more likely and agrees with the observation that less amorphous material is present in regions processed in the brittle cutting regime dominating at higher depth of cut. The graphic shows furthermore, that larger amounts of amorphised Si are present at total indentation depths h smaller than approximately $2 \mu\text{m}$, the threshold below which the pressure is high enough for a phase transition between Si-I and Si-II. However, the determination of the scratch geometry is only possible where at least partially ductile behaviour was observed, meaning that no purely brittle scratches were measured. Therefore, the dataset is biased in this context. A lower limit is identified at around $r_{\alpha-IV} = 25$,

which could indicate a minimum thickness or a detection limit of the amorphous layer.

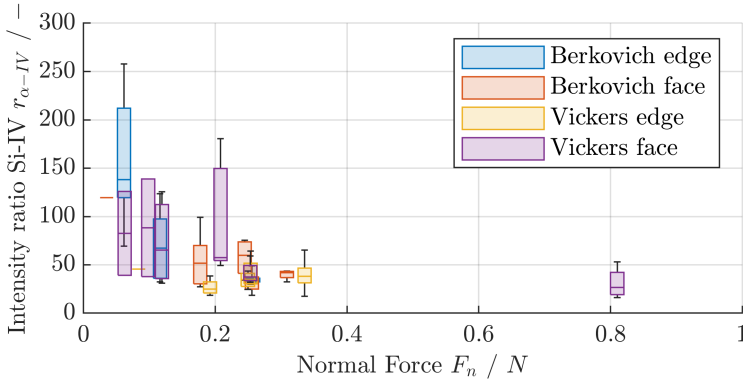


Figure 4.32: Box plot of the intensity ratio $r_{\alpha-IV}$ plotted over the normal force F_n .

Analysing the effect of increasing normal force in Fig. 4.32 shows a similar trend as the total indentation depth, as expected due to the correlation between normal force and penetration depth.

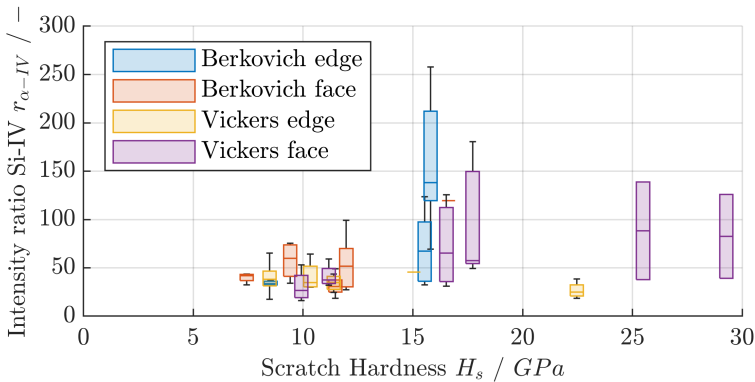


Figure 4.33: Box plot of the intensity ratio $r_{\alpha-IV}$ plotted over the scratch hardness H_s .

When intensity ratio is plotted against the scratch hardness, a trend of higher amorphisation with higher contact pressure can be observed in Fig. 4.33, with the exception of one sample scratched with Vickers in edge first orientation. Scratch hardness presents a measure for the contact pressure between indenter and material. The trend is reasonable considering that more Si-I is changed to Si-II if the contact pressure is higher and the critical pressure is upheld further into the plastic zone.

YAN et al. [178] measured the thickness of the amorphous layer and correlated it with the Raman intensity ratio $r_{\alpha-I}$. In their work, a ubiquitous presence of the Si-I and ubiquitous absence of the Si-IV phase was observed, which is not the case in the experiments presented here. Their correlation cannot be applied to the here-determined Raman intensity ratio $r_{\alpha-IV}$. Further investigation of the depth of the amorphous layer is therefore not possible on the basis of the data available. Analysing the intensity ratio between Si-I and Si-IV $r_{I-IV} = \frac{I_{Si-I}}{I_{Si-IV}}$ shows no trends and scatter of 20 orders of magnitude, as either the intensity of Si-I or Si-IV tends to be very small. Fig. 4.34 uses all data points (regardless of whether they are outliers or not) where $0.1 \leq r_{I-IV} \leq 10$, illustrating the scatter in a range of values that would be relevant.

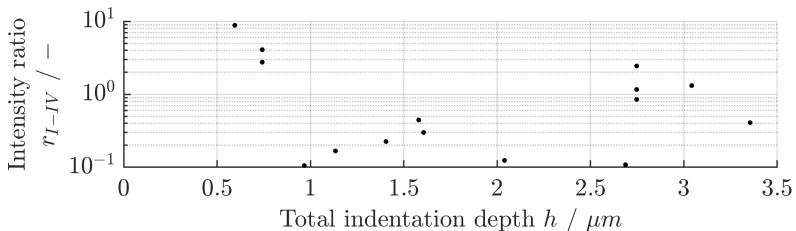


Figure 4.34: Scatter plot of the intensity ratio between Si-I and Si-IV r_{I-IV} .

Similar observations are made when analysing the intensity ratio between amorphous Si and Si-I $r_{\alpha-I} = \frac{I_{\alpha-Si}}{I_{Si-I}}$ as seen in Fig. 4.35. The scatter plot illustrates the typically very small intensities of Si-I which lead to very high intensity ratios. From the plot it cannot be deduced that a thicker layer of amorphous Si is produced at low depth of cut where removal is mostly ductile and proportionally a lot of material undergoes phase

change.

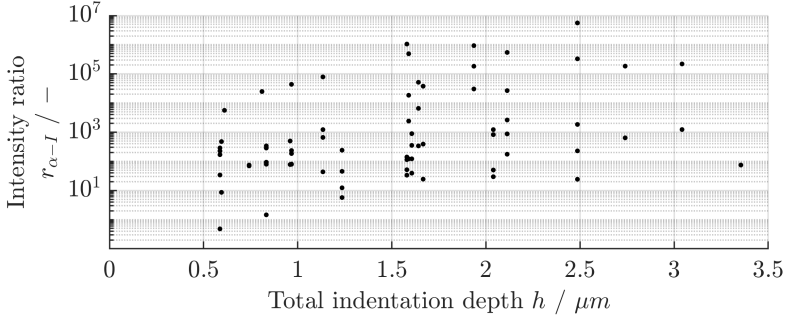


Figure 4.35: Scatter plot of the intensity ratio between α -Si and Si-I $r_{\alpha-I}$.

Summarised, Raman spectra for scratches produced with different orientations and geometries exhibit mostly the same residual phase changed material on the scratch surface. The Raman intensity ratio is a parameter which describes and quantifies the relative presence between two phases, in this case Si-IV and α -Si, giving an estimation for the quantity of material in each phase present. This ratio is a measure for the density change of the material on the machined surface and therefore a measure for the compressive residual stress as α -Si shows a 10-15% lower density than pristine Si [123]. It is shown that for higher cutting depths, this ratio decreases, meaning that relatively less amorphous silicon is produced. No significant change in the intensity ratio is found on the comparison of different indenters or orientations - the amount of phase produced is not controlled by these parameters.

The result of no effect of the grain shape on the Raman intensity ratio is contradictory to the expectation, which results from the observation that the shape influences the ductile to brittle transition (see for example Fig. 4.14). Two potential causes for the inconsistency are identified:

1. In terms of observed scratch ductility, only the Vickers indenter in edge first orientation differs statistically significantly with regards to total indentation depth at which predominantly ductile removal

is observed, see Fig. 4.14. The effect is not strong and it is possible, that it lost in the scatter of the measurement data. Since only few data points at a given depth of force level are available, the uncertainty regarding statistical significance remains high.

2. The Raman intensity ratio measures the composition of the material after scratching, not during scratching. It is plausible that different contact stresses during the loading phase could result significantly different phase transitions and different material removal modes. However, after unloading, stress relaxation occurs with various phase transitions and potential cracking. Additionally, the degree of elastic recovery could vary. As a result, the residual stress state for all indenters may eventually become equal. Since all phases of Si other than Si-I are metastable at room temperature, it is possible that the residual Si-IV phase is only present due to high residual compressive stress. If further all indenter shapes yield similar residual stress in the scratch ground this may lead to an equalised residual phase composition.

This observation is important for the DWS technique as phase transitions occurring during sawing cannot be attributed to the the shape and wear of the diamonds. It furthermore shows that ductile removal comes at the expense of compressive residual stress on the surface. If unevenly distributed over the wafer surfaces, it has the potential to warp the wafer.

Finally, the scattering intensity ratio within one scratch shows that the Raman intensity ratio is very sensitive to the position where the analysis is made and as many measurements per conditions as possible should be performed.

4.5 Conclusions: Material Removal Mechanism of Si

This chapter prepares the foundations for the analysis and modelling of the diamond wire sawing process. Based on fundamental single grain ex-

periments with different grain geometry and orientation, empirical equations for the determination of the specific cutting force are derived by the scratch and ploughing hardness and are extensively discussed. The experimental conditions are comparable with the sawing process in terms of cutting speed, contact length and depth of cut.

The scratch hardness using a Vickers indenter in face-first orientation is discussed in detail. The literature suggests a load bearing ratio of 1/4 of the total area, but it is shown that the assumption of a bearing ratio of 3/4 leads to more accurate results.

The discussion also looks at the recovery rate, noting that much of the recovered depth cannot be attributed to elastic recovery and must instead come from the volume change associated with the phase change.

The coefficient of friction of $\mu = 0.062$ determined here is slightly smaller than the only comparable value found in the literature for friction at the macroscopic level between diamond and Si in the (100) plane. The ratio between cutting and normal force is derived and discussed.

In particular, the investigation of the crystalline phase at the scratched surface shows that the grain shape has no significant influence on the phase composition and the amount of amorphised material. Amorphisation due to a reconversion of the material after a previous transformation from Si-I to Si-II occurs mainly up to undeformed chip thickness in the range of 0.95 to 1.95 μm . Higher undeformed chip thickness leads to insufficient pressure for the transformation. Below this range, the contact pressure is certainly high enough for the phase transition to happen. As plastic flow of Si requires the presence of a metallic phase, such as Si-II, the transition from primarily ductile removal to primarily brittle removal is expected to happen as a depth of cut of 0.95 to 1.95 μm . This simplified analysis agrees well with observation of the scratch appearance for all geometries, where predominantly ductile behavior is observed up to an indentation depth of $h = 2 \mu\text{m}$.

Furthermore, the higher amorphisation rates at smaller depths of cut lead to an increased formation of amorphised Si, which can lead to residual compressive stresses due to the lower density in comparison to pristine

Si-I and residual Si-IV. Additional measurement of the thickness of the amorphous layer, ideally with stress measurement, is necessary to reach a final conclusion and to correlate the α -Si to Si-IV Raman intensity ratio with the amorphous layer thickness.

Chapter 5

Process Modelling of Diamond Wire Sawing

5.1 Motivation: Kinematic Modelling of the Diamond Wire Sawing Process

At the time this research work was launched, no holistic kinematic models for the DWS process were available in literature. A mathematical formulation for the wire bow had also not yet been derived and the assumptions made by LIEDKE AND KUNA [109] for LAS had not yet been discussed with the boundary conditions of diamond wire sawing. Notably, a function linking contact pressure and cutting speed with removal rate has to be discussed, as well as the assumption of a constant coefficient of friction or force ratio.

The results of chapter 4 offer a relationship of load-bearing area and force, in other words contact pressure, with penetration depth and residual depth for sharp grains. It has to be verified that this formulation accurately describes the conditions present in DWS when used for the derivation of the missing removal-rate function.

The identified dependence of the force ratio $\hat{\mu}$ on grit shape and orientation

results in the assumption that the force ratio is distributed similarly to the shape distribution of the grains.

5.2 Chapter Outline

This chapter deals with the kinetics of the DWS process. Experimental analysis was performed on a laboratory-scale diamond wire saw, which was developed and is introduced first. The saw requires the use of a wire loop whose characteristics differ from those of the electroplated wire used in industry.

A macroscopic model to describe the wire bow is derived. The process is analysed with the help of the model and verified experimentally. Observations on the cutting-force ratio are discussed with results from the single-grain experiments, described in the preceding chapter.

Following the general process kinetics and kinematics, a model for the prediction of the material removal rate based on process forces and cutting speed is derived on grain and topography level. Wear and wire topography are analysed in detail before the material removal rate model can be evaluated.

5.3 Experimental Materials and Methods

The experimental analysis of the DWS process in a laboratory is difficult due to several properties of the industrially applied process:

- Diamond wire saws are built for cutting several hundred wafers at once. The spacing between the wires in the web is set by grooves on the guide rolls and while individual grooves can be skipped to increase the space, it remains small. The web also continues in front of and behind the ingot, limiting accessibility to the first and last wire in contact and impeding bow measurement from the side. To date, there is no commercial solution available for measuring the

bow of an individual wire on these saws.

- Measurement of forces on the ingot is possible with force sensors, however as these are designed for analysing the forces acting when several hundred wafers are cut and their sensitivity is not sufficient for reliably measuring the small forces resulting from a single cut.
- The high cutting speed typically applied when slicing wafers leads to a very high wire consumption. Considering that the wire has to be accelerated, even a short cut of 10s duration requires well over 250 m of wire, assuming a cutting speed of 25 m/s. To study the process in a stable condition, the wire must be run in a single direction for a prolonged period. However, in industrial applications, the process is operated in pilgrim mode, which involves periodically reversing the direction of the wire. As a result, the wire needs to be several hundred meters in length. This leads to high tool costs, and experimenting with different wires becomes expensive. Moreover, repeated identification and analysis of the same individual wire sections is complex.
- With up to several km of wire on the industrial machines, investigating the wear of individual grains on a specific section is impossible. Additionally, if only one pilgrim cycle is examined, the contact length per unit wire length is minimal.
- On industrial machines, the cutting energy is introduced to the wire through the accelerated guide rolls, resulting in small slip on the guide roll surfaces. This leads to loss of wire tension in the web. While the tension can normalise with time, it imposes an additional boundary condition, as the wire tension is then time dependent.

Due to the above mentioned reasons, researchers often use single wire saws that differ from the industrial saws. In order to analyse specific aspects of the process, the rigs are normally limited in emulating the whole of the cutting process, especially in terms of cutting speed. The cutting speed normally falls well behind the high speeds used in production (≤ 1.3 m/s [107, 183, 184], ≤ 2 m/s [54], ≤ 3 m/s [145], ≤ 5 m/s [81] or

6 m/s [174]). WANG et al. [168] overcome this limitation by rotating the workpiece, achieving a cutting speed of 5 m/s superposed with a work piece rotative speed of up to 50/min; the contact conditions do however differ significantly from those of the industrial process. Some researchers use industrial saws with a single winding [108] or several windings [110]. KNOBLAUCH et al. [89] and COSTA et al. [33, 34] employ an endless wire sawing rig that applies wire welded to a loop, achieving cutting speeds of up to 26 m/s. The approach applying a wire loop is the only one that allows for long cutting duration at high speed without changing the wire direction or interrupting the cut, therefore this approach is pursued.

In the following sections, the developed endless-wire saw, along with incorporated measurement systems and analysis methods are presented.

5.3.1 Test Rig: Endless Wire Saw

A test bench was designed, built and qualified. The concept is based on a wire loop run around five pulleys where each pulley fulfils one single purpose. A schematic illustrating the arrangement of the pulleys, motions and acting forces is presented in Fig. 5.1.

The wire loop is guided around five rolls. While the wire can run in both directions, in the presented work it always runs counter-clockwise, driven by a pulley in the centre. The wire tension is set by a movable tensioning pulley, which can move up and down and thereby compensate the additional wire length necessary as the wire bow develops. The wire is guided vertically to and from the pulley, so the tension in the wire F_s is approximately equal to half of the force applied to the pulley. The subsequent two idler pulleys guide the wire to and from the workpiece. The workpiece is placed between the two pulleys and fed vertically into the wire. The fifth idler pulley serves the purpose of increasing the wrap angle of the drive pulley and is therefore positioned above the drive pulley. Increasing the wrap angle ensures that the wire does not slip as the momentum necessary to achieve the cutting force on the workpiece is transferred to the wire.

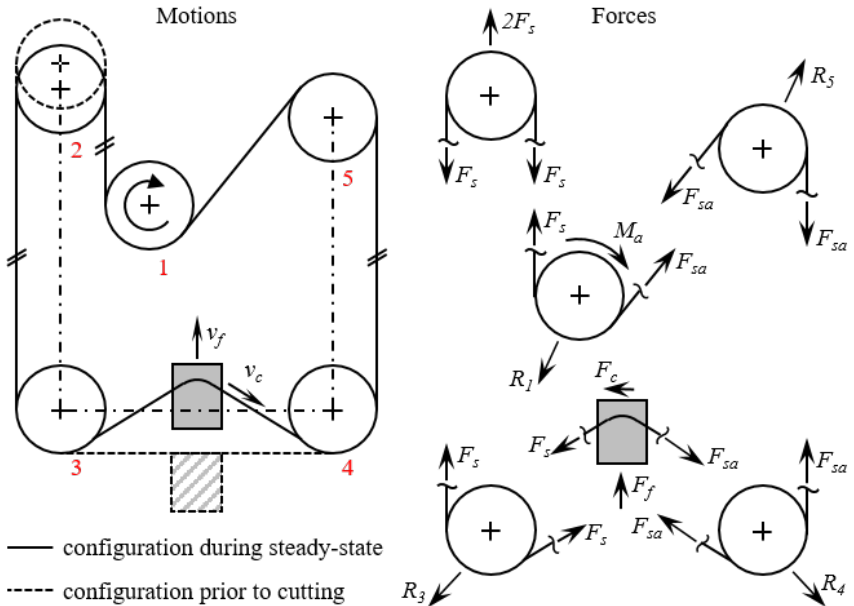


Figure 5.1: Principle of an endless-wire saw with five pulleys: 1 driven pulley, 2 moveable idler, 3 and 4 deflection rollers at the workpiece, 5 pulley to increase the wrap angle on pulley 1. Motion of the workpiece (grey) and wire is shown on the left with feed rate v_f and cutting speed v_c , respectively. Forces acting on wire (F_s and F_{sa}) and workpiece (feed force F_f and cutting force F_c), as well as pulley-reaction forces R_i and drive torque M_a are shown on the right. Dimensions are not to scale.

The wire tension is set in the idle side of the pulley system so the pre-set tension force does not change as the bow develops and as the spindle applies the additional momentum needed to supply the cutting force. If the wire was tensioned on the loaded strand, the wire would slacken in the idle strand, which is possible in principle but would require a different formulation of the wire bow differential equation developed in section 5.4. Furthermore, in the extreme case that the cutting force equals the tensioning force, the cutting process would take all the tension out of the wire. When the idle side is tensioned, the tension on that side is defined and

does not change while the maximum tension in the loaded side is defined by the spindle torque and the friction around the driven guide roll.

A CAD model and a photo of the machine are shown in Fig. 5.2.

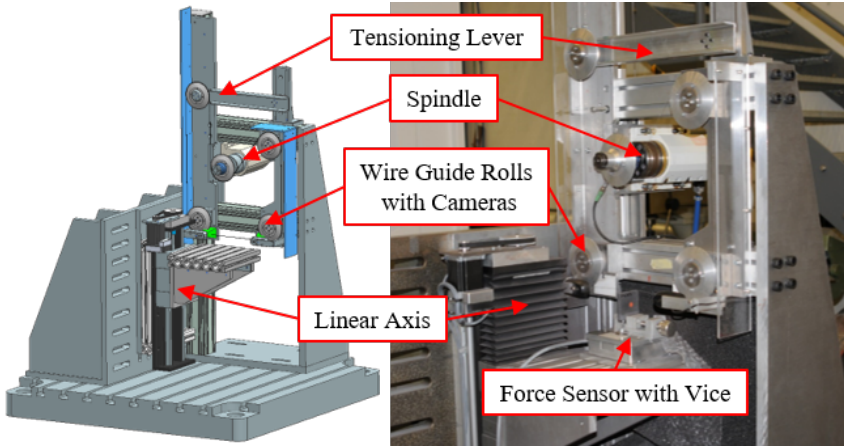


Figure 5.2: CAD model and photo of the wire sawing test rig with indication of the most important components.

The drive pulley is accelerated by a dressing spindle AES-72x260/1 GAP (Fischer Spindle Group AG), which is supplied by an Altivar ATV74 (Schneider Electric) frequency converter. The spindle is powered by an asynchronous motor, where slip increases with increasing drive torque. The actual speed is therefore lower than the speed specified by the frequency inverter. Accordingly, speed control is necessary, which is realised with an inductive proximity sensor (IFRM 08P1701/S35L, Baumer Electric AG) placed behind the drive pulley. A crown-shaped sensor ring mounted to the pulley is designed in such a way that the sensor measures a rectangular signal with 6 rising and falling edges per revolution. At high speeds, the Nyquist-Shannon theorem must be observed, which specifies the minimum sampling frequency for controlling the highest frequency that occurs. If the theorem was not met, aliasing effects would return a frequency that is too low and the control would increase the frequency unrestrained. Furthermore, the speed must not change abruptly, as the

inertia of the system would lead to wire breakage or very high wear on the rollers when the wire slips. The control is realised with an Arduino computer. The cutting speed v_c is derived from the switching frequency f with the pulley radius r according to (5.1)

$$v_c = 2\pi r f \quad (5.1)$$

The effectiveness of the cutting speed control system was verified through measurement with a high-speed camera.

The linear vertical motion of the tensioning pulley is realised as it pivots around a hinged vertical lever. Typical wire bows lead to negligibly small rotations of the lever; the motion of the tensioning roll is therefore nearly vertical, keeping the wire tension constant as the bow develops. The lever is pulled upward by a cable attached to a weight.

The linear axis realising the feed motion consists of a stepper motor (PANdrive PD-109-57 with NEMA-23 Stepper Motor Mechatronic Module, Trinamic Motion Control GmbH & Co KG) and a ball screw drive (Schneeberger AG Lineartechnik). The motor is linked with the ball screw drive through a synchronous belt. The feed rate can be established in two ways - by using a constant feed or by controlling the feed rate through the feed force, with the feed rate as the manipulated variable. The controlled feed rate has the advantage of quickly achieving a steady process state, where the wire bow remains constant and the force applied to the workpiece through the wire tension stays constant. In this state, the feed rate equals the material removal rate. Using feed-force-controlled feed rate, the wire displacement approaches the ultimate level quickly, and the feed rate is adapted while the workpiece takes the shape of the final bow. The PID-controller takes input parameters such as a target feed force ($F_{f,ref}$), a maximum feed rate ($v_{f,max}$) and the largest permitted change of the feed rate over one control sequence ($\delta v_{f,max}$). The controller parameters, including proportional, integral and derivative gain, need to be determined experimentally since the transfer function of feed force to feed rate is unknown.

The measurement of cutting and feed force is realised with strain-gauge-

based 3-axis force sensor K30D120-100N and a GSV-4USB M12 amplifier (both ME Meßsysteme GmbH). The force sensor is designed for a nominal load of 100 N and features an accuracy of 1%. Static noise is in the order of 0.05 N.

The wire bow is captured with two USB cameras (C310, Logitech international SA) which are mounted next the left and right guide pulleys. The wire image is first converted into a black and white image. Next, a Hough transformation is used to detect and assign weights to the straight lines. The angle of the line representing the wire relative to the angle of the line detected at zero deflection before the cutting process began is then determined. The resolution of the bow angle measurement is 0.1° , the accuracy is estimated to be $\pm 0.3^\circ$ but worsens with wire vibration.

A computer runs the control of the machine which is implemented in C#. The same environment also logs the measured process forces, current cutting speed and feed rate and measured wire bow. As the process is not very dynamic, a low sample rate between 4 and 10 Hz is chosen.

A cooling system has been added to the wire saw, however, in order to keep the process simple, to avoid interference between the coolant and the measured process forces and to ensure comparability with the scratch tests, all tests are performed dry. The cooling system is not shown in Fig. 5.2.

5.3.2 Workpiece: Silicon Bricks

Si bricks are sawn from an as-drawn Si-[100] ingot with diameter 130 mm supplied by Tianjin Century Electronics Co., Ltd. First, disks of the proper thickness are sawn off, which are then squared and cut into 4 bricks per disk. The resulting workpieces have the dimensions $l = 14..24..35$ mm by $h = 45$ mm by $t = 90$ mm. l is the width of the workpiece and is approximating the contact length l_i between wire and workpiece in the experiments. This simplification underlies the assumption that the elongation of the contact length due to the curvature of the wire is negligible. h is the height of the workpiece in feed direction. t is the usable length of the workpiece from which specimen of approximately 2 to 3 mm thick-

ness will be sliced off. Feed and cutting direction in the experiments are oriented along the $\langle 100 \rangle$ axes.

5.3.3 Tool: Stranded Diamond Wire

The requirement of having to use a wire loop with the endless wire saw presents a significant challenge: Electroplated diamond wire loops with high tensile strength are commercially not available. The currently available devices for electroplating wires require the wires to be fed through a hole, meaning that only open wires can be equipped with diamonds by galvanisation.

KNOBLAUCH [89, 90] approached this challenge by butt-welding a commercial wire to a loop. Upon testing these wires it was found that the strength of the weld is insufficient for the high tension required and the exposure to a frequent reciprocal bending load. A new, improved welding device was designed and tested, however, the strength of the weld was insufficient to reliably use the wire loops on the test rig.

Instead of using electroplated diamond wire, loops of stranded wire coated with diamonds were acquired from Insoll Tools Technology Co., Ltd. The attachment process of the diamonds to the wire loops is undisclosed, but it is presumed that the wires are coated with solder and pressed into loose diamonds while the solder solidifies. This results in high grain density and bare-laying grains, as seen in Fig. 5.3.

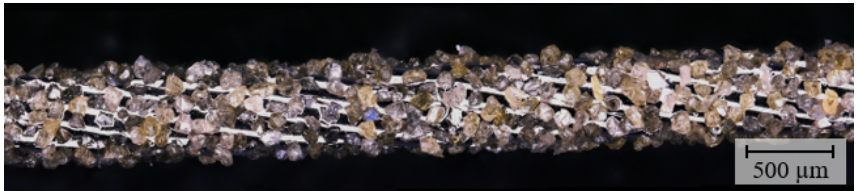


Figure 5.3: Stranded diamond wire, core diameter $d_w = 450 \mu\text{m}$, grain size $d_g \approx 50 \pm 20 \mu\text{m}$ (not specified), grain density $\rho_g = 100\%$.

The wires were ordered in loops of length $L_w = 1950 \text{ mm}$. At the time

the wires used in this study were ordered, the grain size could only be specified as "normal" or "small", while the average grain diameter for the specification "normal" is estimated as $d_g \approx 50 \pm 20 \mu\text{m}$. Grain densities were specified to $\rho_g = 100\%$, $\rho_g = 60\%$ and $\rho_g = 50\%$. The grain density is however not constant over the wire length. There are sometimes sections with higher and lower density. Furthermore all wires show slight kinks with fewer grains.

5.4 Model for the Description of the Wire Bow

In this section, the analytic wire bow model is derived and discussed. The model describes the fully developed wire bow in steady state.

5.4.1 General Process Kinematics

Fig. 5.4 shows the wire bow schematically, with two guide rolls on the left and right, an ingot indicated in grey centrically between the guide rolls and a wire forming a bow. The ingot is being pushed upwards into the wire, which travels left-to-right.

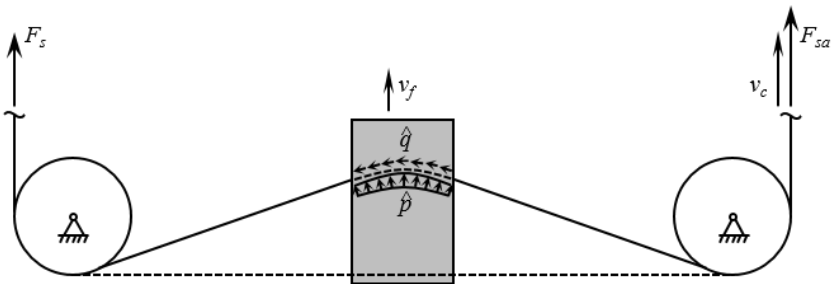


Figure 5.4: Schematic of the conditions at steady-state with cutting speed v_c , feed rate v_f , wire tension on the workpiece entry side F_s and exit side F_{sa} , as well as the distributed normal force \hat{p} and cutting force \hat{q} acting on the wire in the ingot.

In the beginning of the process, the feed rate v_f is higher than the material removal rate r_r , which leads to the development of a wire bow. As the bow increases, the tension in the wire acts as a feed force F_f , distributed onto the workpiece as a vertical line load \hat{p} , which indents the grains on the wire deeper into the workpiece. Due to the lateral movement of the wire with cutting speed v_c , a cutting force F_c acts on the wire as the grains are sliding on and indenting into the material. The cutting force is distributed along the wire as an axial line load \hat{q} , leading to an asymmetry in the wire tension. The wire tension on the workpiece entrance side F_s is therefore smaller than on the workpiece exit side F_{sa} . Once the material removal rate equals the feed rate, the process reaches steady-state. In steady state, the wire bow is developed as schematically indicated in Fig. 5.4.

5.4.2 Wire Deflection Model

The wire deflection model has to consider all geometrical process parameters as indicated in Fig. 5.5.

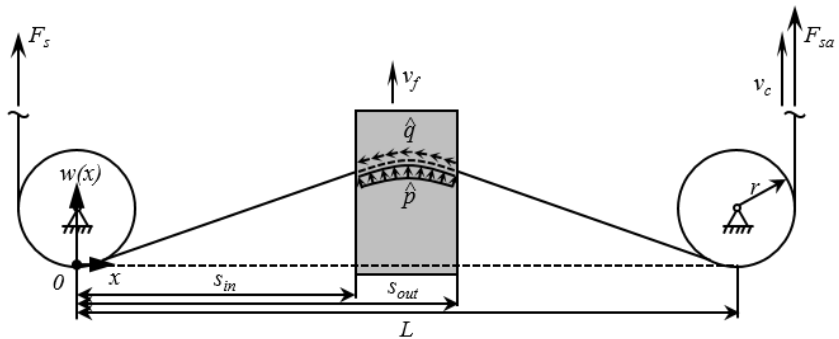


Figure 5.5: Geometric dimensions of the diamond wire sawing process with coordinate origin at the bottom of the left guide roll: vertical distance between the pulleys L , vertical distance from the guide roll centre to the beginning of the workpiece s_{in} and its end s_{out} , and guide roll radius r .

Two guide rolls of radius r are positioned at a horizontal distance L .

The coordinate origin lays vertically below the bearing point of the left guide roll on the radius of the pulley. The wire enters the ingot at position $x = s_{in}$ and exits at $x = s_{out}$, defining the width of the ingot $l = s_{out} - s_{in}$. The vertical deflection of the wire at position x equals $w(x)$. The derivatives of w , w' and w'' indicate the slope of the wire and its curvature, respectively. The wire is characterised by its core diameter d_w and its material's Young's modulus E .

Derivation of a Differential Equation Describing the Displacement of the Wire under Acting Forces

The shape of the deflected wire inside and outside the workpiece can be derived analytically based on geometry (distance between the guide rolls, diameter of the rolls, width and position of the workpiece), properties of the wire (diameter and Young's modulus) and the acting forces (wire tension, feed and cutting force). Such a model has been presented by LIEDKE AND KUNA [109] for the LAS process. The kinematic of the DWS process is similar to that of the LAS process, with major differences only in the acting forces. The following model is based upon LIEDKE AND KUNA's work.

The model is derived upon the observation of forces and moments on an infinitesimal element of the wire as shown in Fig. 5.6.

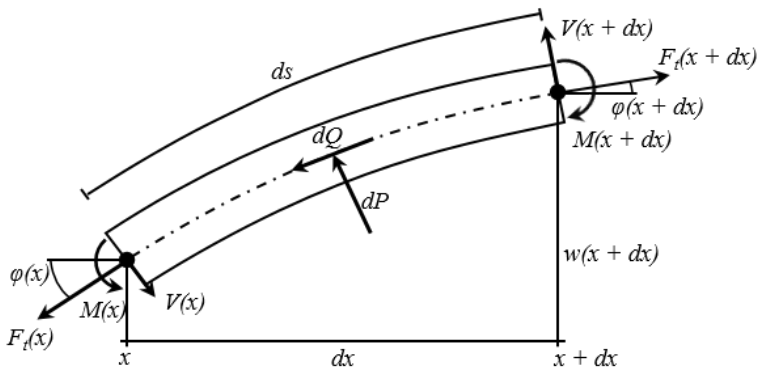


Figure 5.6: Forces and moments acting on an infinitesimal wire segment.

The tangential force F_t stems from wire tension, the line loads \hat{q} and \hat{p} are reduced to single forces acting on the centre of the wire segment, indicated as $dQ = \hat{q}(x)ds$ and $dP = \hat{p}(x)ds$ respectively. Bending moments M and shear forces V are considered due to the stiffness of the wire. The local deflection angle φ indicates the slope at the segment ends. Centrifugal forces due to the movement of the wire along a curve, as well as a force resulting from the weight of the wire are insignificant in relation with acting process forces and are neglected.

The following simplifications are made prior to the development of the equilibria of forces and moments. Firstly, ds can be approximated by linearising $w(x + dx)$ with a first-order Taylor expansion as

$$\begin{aligned}
 ds &\approx \sqrt{dx^2 + (w(x + dx) - w(x))^2} \\
 &\approx \sqrt{dx^2 + (w(x) + \frac{\partial w(x)}{\partial x} dx - w(x))^2} \\
 &= \sqrt{dx^2 + w'(x)^2 dx^2} \\
 &= \sqrt{1 + w'(x)^2} dx
 \end{aligned} \tag{5.2}$$

Secondly, since the deflection of the wire is typically one order of magnitude smaller than the distance between the guide rolls, a small angle approximation is reasonable for φ . This leads to $\varphi(x) = \arctan(\partial w(x)/\partial x)$ and then $\varphi(x) \approx \partial w(x)/\partial x = w'(x)$, $\sin\varphi(x) \approx w'(x)$ and $\cos\varphi(x) \approx 1$. On basis of the same argumentation, terms including $w'(x)^2$ and shear force values that are diminished by a product of derivatives of the wire deflection are ignored. Shear force values are small due to the small diameter of the wires and the resulting low stiffness. Lastly, higher-order terms $\mathcal{O}(dx^2)$ are neglected.

A differential equation for the wire deflection at horizontal distance x from entrance side of the workpiece is then derived from the equilibrium of forces and moments:

$$\begin{aligned}
 \Sigma F_x \stackrel{\perp}{=} 0 &= -F_t(x) \cos \varphi(x) + V(x) \sin \varphi(x) - dQ \cos \varphi(x) - dP \sin \varphi(x) \\
 &\quad + F_t(x+dx) \cos \varphi(x+dx) - V(x+dx) \sin \varphi(x+dx) \\
 &\approx -F_t(x) \cos w'(x) + V(x) \sin w'(x) - dQ \cos w'(x) - dP \sin w'(x) \\
 &\quad + F_t(x+dx) \cos w'(x+dx) - V(x+dx) \sin w'(x+dx) \\
 &\approx -F_t(x) + V(x)w'(x) - dQ - dPw'(x) \\
 &\quad + F_t(x+dx) - V(x+dx)w'(x+dx), \tag{5.3}
 \end{aligned}$$

$$\begin{aligned}
 F_t(x+dx) &= F_t(x) + dQ + dPw'(x) - V(x)w'(x) + V(x+dx)w'(x+dx) \\
 &= F_t(x) + dQ + dPw'(x) + V(x)w'(x)w''(x)dx + V'(x)w'(x)^2dx \\
 &\quad + \mathcal{O}(dx^2), \tag{5.4}
 \end{aligned}$$

$$\begin{aligned}
 \Sigma F_y \stackrel{\perp}{=} 0 &= -F_t(x)w'(x) - V(x) + dP - dQw'(x) + F_t(x+dx)w'(x+dx) \\
 &\quad + V(x+dx) \\
 &\approx -F_t(x)w'(x) + dP - dQw'(x) + (F_t(x) + dQ + dPw'(x) \\
 &\quad + V(x)w'(x)w''(x)dx + V'(x)w'(x)^2dx)(w'(x) + w''(x)dx) \\
 &\quad + V'(x)dx \\
 &= dP(1 + w'(x)^2) + F_t(x)w''(x)dx + V'(x)(1 + w'(x)^2)dx \\
 &\quad + V(x)w'(x)w''(x)dx + \mathcal{O}(dx^2) \\
 &= \hat{p}(x)\sqrt{(1 + w'(x)^2)^3}dx + F_t(x)w''(x)dx + V'(x)(1 + w'(x)^2)dx \\
 &\quad + V(x)w'(x)w''(x)dx + \mathcal{O}(dx^2) \\
 &\approx \hat{p}(x) + F_t(x)w''(x) + V'(x), \tag{5.5}
 \end{aligned}$$

$$\begin{aligned}
 \Sigma M_{x+dx} \stackrel{\perp}{=} 0 &= -M(x) + M(x+dx) - (1 + w'(x)^2)V(x)dx + \mathcal{O}(dx^2) \\
 &\approx M'(x) - V(x), \tag{5.6}
 \end{aligned}$$

$$\Rightarrow V'(x) = M''(x) \tag{5.7}$$

which finally yields

$$\hat{p}(x) + F_t(x)w''(x) + M''(x) = 0 \tag{5.8}$$

Modelling the wire as an Euler-Bernoulli beam with $M = -EIw''$ leads to

$$\hat{p}(x) + F_t(x)w''(x) - EIw''''(x) = 0 \tag{5.9}$$

For an analysis of the effect of bending stiffness, this differential equation can be changed to that of a limp rope by letting EI approach zero:

$$w''(x) = -\frac{\hat{p}(x)}{F_t(x)} \quad (5.10)$$

Definitions of Forces and Boundary Conditions

In order to solve equations (5.9) and (5.10), relevant forces and boundary conditions have to be defined.

In steady state, the wire is moving only in axial direction and the wire deflection $w(x, t)$ remains constant in time, $dw(x, t)/dt = 0$, and the removal rate r_r equals the feed rate v_f . Especially, v_f has to be constant over the ingot width. As the wire bow does not change, the forces acting upon the wire do not change either and \hat{p} does not depend on x . Consequently, $\hat{p}(x)$ is independent in space and time in the equilibrium state. It can therefore be concluded that a force F_n applied to the ingot will be distributed equally over the wire length that is in contact with the ingot. Furthermore, due to the small-angle-approximation, the length of the wire arc in contact with the ingot is approximately as long as the width of the ingot. No force other than the wire tension acts upon the wire outside of the ingot. $\hat{p}(x)$ can be stated as

$$\hat{p}(x) \approx \begin{cases} \frac{F_n}{s_{out} - s_{in}} & s_{in} \leq x \leq s_{out} \\ 0 & \text{else} \end{cases} \quad (5.11)$$

The axial tension force $F_t(x)$ acting on the wire is equal to the wire pretension F_s before the wire begins to cut the ingot. The axial line load $\hat{q}(x)$, stemming from the cutting force F_c , increases the tension along the length that is in contact with the ingot. After the wire left the ingot, the tension force is equal to F_{sa} . As already stated in [109, 179], $F_t(x)$ can

therefore be expressed as

$$\begin{aligned}
 F_t(x) &= F_s + \int_0^x \hat{q}(x) ds \\
 &\approx F_s + \int_0^x \hat{q}(x) \sqrt{1 + w'(x)^2} dx
 \end{aligned} \tag{5.12}$$

In LAS, the cutting force, resulting from the relative movement between wire and workpiece with velocity v_c under acting lapping pressure $p(x)$, is described by a Coulomb friction force $\mu p(x)$ and a viscous friction force $\eta v_c / s_p$ with coefficient of friction μ , slurry viscosity η and gap between wire and ingot s_p [109]. The reference area for the determination of the Coulomb friction force is the projected wire area $A_p = d_w dx$, for viscous friction it is the surface in contact $A_s = \frac{1}{2} \pi d_w dx$. The expression of the tangential force of the wire in contact is thus

$$\hat{q}(x) = \int_0^x \mu \hat{p}(x) d_w + \frac{\eta v_c}{s_p} \frac{1}{2} \pi d_w ds \tag{5.13}$$

Due to the continuous two-body contact in DWS and the absence of a slurry, viscous friction is negligible. A dependence of the cutting force from the cutting speed is therefore not obvious. Furthermore, observations from experiments with fixed abrasives showed, that μ is not a constant describing Coulomb friction but a coefficient $\hat{\mu} = \frac{F_n}{F_c}$ that seemingly depends on process parameters and wear. The force ratio was discussed on the basis of forces acting on single grains in 4.4.6. The cutting force is derived from the normal force by assuming constant proportionality with the constant $\hat{\mu}$, which was also suggested e.g. in [157].

$$\hat{q}(x) = \int_0^x \hat{\mu} \hat{p}(x) ds \tag{5.14}$$

$\hat{\mu}$ has to be determined for each stable process condition, verification experiments require the measurement of F_n and F_c . Combining equa-

tions (5.12) and (5.14) leads to the expression

$$F_t(x) \approx F_s + \int_0^x \hat{\mu} \hat{p}(x) dx \quad (5.15)$$

Initial conditions for the solution of the differential equations (5.9) and (5.10) are derived from the geometric constraints at the guide rolls as exemplarily shown for the left pulley in Fig. 5.7:

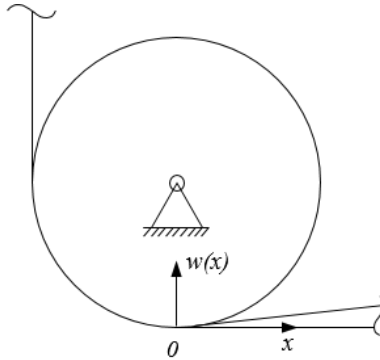


Figure 5.7: Wire deflection at the left guide roll.

At $x = 0$ the wire will be guided by the pulley roll and therefore the deflection as well as the slope have to be equal to zero. The same applies at the right pulley where $x = l$, so that the following boundary conditions have to be satisfied:

$$w(x = 0) = w'(x = 0) = w(x = l) = w'(x = l) = 0 \quad (5.16)$$

Furthermore, the deflection of the wire cannot be larger than the guide

roll:

$$\begin{aligned}
 w(0 \leq x \leq r) &\leq r - \sqrt{r^2 - x^2} \\
 w(l - r \leq x \leq l) &\leq r - \sqrt{r^2 - (x - l)^2}
 \end{aligned}
 \tag{5.17}$$

where r is the radius of the guide roll. In practice, r is not large and $w(x)$ only violates (5.17) for small bending stiffness when it approaches $x = 0$. The effect of (5.17) is negligible due to the small deflection of the wire bow compared to the pulley radius and the distance between the guide rolls and the ingot, as the following analysis shows.

The exact contact situation is evaluated with the assumption that stiffness is negligibly small and shown in Fig. 5.8.

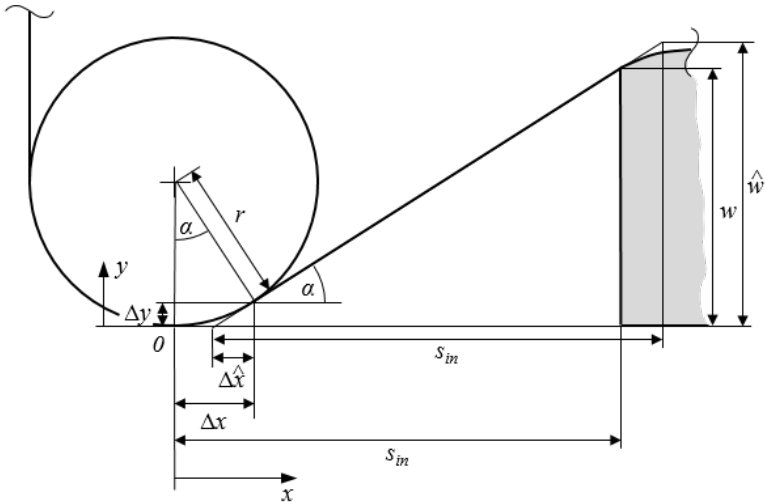


Figure 5.8: Exact contact conditions at the left pulley.

Displayed is the left guide roll with the wire leading into the workpiece. The coordinate origin is vertically below the centre of the pulley. The limp wire is guided by the pulley to the point shifted by Δx and Δy where the

wire loses contact with the pulley. The angle α rotating about the pulley bearing spans the arc from the coordinate origin to the point of loss of contact. α is also the measured "real" wire bow angle, as the wire touches the pulley tangentially due to its bending compliance. Δx is given as

$$\Delta x = r \sin \alpha \quad (5.18)$$

and Δy follows as

$$\Delta y = r - r \cos \alpha \quad (5.19)$$

The horizontal distance from the centre of the pulley to the workpiece is s_{in} , the wire deflection at the entry point is w . The radius of the pulley is r .

The vertical wire displacement is always determined from the coordinate origin. The shift Δy is not considered and the assumed contact point is closer to the origin than the actual one. The horizontal shift $\Delta \hat{x}$ back towards the origin is given by

$$\Delta \hat{x} = \frac{\Delta y}{\tan \alpha} \quad (5.20)$$

When using this contact point for calculating the wire deflection at the workpiece, a wrong deflection \hat{w} is determined:

$$\hat{w} = s_{in} \tan \alpha \quad (5.21)$$

The real deflection w can be found when reducing s_{in} by the distance of the virtual contact point to the origin $\Delta x - \Delta \hat{x}$. The real deflection is then given as

$$w = (s_{in} - (\Delta x - \Delta \hat{x})) \tan \alpha \quad (5.22)$$

The error ϵ can be calculated from the ratio of the virtual deflection with the real deflection $\frac{\hat{w}}{w}$. Substituting equations (5.18) to (5.22) yields

$$\epsilon = \frac{s_{in}}{s_{in} - \left(r \sin \alpha - \frac{r - r \cos \alpha}{\tan \alpha} \right)} - 1 \quad (5.23)$$

In the experiments presented in section 5.4.4, the largest observed wire bow angle was $\alpha = 3.6^\circ$, for a workpiece clamped at $s_{in} = 141$ mm. The radius of the pulley is $r = 48$ mm. For this configuration, the error amounts to $\epsilon = 1.5\%$. The real displacement is $w = 8.67$ mm instead of the measured one $\hat{w} = 8.8$ mm, which is acceptable. Wire stiffness reduces the error, larger pulleys or smaller distance from the pulley to the workpiece increase the error. Configurations with larger workpieces and therefore smaller distance between pulley and workpiece do not show larger errors. Obviously the error increases when larger wire bows are present.

For the rope-like model (5.10), analogous to [109], only the boundary conditions

$$w(x = 0) = w(x = l) = 0 \quad (5.24)$$

are applied. Applying this condition on $w'(x)$ makes the wire bow equation without bending stiffness unsolvable. As $\hat{p}(x)$ is equal to zero outside the ingot, $w'(x)$ has to be constant and non-zero if $\hat{p}(x)$ is non-zero in the ingot.

Numerical Solution to the Wire Bow Differential Equation

The solution to the differential equations for the wire considering bending stiffness (5.9) and the flexible rope neglecting stiffness (5.10), applying boundary conditions (5.16) and (5.24) respectively, is obtained numerically through an implementation in the numerical computing environment MATLAB. The MATLAB function *bvp4c* is used for solving boundary value problems for ordinary differential equations and can thus be used to solve the wire bow differential equations for $w(x)$.

5.4.3 Verification of the Wire Bow Differential Equation by FEM modelling

In the following, the solution of the wire bow differential equation is compared with the deflection derived from a finite element model implemented in ABAQUS. The wire is modelled as a static beam element as shown in Fig. 5.9

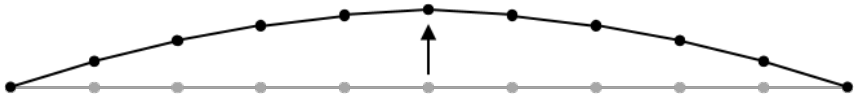


Figure 5.9: A simple representation of the wire as a chain of rigidly connected finite beam elements, not displaced in grey and displaced in black as indicated by the arrow on the top.

The grey beam shows the initial configuration, the black beam shows the displaced model with forces F_n and F_c applied. The beam is hinged at its ends, allowing free rotation while being constrained against translation. A beam in this configuration elongates with deflection. Axial stress increases with increasing displacement. In DWS, the wire is not elongated, as additional wire can be fed into the web. A more accurate representation of the problem is one, where the translation is unrestrained and that virtualises the additional wire fed into the wire arc, illustrated in Fig. 5.10.

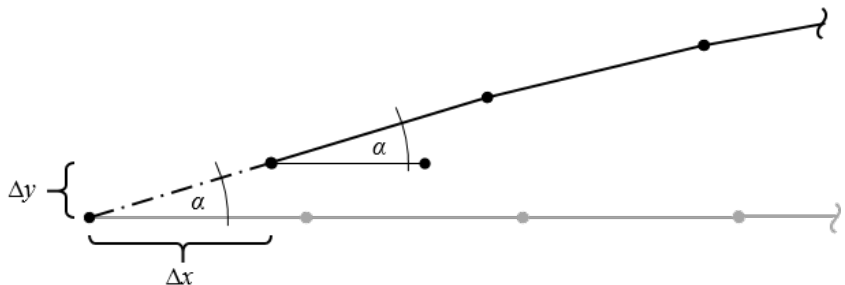


Figure 5.10: Approximation of the boundary condition at the left pulley.

The displayed boundary condition is neglecting bending stiffness and the guiding effect of the pulley surface. As the length of the beam does not change, the leftmost node has to move along the dash-dotted line. The displacement in y -direction is then

$$\Delta y = \Delta x \tan \alpha \quad (5.25)$$

where α is the bow angle in the first element or the rotation in the x - y -plane and Δx is the horizontal translation of the first node. The displacement in one degree of freedom dependant on a displacement in another degree of freedom is a non-linear constraint equation, that requires a multiple-point-constraint. A multiple-point-constraint can be implemented in ABAQUS with a user-subroutine, which is attached in the appendix B.

When the boundary condition is applied to the other end, there is no constraint to the displacement in x -direction. The system is statically indeterminate and would result in a rigid body motion. In the DWS process, the rigid body motion is restrained due to the force equilibrium with the wire tension. For this reason, the displacement in x -direction has to be restrained at the right pulley in the FEM implementation, leading to a less accurate representation of the process on the right side than on the left.

The beam model is implemented with 1000 round beam elements diameter $d_w = 100 \mu\text{m}$, Young's modulus $E = 210 \text{ GPa}$ and a total length of $L = 100 \text{ mm}$. The beam is subjected to a vertical load $F_n = 5 \text{ N}$ and horizontal load $F_c = 1.5 \text{ N}$ distributed onto the elements between $x = 40 - 60 \text{ mm}$ to simulate the contact with an ingot. Horizontal tension $F_s = 25 \text{ N}$ is applied to the leftmost node. The parametrisation is approximately that of a sawing process on an industrial diamond wire saw, except for higher normal and cutting forces. These are chosen higher to achieve larger displacement facilitating the comparison between the models.

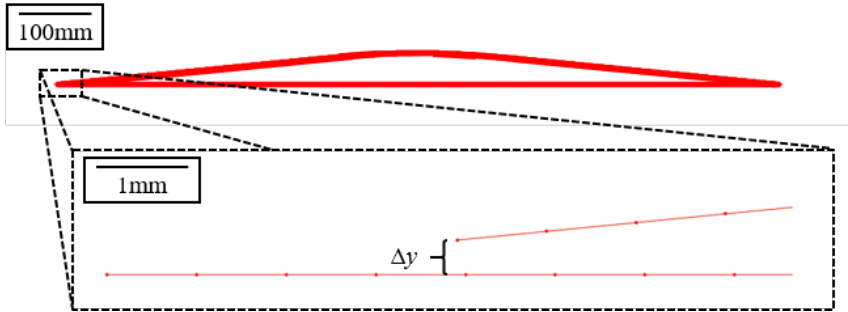


Figure 5.11: Evaluation of the boundary condition in the FEM model.

The resulting displacement is shown in Fig. 5.11. The displacement in y -direction is small. Therefore, it is reasonable to suppress the displacement in the vertical direction at the ends of the beam. This suppression condition is more stringent than the boundary condition that limits the deflection to the contact between the beam and the guide roll surface.

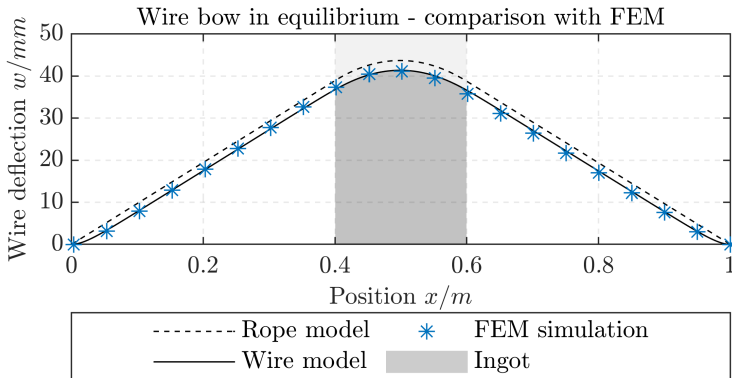


Figure 5.12: Comparison of the analytic model with the FEM model.

To account for bending stiffness, the rotation of the ends has to be constrained. In Fig. 5.12, the resulting model is compared to the analytic wire bow model with the same geometry, material parameters and forces applied. The displacements predicted by the two models agree well.

It can be concluded that the analytic model describes effects of bending stiffness accurately. The boundary conditions are more accurate in the analytic model, it is therefore considered more accurate than the FEM model.

5.4.4 Experimental Verification of the Wire Bow Model

The wire bow model predicts the wire deflection on the basis of acting forces F_f and F_c , the wire tension F_s , the geometry prescribed by the wire guide distance L , workpiece width l and position s_{in} and wire stiffness $f(d_w, E)$. Effects of wire parameters such as the grain size d_g and density ρ_g or the cutting speed v_c are not modelled directly.

Preliminary Assumptions

Several assumptions are necessary to evaluate the wire bow model with the test rig available:

1. The stiffness of the stranded wire is not known and not easily derived, because the properties of the wire (diameter of the individual strands, wrapping pitch, material) and of the coating (influence on stiffness, thickness and material) are unknown. For reasons of simplicity, it is therefore assumed that the bending stiffness is the same as that of a solid wire with the same diameter. This assumption is certainly wrong, it is known that the stiffness of stranded wire is lower than that of a solid strand. However, it is an assumption towards the worst case in which the stiffness becomes relevant and an estimation towards lower deflection, while the other extreme case, the limp rope, provides an estimation towards higher deflection. It is further assumed, that the Young's modulus is that of steel $E = 210$ GPa.
2. The wire bow is sufficiently symmetric and shallow that the force in horizontal direction F_x and vertical direction F_z acting on and measured below the workpiece represent the force exerted normally

F_n and tangentially F_t by the wire. These forces then equal the feed and cutting force F_f and F_c , respectively.

3. Equation 5.14 is valid: The force ratio $\hat{\mu}$ is the same for all grains in contact and the ratio of cutting force to normal force can be used to derive \hat{q} from \hat{p} .
4. Equation 5.30 is valid: The normal force is evenly distributed onto the wire through the grains, leading to the line load \hat{p} distributed with $n = 0$.
5. Measurement of the wire bow angles α_{in} and α_{out} allows for the calculation of wire deflection at the entry of the wire into the brick and its exit by application of equations

$$w(x = s_{in}) = s_{in} \tan \alpha_{in} \tag{5.26}$$

and

$$w(x = s_{out}) = (L - s_{out}) \tan \alpha_{out} \tag{5.27}$$

Experimental Plan and Procedure

The five parameters varied are feed force F_f , cutting speed v_c , brick width l , grain density ρ_g and wire tension F_s . Each factor is tested on three levels. As the grain density can not be chosen on three approximately equidistant levels, it is tested only on two levels. Three repetitions are necessary to spread the effect of process disturbances, most importantly that of wear. In order to keep the experimental effort on a reasonable level, a reduced experimental plan is chosen, as shown in Tab. 5.1.

Table 5.1: Experimental plan, - indicating the low factor level, 0 the medium and + the high level, respectively.

Exp.	1	2	3	4	5	6	7	8	9	10	11	12	13	14	15	16	17	18
F_f	-	-	-	+	-	+	+	+	0	-	+	0	0	0	0	0	0	0
v_c	-	-	+	-	+	-	+	+	0	0	0	-	+	0	0	0	0	0
l	-	+	-	-	+	+	-	+	0	0	0	0	0	-	+	0	0	0
ρ_g	+	+	+	+	+	+	+	+	-	-	-	-	-	-	-	+	+	+
F_s	+	+	+	+	+	+	+	+	+	+	+	+	+	+	+	-	0	+

This plan consists of a full factorial plan (experiments 1 to 8) for testing feed force F_f , cutting speed v_c and ingot width l at high grain density ρ_g at two levels with an additional centre point (experiment 18). The low grain density level is tested once at high and low level of each factor, while the other factors remain at the medium level, except for wire tension F_s which is always high (experiments 10 to 15), again with one centre point where all factors are at medium level (experiment 9). The factor wire tension F_s is kept at high level for all experiments. Two additional experiments (16 and 17) are conducted at low and medium wire tension level, with all other factors remaining at medium level. The order of the experiments and their repetitions is randomised.

The settings of the levels were determined in pre-trials, where the critical points were evaluated regarding stability of the feed control (reaching and maintaining a stable state before half the specimen is cut) and the maximum wire bow (aimed to be smaller than 10 mm). The settings chosen are summarised in Tab. 5.2.

Table 5.2: Settings of the levels for all tested factors.

Parameter	Unit	Levels		
		-	0	+
feed force F_f	N	1.5	2.25	3
cutting speed v_c	m/s	12	24	36
workpiece length l_i	mm	14	24	35
grain density ρ_g	%	50		100
wire tension F_s	N	20.35	25	30.25

Relevant parameters that are not manipulated are the distance between the pulleys $L = 307$ mm, wire diameter $d_w = 450$ μ m, assumed Young's modulus of the wire $E = 210$ GPa and height of the workpiece $h = 45$ mm.

The quantities feed, cutting and passive force F_f , F_c and F_p are measured throughout the experiment. The passive force is approximately zero and its measure only serves the purpose of evaluating the stability of the cut and detecting disturbances. Furthermore, the wire bow angle on the left

and right, α_{in} and α_{out} , respectively, is logged, along with the current feed rate v_f and cutting speed v_c .

Results: Verification of the Model

Fig. 5.13 shows the predictions of the model for all experiments. The presumed feed force F_f is the target force set in the experiments, the force ratio is $\hat{\mu} = 0.3$.

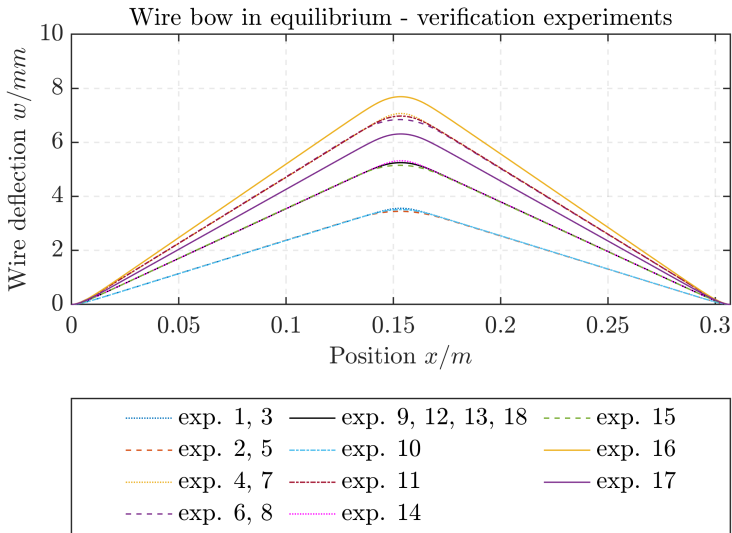


Figure 5.13: Predicted wire bow deflections of the experiments.

Several settings are equivalent as v_c and ρ_g do not influence the deflection in the model directly. It can also be seen, that settings that differ only in the level of the workpiece width show the same wire bow angles at the pulleys; dotted lines belong to narrow workpieces, dashed lines to medium workpieces and dash-dotted lines to wide workpieces. The solid lines show the experiments where the wire tension is varied. Five groups of settings can be made out in Fig. 5.13.

The experimental results and model predictions (based on measured forces F_f and F_c) are shown in Fig. 5.14 for the deflection at the workpiece

entrance side.

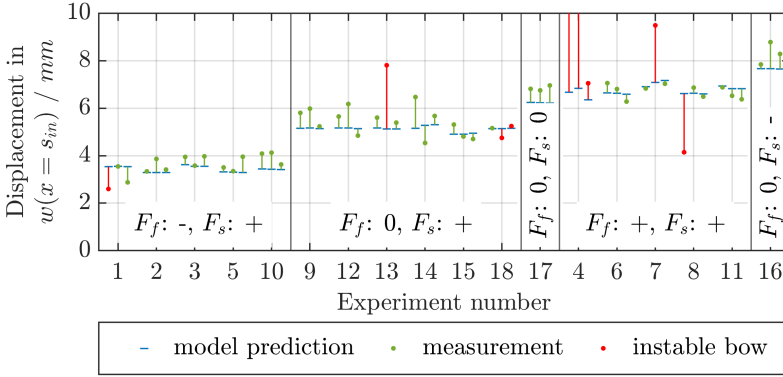


Figure 5.14: Predicted and measured wire bow deflections on the workpiece entrance side, grouped by feed force and wire tension level settings.

The first observation is that grouping the experiments by feed force F_f and wire tension F_s level settings is reasonable. Smaller feed force F_f and larger wire tension F_s lead to a smaller wire bow. Workpiece width l has a minor effect. As the workpieces are clamped centrally between the guide pulleys, the bow angle does not change with varying workpiece width l . Scatter of the measured forces between the repetitions of experiments is low. The change of the wire bow with variation of the cutting speed v_c or grain density ρ_g is negligibly small. A significant manifestation of changes in the cutting speed and grain density on the cutting force, the force ratio or the asymmetry of the bow is further not identified.

The wire bow model predicts the wire displacement at the edges of the workpiece accurately when it is evaluated with measured forces and compared against experimentally determined displacements. Fig. 5.15 shows measured displacements with modelled ones for the workpiece entrance (left) and exit side (right).

Experimental points where the process or the measurement of the wire bow was unstable are marked in red. This concerns a total of 12 out of 108 data points. Of all valid data points, only 6 show a difference of more than 1 mm between the measured and simulated displacement. The

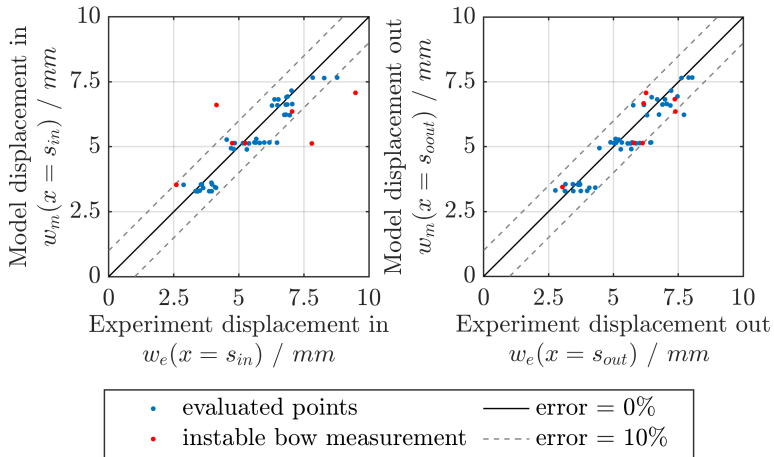


Figure 5.15: Measured and modelled displacements at the workpiece entrance (left) and exit side (right). The solid line signifies a perfect fit, the dashed lines a absolute error of ± 1 mm.

simulation tends to under-estimate the bow. The error scatters regularly over all experiments, no systematic errors are detected.

Discussion of the Signal Quality

Whenever the angle measurement signal is good, the model shows very good agreement with the experiments, as exemplified in Fig. 5.16.

The settings of experiment 4 (high feed force, low cutting speed, small workpiece) resulted in an unstable process that did not reach a steady state. Instead, both the controller-set feed rate and the measured feed force oscillated, and by the time the oscillation had decayed, the workpiece had already been cut. It was not possible to find suitable control parameters that could reach a steady state in a shorter time than the duration of the cut.

After conducting the experiments it was noticed that the cameras often did not return reasonable angle results. The right camera on the exit side

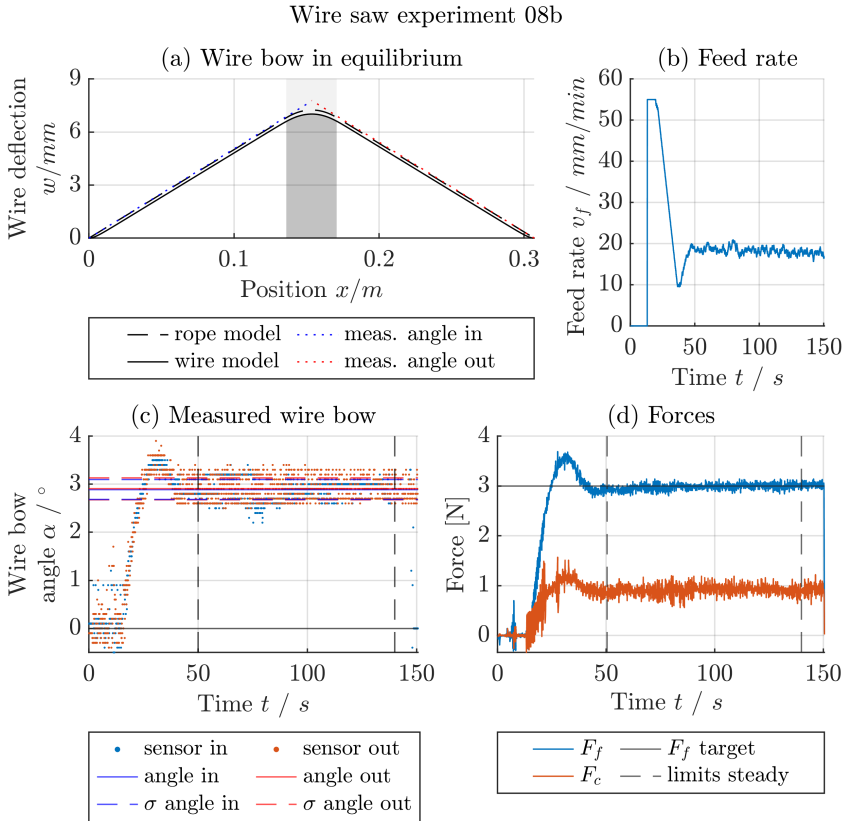


Figure 5.16: Example of the analysis of an experiment: (a) Wire bow model with projected measured angles, (b) prescribed feed rate during the experiment, (c) camera signal of the bow measurement, (d) force signal.

often returned an unchanging value for several seconds, the left camera often returned unreasonably large or negative values. An example is shown in Fig. 5.17.

A signal section where the bow measurement was deemed reasonable and in which the measured angle was averaged, was manually chosen as indicated by dashed lines in Fig. 5.17c. The presented signal is still considered

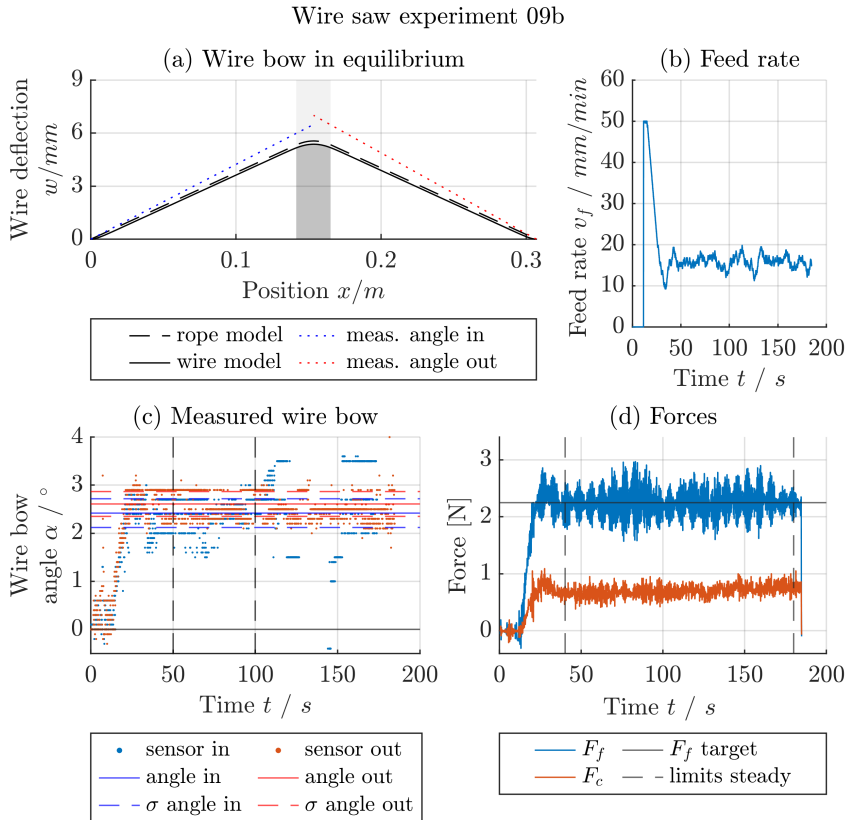


Figure 5.17: Example of the analysis of an experiment with poor wire bow measurement quality. The measured deflection is larger than the one modelled (a), the wire bow measurement scatters (c) and variation in the feed rate (b) and force signal (d) is large.

”stable”. If no reasonable section was identified, the bow measurement was labelled ”instable”.

In addition, the determination of the angle of the undeflected wire before the start of the spindle, sometimes resulted in an angle that did not accurately reflect the true angle of the undeflected moving wire. Consequently,

the zero level angle was manually averaged from a signal section where the spindle was being accelerated and the wire was not in contact with the workpiece. The mean standard deviation of the angle measurement on the in-side was $\sigma_{\alpha,\text{in}} = 1.42^\circ$, on the out-side $\sigma_{\alpha,\text{out}} = 0.24^\circ$.

Discussion of the Preliminary Assumptions

In the following, the validity of the assumptions stated in the beginning of this section is discussed.

Because of the inherent variability in the process, it is more appropriate to verify assumptions 1 (stiffness of the stranded wire) and 2 (symmetry of the bow) using the wire bow model within the constraints of the experimental framework, rather than relying on the experimental results. The wire bow model is evaluated with the parameters of the centre point experiment 9, which is equivalent to experiments 12, 13 and 18, and the overall largest observed force ratio $\hat{\mu} = 0.43$, representing the largest asymmetry.

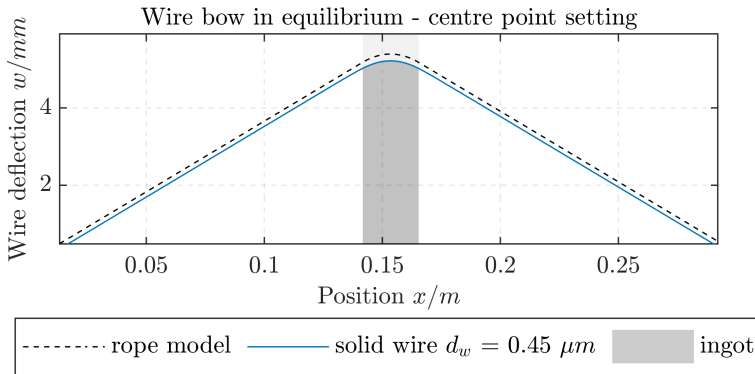


Figure 5.18: Effect of bending stiffness assumptions under the experimental framework conditions.

The model predicts a wire deflection of $w = 5.03$ mm on the brick entrance and exit side for the wire with bending stiffness and $w = 5.19$ mm without stiffness. The resulting difference is about 3% of the total deflection and with an absolute value of around $160 \mu\text{m}$ deemed negligible. The height difference of the deflection on wire entrance and exit side is $\Delta w < 10 \mu\text{m}$.

The asymmetry is therefore negligible. Assumptions 1 and 2 with regards to symmetry are therefore justified.

Assumption 2 (the bow being shallow enough for F_f to represent F_n) and assumption 3 (equal distribution of forces) can be tested by reducing the distributed load to a point load. In this extreme case, the load is carried by a single grain and the resulting forces can be measured vertically and horizontally using the sensor. Figure 5.19 shows the model with a load distributed over $l = 50 \mu\text{m}$, which is the width of a single grain, compared to the same load distributed evenly over the contact. The narrow width is necessary to avoid a singularity in the model.

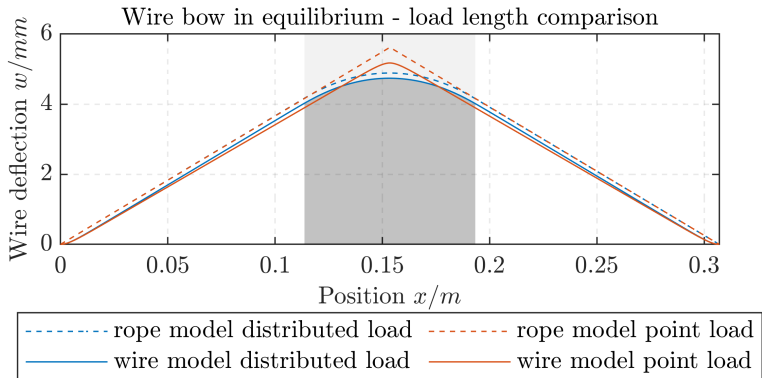


Figure 5.19: Wire bow with a point load in comparison with a distributed load.

The effect of the changing workpiece width is obvious and the effect of bending stiffness becomes dominant. Assuming a rope, the slope of the free wire does not change. In case of consideration of bending stiffness, curvature approaches zero with sufficiently large distance from the force application position. In the presented case, the angle of the free standing wires with bending stiffness differ until the wire reaches the pulley. The distance between the pulleys is not large enough, however when $L = 1 \text{ m}$, the effect of the load distribution diminishes at the workpiece edges, as seen in Fig. 5.20.

It may therefore be assumed, that F_f represents F_n sufficiently well and

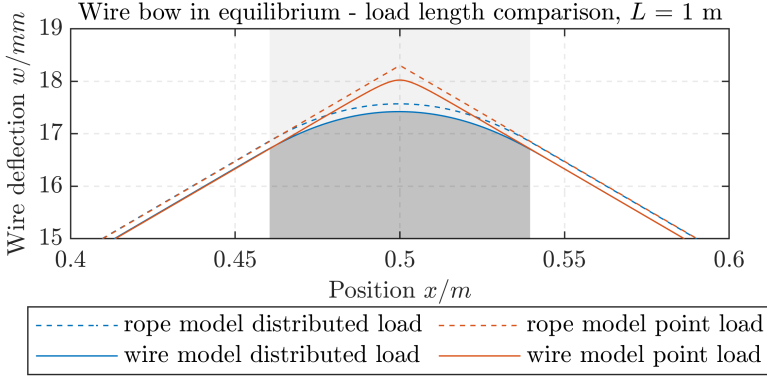


Figure 5.20: Wire bow with a point load, larger pulley distance and zoomed into the workpiece.

that F_f is equally distributed when the stable state is reached.

Assumption 4 ($\hat{\mu}$ is equal for all grains, \hat{q} derived from \hat{p}) cannot be tested with the given means and would require additional measurement of the wire tension force in the loaded side to check if $F_{sa} = F_s + F_c$ at all times.

Assumption 5 (calculation of $w(x = s_{in})$ from α_{in}) essentially combines the assumption that bending stiffness is negligible and that the guiding effect of the pulleys is negligible. The earlier assumption has been discussed and accepted with assumption 1. The error due to the guiding effect can be calculated by considering the exact contact conditions, which is shown in section 5.4.2, pp. 129. The error is at most 1.5% for the conditions tested in the experiments, amounting to an over-estimation of the wire displacement of no more than 130 μm .

In summary, the assumptions 1,2,3 and 5 are accepted and 4 cannot be tested. Since the experimental results agree well with the model, the model is considered to be verified.

5.4.5 Parameter Analysis of the Wire Bow in Equilibrium

In the following, the effect of varying process parameters on the wire bow will be graphically evaluated by solving the wire bow differential equation and plotting the resulting wire shape. The baseline condition is solved for the parameter set shown in Tab. 5.3. Derivations from these parameters are indicated in the respective figures.

Table 5.3: Baseline parameters for wire bow evaluation.

Parameter	Value
wire tension F_s	25 N
feed force F_f	5 N
force ratio $\hat{\mu}$	0.3
distance between pulleys L	1 m
ingot width l	200 mm
ingot position in s_{in}	0.4 m
wire diameter d_w	0.1 mm
Young's modulus wire E	210 GPa

Effect of Bending Stiffness

Firstly, the importance of wire stiffness is evaluated as it is typically neglected in other wire bow solutions. The wire diameter is changed to model the effect and shown in Fig. 5.21. A limp rope is also evaluated as it neglects bending stiffness.

The solution for a wire of diameter $d_w = 0.1$ mm covers the solution for the limp rope. The results show that wire stiffness can be neglected for typical wire diameters applied in diamond wire sawing of Si. The effect of stiffness becomes increasingly pronounced when the wire diameter exceeds $d_w = 1$ mm and leads to a shallower bow.

Furthermore, if non-constant distributions of \hat{p} are to be considered as

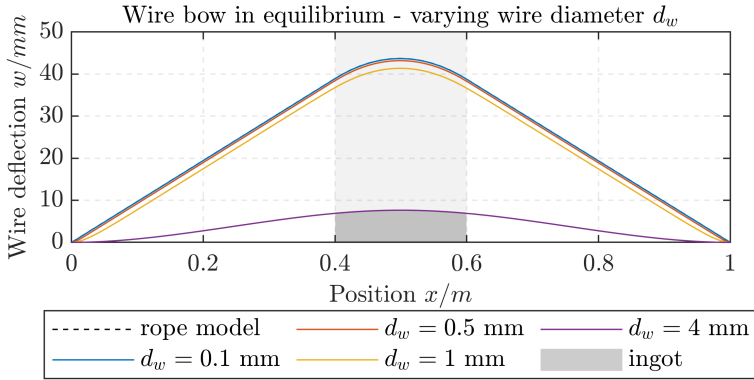


Figure 5.21: Effect of different wire diameters d_w on the wire bow, modelling different wire stiffness.

they may appear while the bow develops or changes (see section 5.4.6), sharper bending at the edges may occur. For this reason, bending stiffness is still taken into account in the further analysis.

Effects of Feed Force and Wire Tension

An increase of the feed force F_f increases the maximum wire deflection, as well as the deflection at entrance and exit of the ingot as seen in Fig. 5.22.

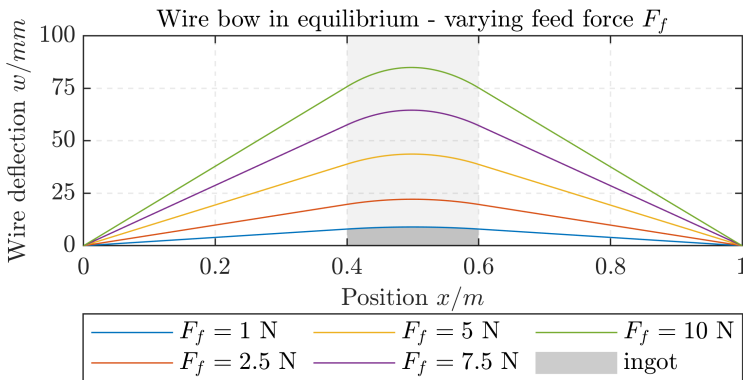


Figure 5.22: Effect of different force forces F_f on the wire bow.

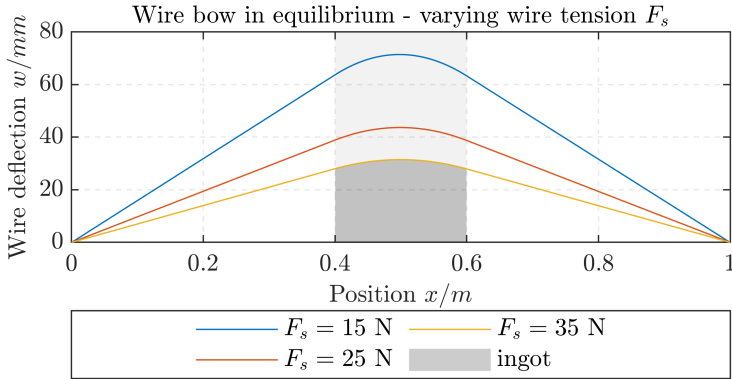


Figure 5.23: Effect of different wire tension F_s on the wire bow.

Decreasing the wire tension F_s has the same effect as increasing the feed force. Wire tension and feed force, as well as a part of the cutting force, have to cancel each other out to satisfy the equilibrium. Decreasing F_s leads to a larger wire bow as shown in Fig. 5.23.

Effect of Cutting Force

Increasing the cutting force F_c is modelled by increasing the force ratio $\hat{\mu}$. The effect is shown in Fig. 5.24.

The difference between wire tension on the wire entrance side $F_t(x = s_{in})$ and wire exit side $F_t(x = s_{out})$ increases. The bow becomes increasingly asymmetric and the position of maximum deflection shifts towards the wire entrance side, where the tension is lower. Furthermore, the overall deflection of the wire decreases as a consequence of the increasing wire tension. Increasing wire tension leads to an increasing vertical force component opposing the feed force. In order to satisfy the equilibrium condition of the steady state, the slope of the wire has to be smaller, resulting in a shallower bow.

A force ratio of $\hat{\mu} = 0$ results in no cutting force at all and a symmetric bow. The realistic case $\hat{\mu} = 0.3$ (refer to section 4.4.5) is barely distinguishable from the case with no cutting force, showing that the simplified

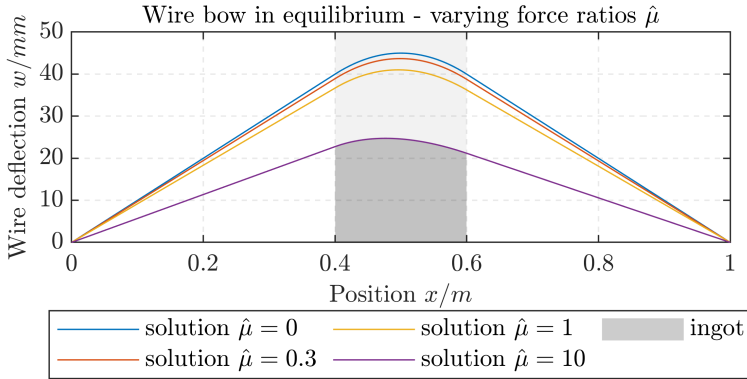


Figure 5.24: Effect of different force ratios $\hat{\mu}$ on the wire bow.

assumption of a symmetric wire bow as considered in e.g. [84, 102] leads to only small errors. As the force ratio reaches very large values, the above described effects become obvious: the maximum deflection decreases and shifts toward the wire entrance side. Based on the model it can be concluded, that an possible effect of wear on the force ratio has no significant effect on the wire bow.

Effects of Ingot Width and Positioning

A wider ingot, subjected to the same feed force, produces a smaller line load \hat{q} . The wire bow will therefore decrease as shown in Fig. 5.25. The deflection at the entrance $w(x = s_{in})$ and the exit of the ingot $w(x = s_{out})$ does not change significantly as long as bending stiffness is negligible.

Several effects can be observed when the ingot is displaced to the left or right, as shown in Fig. 5.26. Note that the wire travels left to right.

In Fig. 5.26, the ingot is displaced by an equal distance of 0.3 m to the left and right. It is obvious that the wire bow becomes asymmetric and the maximum displacement in the ingot is shifted towards the centre between the pulleys. Moreover, the maximum wire displacement decreases with the shift. Upon observing the detail in the to right of the image, it can moreover be noted that the maximum displacement with a shift of the

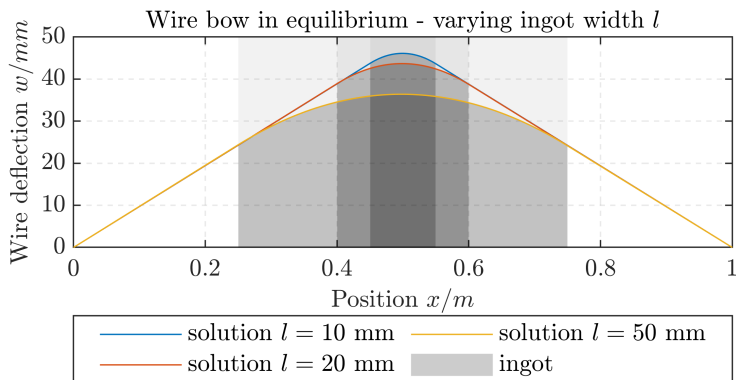


Figure 5.25: Effect of different ingot width l on the wire bow.

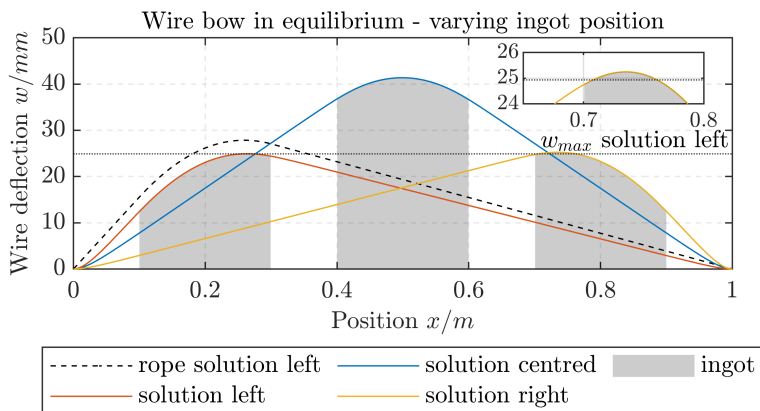


Figure 5.26: Effect of different ingot width positions on the wire bow.

ingot to the left (indicated by the dotted line) is lower than that resulting from a shift to the right. The acting cutting force displaces the centre of the bow towards the left where the wire tension is lower. The effects of shifting the bow away from the centre of the ingot by displacing it combined with the asymmetry due to cutting force has an effect on the maximum displacement, albeit a negligibly small one.

Lastly, a curvature near the pulleys becomes visible, which means that if the ingot is too close to the pulleys, the effect of stiffness may become considerable. This conclusion can also be reached from the observation that the difference between the rope and the wire solutions for the shift to the left is considerable.

5.4.6 Dynamic Bow Creation

In the transient state, the removal rate does not equal the feed rate. Practically, scenarios in which the process state changes are for example run-in phase, wear, changing ingot cross-section, or change of the cutting direction.

Run-in Phase

In the beginning of the process the ingot is initially fed into the wire and the wire starts cutting. While the bow is not fully developed, the normal force is not large enough for the grains to sufficiently penetrate the material, the removal rate is consequently smaller than the feed rate and the wire bow grows. Since the shape of the kerf ground does not correspond to the shape the wire bow would assume in steady state, the pressure along the wire is not evenly distributed. It may be assumed, that the local pressure is proportional to the material surplus; in other words the larger the difference between $w(x, t = t_0)$ and $w(x, t = \infty)$, the higher the local pressure $\hat{p}(x, t = t_0)$. This assumption leads to high pressure on the workpiece edges and low pressure in the centre as shown in Figure 5.27.

Figure 5.27 shows a simplified approximation for the shape of the distribution of $\hat{p}(x)$. For a qualitative evaluation of the bow development, the pressure distribution can be described as a polynomial with even exponents and its axis of symmetry in the middle of the ingot.

$$\hat{p}(x) = c \left(x - \frac{s_{in} + s_{out}}{2} \right)^{2n} \quad \forall s_{in} \leq x \leq s_{out}, n \in \mathbb{N}_0 \quad (5.28)$$

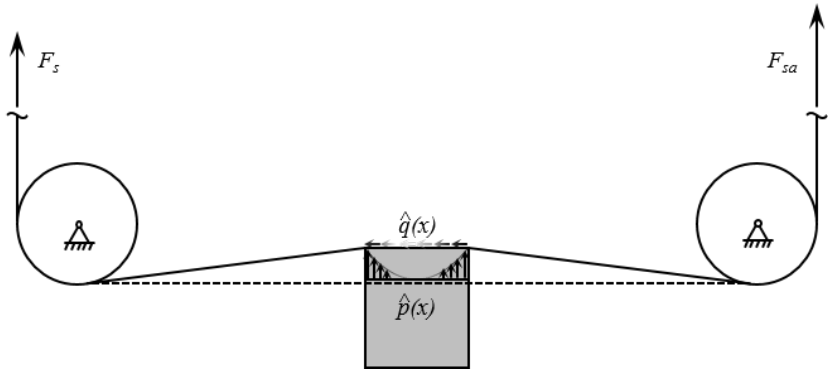


Figure 5.27: Wire deflection and force distribution in the transient state, shortly after the beginning of the cut.

The coefficient c takes into account the requirement that the applied feed force must equal the integral of $\hat{p}(x)$ over the wire bow length that is in contact with the ingot.

$$F_n = \int_{s_{in}}^{s_{out}} \hat{p}(x) ds = \int_{s_{in}}^{s_{out}} c \left(x - \frac{s_{in} + s_{out}}{2} \right)^{2n} ds \quad (5.29)$$

leading to the following equation for $\hat{p}(x)$:

$$\hat{p}(x) = \frac{2^{2n} F_n (2n + 1)}{(s_{out} - s_{in})^{2n+1}} \left(x - \frac{s_{in} + s_{out}}{2} \right)^{2n} \quad \forall s_{in} \leq x \leq s_{out} \quad (5.30)$$

For $n = 0$, the distribution is that of the steady state. For $n > 0$, the distribution of the line load is shifted increasingly towards the edges which is shown in 5.28. Fig. 5.29 shows the wire bow solution for different assumed distributions. The solutions are stacked for better visibility. Larger values for n lead to sharper bending around the workpiece edges.

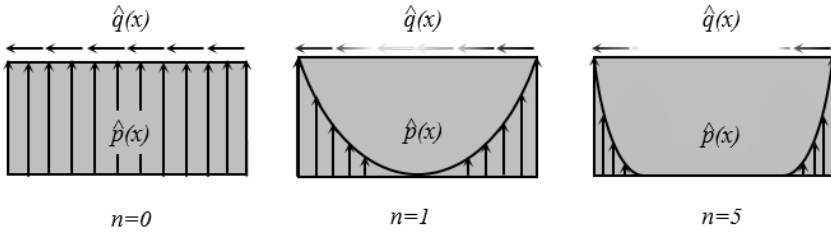


Figure 5.28: Distribution of normal force distribution $\hat{p}(x)$ and cutting force distribution $\hat{q}(x)$ in the ingot as a function of the distribution parameter n .

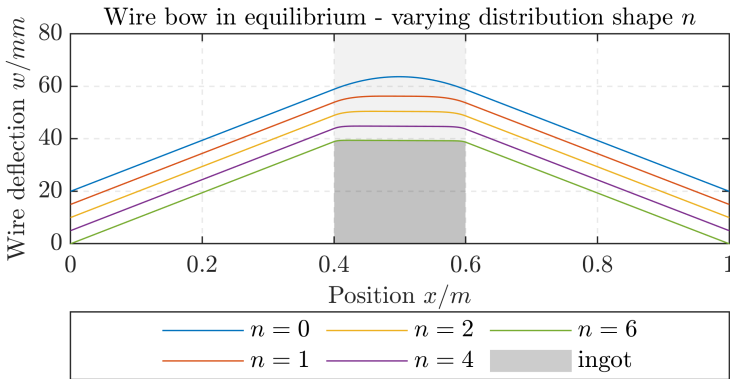


Figure 5.29: Effect of different force distributions n on the wire bow.

Wear

With increasing wear, the cutting ability of the wire decreases gradually. Several scenarios regarding the effect of the lowered cutting are conceivable and can be captured by the wire bow model.

One effect of wear is that the cutting force resulting from a given normal force changes. The effect is shown in Fig. 5.24 and discussed above with the parameter analysis on p. 151.

Another effect of wear is the change of the amount of active grains. If the amount of active grains increases as more protruding grains are worn off

and less protruding grains are activated, the normal load is distributed onto a larger area. On the other hand, if the amount of active grains decreases due to pull-outs of grains, the normal load is distributed onto fewer grains and a smaller area. However, the load applied per unit wire length remains the same: The effect cannot be represented in a model assuming a line load and requires the consideration of individual grains. As long as the load is evenly distributed along the wire, the bow does not change with a change in the amount of active grains.

Changing Ingot Cross-Section

When the ingot cross section changes, as is the case when cutting round ingots, the normal pressure $\hat{p}(x)$ decreases with increasing cutting length and increases with decreasing cutting length, if the feed force remains constant. This leads to a decreasing removal rate for increasing cross sections and vice versa. A smaller pressure leads to a smaller wire bow, as shown in Fig. 5.25 and discussed on p. 152.

5.4.7 Conclusion: Wire Bow Model

The wire bow model has been verified and is able to represent the deflection of the wire. Experiments testing the factors feed force, wire tension, cutting speed, grain density and workpiece length have been conducted, testing all factors on three levels except for the grain density, which was tested on two levels. All experimental settings except for one lead to stable processes with constant wire bow and feed rate. The deflection changes as expected, deviations between the modelled and observed wire deflection are attributed to measurement errors of the wire bow angle.

The wire bow model can be employed to provide an input for the cutting path in kinematic models. It can also be used to derive the currently acting cutting force distributions when the wire bow can be measured accurately. This is of advantage on industrial machines, where the cutting conditions in the wire web change from the wire-supply side to the wire-take-up side: While it is not possible to measure the acting forces in the front and back of the ingot individually, it is generally possible to measure the bow at

different positions of the web.

The parameter study evaluates the impact of varying process parameters on the wire bow, such as wire stiffness, feed force, wire tension, cutting force, ingot width, and ingot positioning. The results show that wire stiffness can be neglected for typical wire diameters used in diamond wire sawing of silicon. Increasing the feed force and decreasing wire tension increase the maximum wire deflection, while an increase in cutting force results in an asymmetric bow with a shift towards the wire entrance side. The results show that a wider ingot, subjected to the same feed force, produces a smaller line load, and thus, the wire bow decreases. The deflection at the entrance and exit of the ingot, however, does not change significantly as long as flexural rigidity is negligible. When the ingot is displaced to the left or right, the wire bow becomes asymmetric, the maximum displacement in the ingot is shifted from the centre of the ingot towards the centre between the pulleys, and the maximum wire displacement decreases. Additionally, the acting cutting force displaces the centre of the bow towards the side where the wire tension is lower, and a curvature near the pulleys becomes visible, which could lead to considerable stiffness effects if the ingot is too close to the guide rolls.

The findings provide insights into the factors that affect wire bow in diamond wire sawing and how they can be controlled. This knowledge can be used to optimise the process parameters for cutting different materials and improve the accuracy of cutting paths. Additionally it shows, that the ability to measure the wire bow accurately can help to understand the cutting forces acting on the wire, which is important for improving the efficiency and quality of the cutting process.

5.5 Discussion of the Force Ratio

The cutting-to-feed-force ratio $\hat{\mu} = \frac{F_c}{F_f}$ has been observed to vary significantly throughout all experiments conducted. In the following section, the experiments conducted for the verification of the wire bow model are analysed with the goal to determine a relationship between process para-

meters and the force ratio.

5.5.1 Effects of Process Parameters

It was initially believed that cutting speed might influence the force ratio, due to an observed increase of the amorphisation rate associated with ductile cutting upon increasing cutting speed [164]. Furthermore, the grain density may have an effect as the force is distributed onto more grains at higher density and therefore decreases the depth of cut per grain, leading to higher ploughing hardness. The assumptions are tested by observing the averaged effect of changes in cutting speed and grain density on the force ratio as shown in Fig. 5.30.

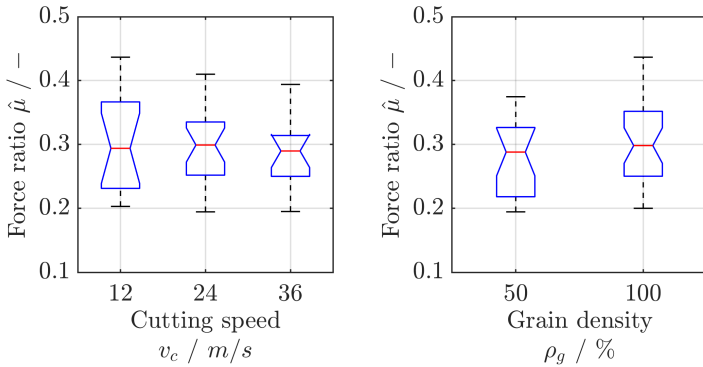


Figure 5.30: Dependence of the force ratio $\hat{\mu}$ on cutting speed v_c and grain density ρ_g .

Fig. 5.30 shows box plots of the experimentally determined force ratios in dependence on the cutting speed and the grain density. The red lines indicate the medians, the blue boxes the 25th-to-75th percentile of the data and the black whiskers correspond to 2.7σ of the data, assuming normal distribution [116]. The first observation is, that all observed force ratios fall in the range $0.2 \leq \hat{\mu} \leq 0.44$, and the median always lays very close to $\hat{\mu} = 0.3$ as predicted on the basis of the scratch tests in chapter 4.

Further, increasing cutting speed tends to decrease the force ratio, which does not agree with the assumption that higher ductility of the cut may be a dominant underlying mechanism. On the other hand, the slight increase of the force ratio with higher grain density is reasonable, as the lower depth of cut per grain leads to more ductile removal and therefore higher cutting force. However, the trends are not statistically significant, as the analysis of the notches in Fig. 5.30 reveals. The notches indicate comparison intervals for the position of the median within the 25th and 75th percentile of the data set. They mark a 95% confidence interval for the median. If the intervals of two datasets do not overlap, the medians differ significantly at the 5% significance level [116]. Since all intervals overlap, the difference is not statistically significant.

Analysis of variance (ANOVA) further shows, that feed force, cutting speed and contact length as well as their interactions have no statistically significant influence on the force ratio, as summed up in Tab. 5.4.

Table 5.4: Results of the ANOVA to determine significant difference of the mean effects of the parameters feed force F_f , cutting speed v_c and contact length l on the force ratio $\hat{\mu}$.

Source	Sum of squares	DOF	Mean of squares	F	p-Value
F_f	0.00046	1	0.00046	0.1	0.7536
v_c	0.00144	1	0.00144	0.32	0.579
l	0.00564	1	0.00564	1.26	0.2782
$F_f \cdot v_c$	0.0046	1	0.0046	1.03	0.326
$F_f \cdot l$	0.00078	1	0.00078	0.17	0.6816
$v_c \cdot l$	0.02255	1	0.02255	5.04	0.0393
$F_f \cdot v_c \cdot l$	0.00043	1	0.00043	0.1	0.7601
Error	0.07162	16	0.00448		
Total	0.10751	23			

ANOVA tests the hypothesis that all means of the force ratio derived with groups of different factor settings are equal against the hypothesis that at least one group shows a different mean force ratio. The F-statistic in the second to last column of Tab. 5.4 shows the quotient of variation

between sample means and the variation between samples, or the mean squares of a source divided by the mean squares of the error. A large F-statistic signifies a large variation of sample means in comparison to the variation within samples. Therefore, a large F-statistic indicates a possible difference between the group means. The statistic significance is determined by the p-value, which gives the probability of obtaining an F-ratio greater than or equal the observed one, assuming that all force ratios derived from different factor settings are equal.

The table shows that only the two-level interaction between the factors v_c and l differs significantly at a 95% confidence level ($0.034 < 0.05$). Performing a second ANOVA with groups F_f and $v_c \cdot l$ only shows no statistically significant difference of the means. No parameter combination with significantly different mean force ratio can be identified as seen in Fig. 5.31.

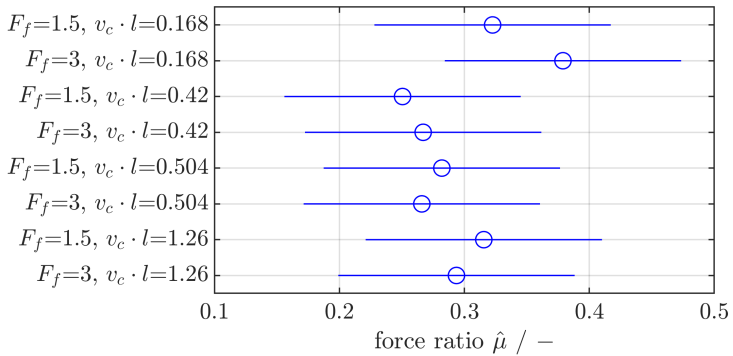


Figure 5.31: Mean force ratio $\hat{\mu}$ for parameter combination groups of feed force F_f and interaction between cutting speed v_c and contact length l .

Since all parameter combination groups overlap, they are not significantly different. It is therefore concluded, that the interaction of cutting speed and contact length is also not significantly influencing the force ratio.

5.5.2 Effects of Wear

As the deviation in the force ratio can not be explained with changes in any of the tested parameters, it is conceivable, that the wires wore during the experiments. Indeed, plotting the measured force ratio over the number of the experiments performed with that wire shows a clear trend of decreasing force ratio, see Fig. 5.32.

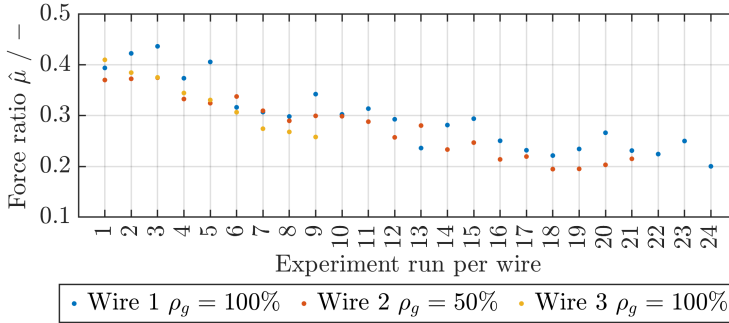


Figure 5.32: Dependence of the force ratio $\hat{\mu}$ on the number of experiments performed with each wire.

The effect of wear becomes obvious when observing the decrease of the force ratio $\hat{\mu}$ with increasing cutting distance as shown in Fig. 5.32. This observation serves as a starting point for further analysis. It is assumed, that the force ratio changes with the grain volume worn. A popular relation describing the wear volume dW in cutting processes was presented by USUI et al. [158]

$$\frac{dW}{\sigma_n dL} = C_1 \exp\left(\frac{C_2}{T}\right) \quad (5.31)$$

where C_1 and C_2 are constants, σ_n is the normal stress on the contact surface, dL is the sliding distance and T the temperature on the contact surface. A simplified relationship to describe the proportionality can be derived with parameters known from the experiments, when the contact length is derived from the cutting speed v_c and the contact time d_t

$dL = v_c dt$ and the contact stress is derived from the feed force F_f acting on the area of the wire in contact projected into a plane normal to the feed direction. In a first approximation, the normal contact area of the wire is given as

$$A_s = ld_w \rho_g \quad (5.32)$$

yielding the proportionality of

$$dW \propto \frac{F_f}{ld_w \rho_g} v_c dt \quad (5.33)$$

upon assuming the exponential term to be constant. More precisely, since F_f is not constant in time, dW is

$$dW \propto \int \frac{F_f(t)}{ld_w \rho_g} v_c dt \quad (5.34)$$

Another, simpler approach, is to assume that the worn volume is proportional to the work done by the cutting force;

$$dW \propto \int F_c(t) v_c dt \quad (5.35)$$

In order to discuss the force ratio with the wear state, the wear states at each experimental condition have to be evaluated, which is done by simply cumulating a wear proportionality coefficient after each experiment i . Two values are derived, W_u assuming a wear proportionality with an USUI-based factor and W_e for the proportionality with the cutting energy. Accordingly, W_u is defined as

$$W_u = \sum_{i=1}^N \int_0^{t_{cut,i}} \frac{F_f(t)}{l_i d_w \rho_g} v_{c,i} dt \quad (5.36)$$

and W_e

$$W_e = \sum_{i=1}^N \int_0^{t_{cut,i}} F_c(t) v_{c,i} dt \quad (5.37)$$

where the subscript i indicates the experimental conditions of experiment i , and $t_{cut,i}$ indicates the cutting duration of the experiment. The resulting relations are presented in Fig. 5.33.

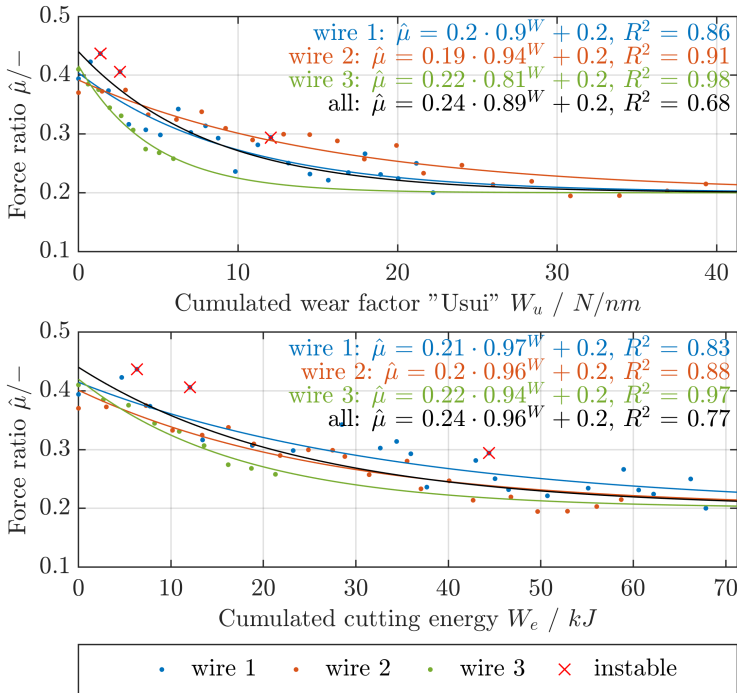


Figure 5.33: Relation between force ratio $\hat{\mu}$ and the introduced wear factors on the basis of USUI on the top and on the cutting energy in the bottom.

A difference between the individual wires is clearly visible. There is however no obvious pattern in the behaviour on the basis of the grain density, as wires 1 and 3 both show a grain density of 100% and wire 2 of 50%.

All wires approach a force ratio of $\hat{\mu} = 0.2$ towards the end of their service time. Especially wire 1 was changed after it showed macroscopic signs of wear in the shape of chipping of the coating layer and disintegration of the individual wire strains.

Due to the asymptotic behaviour, fitting of an exponential function of the form $y = a \cdot b^x + 0.2$ was chosen. The fit quality is generally good, but slightly better for the relation on the basis of USUI. By setting $a = 0.24$, an upper bound for the function at $x \in \mathbb{R}_{\geq 0}$ is prescribed and the range of the possible force ratios is limited to that predicted on the basis of the scratch tests presented in chapter 4. The function is fit to all data points and is plotted in black in Fig. 5.33 and also shows good agreement with the experimental data.

5.5.3 Conclusion: Force Ratio in DWS

The recorded force ratio could not be linked to process parameters, the range of observed force ratios does however agree with the force ratio observed in single grain cutting experiments. In single grain experiments, the force ratio depends on the geometry and orientation of the tool body. For this reason, it is assumed that the change of the microscopic wire topography due to wear is causal for changes of the force ratio.

Functions for the calculation of the force ratio on the basis of the analytic prediction of wear by USUI et al. and of the cutting energy are derived and discussed. While the actual wear is not calculated, cumulative quantities proportional to wear are introduced. Models on the basis of cutting energy have the advantage, that they can be applied to industrial machines easier, as the cutting energy is directly proportional to the spindle power.

The functions can probably be improved by the consideration of temperature. In case of the USUI-wear model, the dependence of wear on the temperature has been shown [158]. In case of the cutting energy function, it is relevant, what proportion of the cutting energy is used for material separation and what is dissipated in heat - and then whether the mechanical stress or the deteriorating effect of heat affects the wear of diamond more.

5.6 Model for the Derivation of the Material Removal Rate

The material removal rate ultimately depends on the interaction of individual grains with the workpiece. A single grain loaded with a normal load F_n indents into the softer workpiece surface. As indentation depth h increases, the additional load δF_n necessary to increase the indentation depth by δh is monotonously and over-proportionally increasing due to the increasing displaced volume and the elastic response of the material. This functional dependence has been analytically derived by SNEDDON [150] for axisymmetric punches of arbitrary profile and is regularly applied for the experimental determination of hardness following the theory coined by OLIVER AND PHARR [126, 127], as derived in the literature review and applied in the previous chapter. This theory, along with the findings of the previous chapter, is in the following applied to derive a model for the removal rate in the DWS process in dependence of process parameters.

5.6.1 Analytical Description of the Removal on Grain Level

In order to derive a relationship between the feed force F_f and the feed rate v_f , F_f is distributed on the individual grains active in the cutting process:

$$F_f = \sum_{i=1}^{\tilde{N}} F_{n,i} \quad (5.38)$$

where \tilde{N} is the number of active grains. The microscopic, grain-based process kinematics with forces $F_{n,i}$ and $F_{c,i}$ acting on grain i are shown in Fig. 5.34.

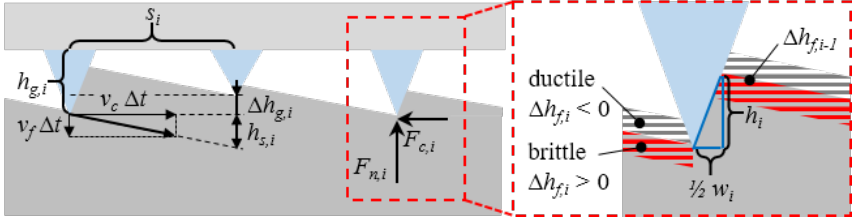


Figure 5.34: Kinematics on grain level.

The undeformed chip thickness of a grain is equal to its penetration h_i . As shown in the left part of Fig. 5.34, the vertical height of the undeformed chip depends on the distance between two active grains on the same path s and their height difference $\Delta h_{g,i}$. Furthermore, added to the kinematic proportion of the penetrated depth as shown in the right, is a removal-mode dependent residual height $\Delta h_{f,i-1}$ left by the previous grain: $\Delta h_{f,i} < 0$ for ductile removal due to elastic recovery and volume change from phase changed material and $\Delta h_{f,i} > 0$ if additional material is removed due to brittle fracture. The removal mode depends primarily on the penetrated depth and therefore $\Delta h_{f,i} = f(h_i)$.

Overall, the penetration depth of the active grain i is:

$$h_i = h_{s,i} + \Delta h_{g,i} + \Delta h_{f,i-1} \quad (5.39)$$

with

$$h_{s,i} = \frac{v_f}{v_c} s_i \quad (5.40)$$

and

$$\Delta h_{g,i} = h_{g,i} - h_{g,i-1} \quad (5.41)$$

The final height of material removed $h_{f,i}$ depends on the material removal

mechanism and equals

$$h_{f,i} = h_i + \Delta h_{f,i} \quad (5.42)$$

Substituting (5.39) to (5.41) into (5.42) gives

$$h_{f,i}(h_i) = \underbrace{\frac{v_f}{v_c} s_i(h_i) + (h_{g,i} - h_{g,i-1}) + \Delta h_{f,i-1}}_{\text{penetration depth } h_i} + \underbrace{\Delta h_{f,i}(h_i)}_{\text{removal mode}} \quad (5.43)$$

The removed material height of an individual grain therefore depends on the preceding active grain and kinematic process parameters. It is furthermore a function of the protrusion $h_{g,i}$. The removal rate r_r must equal the removed depth h_f of the active grains per pass. The duration of a pass Δt is the time one grain needs to pass the contact length l :

$$\Delta t = \frac{l}{v_c} \quad (5.44)$$

The removal rate of all grains \tilde{N} is then

$$r_r = \sum_{i=1}^{\tilde{N}} \frac{h_{f,i}}{\Delta t} \quad (5.45)$$

The steady state in which the removal rate r_r equals the feed rate v_f is reached, when the material response equals the prescribed load. The hardness functions (2.11) and (2.12) introduced in the state of the art 2.2.1 and parametrised in section 4.4.3 describe the dependence of the contact pressure with the penetration depth:

$$\frac{F_{n,i}(h_i)}{A_{n,i}(h_i)} = k_n h_i^{m_n} \quad (5.46)$$

with constants $k_n = 13.22 \text{ mN}/\mu\text{m}^3$ and $m_n = -0.76$ for an average, pointy grain.

By solving (5.46) for $F_{n,i}$ and recursively analysing the contact of each grain, the total force per grain acting on the wire (5.38) can be determined for a given wire topography and and $\frac{v_f}{v_c}$ -ratio. This requires parametrisation of all grains and furthermore a parametrisation of (5.42), since $\Delta h_{f,i}$ is also a function of the penetrated depth. Such relations are available for brittle removal (see section 2.2, equation (2.13)) but are not yet derived for ductile removal with the necessary consideration of material recovery (see section 4.4.2). The approach based on individual grains is therefore not practical. Some approximations can be made for the whole of all grains in contact, that lead to a description of the removal rate on wire-topography level.

5.6.2 Description of the Removal on Topography Level

Generalisation for Average Active Grains

When assuming that only the currently largest grains are kinematically active and approximately of the same size, Δh_g can be set zero. If then the kinematically active grains are approximately equally spaced, s_i can be set \tilde{s} , \tilde{s} signifying a spacing parameter of currently active grains, that therefore remains a function of the mean penetration of active grains \tilde{h} . With similar penetration of all grains, the removal-mode-related terms with Δh_f are not dependent on individual grains and are summed up in $\Delta \tilde{h}_f$. In this case (5.43) is simplifies to

$$h_f = \frac{v_f}{v_c} \tilde{s}(\tilde{h}) + \Delta \tilde{h}_f(\tilde{h}) \quad (5.47)$$

where the first term is the penetrated depth of an average, kinematically active grain \tilde{h} :

$$\tilde{h} = \frac{v_f}{v_c} \tilde{s}(\tilde{h}) \quad (5.48)$$

With eqs. (5.45) to (5.47) follows a general relation for the removal rate

$$r_r = (\tilde{h} + \Delta\tilde{h}_f(\tilde{h})) \frac{v_c}{l} \quad (5.49)$$

where the removal rate depends on the penetration depth, the removal mode and the contact duration, determined by the contact distance and the cutting speed. The penetration of \tilde{N} active grains can be derived from (5.46):

$$\sum_{i=1}^{\tilde{N}} \frac{F_{n,i}(h_i)}{A_{n,i}(h_i)} = \tilde{N}k_n\tilde{h}^{m_n} \quad (5.50)$$

which, when solved for \tilde{h} gives

$$\tilde{h} = \left(\frac{1}{\tilde{N}k_n} \sum_{i=1}^{\tilde{N}} \frac{F_{n,i}(h_i)}{A_{n,i}(h_i)} \right)^{\frac{1}{m_n}} \quad (5.51)$$

The force on active grains $F_{n,i}(h_i)$ has to be the same for all active grains \tilde{N} in steady state and their sum has to equal the feed force F_f . $F_{n,i}(h_i)$ can therefore be replaced with

$$F_{n,i}(h_i) = \frac{F_f}{\tilde{N}} \quad (5.52)$$

Consideration of the Wire Topography-Dependent Load-Bearing Area

The load-bearing area in normal direction A_n can conveniently be derived from the bearing area fraction curve, or Abbott-Firestone curve [1]. This curve represents the material portion at height $z = h$ above the reference plane and is the cumulative probability density function of the profile height z . The reference plane is typically the mean of the profile. As such, assuming the height probability function $p(z)$ is normally distributed with

mean μ and standard deviation σ

$$p(z) = \frac{1}{\sigma\sqrt{2\pi}} e^{-\frac{(z-\mu)^2}{2\sigma^2}} \quad (5.53)$$

the cumulated probability that the local height of the profile is below the level at height h is given by

$$P(h) = \int_{-\infty}^h p(z) dz \quad (5.54)$$

The bearing ratio t_p at height h is the complement of the cumulative probability density function [155]:

$$\begin{aligned} t_p(h) &= \int_h^{\infty} p(z) dz \\ &= 1 - P(h) \end{aligned} \quad (5.55)$$

Multiplying with the reference area A_{ref} returns the load bearing area A_n :

$$A_n(h) = A_{ref} t_p(h) \quad (5.56)$$

Practically, the bearing ratio can be derived by integrating the profile of a surface [47]. Fig. 5.35 shows an example of a normally distributed random profile ($\mu = 0$ and $\sigma = 0.3$), the corresponding profile height distribution and the bearing ratio curve.

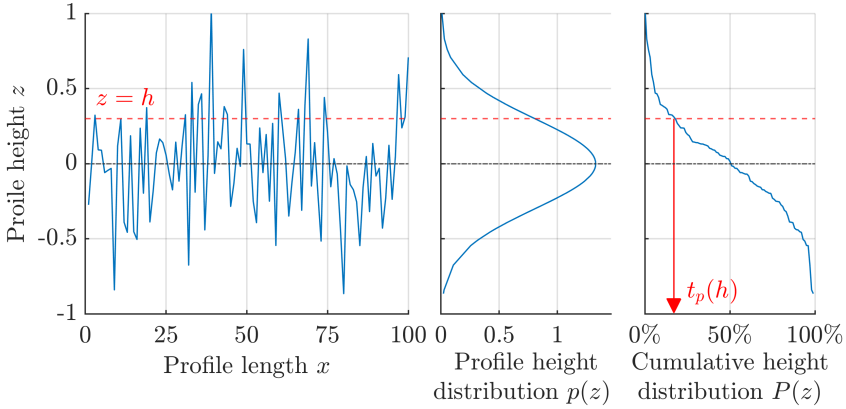


Figure 5.35: Random profile trace with normally distributed height as a model of the profile of a wire, with profile height distribution $p(z)$ and cumulative probability density function $P(z)$ (Abbott-Firestone curve). The red dashed line marks the given height h , the red arrow illustrates the graphical derivation of the bearing ratio $t_p(h)$ from the cumulative height distribution.

When the reference plane is chosen as the wire surface and the maximum protrusion is z_{max} , evaluating the bearing ratio curve at $t_p(z = z_{max} - h)$ returns the proportion of the area which is in contact with a surface that is penetrating by vertical distance h into the profile. The theoretical reference area is the total projected kerf surface $A_{n,k}$, since the grains protrude perpendicular to the wire surface. $A_{n,k}$ is equal to the width of the kerf, which is twice the kerf radius r_k , multiplied with the contact length l .

$$A_{n,k} = 2r_k l \quad (5.57)$$

Since the grains are moved across the surface, only approximately half the static area bears load and the reference area A_{ref} is chosen as

$$A_{ref} = r_k l \quad (5.58)$$

The load bearing area at penetration h is then

$$A_n(h) = r_k l [1 - P(z = z_{max} - h)] \quad (5.59)$$

The kerf front has a half-cylindrical shape, therefore the profile height of the contact line cannot be immediately derived but requires a transformation of the wire profile into the flat, shifted kerf front. The transformation corresponds neither to unrolling nor to projecting the profile. Instead all points across the wire diameter are shifted along wire feed direction by the distance of the idealised kerf front to the plane normal to the feed direction, in which the profile height distribution needs to be determined. The transformation is illustrated in Fig. 5.36.

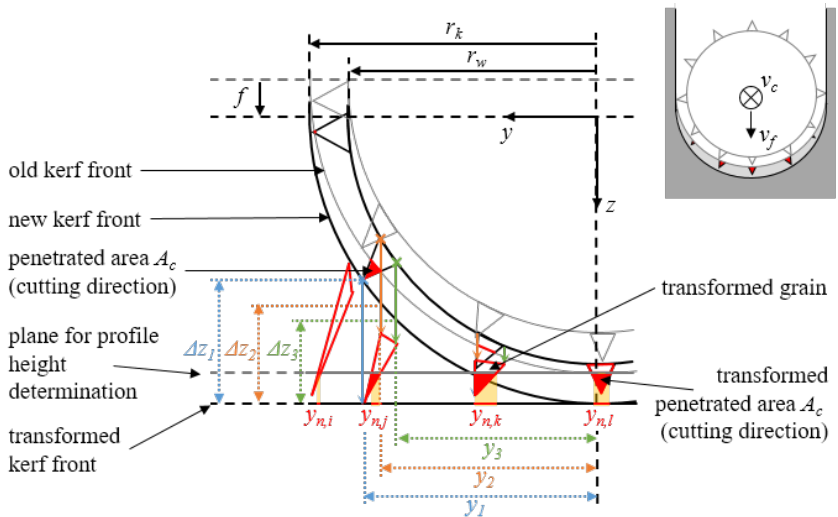


Figure 5.36: Schematic of the kerf transformation for the derivation of the profile height distribution. Shown is a quarter of a wire cross-section with grains in a plane normal to the cutting direction. Initial wire and kerf outline displayed in grey and final position after a vertical shift by f in black. Penetrated area and transformed grain shape are shown in red, y_n marks the load-bearing width of the grain.

The top right of Fig. 5.36 sketches a cross-section of the wire in the kerf. A vertical feed by f leads to penetration of grains on the wire surface into the idealised kerf front, as shown in red; "vertical" and "horizontal" refer to Fig. 5.36. The centre of Fig. 5.36 shows a quarter of the wire cross section. The kerf ground in the cross-section is assumed to be a half-circle with radius r_k , in which the wire with radius r_w lies concentrically; no grains protrude further than r_k . The initial configuration of the wire with grains and kerf front are outlined in grey, the final one in black is shifted downwards by f . A solid horizontal black line marks the final transformed kerf front, the horizontal grey line above marks the initial transformed kerf front. The grey line furthermore indicates the relevant height of the transformed profile, from which the load-bearing area has to be determined. The transformed grains i, j, k and l are shown in red, the transformation of the wire surface is not shown.

The transformation is exemplified on grain j: Three points highlighted in blue, orange and green mark the corner points determining the grain outline. The points are positioned at horizontal distances y_1 , y_2 and y_3 from the centre of the wire. The vertical distances Δz_1 , Δz_2 and Δz_3 indicate the span by which the points have to be shifted downwards in the transformation, marked by solid coloured arrows. The span is determined by the vertical distance from the kerf front to the transformed kerf front. The vertical transformation of the z -coordinate in dependence of its y -coordinate of any point P on the wire profile with wire centre-point M in the cross-section plane E that satisfies $\{P \in E \mid r_w \leq \overline{PM} \leq r_k\}$ is given by $f(y, z)$

$$f : z \longrightarrow z - r_k + \sqrt{r_k^2 - y^2} \quad (5.60)$$

The transformed grains become increasingly distorted the further they are away from the vertical axis. Grains near the vertical axis, such as grain l, are almost not affected by the transformation as they penetrate normally in feed direction. Grain i indicates the other extreme of a grain that is almost aligned with the horizontal axis and heavily distorted. This grain scratches the surface with a very low penetration depth and the area projected in normal direction is small. Due to the transformation,

the penetrated area and contact cross-section increase in the same way as when the grain ploughs into the initial kerf front. Its contribution to the load-bearing area is small as indicated.

To illustrate the effect of the transformation, an idealised wire with grains shaped like Berkovich indenters is exemplified in Fig. 5.37. The grains are placed at different distances from the vertical axis, expressed as the angular position of the grains φ . The distance from the vertical axis is $y = r_k \cos(\varphi)$. The distortion is clearly visible and the grains become increasingly narrow with growing position angle.

The bearing ratio $P(z = z_{max} - h)$ in (5.59) is determined from the accumulated cross sections of the wire in contact. The idealised kerf front from which the height h of the bearing ratio is determined, is always set by the grain with the highest protrusion z_{max} , which by definition is the difference of the radius of the kerf front r_k and the wire radius r_w :

$$z_{max} = r_k - r_w \quad (5.61)$$

As the penetrations h is gradually increased, the bearing ratio increases and more grains become active. h is however the penetration depth of the grain with the largest protrusion, less prominent grains indent less deeply. Fig. 5.36 shows a two-dimensional schematic, only the load-bearing width y_n is marked by a red solid line on the transformed kerf front. In order to derive the load-bearing area A_n , the three-dimensional surface has to be considered rather than the silhouette of a cross section. Due to the distortion, the load-bearing area decreases significantly and non-linearly with increasing angular position, as illustrated in Fig. 5.38. The contribution to the load-bearing area of grains placed at angles $\varphi > 60^\circ$ is negligible.

Count of Kinematically Active Grains

The count of the grains in contact \tilde{N} cannot be explicitly established by the analysis of the bearing-ratio curve. Due to the non-linear dependence of the scratch hardness from the penetrated depth, it makes a difference, whether one large grain is penetrated deeply or several smaller ones less deeply to achieve the force equilibrium and define A_n . The grains in

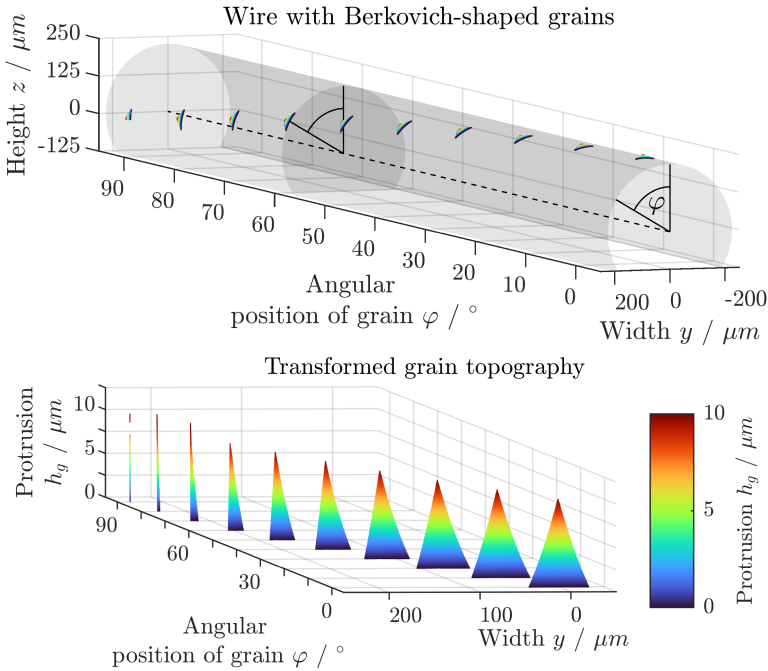


Figure 5.37: Schematics illustrating the transformation of wire topography with idealised grains with the shape of a Berkovich indenter: The top image shows a wire with grains placed around its circumference at different angles φ , φ increases along the wire axis and the cross-section at $\varphi = 60^\circ$ is highlighted. The bottom graphic shows the grain shapes after the deformation according to (5.60): The shape gets increasingly distorted with larger angular position.

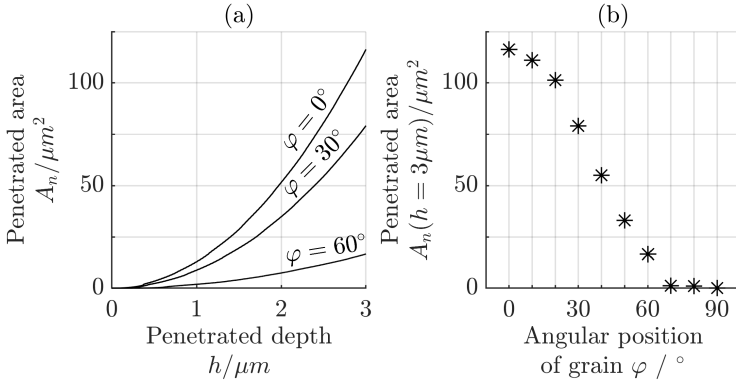


Figure 5.38: Plots highlighting the dependence of the penetrated, load-bearing area A_n of Berkovich-shaped grains at different angular positions φ . The left-hand plot (a) shows the relationship between the penetrated depth h and the penetrated area A_n for three grains placed at different angles φ . The right-hand plot (b) shows the non-linear decrease of the area penetrated at an indentation depth of $h = 3 \mu\text{m}$ with increasing angular position φ .

contact on one evaluated wire section can be combined into one large representative, active grain, even though they penetrate to different depth. Due to the introduced transformation, this representative grain is parametrised regarding its load-bearing characteristics in terms of its actual position on the wire circumference. Even though material is removed all over the kerf, the load-bearing area is transformed to the kerf centre and all transformed active grains may be assumed to be aligned one after the other along the cutting direction.

In order to reduce the dominating effect of individual very large grains and account for the contact of multiple grains, several wire sections of characteristic length, ideally with only one grain in contact in each section, are to be considered over the whole contact length l . This characteristic length can be interpreted as the average distance between two grains aligned one after the other on the wire surface along the cutting direction, the same as the spacing parameter \tilde{s} in (5.47). With this approximation the count

of active grains \tilde{N} is

$$\tilde{N} = \frac{l}{\tilde{s}} \quad (5.62)$$

The characteristic length has to be estimated. A lower bound for the amount of active grains and therefore sections of characteristic length is three, since the system *wire in three-dimensional kerf* must be statically determined. The definite limit for the characteristic length is the average grain protrusion, with the assumption that the expansion of the grains is the same in all spatial directions and all grains touch each other along the axial direction of the wire. A less conservative approximation is the assumption that one active grain supports the wire at least along the distance of the wire core diameter and up to that length where bending of the wire due to acting forces will occur.

Formulation of the Penetrated Depth

The average penetrated depth \tilde{h} , per (5.51), when substituting $F_{n,i}$ with (5.52) and $A_{n,i}$ with (5.59) for \tilde{N} individually evaluated contact sections of length $\frac{l}{\tilde{N}}$, yields

$$\begin{aligned} \tilde{h} &= \frac{1}{\tilde{N}} \sum_{i=1}^{\tilde{N}} h_i \\ &= \left(\frac{1}{\tilde{N}k_n} \sum_{i=1}^{\tilde{N}} \frac{F_{n,i}}{A_{n,i}} \right)^{\frac{1}{m_n}} \\ &= \left(\frac{1}{\tilde{N}k_n} \sum_{i=1}^{\tilde{N}} \frac{\frac{F_f}{\tilde{N}}}{r_k \frac{l}{\tilde{N}} [1 - P(z = z_{max} - h_i)]} \right)^{\frac{1}{m_n}} \\ &= \left(\frac{1}{\tilde{N}k_n} \frac{F_f}{r_k l} \sum_{i=1}^{\tilde{N}} [1 - P(r_k - r_w - h_i)]^{-1} \right)^{\frac{1}{m_n}} \end{aligned} \quad (5.63)$$

$P(z)$ has to be evaluated for \tilde{N} sections on the wire. $P(z)$ can either be evaluated with topographic data and an empiric distribution function or, when the current distribution parameters μ and σ are known, with a theoretical distribution and error function directly.

Consideration of the Removal Mode

To determine the removal rate with (5.49), $\Delta h_f(\tilde{h})$ has to be estimated. As mentioned above, $\Delta h_{f,d} < 0$ in case of ductile removal, where recovery reduces the removed depth, and $\Delta h_{f,b} > 0$ in case of brittle removal when additional material breaks away due to fracture.

Considering brittle removal, often the model of the lateral crack system proposed by MARSHALL et al. [113] is used to estimate the length and depth of lateral cracks growing to the surface and removing material (e.g.. [97, 169, 177]). As the lateral cracks propagate from the the edge of the plastic zone below the indenter (see Fig. 2.8, p. 28), the depth of the removed material is the vertical dimension of the plastic zone h_p . The depth is derived from (2.13) and yields

$$h_p = \sqrt[3]{\frac{Ac_l^2 F_n}{E h}} \quad (5.64)$$

with lateral crack length c_l according to (2.15). With (2.15), h_p becomes dependent on the half-included indenter angle φ .

The relations are derived upon the analysis of static indentation. When the indenter is displaced, the stress field generated in the elastic-plastic contact changes. The tangential force component has an important effect on the crack driving force [28]. Another prediction of the dimensions of the plastic zone when scratching across a surface has been introduced by AHN et al. [2], who assumed that the radius of the plastic zone is equal to the scratch half width. JING et al. [75] suggested that the plastic zone must be larger. They proposed an expanding cylindrical cavity modelling

approach to analytically derive the size of the plastic zone:

$$h_p = \frac{w}{2} \left[\frac{3(1-2\nu)}{5-4\nu} + \frac{2\sqrt{3}}{\pi(5-4\nu)} \frac{E}{\sigma_{yield}} \cot \varphi \right]^{\frac{1}{2}} \quad (5.65)$$

with the material yield strength σ_{yield} . The yield strength of Si is assumed to be the fracture strength σ_f due to its brittle properties [152]. JING et al. assumed that the scratch is as deep as it is wide. Their approach accounts for the generally accepted assumption that $h_p > w$, and since it has been derived on the presumption of contact conditions in scratching, it is used to estimate the removed depth in brittle removal.

w is not immediately accessible from the analysis above. It is assumed, that the average cross section of an active grain in contact is circular. The average half-width $\frac{\tilde{w}}{2}$ is then the radius of the cross section and derived as

$$\frac{\tilde{w}}{2} = \sqrt{\frac{1}{\pi} \frac{r_k l}{\tilde{N}} [1 - P(z = z_{max} - \tilde{h})]} \quad (5.66)$$

The half-included indenter angle φ is also unknown. It can either be derived from the aspect ratio of w with \tilde{h} assuming a cone-shaped or pyramidal grain

$$\varphi = \text{atan} \left(\frac{w}{2\tilde{h}} \right) \quad (5.67)$$

or, since the hardness functions are derived from Vickers indenters with φ_V and Berkovich indenters with φ_B , $\varphi_B \leq \varphi \leq \varphi_V$, e.g. $\varphi = 66^\circ$.

The additionally removed height due to brittle fracture is then

$$\Delta h_{f,b}(\tilde{h}) = h_p(\tilde{h}) - \tilde{h} \quad (5.68)$$

In the case of ductile removal, no analytical description of the material re-

covery is known. The relation would have to account for phase transition. The mechanism has not been understood sufficiently to account for e.g. effects of the strain rate, which have been observed in experiments [164]. The lack of an obvious dependence of the recovery on grain shape and penetration depth as demonstrated in sec. 4.4.2 indicate the complexity. It is therefore proposed to employ the experimentally derived formulation for the scratch hardness on the basis of the final depth to account for ductile removal:

$$H_s = \frac{F_n}{A_n} = k_{n,f} h_f^{m_{n,f}} \quad (5.69)$$

with $k_{n,f} = 9.62 \text{ kN}/\mu\text{m}^2$ and $m_{n,f} = -0.46$ per Tab. 4.2 on p. 90. With the constant scratch hardness H_s follows

$$k_n \tilde{h}^{m_n} = k_{n,f} h_f^{m_{n,f}} \quad (5.70)$$

and then

$$\begin{aligned} h_f &= \left(\frac{k_n}{k_{n,f}} \tilde{h}^{m_n} \right)^{\frac{1}{m_{n,f}}} \\ &= \left(\frac{13.22}{9.62} \tilde{h}^{-0.76} \right)^{-\frac{1}{0.46}} \\ &= 0.5 \tilde{h}^{1.65} \end{aligned} \quad (5.71)$$

Finally, a criterion for the ductile to brittle transition is required. The most popular criterion is (2.18) put forth by BIFANO et al. [10]. This expression does not account for the micro-geometry of the grain. Furthermore, in this context, it is more relevant which mode dominates the material removal in terms of removed material quantity than at what critical depth of cut cracks appear. It is therefore suggested, that a criterion based on contact stress that is sufficiently high to induce phase transition from Si-I to Si-II provides a more general indication of the dominating

removal mode. This approach is discussed in sec. 4.4.7. Using a conservative approximation, $h_{crit} = 0.95 \mu\text{m}$ is suggested. Obviously, the threshold can also be calculated from the contact of each single grain with $P_{crit} = \frac{F_n(h_i)}{A_n(h_i)} \geq 16 \text{ GPa}$.

Formulation of Material Removal Rate Model

The proposed model for the material removal rate in DWS is

$$r_r = h_f(\tilde{h}) \frac{v_c}{l} \quad (5.72)$$

with

$$h_f(\tilde{h}) = \begin{cases} 0.5 \tilde{h}^{1.65} & \tilde{h} < 0.95 \mu\text{m} \\ \sqrt{\frac{r_k l}{\pi N} [1 - P(r_k - r_w - \tilde{h})]} & \tilde{h} \geq 0.95 \mu\text{m} \\ \left[\frac{3(1-2\nu)}{5-4\nu} + \frac{2\sqrt{3}}{\pi(5-4\nu)} \frac{E}{\sigma_{yield}} \cot \varphi \right] & \end{cases} \quad (5.73)$$

5.6.3 Experimental Verification of the Material Removal Rate Model

Verification of the material removal rate model requires the measurement and processing of the wire topography. An experimental plan, where the effect of wear is used to generate different topographies, is proposed. The material removal model is implemented in Matlab and the results are discussed.

Experimental Plan and Procedure

Analysis of the removal rate observed during the experiments for the verification of the wire bow model show, that the wear state of the wire affects the removal rate. Later repetitions of experiments with the same parameter sets show a lower material removal rate than earlier ones. It is

assumed that the change of the wire topography due to wear is reflected in the bearing ratio of the three-dimensional wire profile.

Preliminary experiments show, that the service life of the wires depends not on the reduction of grain protrusion as on electroplated wires but on the integrity of the brazing layer and the cohesiveness between the individual wire strands. Fig. 5.39 shows the evolution of the wire topography in a microscopic false-colour image.

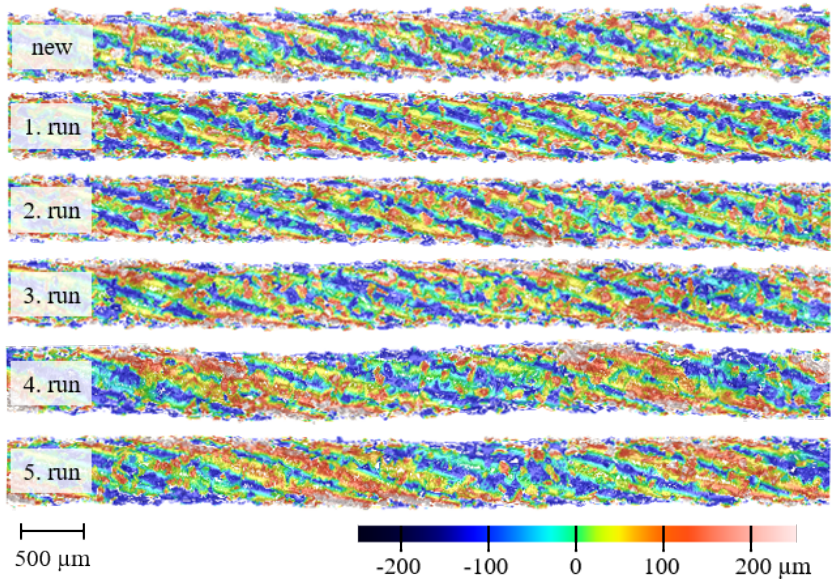


Figure 5.39: Deterioration of the wire integrity with increasing service life: new wire on the top and state after each consecutive experimental run. False-colour is indicating elevation.

Until after the second run, no obvious signs of deterioration of the wire integrity can be identified. Then, the wire starts to develop a waviness with a wavelength of approximately 3 mm. Especially the image of the wire after the fourth run shows, that the shape deviation is three-dimensional. The wire is clearly not straight any more, owing to the loss of cohesion between the individual wire stands. The structuring of the wire leads to

an increased removal rate at otherwise unchanging process parameters. This macroscopic change of the wire topography defines a limit for the experimental analysis of the dependence of the material removal rate on the microscopic wire topography.

Eqs. (5.72) and (5.73) summarise the quantities determining the removal rate: The material removal rate depends in the prescribed feed force F_f , amount of active grains \tilde{N} , the bearing characteristics of the wire expressed by the bearing ratio t_p , the area onto which the feed force is distributed determined generally by the workpiece width l and radius of the kerf r_k , and the cutting speed v_c . Furthermore the material removal mode affects the removal rate, primarily determined by the mechanical properties of the workpiece.

Different feed force and cutting speed can be prescribed with low effort. The contact area can only be influenced with the contact length since only wires with a core radius of $r_w \approx 225 \mu\text{m}$ are available. A large contact length is desirable to generate a large volume of material removed while not wearing the wire excessively in between time consuming wire topography measurements. A workpiece width of $l = 35 \text{ mm}$ is chosen for all experiments. Wires with a grain density of $\rho_g = 60 \%$ are used.

The experimental plan is:

- setting 1, experiments 1, 2, 3: wire 1, $F_f = 2.25 \text{ N}$, $v_c = 24 \text{ m/s}$
- setting 2, experiments 4, 5, 6: wire 2, $F_f = 1.5 \text{ N}$, $v_c = 24 \text{ m/s}$
- setting 3, experiments 7, 8, 9: wire 3, $F_f = 1.5 \text{ N}$, $v_c = 36 \text{ m/s}$

Each setting is tested in three consecutive runs. The wire topography is measured optically with the Sensofar Nexo S microscope using focus variation with a 20x magnification prior to each cut. Three sections of at least 6 mm length are captured. Illumination of the wire is crucial and a ring light is employed which provides diffuse light. The wire is continuously cleaned during the cut by exposing it to a sharp jet of pressurised air at the top right guide roll. The material removal rate is equal to the feed rate prescribed by the control at steady process state and logged along with process forces during the experiments.

Processing and Transformation of the Wire Topography

Implementation of the material removal model into a Matlab environment requires pre-processing of the captured point-clouds representing the wire. With the wire surface transformed as illustrated in Fig. 5.36, the bearing ratio of individual wire sections can be determined.

At maximum resolution, the Sensofar microscope provides a lateral resolution of $0.69\ \mu\text{m}$ with 20x magnification, resulting in several million data-points for a measured length of $\sim 6\ \text{mm}$. The measured topography shows hundreds of artefacts stemming from reflection on the blank wires as well as on the diamonds themselves, which have to be removed before the topography can be analysed. The point-clouds representing the measured data, the denoised and filtered data and the flattened wire topography are shown in Fig. 5.40.

The axis of the wire is determined by fitting a cylinder into the point-cloud and the data is shifted so the axis aligns with the x-axis of the coordinate system. With the position of the axis known, wire core radius r_w is estimated and data points with a radial distance smaller r_w are deleted to increase computational efficiency. The kerf radius r_k is initially estimated as the maximum absolute value in y-direction. The data-points are then shifted along the z-axis according the transformation (5.60), described in section 5.6. The transformed data is denoised by applying a nearest-neighbour search and removing all data-points whose distance to their nearest neighbours is more then 1/10–th of the standard deviation of the mean distance between the 50 closest data points. The data is transformed back into cylindrical shape as shown in the middle image of Fig. 5.40. The final flattened topography of a wire section is generated with the local kerf radius to minimise error from miss-alignment.

The wire is split into sections of characteristic length $s = 500\ \mu\text{m}$, which is approximately equal to the wire diameter. The local kerf radius is determined as the maximum radial distance of any data point and the data is transformed applying (5.60). The wire surface is assigned the z-coordinate 0; the protrusion of the data points can then be read immediately from the z-coordinate. The highest protrusion is $z_{max} = r_k - r_w$.

The bearing ratio t_p is determined from the z-coordinates. Since the area

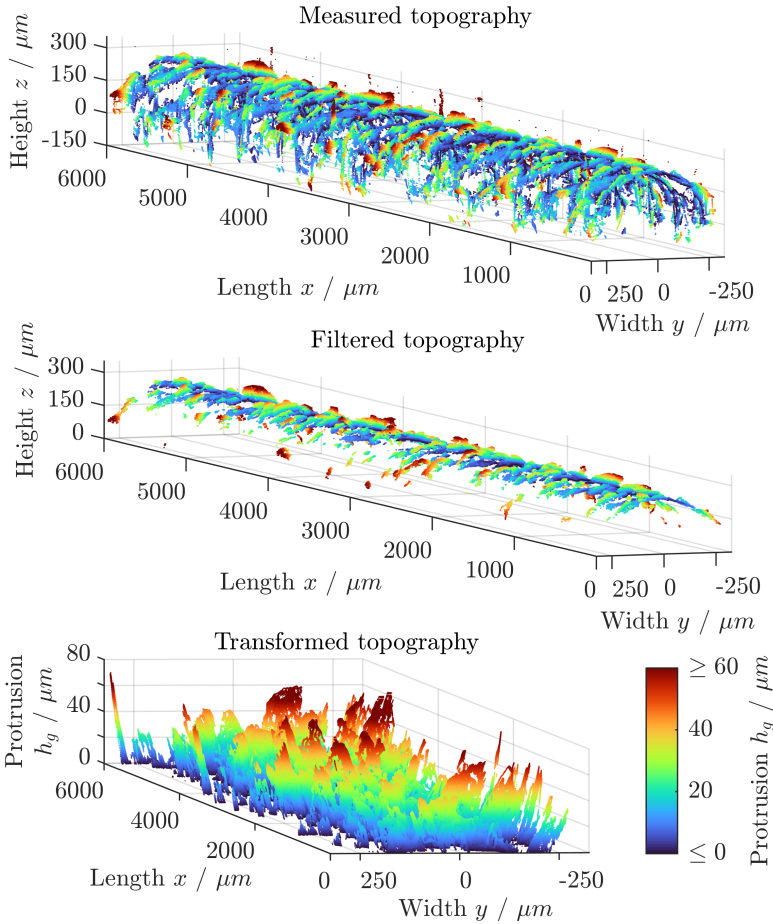


Figure 5.40: Point-cloud representation of the wire topography: Top shows the aligned, unfiltered point-cloud, centre the denoised data and the bottom the flattened topography. The colour indicates the radial distance from the assumed wire surface.

at $A_n(z = 0) \neq 2r_k\tilde{s}$ due to the missing data points, the reference area A_{ref} is derived as the bounding area of a shape which envelopes the data-points representing grains. It is implemented in MATLAB by means of an *alphaShape*-object [115], with an *alpharadius* of 5 to reasonably suppress holes. The resulting penetrated area A_n is plotted over the penetrated depth h for some typical wire sections in Fig. 5.41.

Fig. 5.41 illustrates that the load-bearing properties of the wire sections differ strongly, even if local references are assumed. As the load-bearing area of a wire section at small penetration depth typically depends on one or two large grains, the load-bearing area is relatively insensitive to the choice of the characteristic length. Blocky grains with a high width-to-height-aspect ratio dominate the bearing-ratio at small penetration especially when they are near the centre of the wire.

In order to smoothen the topography and avoid the representation of the highest grain by few, isolated points, additional filtering is performed on the section topographies. All data-points are assigned to bins representing their protrusion. Bins have a width of 100 nm. The first, highest bin to contain a certain number of data-points is identified and all data-points in bins higher than the one identified are removed. The filter can be parametrised by the threshold number of data-points and leads to a flattening of the load-bearing curve. This corresponds to a higher penetrated area for low penetration depths, as shown in Fig. 5.42 for a threshold of 35 data-points, where the same wire sections as in Fig. 5.41 are analysed.

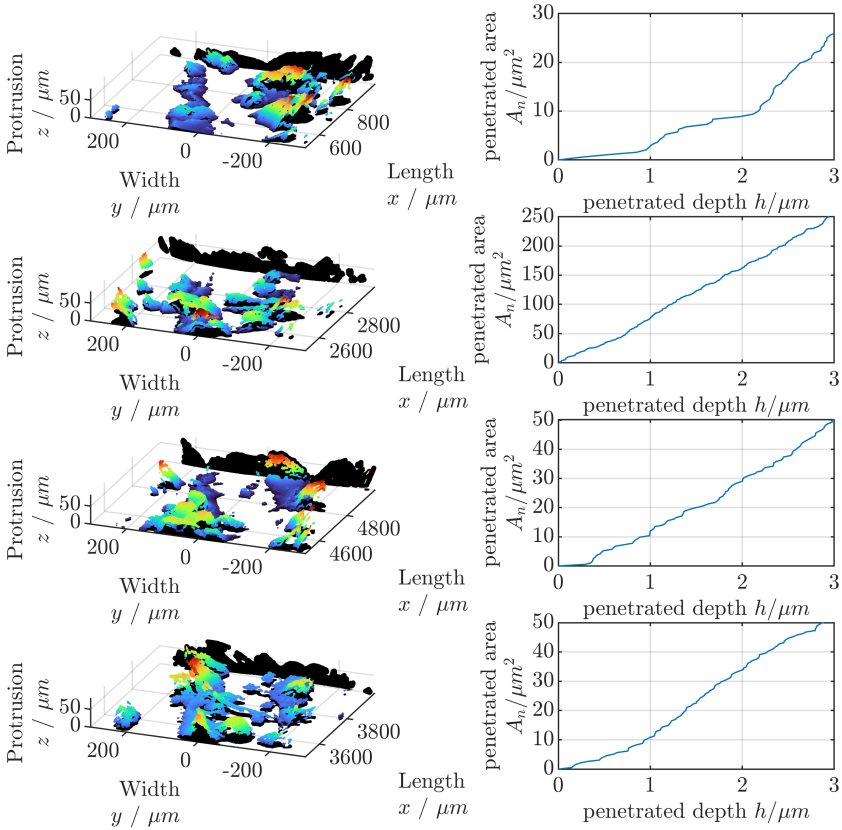


Figure 5.41: Sample of four transformed wire sections with their corresponding penetrated area in normal direction plotted over the penetrated depth. False colour indicates protrusion, black shadows are plotted with the point clouds illustrating the projected area of the grains in the sections. No additional filtering is performed, representing a conservative filter setting.

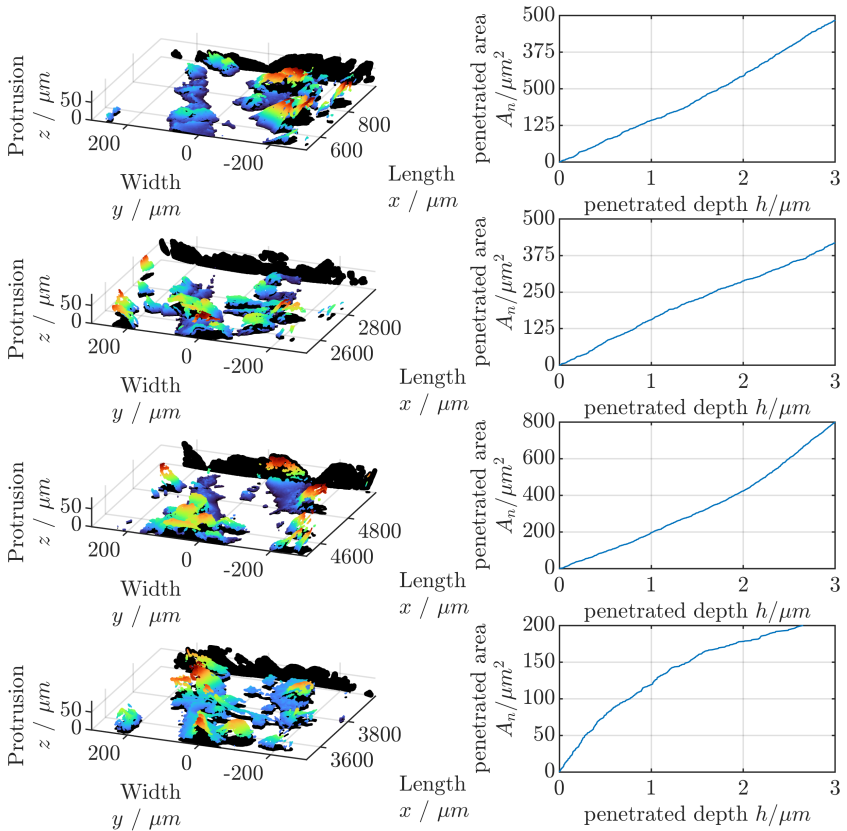


Figure 5.42: Sample of four transformed wire sections with their corresponding penetrated area in normal direction plotted over the penetrated depth. False colour indicates protrusion, black shadows are plotted with the point clouds illustrating the projected area of the grains in the sections. Additional filtering on the wire sections is performed with a threshold count of 35 data-points to present the highest 100 nm, which represents an aggressive filter setting.

Implementation of the Material Removal Rate Model

The contact condition for each section is recursively approximated by creating a balance of acting forces. The contact length l is larger than the total of the measured wire sections, which amounts to approximately $l_{meas} \approx 18$ mm. A random combination of $N = \frac{l}{s} = 70$ sections is chosen from all sections determined for an experimental setting. The analysis is repeated for 30 random combinations of wire sections to estimate the scatter of results.

The contact depth is iteratively determined on the basis of a force balance. The sum of the forces acting on all N wire sections must equal prescribed feed force:

$$\begin{aligned}
 F_f &= \sum_{i=1}^N F_n(h_i) \\
 &= \sum_{i=1}^N k_n h_i^{m_n} A_{n,i} \\
 &= \sum_{i=1}^N k_n h_i^{m_n} t_{p,i}(h_i) A_{ref,i}
 \end{aligned} \tag{5.74}$$

The penetrated depth h_i of a section on the wire depends on its prominence z_i in relation to the section with the largest protrusion z_{max} and the infeed, which equals the penetrated depth of the section with the largest protrusion h_{max} :

$$h_i = z_i - z_{max} + h_{max} \tag{5.75}$$

When $h_i < 0$, its value determines the distance from the kerf front, while $h_i \geq 0$ indicates that section i is active and penetrated by h_i .

The infeed h_{max} is increased from 0 nm in steps of 10 nm until (5.74) is satisfied. The relation is solved for each wire section. Since $t_{p,i}(h_i \leq 0) = 0$, inactive grains do not contribute to the force balance per (5.74). The av-

average penetration depth \tilde{h} is determined as the arithmetic mean of active sections. This implementation implicitly assumes that the wire is rigid and local bending around an active grains does not affect the penetrated depth of other grains.

The average removed depth \tilde{h}_f is derived per (5.73). The ductile solution can immediately be calculated by applying (5.47). The brittle solution is derived from a hypothetical average wire section generated on the basis of the evaluated sections. The load-bearing area at penetration depth \tilde{h} is the average of the evaluated load-bearing areas at \tilde{h} .

Finally, the removal rate is determined by applying (5.72).

5.6.4 Results and Discussion

Comparing modelled removal rates with experimentally determined ones shows no agreement of the model with measured results. Fig. 5.43 illustrates the modelled and measured removal rates.

Plotted in Fig. 5.43 are the experimentally determined removal rates with error bars showing the standard deviation as a measure for the fluctuation of the removal rate over the duration of the cut. Blue x mark the average modelled removal rates obtained from a hypothetical wire topography at height \tilde{h} , with error bars indicating the standard deviation between the obtained solutions. It can be seen that the majority of all modelled removal rates are either much larger than the experimentally determined ones or significantly smaller. The scatter in the modelled data is large, indicating a strong dependence of the modelled solution on the random wire composition. The experimental removal rate is, if at all, only met randomly. An analysis of the determined amount of active sections shows deviations for all experimental runs as well, as depicted in Fig. 5.44.

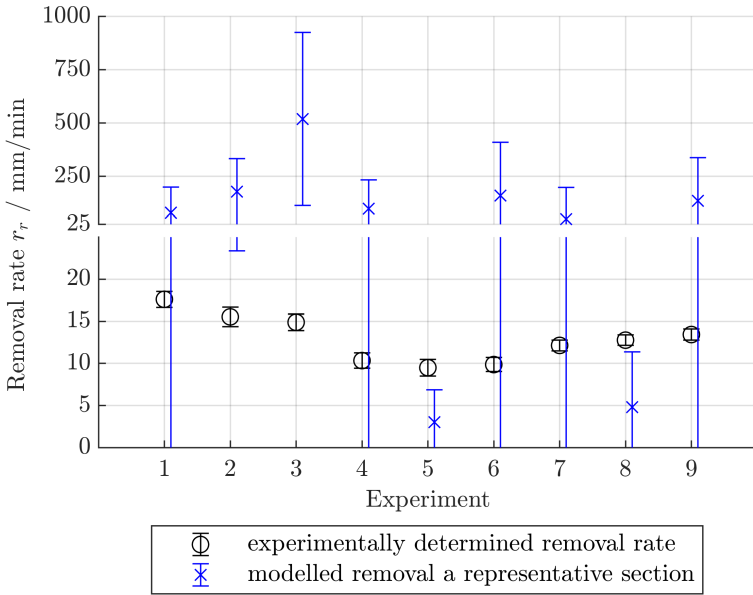


Figure 5.43: Measured and modelled removal rates r_r for different experimental conditions. Note the broken ordinate with different scaling.

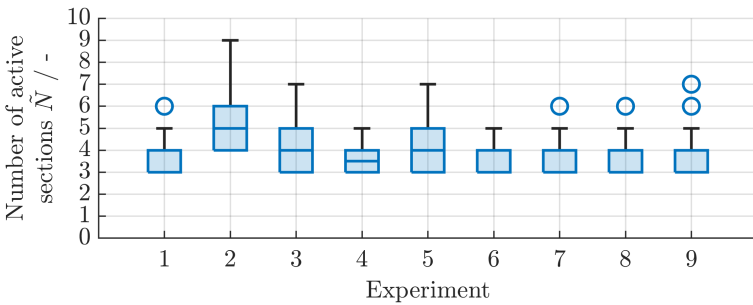


Figure 5.44: Number of active wire sections \tilde{N} for each experimental run.

Solutions with fewer than three active sections are not plausible since the system would be mechanically undetermined, combinations which yield fewer than three contacts are therefore repeated and the graph is consequently cut sharply at three active sections. From the analysis of Fig. 5.44 follows that all modelled wires are dominated by at most nine wire sections, while many seem to be determined by only three active grains.

The modelled removal rate is affected by the shape and size of grains on the wire. Sections with pointy or large grains near the kerf side penetrate deeply but do not contribute much to the load-bearing area, leading to high removal but low load bearing. In contrast, large and blocky grains near the centre yield high forces with low indentation. When excessive modelled removal rates are observed, mostly only a few dominant wire sections are active, typically those with a blocky grain close to the kerf centre. Because of the low number of active sections in this case, these still have to penetrate deeply in order to satisfy the force balance. When more different sections are active and a high removal rate is modelled, blocky grains with low penetration bear the load while sharp grains penetrate deeply but bear little load. Therefore, the inhomogeneity of the analysed grain sections and the opposing significance of sharp and dull grains with regards to load-bearing and removal characteristics present a major limitation for experimental verification.

Solutions, where the modelled removal rate agrees with the experimentally measured one are mostly generated from section combinations, where the topography of only one section is replicated multiple times. However, not all solutions with only one topography replicated yield results that agree with the experiments. This indicates, first, that not all sections represent the wire well, and second, that the force is not sufficiently evenly distributed amongst the grains when the difference between the active grains is too large.

The precise reproduction of the wire topography is crucial and the poor data point density on the grains is problematic. The filtering method and filter parametrisation applied to the measured wire topography has a strong effect on the bearing characteristics and the modelled removal

rate. Aggressive filtering leads to the removal of larger, isolated groups of data-points and to flatter grains and bearing-ratio curves. Conservative filtering allows for spikes and grain geometry features being represented by few, isolated points, which results in pointy grains and steep bearing-ratio curves. Also, the difference in maximum protrusion of different sections is larger with conservative filtering. The effect of different filter parametrisation becomes obvious when comparing the modelled removal from conservatively filtered wire sections illustrated in Fig. 5.45 with the results from more aggressive filtering in Fig. 5.43.

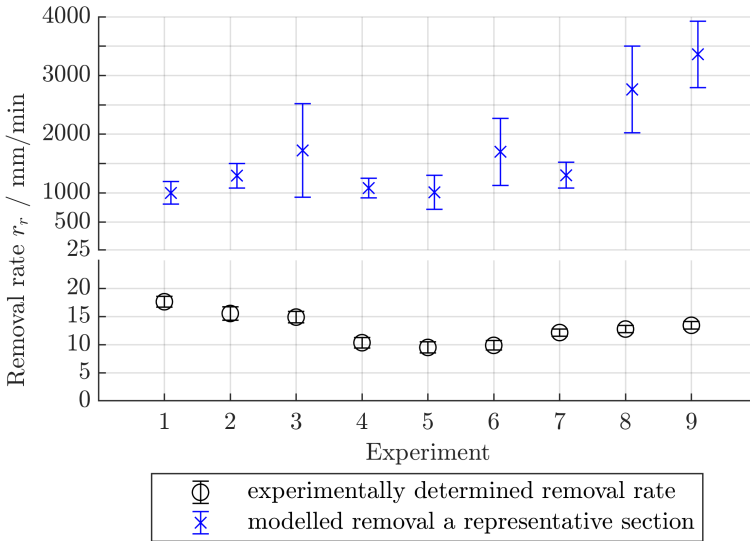


Figure 5.45: Measured and modelled removal rates r_r for different experimental conditions with conservative filter parameters allowing for fewer data points representing a grain, otherwise same parameters as Fig. 5.43. Note the broken ordinate with different scaling.

The model parametrisation which results in the data shown in Fig 5.45 is the same as above except for a more conservative spike removal filter setting. The setting results in the representation of grain tips by fewer data points and consequently steeper bearing ratio curves. The modelled

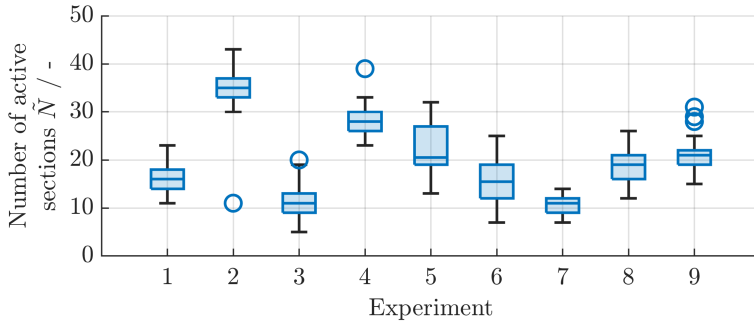


Figure 5.46: Number of active wire sections \tilde{N} for each experimental run for a more conservative filter setting which allows for fewer data points representing a grain.

penetrated depth is higher, leading to brittle removal and much higher removal rates. Furthermore, due to the larger difference in maximum protrusion on the wire sections more sections are active, as seen in Fig. 5.46.

In order to better understand the removal model and the reason for the poor agreement with the experimental data, the removal is modelled on the basis of the idealised wire introduced in sec. 5.6.2 and illustrated in Fig. 5.37. The wire is generated from sections with one Berkovich-shaped grain distributed at random angles $\varphi = 0^\circ, 10^\circ, \dots, 90^\circ$. Furthermore the protrusion of the grains is randomly increased by 0 to $1 \mu\text{m}$. Since the typical indentation depth is $h_i > 1 \mu\text{m}$, all solutions yield $\tilde{N} = \frac{s}{l}$ active grains.

Fig. 5.47 shows, that under these idealised conditions, the model provides results that agree better with the experimental observation. The large modelled standard deviations in experiments 1 and 2 are due to a transition to brittle removal and therefore higher removal rates in some solutions. These experiments are the ones with the highest measured feed force. In all solutions, all modelled grains are active. Increasing the critical depth of cut for the ductile to brittle transition to $h_{crit} = z_{max}$, that is, only the ductile solution for (5.73) is considered, improves the agreement between experiment and model, as the comparison between Figs. 5.47

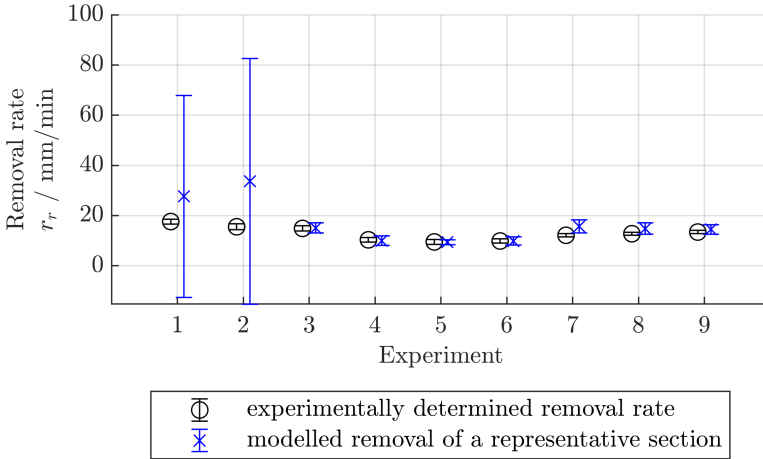


Figure 5.47: Modelled removal rate determined from the idealised wire with randomly placed and protruding Berkovich grains. The random difference in grain protrusion ranges from 0 to 1 μm , which results in 70 active grains in all solutions.

and 5.48 shows. Since the curve fitting for the derivation of the parametrisation of (5.71) is based upon scratch tests exhibiting ductile and brittle material removal, brittle removal is reflected in the equation and the neglect of additional brittle removal can also be argued for.

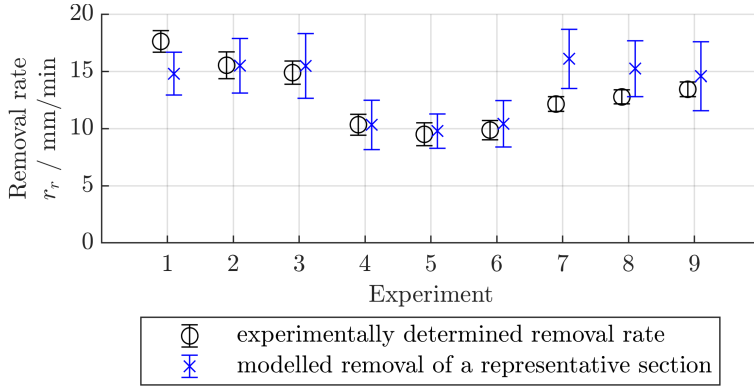


Figure 5.48: Modelled removal rate determined from the idealised wire with randomly placed and protruding Berkovich grains and no brittle removal. The random difference in grain protrusion ranges from 0 to $1\ \mu\text{m}$, which results in 70 active grains in all solutions.

An increase of the maximum protrusion difference from $1\ \mu\text{m}$ to $10\ \mu\text{m}$, well above the average penetration, results in much higher removal rates, as shown in the left of Fig. 5.49, and fewer active sections, as shown in the right box plot of the same figure.

A possible reason for the observed deviations between model and experiment is a faulty force model, that is, the observations on scratch hardness made in experiments with single grains are not transferable to the diamond wire sawing process. The shape difference between wire sections and the Vickers and Berkovich grains used for the determination of the coefficient becomes obvious in the direct comparison of the load bearing curves, as illustrated in Fig. 5.50.

Fig. 5.50 shows a comparison of the load bearing areas A_n of indenters and wire sections. Plotted are the curves corresponding to idealised and measured indenter geometries and the wire sections shown in Fig. 5.41. A difference between the indenters and the wire topography is clearly visible even for the conservative filter setting. More aggressive filter settings lead to smoother and flatter curves such as those displayed in Fig. 5.42, that reach the bearing surface of $A_n = 60\ \mu\text{m}^2$ at profile heights $z < 0.5\ \mu\text{m}$.

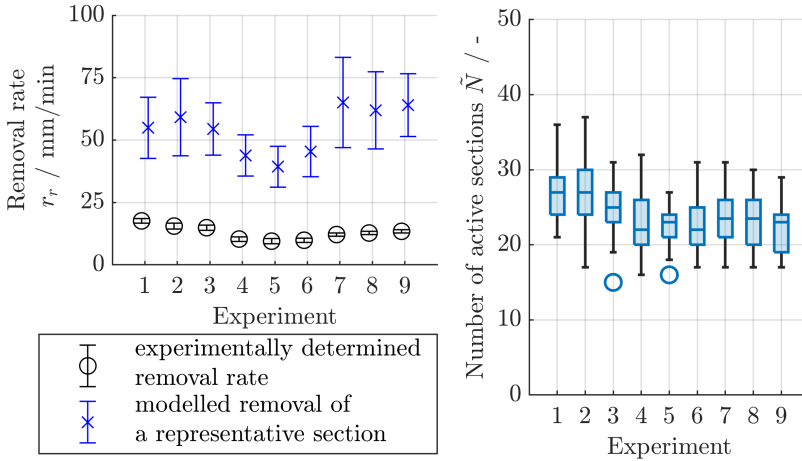


Figure 5.49: Modelled removal rate (left) and corresponding active grains (right) determined from the idealised wire with randomly placed and protruding Berkovich grains and no brittle removal. The random difference in grain protrusion ranges from 0 to 10 μm .

As seen in Fig. 5.50, the load-bearing characteristics of some wire sections bear resemblance with the load-bearing characteristics of Berkovich and Vickers indenters at low indentation depth. With idealised grains, the indentation depth is in the range of $\tilde{h} = 0.5$ to 1 μm . If only wire sections with a load-bearing area of $12 \mu\text{m}^2 \geq A_n(z = 1 \mu\text{m}) \leq 19 \mu\text{m}^2$ are considered for the composition of the modelled wire, only a slight improvement of the modelled removal rate is achieved, which is shown in Fig. 5.51.

The requirement for a similar load-bearing area is only met by a small number of wire sections, typically ranging from one to nine per tested wire. The varying protrusions of the largest grains on these sections mean that the removal is dependent on very few sections and their frequency on the modelled wire. The bearing area of selected wire sections does not necessarily follow a similar pattern to Berkovich and Vickers indenters at the evaluated depth due to the step-like increase in bearing area as seen in Fig. 5.50. Additionally, the differences in protruding heights of the se-

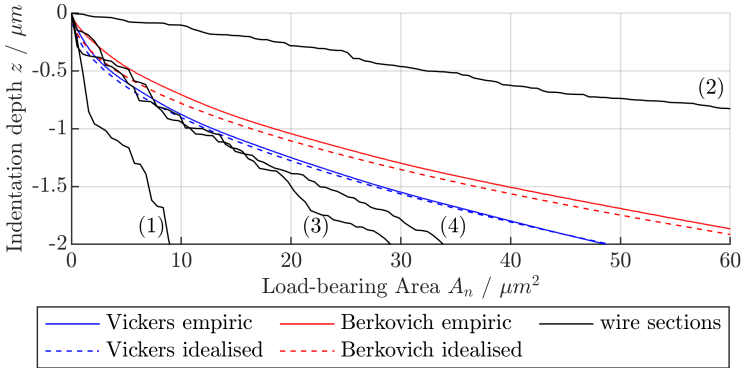


Figure 5.50: Comparison of bearing areas of empiric and idealised Vickers and Berkovich indenters with examples of those of the wire sections presented in Fig. 5.41 where a conservative filter setting was applied. Numbering corresponds to the sections displayed in Fig. 5.41, counting top to bottom.

lected sections lead to deviations in the penetration depth and variations in the number of active sections, explaining the scatter in modelled removal rate. Whether or not the modelled removal rate agrees with the experimentally observed one then depends on the measured and selected sections used for modelling the wire.

Apart from the limitations related to the difference in grain shape, there are further limitations stemming from deriving the specific force model from conditions that differ from the diamond wire sawing process. In DWS, the surface is not flawless and is generally shaped by the passes of previous grains, which results in cracks and a phase-changed outer layer that manifests in poorer mechanical properties. As a result, the final depth is likely higher, resulting in a higher removal rate. However, since the modelled removal rate is not consistently smaller than the experimentally observed one, this cause is not the main reason for the observed difference.

The implementation assumes that the wire is rigid between two active grains and therefore simplifies the distribution of forces onto the modelled sections. The assumption is good for a worn-in wire, when many grains with similar load-bearing characteristics are evenly distributed along the

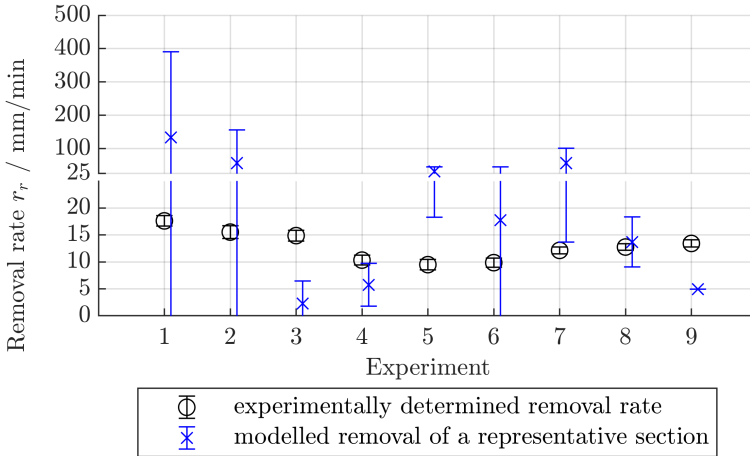


Figure 5.51: Comparison of bearing areas of empiric and idealised Vickers and Berkovich indenters with examples of those of the wire sections presented in Fig. 5.41 where a conservative filter setting was applied. Numbering corresponds to the sections displayed in Fig. 5.41, counting top to bottom.

wire axis, but worsens when the wire is dominated by few sections.

Overall the deviation between modelled and measured removal rates can not be fully explained on the basis of the present data. The data is flawed in several ways:

- Grain density and grain size distributions of the available wires are very broad. This results in only very few (~ 5) captured sections dominating the removal modelling in all tested combinations. Since their dominance is physically plausible, excluding them manually is not reasonable.
- It is possible, that not enough dominating sections are captured to accurately describe the process. Since however none of the modelled combinations provides consistent results and for each experiment at least 36 different topographic sections were available, this is considered a minor problem.

- Optical measurement of the wire topography with focus variation presents another limitation. When looking closely at the plotted grains in Fig. 5.41, it can be seen that the grain surface is showing holes, which affect the bearing ratio. Some faces of diamond grains cannot be captured at all, as they are transparent or reflect the light in such a way, that the light cannot be focused on them. The procedure for despiking in order to remove artefacts associated with reflection also alters the profile and negatively affects the accuracy of the bearing ratio.

On the other hand, the model includes several assumptions that may oversimplify the process. Notable potential sources of error are:

- The force model is parametrised with grains, whose load-bearing characteristics diverge from those of the grains identified on wires. The model based solely on the penetration depth and the bearing area at that depth may be inaccurate for describing the wire sawing process. Improvement of the prediction quality by modelling an idealised wire points at this being the main source of error.
- The ductile-to-brittle transition and brittle removal are inaccurately represented. (5.64) and (5.65) that describe the plastic zone under a loaded indenter and are used to quantify brittle removal both are derived from pointy indenters, which do not represent the grains on the wire in this case. The slight improvement of the prediction quality by relying purely on the empirical removal equation supports this thesis.
- The alteration of material properties by the machining operation is not considered. Cracks or protruding material residuals from previous grain passes are not considered but would likely affect the force and removal models.
- The assumption of a stiff wire is only accurate when the distance between active grains is sufficiently short and the grain protrusion difference is small. The limits depend on the wire stiffness, tension and bow.

- The model reduces removal to representative grains, that would have to be evenly distributed around the wire to remove material uniformly on the kerf front. Deviations, especially when few grains are active and the kerf surface is large, are not considered.

If it is assumed that the limitations stemming from the analysis of the experiments are the main reason for the poor agreement of the model with the experiments, the derived model has to be analysed with experimental data from other sources or with different wires. Ideally electroplated diamond wire in run-in state are to be used, where not the protrusion but the shape of the grains determines the shape of the bearing ratio curve and therefore the removal rate. The model can also be tested by implementing it into a kinematic-physical simulation environment such as those presented in the state-of-the-art. In this way, it may also be tested, whether the force model, derived from scratching with idealised grains, is sufficiently accurate for the description of the diamond wire sawing process.

5.7 Conclusions: Process Modelling of DWS

In this chapter, three contributions to the improvement of the understanding of the diamond wire sawing process are presented:

1. A wire deflection model is developed. The model has the shape of a differential equation that is derived from the consideration of finite beam elements subjected to a load distribution. The model includes the consideration of bending stiffness and predicts asymmetric wire bows on the basis of acting cutting and normal force, wire tension, pulley distance, workpiece width, wire diameter and wire material. Asymmetric positioning of the workpiece in between the pulleys can also be prescribed. Boundary conditions, notably the guiding effect of the pulley curvature, are discussed. The model is validated with the help of an FEM model and experiments. The effects of varying process parameters, wear and a changing ingot cross-section are discussed.

2. The validation experiments of the wire deflection model form the basis of the analysis of the cutting-to-normal-force ratio. It is shown, that the ratio depends only on the topography of the wire and not on prescribed process parameters. The wear-state therefore indicates the cutting ability. With increasing wear, the ratio decreases and lower cutting forces in comparison with normal forces are acting on the material. Force ratios lay between 0.45 and 0.2 for all tested wires; the values agree with those obtained in single grain scratch tests. Two quantities are introduced to parametrise the cutting ability with a power function: a cumulative wear factor on the basis of analytical wear theory proposed by USUI et al. and another on the basis cutting energy which can be estimated by integrating the drive-power consumption over the time period of the cutting process.

3. A material removal rate model is proposed. The goal of the model is to link process forces, process parameters and wire topography with the removal rate. Such a relation, the PRESTON-equation, is well known for lapping processes and LAS, but currently not available for DWS. Based on analytic consideration of the engagement of single grains on the wire, the contact condition is abstracted to be described by topographic parameters. In this way, the removal rate is defined by process parameters cutting speed, engagement length, feed rate, wire and kerf diameters, the average number of active grains and the load bearing characteristics of the wire. The latter can be assessed from the surface profile by means of the Abbott-Firestone curve. The link between normal force, engaged area and penetrated depth is given by the scratch hardness relations derived in chapter 4. Ductile and brittle removal can be considered by application of a transition criterion (based on BIFANO's work [10] or critical pressure for the activation of phase changes), as well as an empiric relation to consider the material recovery in ductile cutting and fracture theory put forth by MARSHALL, LAWN et al. [100, 113] for the brittle case. Brittle removal requires additional assumptions for the grain shape and knowledge of mechanical workpiece material properties. The model is formulated and implemented in a numerical simulation environment and tested with experiments. The model

cannot be verified with the experimental methods available, does however lead to plausible results and reasonable agreement with experiments if an idealised wire is used for modelling of the topography and if brittle removal neglected.

The experimental analysis of the process and model validation experiments are performed on a laboratory-scale DWS specifically designed and built for the present study. In order to being able to analyse the process in steady state, a feed-rate control on the basis of acting normal forces is implemented on the machine. The machine uses a wire loop and is therefore able to run with high cutting speeds while consuming low quantities wire. The drawback of the looped wire is the different wire topography in comparison with industrially applied electroplated diamond wires. The wire loop consists of several strands of thin wire, braided to form a loop and densely covered with diamonds. The grain size and spatial distributions are highly irregular, making it difficult to parametrise the wire topography. Furthermore, the wear behaviour of diamonds cannot be easily analysed as the service life of the tool is determined by the integrity of the cohesion of the strands rather than the protrusion reduction of the diamond grains.

Chapter 6

Summary and Outlook

The present work contributes to the current level of knowledge in the field of machining of Si with diamond tools. Fundamental aspects of material removal and transition of the crystal phase are covered and applied to DWS.

After reviewing the theory and state of the art in chapter 2, the following knowledge gaps are identified:

1. Specific cutting and normal force, expressed by scratching and ploughing hardness, were not yet systematically studied for machining of Si at high speed and with different tool geometries.
2. Similarly, no comprehensive study of the phase-transitions that Si undergoes when subjected to high pressure at high speed and with different tool geometries is known.
3. A simple criterion for the ductile-to-brittle transition which incorporates grain-shape related aspects is not available.
4. The coefficient of friction between diamond and Si at forces and sliding speeds relevant for DWS and the therewith associated contact conditions is not yet known.
5. The cutting-to-normal force ratio in DWS is poorly understood.

6. The material removal rate in on the basis of acting forces and prescribed process parameters has so far only been determined empirically. A derivation on the basis of prescribed forces and the wire topography is currently not reported on.
7. Idealised grain geometries are typically considered when modelling the DWS process; a comparison of the grains on wires with idealised shapes is however typically only done indirectly. Studies investigating the wire topography are rare.

In order to advance the understanding of the DWS process and answer the derived research questions, the work is structured in two parts: Fundamental research investigating material removal phenomena through single grain scratching experiments and application research, where process models for the DWS are developed and validated.

A scratch test rig has been developed that emulates long contact length at cutting speeds of 25 m/s. Scratching experiments with Vickers and Berkovich indenters in edge-first and face-first orientations, as well as with Rockwell indenters have been performed. Contact forces, indenter geometry and scratch topography were recorded. Indentation theory on the basis of the work of OLIVER AND PHARR and models of scratch and ploughing hardness proposed by WILLIAMS were. The following results were obtained and conclusions drawn:

- Empiric relations for specific cutting and normal forces were derived for different engagement parameters (total indentation depth, contact depth, residual depth and acting normal force). It was shown that more than one quarter of the projected area bears normal load when scratching with Vickers indenters in face first orientation, deviating from WILLIAMS' theory and that three-quarters of the projected area is a better approximation for the load-bearing area.
- The coefficient of friction was determined as $\mu = 0.062$.
- The phenomenon of depth recovery, especially in ductile cutting mode, was discussed, however no analytic or empiric quantification of the recovery rate could be derived. Depth recovery is made up of

elastic material response and volume expansion due to amorphisation of the material on the surface.

- Raman spectroscopy of the scratch surface revealed that transition of the crystalline structure to a metallic phase can occur up to undeformed chip thickness of up to 0.95 to 1.95 μm , which explains why partially ductile removal can still be observed at cutting depth significantly larger than the critical cutting depth predicted by BIFANO's theory. The investigation further showed that the composition of the scratched surface does is not significantly influenced by the grain shape.

For the investigation of the DWS process, a wire saw using a wire loop was developed. The machine is equipped with a feed-force-based feed-rate control that allows for the efficient analysis of the steady process state. While wire consumption at high cutting speed is low due to the use of a looped wire, drawbacks due to the composition of the stranded wire loop with high grain density and irregular grain size distribution arise. Two process models were formulated: one describing the wire bow in steady state on the basis of acting forces and geometry of the setup and one for the derivation of the material removal rate on the basis of acting forces, wire topography, cutting speed and engagement length. The following conclusions were drawn from the experimental analysis and application of the models:

- The wire bow model accurately describes the wire deflection with consideration of bending stiffness. Bending stiffness is however negligible for typical wire thicknesses and machine and workpiece dimensions. The asymmetry of the wire bow is also negligibly small in normal cases. The boundary condition resulting from the guidance of the wire by the curvature of the pulley and deviations due to its negligence have been discussed: the effect is negligible for most applications.
- It is shown, that the cutting-to-normal force ratio in DWS does not depend on process parameters but is determined by the wear state,

or, more generally, the topography of the wire. The force ratio decreases from 0.45 for a new to 0.2 for a run-in wire. The values agree with the theoretic values derived from single grain cutting experiments. An empiric model in the shape of a power law is derived two different wear-proportionality factors are presented and discussed: one on the basis of analytic wear prediction by USUI and one suggesting a proportionality with the cutting energy. The latter can possibly be approximated from the power consumption of the drives on industrial machines.

- A material removal rate model is derived with the aim of providing a link between normal force and removal rate, similar to the PRESTON equation applied in LAS. The model considers kinematic process parameters and the wire topography assessed through the Abbott-Firestone curve and is fully formulated to consider ductile and brittle removal. The model could not be validated by experiments, which is attributed predominantly to the irregular wire topography and the poor resulting load bearing parameters. It can however also not be assured, that results from single grain experiments in terms of acting forces at given penetration depth can be unconditionally transferred to DWS, as the grain geometries and therefore load-bearing characteristics differ significantly. Furthermore, the effect of the pristine surface subjected to load in the scratching experiments is thought to exhibit higher strength than the pre-damaged surface in the sawing kerf. Due to the extremely high scatter of the modelled results, it is not possible to separate the effects.

While some of the knowledge gaps are narrowed by the present study, several questions remain and potential for improvement was identified.

When determining the scratch hardness, some assumptions such as the neglecting of pile up for the calculation of sink-in and using the width on the ridges as the scratch width at the averaged height of those ridges were identified as sources of error. Sink-in becomes more pronounced at low depth of cut, at the same time ductile flow and building-up of ridges are more dominant when material is removed in ductile mode or simple displaced. It would be helpful to study these phenomena in more de-

tail, either by microscopic high-speed imaging or appropriate simulation methods. High-speed imaging is challenging due to the small scale, while simulating the process requires constitutive material models that account for the phase transition and consequently volumetric expansion of the material. Such models have been proposed e.g. by WANG et al. [167] and VODENITCHAROVA [161]. Studying whether the ridges form during scratching from plastic deformation or after scratching from phase transition, thereby whether they contribute to the load-bearing area, and adapting the analysis method accordingly will lead to improved empirical functions. This improvement will especially improve the sparse data at very low indentation depths. Furthermore, it will lead to an understanding of the underlying mechanisms of depth recovery in ductile machining, needed for more accurate prediction of the residual surface when cutting in ductile mode.

Currently, there is no study linking the Raman intensity ratio between Si-IV and α -Si and the corresponding thickness of the phase changed layer. Determination of this relationship, for example by measuring the layer thickness with transmission electron microscopy, would be helpful to quantify the amount of phase changed material and estimating the residual stress due to volumetric change.

The developed model for the material removal rate could not be verified by means of experiments with the available tools. Improved tools and ideally electroplated diamond wires welded or otherwise connected to a loop are required to achieve a better data basis. Alternatively, different electroplated wires can be tested on machines that use open wire at lower speed, as the validity of the model can also be proven independently of the used cutting speed. Wire topography measurement remains challenging is also eased by the application of electroplated wires, as the reflectivity of the nickel layer is not as high as that of the alleged brazing layer of the wires used in this study. The transferability of models validated in single grain experiments to the DWS process can then also be discussed in further details.

High potential for improving the process understanding lays in the development of a comprehensive kinematic-physical model for the diamond

wire process. The here presented scratch and ploughing hardness relations provide the basis for efficient force and removal models, as they provide a computationally efficient link between penetrated or final depth, removed area and corresponding force. It is also conceivable that the material removal model can be validated with such a model. In order to advance the currently existing kinematic models, it is however necessary to include aspects of the change of surface integrity other than surface roughness and crack depth. As the sawn wafers become thinner, they are more susceptible to deformation, which can be caused by uneven residual stress states on the surface.

Lastly, the application of the presented analysis models, notably the single grain tests can be applied to different materials such as silicon carbide. The direct comparison can help to further develop efficient processes from the existing processes for the even more challenging machining of SiC.

Appendix A

Scratch and Ploughing Hardness - Plots

This appendix contains the plots showing data points and corresponding fit equations for scratch and ploughing hardness. The plots are referenced in section 2.2.1, tab. 4.2 on p. 90.

The content is:

- scratch hardness H_s vs. total indentation depth h - p. 212
- scratch hardness H_s vs. contact depth h_c - p. 213
- scratch hardness H_s vs. residual depth h_f - p. 214
- scratch hardness H_s vs. normal force F_n - p. 215
- ploughing hardness H_p vs. total indentation depth h - p. 216
- ploughing hardness H_p vs. contact depth h_c - p. 217
- ploughing hardness H_p vs. residual depth h_f - p. 218
- ploughing hardness H_p vs. normal force F_n - p. 219

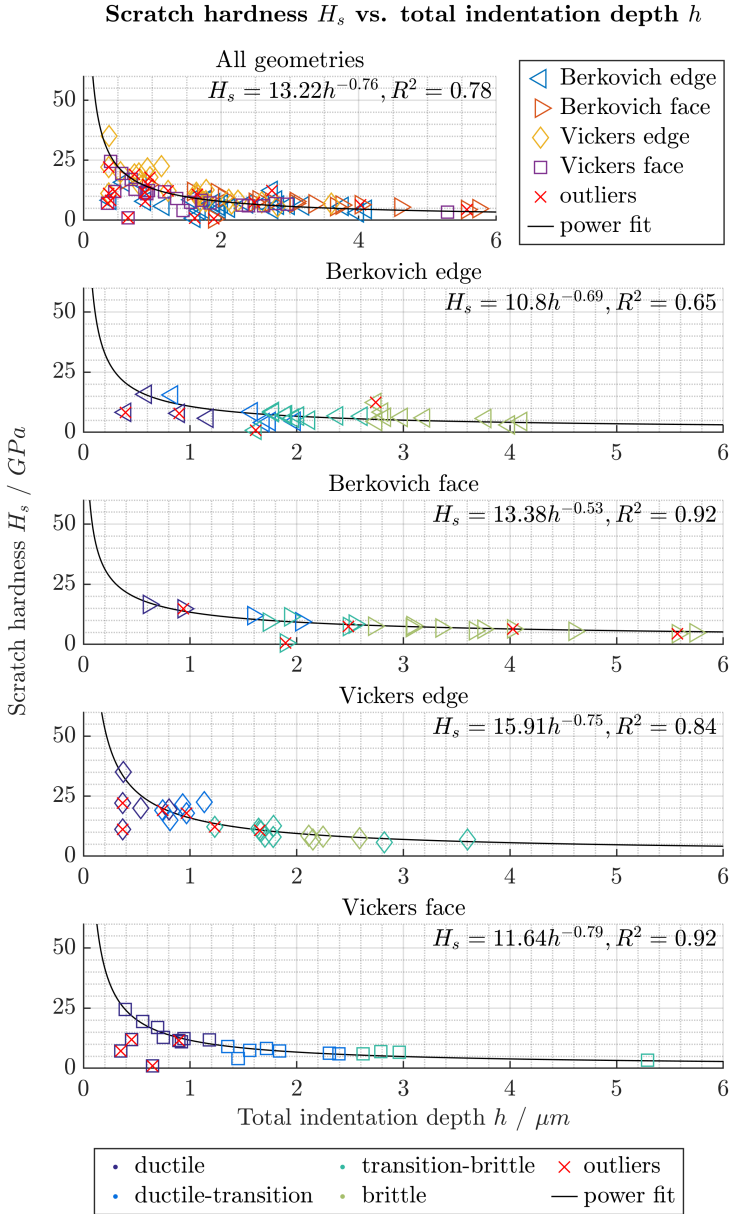


Figure A.1: Plots scratch hardness H_s over total indentation depth h .

Scratch hardness H_s vs. contact depth h_c

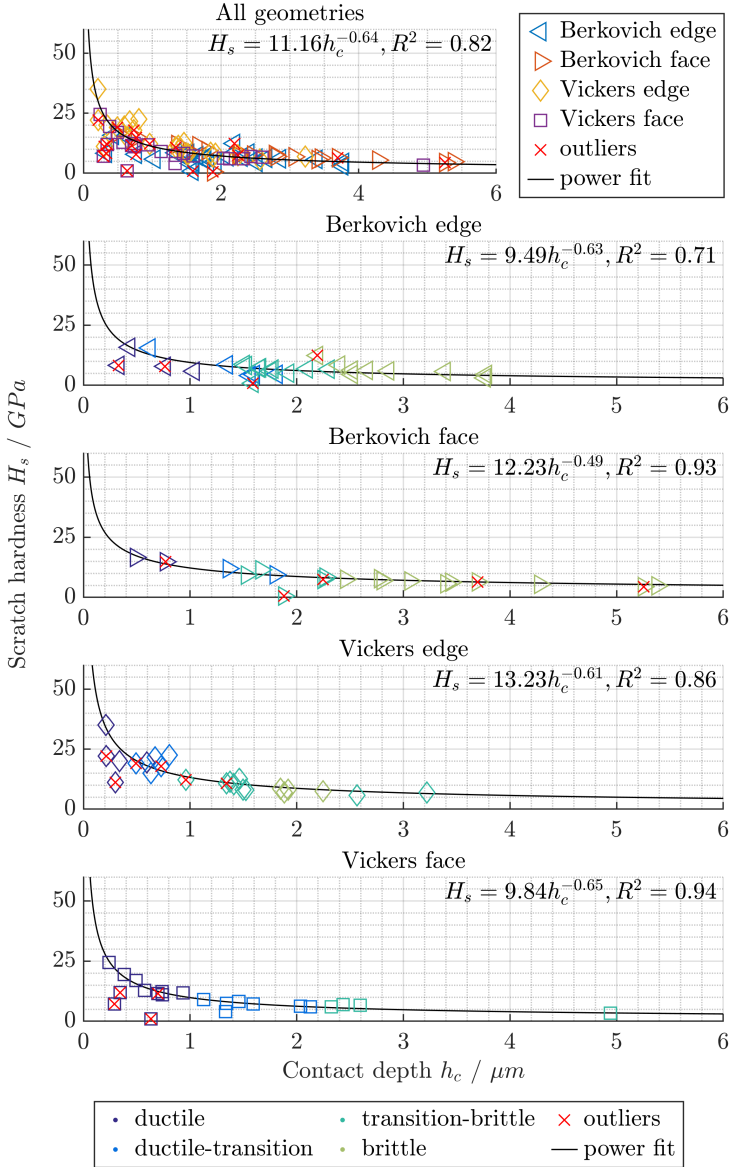


Figure A.2: Plots scratch hardness H_s over contact depth h_c .

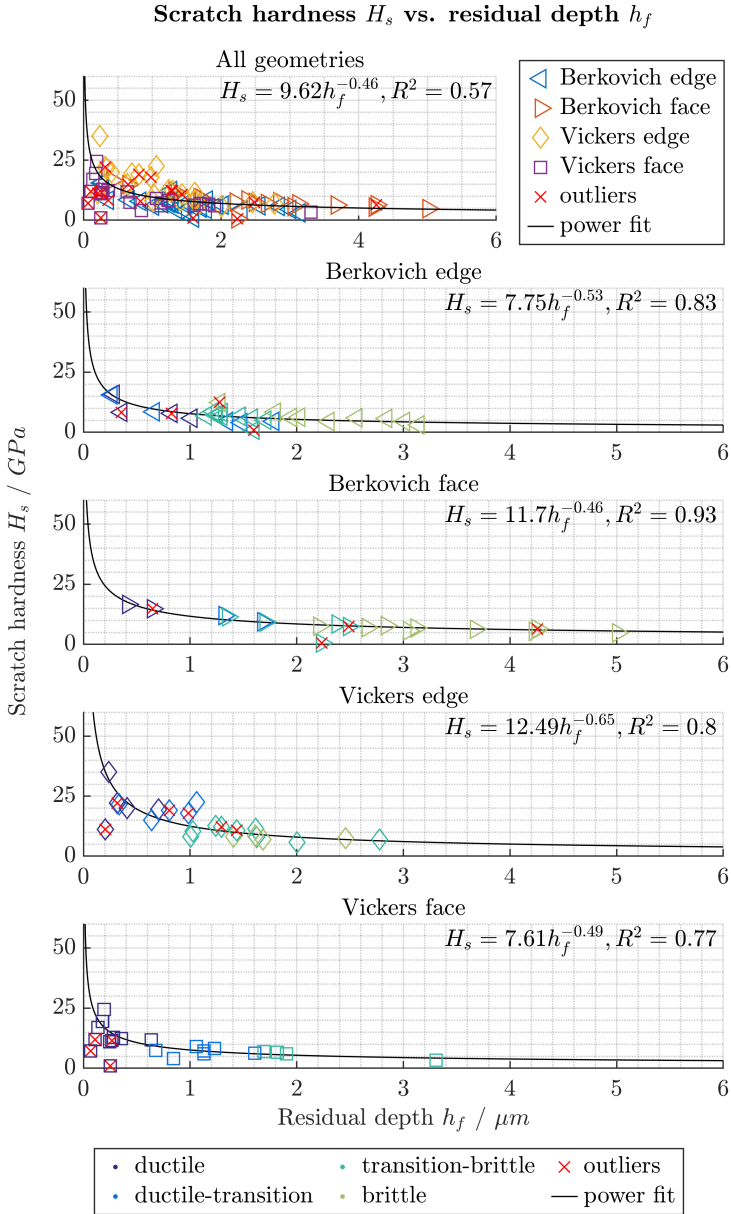


Figure A.3: Plots scratch hardness H_s over residual depth h_f .

Scratch hardness H_s vs. normal force F_n

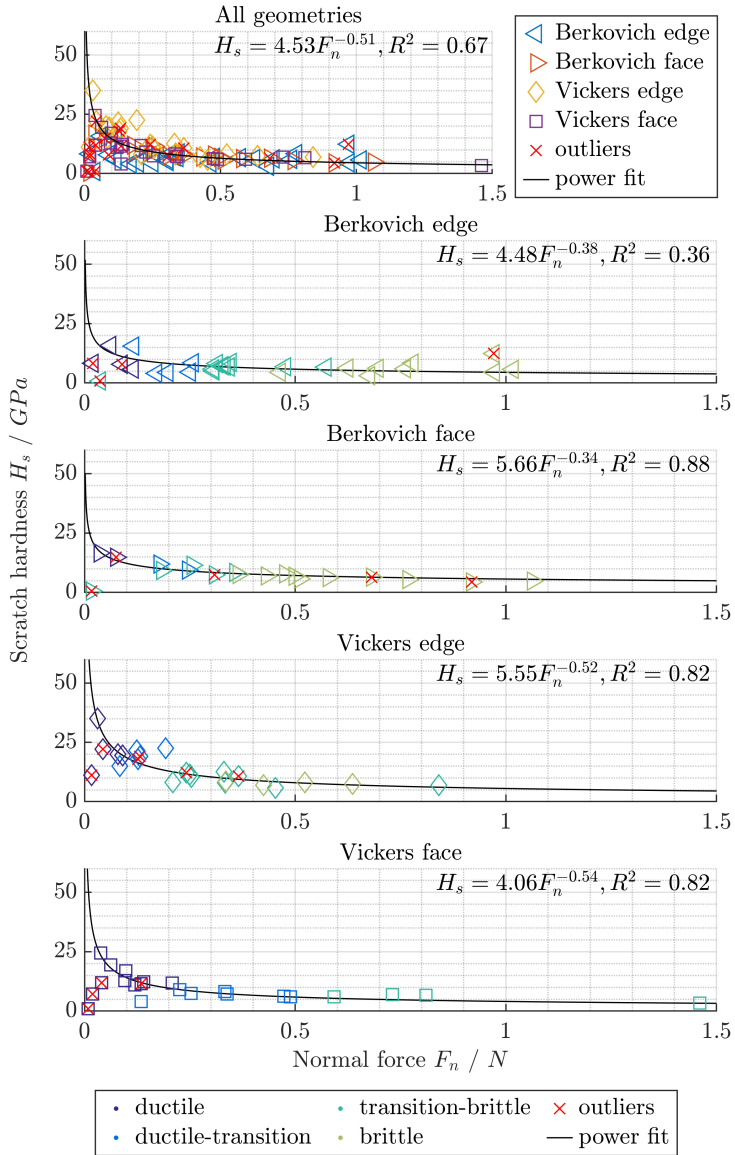


Figure A.4: Plots scratch hardness H_s over normal Force F_n .

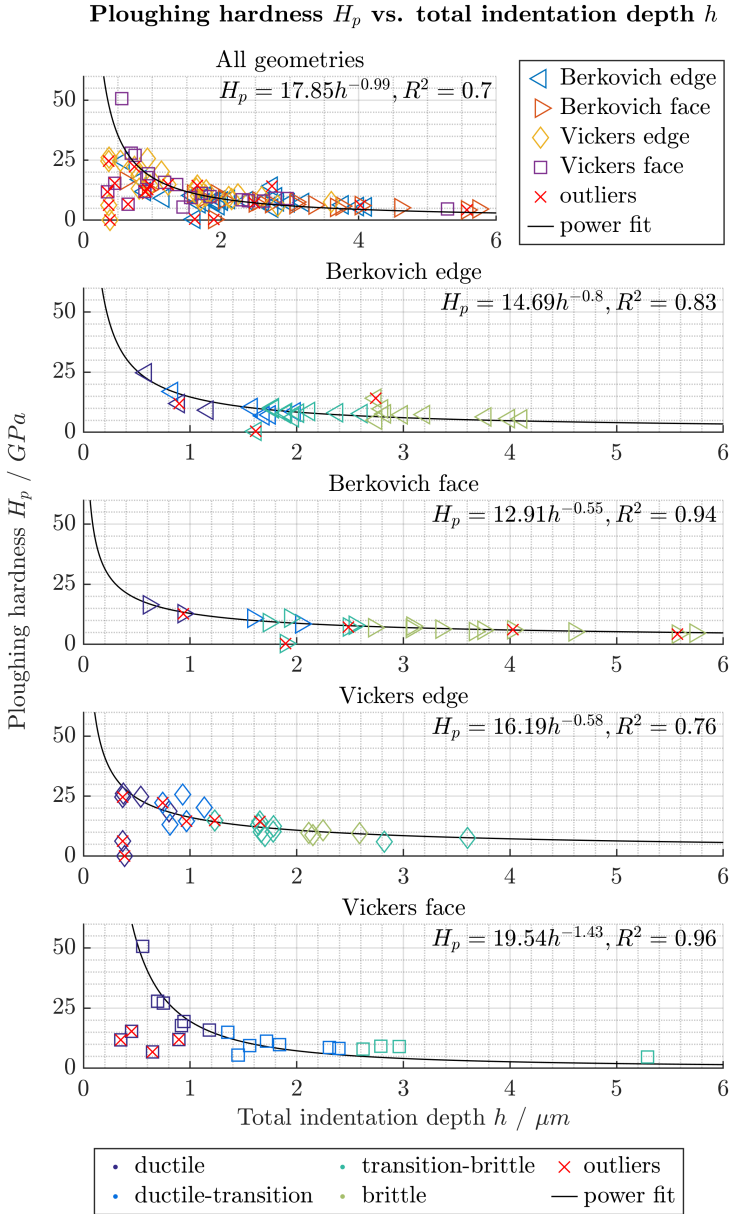


Figure A.5: Plots ploughing hardness H_p over total indentation depth h .

Ploughing hardness H_p vs. contact depth h_c

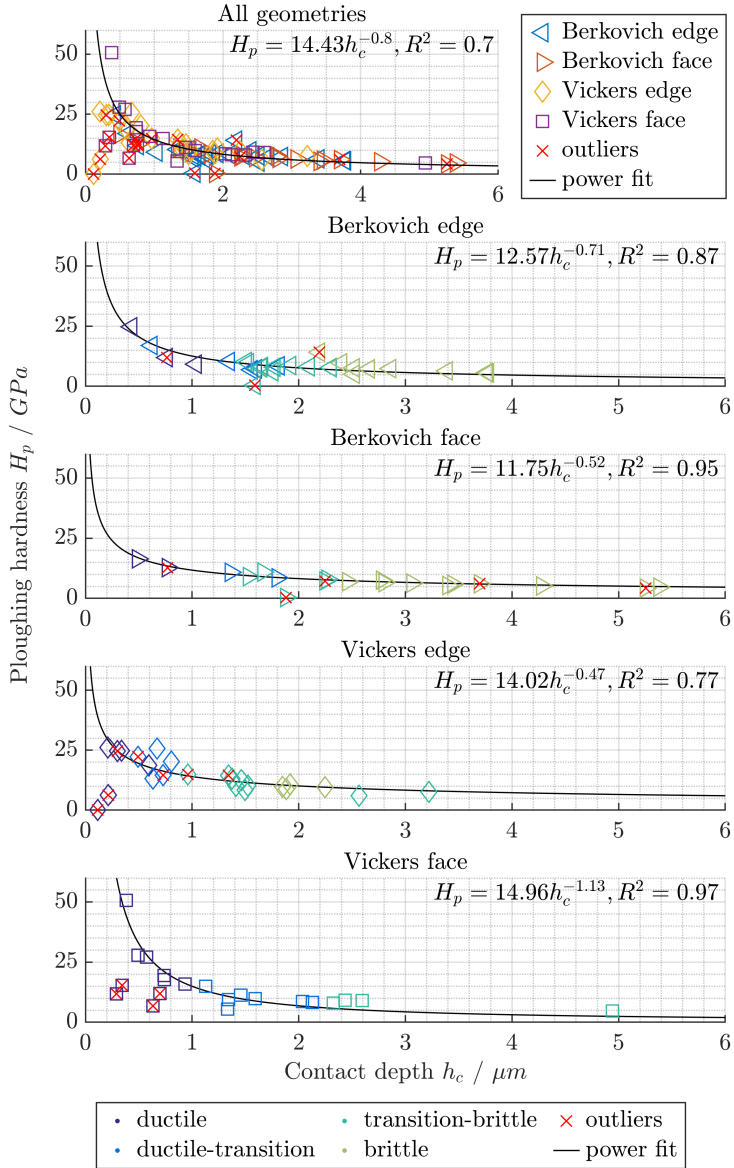


Figure A.6: Plots ploughing hardness H_p over contact depth h_c .

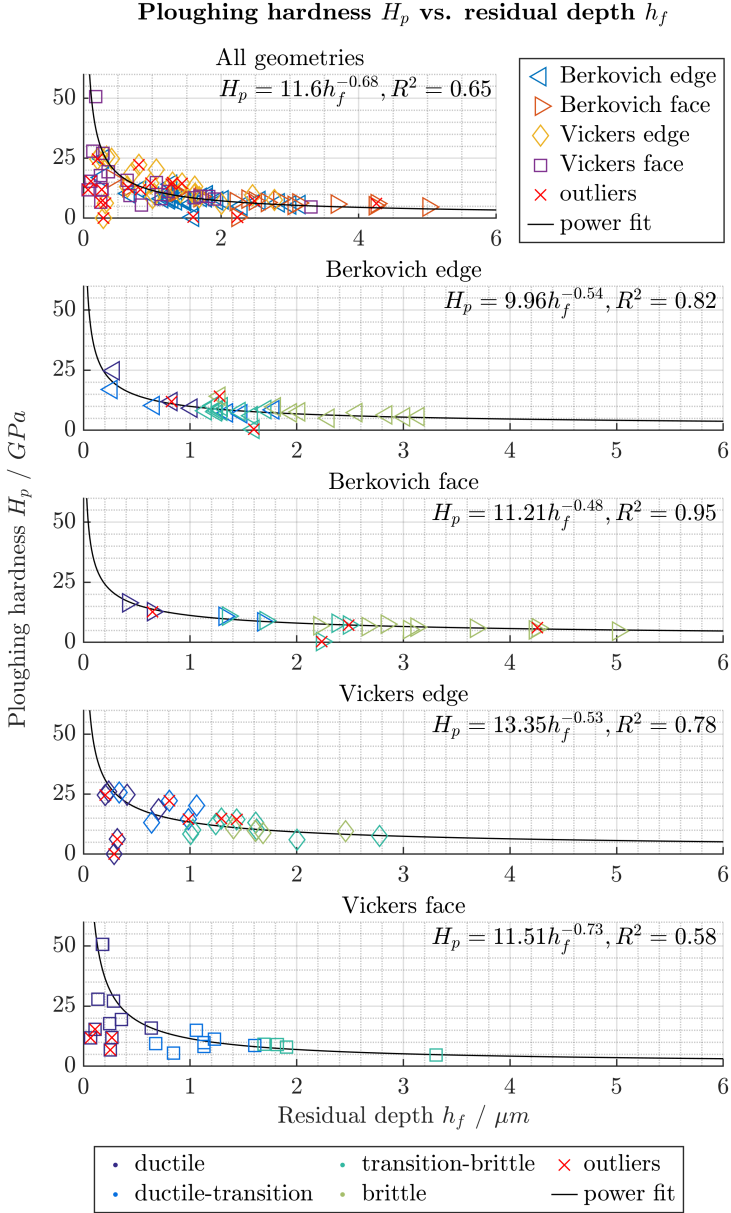


Figure A.7: Plots ploughing hardness H_p over residual depth h_f .

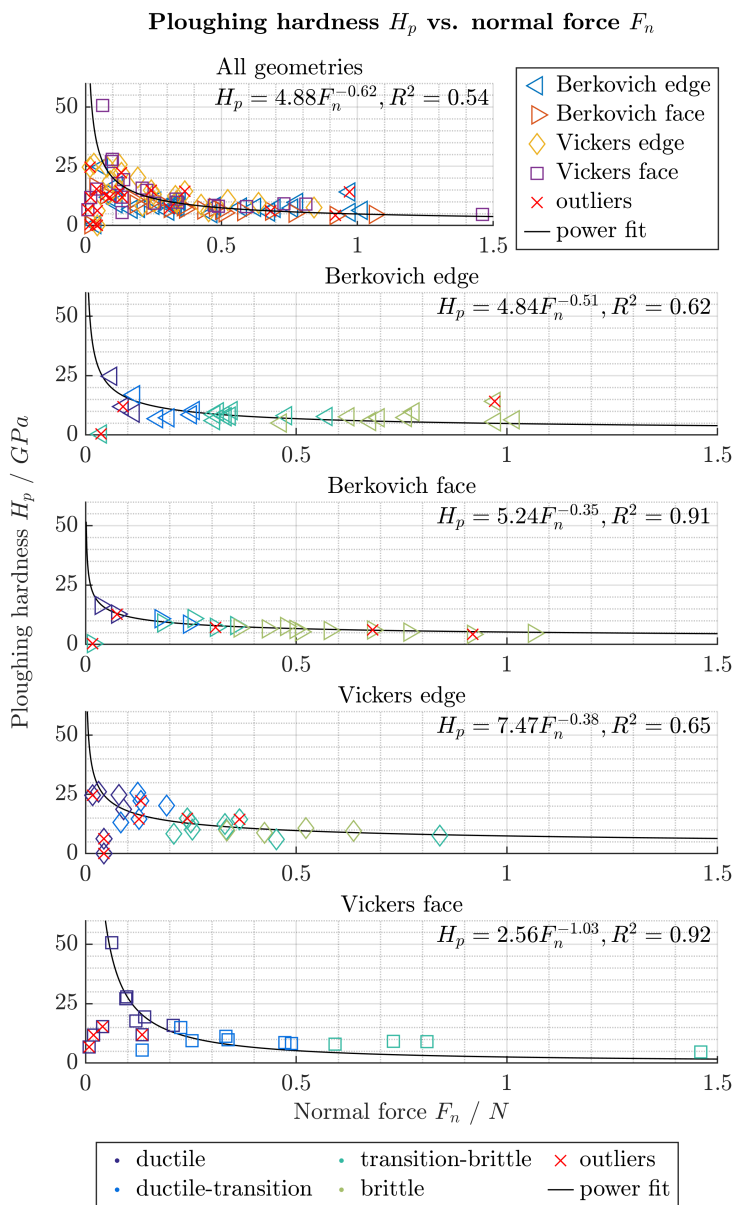


Figure A.8: Plots ploughing hardness H_p over normal Force F_n .

APPENDIX A. SCRATCH AND PLOUGHING HARDNESS - PLOTS

Appendix B

FEM User Constraint: Multiple-point-constraint User-subroutine (Fortran)

While implementing simple boundary conditions that enable or disable specific degrees of freedom at particular nodes is straightforward in any FEM software, obtaining the boundary conditions at the pulleys, as represented by (5.25), is not as simple. However, Multiple-Point-Constraints (MPC) have been found to be an effective solution for integrating these types of boundary conditions. The MPC method enables the coupling of nodes in a general manner, allowing for the treatment of non-linear constraints such as (5.25).

To implement the boundary conditions of the DWS process, the Fortran code presented below, which contains an MPC user subroutine, is used. This code is then utilised to verify the wire bow model using a finite element method model that is implemented in ABAQUS.

APPENDIX B. FEM USER CONSTRAINT

```
1 C=====
2
3 SUBROUTINE MPC(UE,A,JDOF,MDOF,N,JTYPE,X,U,UNIT,MAXDOF,
4 * LMPK,KSTEP,KINC,TIME,NT,NF,TEMP,FIELD,LTRAN,TRAN)
5 C
6 INCLUDE 'ABA_PARAM.INC'
7 C
8 DIMENSION UE(MDOF), A(MDOF,MDOF,N),JDOF(MDOF,N),X(6,N),U(
9 MAXDOF,N),UNIT(MAXDOF,N),
10 * TIME(2),TEMP(NT,N),FIELD(NF,NT,N),LTRAN(N),TRAN(3,3,N)
11 C
12 IF (JTYPE .EQ. 1) THEN
13 UE(1) = U(1,2)*TAN(U(6,2))
14 A(1,1,1) = 1
15 A(1,1,2) = -TAN(U(6,2))
16 A(1,2,2) = -(U(1,2))/(COS(U(6,2))*COS(U(6,2)))
17 JDOF(1,1) = 2
18 JDOF(1,2) = 1
19 JDOF(2,2) = 6
20 C
21 ELSE IF (JTYPE .EQ. 2) THEN
22 UE(1) = U(1,2)*TAN(U(6,2))
23 A(1,1,1) = 1
24 A(1,1,2) = TAN(U(6,2))
25 A(1,2,2) = (U(1,2))/(COS(U(6,2))*COS(U(6,2)))
26
27 JDOF(1,1) = 2
28 JDOF(1,2) = 1
29 JDOF(2,2) = 6
30 C
31 END IF
32 C
33 RETURN
34 END
```

Bibliography

- [1] Abbott E.J. Firestone F.A., 1933, Specifying surface quality: a method based on accurate measurement and comparison, *ASME Journal of Mechanical Engineering*, 55:569–572.
- [2] Ahn Y., Farris T. N., Chandrasekar S., 1998, Sliding microindentation fracture of brittle materials: Role of elastic stress fields, *Mechanics of Materials*, 29(3-4):143–152, doi:10.1016/S0167-6636(98)00012-X.
- [3] Ameli Kalkhoran S. N., Vahdati M., Yan J., 2020, Effect of relative tool sharpness on subsurface damage and material recovery in nanometric cutting of mono-crystalline silicon: A molecular dynamics approach, *Materials Science in Semiconductor Processing*, 108:104868, doi:10.1016/j.mssp.2019.104868.
- [4] Ando T., Li X., Nakao S., Kasai T., Shikida M., Sato K., 2004, Effect of crystal orientation on fracture strength and fracture toughness of single crystal silicon, *Proceedings of the IEEE International Conference on Micro Electro Mechanical Systems (MEMS)*, pages 177–180, doi:10.1109/MEMSYS.2003.1189715.
- [5] Aspnes D. E. Studna A. A., 1983, Dielectric functions and optical parameters of Si, Ge, GaP, GaAs, GaSb, InP, InAs, and InSb from 1.5 to 6.0 eV, *Physical Review B*, 27(2):985–1009, doi:10.1103/PhysRevB.27.985.
- [6] Augusto André, Looney Erin, Cañizo Carlos del, Bowden Stuart G., Buonassisi Tonio, 2017, Thin silicon solar cells: Pathway to cost-effective and defect-tolerant cell design, *Energy Procedia*, 124:706–711, doi:10.1016/j.egypro.2017.09.346.
- [7] Bai L. C., Sha Z. D., Srikanth N., Pei Q. X., Wang X., Srolovitz D. J., Zhou K., 2015, Friction between silicon and diamond at the nanoscale, *Journal of Physics D-Applied Physics*, 48(25):255303, doi:10.1088/0022-3727/48/25/255303.

- [8] Belak J. Stower I., 1991, Molecular Dynamics Modeling of Surface Indentation and Metal Cutting, *Fabrication Technology*.
- [9] Belenkov E. A. Greshnyakov V. A., 2019, Structure Formation of Hexagonal Diamond: Ab Initio Calculations, *Physics of the Solid State*, 61(10):1882–1890, doi:10.1134/S1063783419100081.
- [10] Bifano T. G., Dow T. A., Scattergood R. O., 1991, Ductile-Regime Grinding - a New Technology for Machining Brittle Materials, *Journal of Engineering for Industry-Transactions of the Asme*, 113(2):184–189, doi:10.1115/1.2899676.
- [11] Black A. J., Kopalinsky E. M., Oxley P. L. B., 1988, An Investigation of the Different Regimes of Deformation Which Can Occur When a Hard Wedge Slides over a Soft Surface - the Influence of Wedge Angle, Lubrication and Prior Plastic Working of the Surface, *Wear*, 123(1):97–114, doi:10.1016/0043-1648(88)90089-0.
- [12] Blake P. N. Scattergood R. O., 1990, Ductile-Regime Machining of Germanium and Silicon, *Journal of the American Ceramic Society*, 73(4):949–957, doi:10.1111/j.1151-2916.1990.tb05142.x.
- [13] Bolshakov A. Pharr G. M., 1998, Influences of pileup on the measurement of mechanical properties by load and depth sensing indentation techniques, *Journal of Materials Research*, 13(4):1049–1058, doi:10.1557/JMR.1998.0146.
- [14] Boussinesq Joseph, 1885, Application des potentiels à l'étude de l'équilibre et du mouvement des solides élastiques, Report, Impr. L. Danel (Lille).
- [15] Bowden F.P. Tabor D., 2001, *The Friction and Lubrication of Solids*. Clarendon Press, Oxford.
- [16] Brinksmeier E., Aurich J. C., Govekar E., Heinzel C., Hoffmeister H. W., Klocke F., Peters J., Rentsch R., Stephenson D. J., Uhlmann E., Weinert K., Wittmann M., 2006, Advances in modeling and simulation of grinding processes, *Cirp Annals-Manufacturing Technology*, 55(2):667–696, doi:10.1016/j.cirp.2006.10.003.
- [17] Brookes C. A., Harrison P. H., Green P., Moxley B., 1972, Some Observations on Scratch and Indentation Hardness Measurements, *Journal of Physics D-Applied Physics*, 5(7):1284–1295, doi:10.1088/0022-3727/5/7/313.

- [18] Budnitzki M. Kuna M., 2019, Scratching of silicon surfaces, *International Journal of Solids and Structures*, 162:211–216, doi:10.1016/j.ijsolstr.2018.11.024.
- [19] Bulychev S. I., Alekhin V. P., Shorshorov M. Kh, Ternovskii A. P., Shnyrev G. D., 1975, Determining Young’s modulus from the indenter penetration diagram, *Ind Lab (USSR)*, 41:1409–1412.
- [20] Buttery T. C. Archard J. F., 1970, Grinding and Abrasive Wear, *Proceedings of the Institution of Mechanical Engineers*, 185(1):537–551, doi:10.1243/pime_proc_1970_185_058_02.
- [21] Callahan D. L. Morris J. C., 1992, The Extent of Phase-Transformation in Silicon Hardness Indentations, *Journal of Materials Research*, 7(7):1614–1617, doi:10.1557/Jmr.1992.1614.
- [22] Cannon J. F., 1974, Behavior of the Elements at High Pressures, *Journal of Physical and Chemical Reference Data*, 3(3):781–824, doi:10.1063/1.3253148.
- [23] Carpinteri A. Paggi M., 2005, Size-scale effects on the friction coefficient, *International Journal of Solids and Structures*, 42(9-10):2901–2910, doi:10.1016/j.ijsolstr.2004.10.001.
- [24] Chacham H. Kleinman L., 2000, Instabilities in diamond under high shear stress, *Phys Rev Lett*, 85(23):4904–7, doi:10.1103/PhysRevLett.85.4904.
- [25] Challen J. M. Oxley P. L. B., 1979, An explanation of the different regimes of friction and wear using asperity deformation models, *Wear*, 53(2):229–243, doi:10.1016/0043-1648(79)90080-2.
- [26] Chandra A., Anderson G., Melkote S., Gao W., Haitjema H., Wegener K., 2014, Role of surfaces and interfaces in solar cell manufacturing, *Cirp Annals-Manufacturing Technology*, 63(2):797–819, doi:10.1016/j.cirp.2014.05.008.
- [27] Chavoshi S. Z., Gallo S. C., Dong H. S., Luo X. C., 2017, High temperature nanoscratching of single crystal silicon under reduced oxygen condition, *Materials Science and Engineering a-Structural Materials Properties Microstructure and Processing*, 684:385–393, doi:10.1016/j.msea.2016.11.097.
- [28] Chen S. Y., Farris T. N., Chandrasekar S., 1991, Sliding Microindentation Fracture of Brittle Materials, *Tribology Transactions*, 34(2):161–168, doi:10.1080/10402009108982023.

- [29] Choi D. H., Lee J. R., Kang N. R., Je T. J., Kim J. Y., Jeon E. C., 2017, Study on ductile mode machining of single-crystal silicon by mechanical machining, *International Journal of Machine Tools and Manufacturing*, 113:1–9, doi:10.1016/j.ijmachtools.2016.10.006.
- [30] Chung C. H. Le V. N., 2015, Depth of cut per abrasive in fixed diamond wire sawing, *International Journal of Advanced Manufacturing Technology*, 80(5-8):1337–1346, doi:10.1007/s00170-015-7089-z.
- [31] Chung Young J., Lee Gi H., Beom Hyeon G., 2022, Atomistic Insights into the Phase Transformation of Single-Crystal Silicon during Nanoindentation, *Nanomaterials*, 12(12), doi:10.3390/nano12122071.
- [32] Clarke D. R., Kroll C. M., Kirchner P. D., Cook R. F., Hockey B. J., 1988, Amorphization and conductivity of silicon and germanium induced by indentation, *Phys Rev Lett*, 60(21):2156–2159, doi:10.1103/PhysRevLett.60.2156.
- [33] Costa E. C., Santos C. P. dos, Xavier F. A., Weingaertner W. L., 2020, Experimental Investigation of the Sawn Surface of Monocrystalline Silicon Cut by Endless Diamond Wire Sawing, *Materials Research-Ibero-American Journal of Materials*, 23(4), doi:10.1590/1980-5373-MR-2020-0013.
- [34] Costa E. C., Xavier F. A., Knoblauch R., Binder C., Weingaertner W. L., 2020, Effect of cutting parameters on surface integrity of monocrystalline silicon sawn with an endless diamond wire saw, *Solar Energy*, 207:640–650, doi:10.1016/j.solener.2020.07.018.
- [35] Costa Erick Cardoso, Weingaertner Walter Lindolfo, Xavier Fabio Antonio, 2022, Influence of single diamond wire sawing of photovoltaic monocrystalline silicon on the feed force, surface roughness and micro-crack depth, *Materials Science in Semiconductor Processing*, 143:106525, doi:10.1016/j.mssp.2022.106525.
- [36] Crain J., Ackland G. J., Maclean J. R., Piltz R. O., Hatton P. D., Pawley G. S., 1994, Reversible pressure-induced structural transitions between metastable phases of silicon, *Phys Rev B Condens Matter*, 50(17):13043–13046, doi:10.1103/physrevb.50.13043.
- [37] Dahmen U., Hetherington C. J., Pirouz P., Westmacott K. H., 1989, The formation of hexagonal silicon at twin intersections, *Scripta Metallurgica*, 23(2):269–272, doi:10.1016/0036-9748(89)90424-9.

- [38] Dehghanimadvar Mohammad, Egan Renate, Chang Nathan L., 2022, Economic assessment of local solar module assembly in a global market, *Cell Reports Physical Science*, 3(2):100747, doi:<https://doi.org/10.1016/j.xcrp.2022.100747>.
- [39] Desai P. D., 1986, Thermodynamic Properties of Iron and Silicon, *Journal of Physical and Chemical Reference Data*, 15(3):967–983, doi:10.1063/1.555761.
- [40] Domnich V., Aratyn Y., Kriven W. M., Gogotsi Y., 2008, Temperature dependence of silicon hardness: Experimental evidence of phase transformations, *Reviews on Advanced Materials Science*, 17(1-2):33–41.
- [41] Domnich V. Gogotsi Y., 2001, Phase Transformations in Silicon Under Contact Loading, *Rev. Adv. Mater. Sci.*, 3.
- [42] Domnich V., Gogotsi Y., Dub S., 2000, Effect of phase transformations on the shape of the unloading curve in the nanoindentation of silicon, *Applied Physics Letters*, 76(16):2214–2216, doi:10.1063/1.126300.
- [43] Duclos S. J., Vohra Y. K., Ruoff A. L., 1987, hcp to fcc transition in silicon at 78 GPa and studies to 100 GPa, *Phys Rev Lett*, 58(8):775–777, doi:10.1103/PhysRevLett.58.775.
- [44] Duclos S. J., Vohra Y. K., Ruoff A. L., 1990, Experimental study of the crystal stability and equation of state of Si to 248 GPa, *Phys Rev B Condens Matter*, 41(17):12021–12028, doi:10.1103/physrevb.41.12021.
- [45] Eremets M. I., Trojan I. A., Gwaze P., Huth J., Boehler R., Blank V. D., 2005, The strength of diamond, *Applied Physics Letters*, 87(14):141902, doi:10.1063/1.2061853.
- [46] e.V. DIN Deutsches Institut für Normung, 2003, Fertigungsverfahren - Begriffe, Einteilung, Standard DIN 8580, Beuth Verlag, Berlin.
- [47] e.V. DIN Deutsches Institut für Normung, 2010, Geometrische Produktspezifikation (GPS) - Oberflächenbeschaffenheit: Tastschnittverfahren - Benennungen, Definitionen und Kenngrößen der Oberflächenbeschaffenheit (ISO 4287:1997 + Cor 1:1998 + Cor 2:2005 + Amd 1:2009); Deutsche Fassung EN ISO 4287:1998 + AC:2008 + A1:2009, Standard DIN EN ISO 4287:2009-11, Beuth Verlag, Berlin.
- [48] e.V. DIN Deutsches Institut für Normung, 2015, Metallische Werkstoffe - Härteprüfung nach Brinell - Teil 1: Prüfverfahren (ISO 6506-1:2014); Deutsche Fassung EN ISO 6506-1:2014, Standard DIN EN ISO 6506-1:2015-02, Beuth, Berlin.

- [49] e.V. DIN Deutsches Institut für Normung, 2016, Metallische Werkstoffe - Härteprüfung nach Rockwell - Teil 1: Prüfverfahren (ISO 6508-1:2016); Deutsche Fassung EN ISO 6508-1:2016, Standard DIN EN ISO 6508-1:2016-12, Beuth, Berlin.
- [50] e.V. DIN Deutsches Institut für Normung, 2018, Metallische Werkstoffe - Härteprüfung nach Vickers - Teil 1: Prüfverfahren (ISO 6507-1:2018); Deutsche Fassung EN ISO 6507-1:2018, Standard DIN EN ISO 6507-1:2018-07, Beuth, Berlin.
- [51] e.V. DIN Deutsches Institut für Normung, 2019, Metallische Werkstoffe - Härteprüfung nach Knoop - Teil 1: Prüfverfahren (ISO 4545-1:2017); Deutsche Fassung EN ISO 4545-1:2018, Standard DIN EN ISO 4545-1:2019-09, Beuth, Berlin.
- [52] Field J. E., 1990, *Natural Diamond: The Standard*, book section 2, pages 17–35. NATO ASI Series B: Physics. Plenum, New York, doi:10.1007/978-1-4684-5967-8.
- [53] Field J. E. Pickles C. S. J., 1996, Strength, fracture and friction properties of diamond, *Diamond and Related Materials*, 5(6-8):625–634, doi:10.1016/0925-9635(95)00362-2.
- [54] Gao Y. F., Ge P. Q., Zhang L., Bi W. B., 2019, Material removal and surface generation mechanisms in diamond wire sawing of silicon crystal, *Materials Science in Semiconductor Processing*, 103, doi:10.1016/j.mssp.2019.104642.
- [55] Gassilloud R., Ballif C., Gasser P., Buerki G., Michler J., 2005, Deformation mechanisms of silicon during nanoscratching, *Physica Status Solidi a-Applications and Materials Science*, 202(15):2858–2869, doi:10.1002/pssa.200521259.
- [56] Gatzen H. H. Beck M., 2003, Investigations on the friction force anisotropy of the silicon lattice, *Wear*, 254(11):1122–1126, doi:10.1016/S0043-1648(03)00323-5.
- [57] Ge M., Chen Z., Wang P., Ge P., 2022, Crack damage control for diamond wire sawing of silicon: The selection of processing parameters, *Materials Science in Semiconductor Processing*, 148:106838, doi:10.1016/j.mssp.2022.106838.
- [58] Ge M. R., Zhu H. T., Ge P. Q., Zhang C., 2019, Investigation on residual scratch depth and material removal rate of scratching machining single crystal silicon with Berkovich indenter, *Materials Science in Semiconductor Processing*, 100:98–105, doi:10.1016/j.mssp.2019.04.037.

- [59] Gogotsi Y., Baek C., Kirscht F., 1999, Raman microspectroscopy study of processing-induced phase transformations and residual stress in silicon, *Semiconductor Science and Technology*, 14(10):936–944, doi:10.1088/0268-1242/14/10/310.
- [60] Gogotsi Y., Zhou G. H., Ku S. S., Cetinkunt S., 2001, Raman microspectroscopy analysis of pressure-induced metallization in scratching of silicon, *Semiconductor Science and Technology*, 16(5):345–352, doi:10.1088/0268-1242/16/5/311.
- [61] Griffith A Taylor G, 1997, VI. The phenomena of rupture and flow in solids, *Philosophical Transactions of the Royal Society of London. Series A, Containing Papers of a Mathematical or Physical Character*, 221(582-593):163–198, doi:10.1098/rsta.1921.0006.
- [62] Hamilton G. M. Goodman L. E., 1966, The Stress Field Created by a Circular Sliding Contact, *Journal of Applied Mechanics*, 33(2):371–376, doi:10.1115/1.3625051.
- [63] Hay J. C., Bolshakov A., Pharr G. M., 1999, A critical examination of the fundamental relations used in the analysis of nanoindentation data, *Journal of Materials Research*, 14(6):2296–2305, doi:10.1557/Jmr.1999.0306.
- [64] Hölscher H. Schwarz U. D., 2001, Friction Studied with the Scanning Force Microscope, *International Journal of Materials Research*, 92(9):1040–1045, doi:10.3139/ijmr-2001-0189.
- [65] Hockey B. J. Lawn B. R., 1975, Electron-Microscopy of Microcracking About Indentations in Aluminum-Oxide and Silicon-Carbide, *Journal of Materials Science*, 10(8):1275–1284, doi:10.1007/Bf00540816.
- [66] Howes V. R., 1962, The Graphitization of Diamond, *Proceedings of the Physical Society*, 80(3):648–662, doi:10.1088/0370-1328/80/3/310.
- [67] Hu J. Z., Merkle L. D., Menoni C. S., Spain I. L., 1986, Crystal data for high-pressure phases of silicon, *Phys Rev B Condens Matter*, 34(7):4679–4684, doi:10.1103/physrevb.34.4679.
- [68] Hu J. Z. Spain I. L., 1984, Phases of Silicon at High-Pressure, *Solid State Communications*, 51(5):263–266, doi:10.1016/0038-1098(84)90683-5.
- [69] Huang N., Yan Y., Zhou P., Kang R. K., Guo D. M., 2019, Elastic-plastic deformation of single-crystal silicon in nano-cutting by a single-tip tool, *Japanese Journal of Applied Physics*, 58(8):086501, doi:10.7567/1347-4065/ab2b71.

- [70] Huang N., Yan Y., Zhou P., Kang R. K., Guo D. M., Goel S., 2020, Elastic recovery of monocrystalline silicon during ultra-fine rotational grinding, *Precision Engineering-Journal of the International Societies for Precision Engineering and Nanotechnology*, 65:64–71, doi:10.1016/j.precisioneng.2020.05.004.
- [71] Hull Robert, 1999, *Properties of crystalline silicon*. INSPEC, London.
- [72] IEA, Solar PV, <https://www.iea.org/reports/solar-pv> (Accessed: 21.09.2022).
- [73] IEA, 2022, Special Report on Solar PV Global Supply Chains, Report, International Energy Agency IEA.
- [74] Jamieson J. C., 1963, Crystal Structures at High Pressures of Metallic Modifications of Silicon and Germanium, *Science*, 139(3556):762–4, doi:10.1126/science.139.3556.762.
- [75] Jing X. N., Maiti S., Subhash G., 2007, A new analytical model for estimation of scratch-induced damage in brittle solids, *Journal of the American Ceramic Society*, 90(3):885–892, doi:10.1111/j.1551-2916.2006.01471.x.
- [76] Joannopoulos J. D. Cohen Marvin L., 1973, Electronic Properties of Complex Crystalline and Amorphous Phases of Ge and Si. I. Density of States and Band Structures, *Physical Review B*, 7(6):2644–2657, doi:10.1103/PhysRevB.7.2644.
- [77] Johnson G. W. Cook, A constitutive model and data for materials subjected to large strains, high strain rates, and high temperatures, In *7th International Symposium on Ballistics*, pages 541–547.
- [78] Juliano T., Domnich V., Gogotsi Y., 2004, *Phase transformations under dynamic loading*, book section 5.4, page 20. CRC Press, Boca Raton, 1 edition, doi:10.1201/9780429144097.
- [79] Kailer A., Gogotsi Y. G., Nickel K. G., 1997, Phase transformations of silicon caused by contact loading, *Journal of Applied Physics*, 81(7):3057–3063, doi:10.1063/1.364340.
- [80] Kasper J. S. Richards S. M., 1964, The crystal structures of new forms of silicon and germanium, *Acta Crystallographica*, 17(6):752–755, doi:10.1107/s0365110x64001840.

- [81] Kayabasi E., Ozturk S., Celik E., Kurt H., 2017, Determination of cutting parameters for silicon wafer with a Diamond Wire Saw using an artificial neural network, *Solar Energy*, 149:285–293, doi:10.1016/j.solener.2017.04.022.
- [82] Kim D., Kim H., Lee S., Jeong H., 2015, Effect of Initial Deflection of Diamond Wire on Thickness Variation of Sapphire Wafer in Multi-Wire Saw, *International Journal of Precision Engineering and Manufacturing-Green Technology*, 2(2):117–121, doi:10.1007/s40684-015-0015-x.
- [83] Kim D., Kim H., Lee S., Lee T., Jeong H., 2016, Characterization of diamond wire-cutting performance for lifetime estimation and process optimization, *Journal of Mechanical Science and Technology*, 30(2):847–852, doi:10.1007/s12206-016-0139-0.
- [84] Kim D. Y., Lee T. K., Park C. J., Lee S. J., Jeong H. D., Kim H. J., 2018, Evaluation of Cutting Ability of Electroplated Diamond Wire Using a Test System and Theoretical Approach, *International Journal of Precision Engineering and Manufacturing*, 19(4):553–560, doi:10.1007/s12541-018-0067-2.
- [85] Kim H., Kim D., Kim C., Jeong H., 2013, Multi-wire sawing of sapphire crystals with reciprocating motion of electroplated diamond wires, *Cirp Annals-Manufacturing Technology*, 62(1):335–338, doi:10.1016/j.cirp.2013.03.122.
- [86] King R. B., 1987, Elastic Analysis of Some Punch Problems for a Layered Medium, *International Journal of Solids and Structures*, 23(12):1657–1664, doi:10.1016/0020-7683(87)90116-8.
- [87] Klippel H., Süßmaier S., Rothlin M., Afrasiabi M., Pala U., Wegener K., 2021, Simulation of the ductile machining mode of silicon, *Int J Adv Manuf Technol*, 115(5-6):1565–1578, doi:10.1007/s00170-021-07167-3.
- [88] Klocke F. König W., 2005, *Fertigungsverfahren 2 - Schleifen, Honen, Läppen*, volume 1 of *VDI-Buch*. Springer, Berlin, 4 edition.
- [89] Knoblauch R., 2019, *Diamond Wire Sawing of Monocrystalline Silicon*, Doctoral thesis.
- [90] Knoblauch R., Silveira C., Campos J., Weingaertner W., 2017, Test rig for welding diamond wires into a loop, *Fifth International Conference on Advances in Civil, Structural and Mechanical Engineering*, pages 37–41.

- [91] Konyukhov A., 2015, Contact of ropes and orthotropic rough surfaces, *Zamm-Zeitschrift Für Angewandte Mathematik Und Mechanik*, 95(4):406–423, doi:10.1002/zamm.201300129.
- [92] Kumar A., Kovalchenko A., Pogue V., Pashchenko E., Melkote S. N., 2016, Ductile mode behavior of silicon during scribing by spherical abrasive particles, *3rd Cirp Conference on Surface Integrity*, 45:147–150, doi:10.1016/j.procir.2016.02.341.
- [93] Kumar A. Melkote S. N., 2017, The chemo-mechanical effect of cutting fluid on material removal in diamond scribing of silicon, *Applied Physics Letters*, 111(1), doi:10.1063/1.4991536.
- [94] Kumar A. Melkote S. N., 2018, Diamond Wire Sawing of Solar Silicon Wafers: A Sustainable Manufacturing Alternative to Loose Abrasive Slurry Sawing, *15th Global Conference on Sustainable Manufacturing*, 21:549–566, doi:10.1016/j.promfg.2018.02.156.
- [95] Kumar A. Melkote S. N., 2018, Wear of diamond in scribing of multicrystalline silicon, *Journal of Applied Physics*, 124(6), doi:10.1063/1.5037106.
- [96] Kumar A., Melkote S. N., Kaminski S., Arcona C., 2017, Effect of grit shape and crystal structure on damage in diamond wire scribing of silicon, *Journal of the American Ceramic Society*, 100(4):1350–1359, doi:10.1111/jace.14732.
- [97] Kumar Arkadeep Melkote Shreyes N., 2020, A fracture mechanics approach to enhance product and process sustainability in diamond wire sawing of silicon wafers for solar cells through improved wire design, *International Journal of Sustainable Manufacturing*, 4(2/3/4), doi:10.1504/ijism.2020.107133.
- [98] Lawn B. Wilshaw R., 1975, Indentation Fracture - Principles and Applications, *Journal of Materials Science*, 10(6):1049–1081, doi:10.1007/Bf00823224.
- [99] Lawn B. R., 1967, Partial Cone Crack Formation in a Brittle Material Loaded with a Sliding Spherical Indenter, *Proceedings of the Royal Society of London Series a-Mathematical and Physical Sciences*, 299(1458):307–+, doi:10.1098/rspa.1967.0138.
- [100] Lawn B. R., Evans A. G., Marshall D. B., 1980, Elastic-Plastic Indentation Damage in Ceramics - the Median-Radial Crack System, *Journal of the American Ceramic Society*, 63(9-10):574–581, doi:10.1111/j.1151-2916.1980.tb10768.x.

- [101] Le Van-Nhat Tran Van-Dung, 2022, Influence of Abrasive Density on the Material Removal Mechanisms in Diamond Wire Sawing of Silicon Crystal, *Advances in Engineering Research and Application*, pages 488–496.
- [102] Lee S., Kim H., Kim D., Park C., 2016, Investigation on diamond wire break-in and its effects on cutting performance in multi-wire sawing, *International Journal of Advanced Manufacturing Technology*, 87(1-4):1–8, doi:10.1007/s00170-015-7984-3.
- [103] Leung T. P., Lee W. B., Lu X. M., 1998, Diamond turning of silicon substrates in ductile-regime, *Journal of Materials Processing Technology*, 73(1-3):42–48, doi:10.1016/S0924-0136(97)00210-0.
- [104] Li X., Gao Y., Liu R., Zhou W., 2022, Experiment and theoretical prediction for subsurface microcracks and damage depth of multi-crystalline silicon wafer in diamond wire sawing, *Engineering Fracture Mechanics*, 266:108391, doi:10.1016/j.engfracmech.2022.108391.
- [105] Li X. Y., Gao Y. F., Ge P. Q., Zhang L., Bi W. B., 2019, The effect of cut depth and distribution for abrasives on wafer surface morphology in diamond wire sawing of PV polycrystalline silicon, *Materials Science in Semiconductor Processing*, 91:316–326, doi:10.1016/j.mssp.2018.12.004.
- [106] Li X. Y., Gao Y. F., Ge P. Q., Zhang L., Bi W. B., Meng J. F., 2019, Nucleation location and propagation direction of radial and median cracks for brittle material in scratching, *Ceramics International*, 45(6):7524–7536, doi:10.1016/j.ceramint.2019.01.046.
- [107] Li X. Y., Gao Y. F., Yin Y. K., Wang L. Y., Pu T. Z., 2020, Experiment and theoretical prediction for surface roughness of PV polycrystalline silicon wafer in electroplated diamond wire sawing, *Journal of Manufacturing Processes*, 49:82–93, doi:10.1016/j.jmapro.2019.11.022.
- [108] Li Z. Q., Ge P. Q., Bi W. B., Li C. Y., Wang C., Meng J. F., 2021, Influence of silicon anisotropy on surface shape deviation of wafer by diamond wire saw, *Materials Science in Semiconductor Processing*, 133:105981, doi:10.1016/j.mssp.2021.105981.
- [109] Liedke T. Kuna M., 2011, A macroscopic mechanical model of the wire sawing process, *International Journal of Machine Tools and Manufacture*, 51(9):711–720, doi:10.1016/j.ijmactools.2011.05.005.
- [110] Liu T. Y., Ge P. Q., Bi W. B., Gao Y. F., 2020, A new method of determining the slicing parameters for fixed diamond wire saw, *Materials*

- Science in Semiconductor Processing*, 120:105252, doi:10.1016/j.mssp.2020.105252.
- [111] Liu T. Y., Ge P. Q., Gao Y. F., Bi W. B., 2017, Depth of cut for single abrasive and cutting force in resin bonded diamond wire sawing, *International Journal of Advanced Manufacturing Technology*, 88(5-8):1763–1773, doi:10.1007/s00170-016-8896-6.
- [112] Lorenz M., 2013, *Berechnungsmodelle zur Beschreibung der Interaktion von bewegtem Sägedraht und Ingot*, Doctoral thesis.
- [113] Marshall D. B., Lawn B. R., Evans A. G., 1982, Elastic Plastic Indentation Damage in Ceramics - the Lateral Crack System, *Journal of the American Ceramic Society*, 65(11):561–566, doi:10.1111/j.1151-2916.1982.tb10782.x.
- [114] Masson G. Kaizuka I., 2022, Trends in Photovoltaic Applications 2022, Report IEA PVPS T1-43:2022, International Energy Agency IEA.
- [115] MathWorks, Documentation of the alphaShape object, https://ch.mathworks.com/help/matlab/ref/alphashape.html?searchHighlight=alphashape&s_tid=srchtitle.alphashape.1 (Accessed: 19.06.2022).
- [116] MathWorks, Documentation of the boxplot object, <https://ch.mathworks.com/help/stats/boxplot.html> (Accessed: 09.08.2022).
- [117] McMahon M. I. Nelmes R. J., 1993, New high-pressure phase of Si, *Phys Rev B Condens Matter*, 47(13):8337–8340, doi:10.1103/physrevb.47.8337.
- [118] Miyoshi K., 1998, Structures and Mechanical Properties of Natural and Synthetic Diamonds, Report, NASA Lewis Research Center, Cleveland, Ohio.
- [119] Möller H. J., 2015, *Wafering of Silicon*, volume Volume 92 of *Semiconductors and Semimetals*, pages 63–109. Elsevier, doi:10.1016/bs.semsem.2015.02.003.
- [120] Mohs F., 1824, Grundriß der Mineralogie, von Friedrich Mohs, *Archiv der Pharmazie*, 10(1):61–79, doi:10.1002/ardp.18240100108.
- [121] Moore A. J. W. Tegart W. J. M., 1952, Relation between Friction and Hardness, *Proceedings of the Royal Society of London Series a-Mathematical and Physical Sciences*, 212(1111):452–458, doi:10.1098/rspa.1952.0234.

- [122] Moore M. A. King F. S., 1980, Abrasive Wear of Brittle Solids, *Wear*, 60(1):123–140, doi:10.1016/0043-1648(80)90253-7.
- [123] Moss S. C. Graczyk J. F., 1969, Evidence of Voids Within the As-Deposited Structure of Glassy Silicon, *Physical Review Letters*, 23(20):1167–1171, doi:10.1103/PhysRevLett.23.1167.
- [124] Mukaiyama K., Ozaki M., Wada T., 2017, Study on Ductile-Brittle Transition of Single Crystal Silicon by a Scratching Test Using a Single Diamond Tool, *2017 8th International Conference on Mechanical and Aerospace Engineering (Icmae)*, pages 40–44.
- [125] Olijnyk H., Sikka S. K., Holzapfel W. B., 1984, Structural Phase-Transitions in Si and Ge under Pressures up to 50 Gpa, *Physics Letters A*, 103(3):137–140, doi:10.1016/0375-9601(84)90219-6.
- [126] Oliver W. C. Pharr G. M., 1992, An Improved Technique for Determining Hardness and Elastic-Modulus Using Load and Displacement Sensing Indentation Experiments, *Journal of Materials Research*, 7(6):1564–1583, doi:10.1557/Jmr.1992.1564.
- [127] Oliver W. C. Pharr G. M., 2004, Measurement of hardness and elastic modulus by instrumented indentation: Advances in understanding and refinements to methodology, *Journal of Materials Research*, 19(1):3–20, doi:10.1557/jmr.2004.0002.
- [128] O'Mara W., Herrring R., Hunt L., Bullis W., Kamins T., Lane R., Liaw H., Rogers L., Schroder D., Seilheimer R., 1990, *Handbook of semiconductor silicon technology*. Materials Science and Process Technology Series. Noyes Publications, New York.
- [129] Oxley P. L. B., 1963, Introducing strain-rate dependent work material properties into the analysis of orthogonal cutting, *Annals of the CIRP*, 13:127–138.
- [130] Page T. F., Oliver W. C., Mchargue C. J., 1992, The Deformation-Behavior of Ceramic Crystals Subjected to Very Low Load (Nano)Indentations, *Journal of Materials Research*, 7(2):450–473, doi:10.1557/Jmr.1992.0450.
- [131] Pala U., 2020, *Experimental Investigation and Modeling of Diamond Wire Sawing of Single-Crystal Silicon*, Doctoral thesis, doi:10.3929/ethz-b-000426867.

- [132] Pala U., Kuster F., Wegener K., 2020, Characterization of electroplated diamond wires and the resulting workpiece quality in silicon sawing, *Journal of Materials Processing Technology*, 276:116390, doi:10.1016/j.jmatprotec.2019.116390.
- [133] Pala U., Süssmaier S., Kuster F., Wegener K., 2018, Experimental investigation of tool wear in electroplated diamond wire sawing of silicon, *8th Cirp Conference on High Performance Cutting (Hpc 2018)*, 77:371–374, doi:10.1016/j.procir.2018.09.038.
- [134] Pala U., Sussmaier S., Wegener K., 2021, Grain flash temperatures in diamond wire sawing of silicon, *Int J Adv Manuf Technol*, 117(7-8):2227–2236, doi:10.1007/s00170-021-07298-7.
- [135] Palathra T. Adomaitis R., 2008, Process Modeling of a Wire Saw Operation, Report, Institute for Systems Research, University of Maryland.
- [136] Pharr G. M. Bolshakov A., 2002, Understanding nanoindentation unloading curves, *Journal of Materials Research*, 17(10):2660–2671, doi:10.1557/Jmr.2002.0386.
- [137] Pharr G. M., Oliver W. C., Brotzen F. R., 2011, On the generality of the relationship among contact stiffness, contact area, and elastic modulus during indentation, *Journal of Materials Research*, 7(3):613–617, doi:10.1557/jmr.1992.0613.
- [138] Philipps W., S.; Warmuth, 24.02.2022 2022, Fraunhofer ISE: Photovoltaics Report, updated: 24 February 2022, Report, Fraunhofer Institute for Solar Energy Systems ISE.
- [139] Piltz R. O., Maclean J. R., Clark S. J., Ackland G. J., Hatton P. D., Crain J., 1995, Structure and properties of silicon XII: A complex tetrahedrally bonded phase, *Phys Rev B Condens Matter*, 52(6):4072–4085, doi:10.1103/physrevb.52.4072.
- [140] Pirouz P., Chaim R., Dahmen U., Westmacott K.H, 1989, The Martensitic Transformation in Silicon I. Experimental Observations, *Acta metallurgica materialia*, 38(2).
- [141] Pirouz P., Dahmen U., Westmacott K. H., Chaim R., 1990, The martensitic transformation in silicon—III. comparison with other work, *Acta Metallurgica et Materialia*, 38(2):329–336, doi:10.1016/0956-7151(90)90063-m.

- [142] Powell D. M., Fu R., Horowitz K., Basore P. A., Woodhouse M., Buonassisi T., 2015, The capital intensity of photovoltaics manufacturing: barrier to scale and opportunity for innovation, *Energy and Environmental Science*, 8(12):3395–3408, doi:10.1039/c5ee01509j.
- [143] Preston F.W., 1927, The Theory and Design of Plate Glass Polishing Machines, *Society of Glass-Technologie Journal*, 11(42):214–256.
- [144] Qiu J., Li X., Ge R., Liu C., 2022, Surface formation, morphology, integrity and wire marks in diamond wire slicing of mono-crystalline silicon in the photovoltaic industry, *Wear*, 488-489:204186, doi:10.1016/j.wear.2021.204186.
- [145] Qiu J., Li X. F., Ge R. P., Zhang S. B., Wang H. C., 2020, Formation mechanism of wire bow and its influence on diamond wire saw process and wire cutting capability, *International Journal of Mechanical Sciences*, 185:105851, doi:10.1016/j.ijmecsci.2020.105851.
- [146] Rabinowicz Ernest, 1995, *Friction and Wear of Materials*. John Wiley and Sons, New York, 2 edition.
- [147] Ruoff A. L., 1979, *The Fracture and Yield Strengths of Diamond, Silicon and Germanium*, volume 2, pages 1557–1580. Springer, Boston, doi:10.1007/978-1-4684-7470-1_194.
- [148] Science Digital Research Solutions Inc., kinematic model... Fields of Research: 0910 Manufacturing Engineering in Publications - Dimensions, https://app.dimensions.ai/discover/publication?search_mode=content&search_text=kinematic%20model%20AND%20grinding&search_type=kws&search_field=full_search&and_facet_for=2899 (Accessed: 25.07.2022).
- [149] Shikimaka O. Prisacaru A., 2019, Deformation mechanisms under nano-scratching of Si: effect of scratching speed, load and indenter orientation, *Materials Research Express*, 6(8):085011, doi:10.1088/2053-1591/ab1a0d.
- [150] Sneddon I. N., 1965, The relation between load and penetration in the axisymmetric boussinesq problem for a punch of arbitrary profile, *International Journal of Engineering Science*, 3(1):47–57, doi:10.1016/0020-7225(65)90019-4.
- [151] Stempflé P. Takadoum J., 2012, Multi-asperity nanotribological behavior of single-crystal silicon: Crystallography-induced anisotropy in friction and wear, *Tribology International*, 48:35–43, doi:10.1016/j.triboint.2011.03.027.

- [152] Sylwestrowicz W. D., 1962, Mechanical properties of single crystals of silicon, *The Philosophical Magazine: A Journal of Theoretical Experimental and Applied Physics*, 7(83):1825–1845, doi:10.1080/14786436208213849.
- [153] Tayebi N., Conry T. F., Polycarpou A. A., 2003, Determination of hardness from nanoscratch experiments: Corrections for interfacial shear stress and elastic recovery, *Journal of Materials Research*, 18(9):2150–2162, doi:10.1557/Jmr.2003.0301.
- [154] Teomete Egemen, 2008, *Mechanics of Wire Saw Machining Process: Experimental Analyses and Modeling*, Thesis.
- [155] Thomas T.R., 1999, *Rough Surfaces*. World Scientific Publishing Company, 2 edition.
- [156] Tsybenko H., Farzam F., Dehm G., Brinckmann S., 2021, Scratch hardness at a small scale: Experimental methods and correlation to nanoindentation hardness, *Tribology International*, 163:107168, doi:10.1016/j.triboint.2021.107168.
- [157] Turchetta S., Sorrentino L., Bellini C., 2017, A method to optimize the diamond wire cutting process, *Diamond and Related Materials*, 71:90–97, doi:10.1016/j.diamond.2016.11.016.
- [158] Usui E., Shirakashi T., Kitagawa T., 1984, Analytical prediction of cutting tool wear, *Wear*, 100(1-3):129–151, doi:10.1016/0043-1648(84)90010-3.
- [159] Venkatachalam Siva, Li Xiaoping, Liang Steven Y., 2009, Predictive modeling of transition undeformed chip thickness in ductile-regime micro-machining of single crystal brittle materials, *Journal of Materials Processing Technology*, 209(7):3306–3319, doi:10.1016/j.jmatprotec.2008.07.036.
- [160] Venkatesan S. Bhushan B., 1994, The Sliding Friction and Wear Behavior of Single-Crystal, Polycrystalline and Oxidized Silicon, *Wear*, 171(1-2):25–32, doi:10.1016/0043-1648(94)90344-1.
- [161] Vodenitcharova T. Zhang L. C., 2004, A new constitutive model for the phase transformations in mono-crystalline silicon, *International Journal of Solids and Structures*, 41(18-19):5411–5424, doi:10.1016/j.ijsolstr.2004.04.025.
- [162] Wallburg F., Kuna M., Budnitzki M., Schoenfelder S., 2020, Experimental and numerical analysis of scratching induced damage during diamond wire sawing of silicon, *Wear*, 454-455:203328, doi:10.1016/j.wear.2020.203328.

- [163] Wallburg F., Kuna M., Budnitzki M., Schoenfelder S., 2022, A material removal coefficient for diamond wire sawing of silicon, *Wear*, 504-505:204400, doi:10.1016/j.wear.2022.204400.
- [164] Wang B., Melkote S. N., Saraogi S., Wang P. Z., 2020, Effect of scratching speed on phase transformations in high-speed scratching of monocrystalline silicon, *Materials Science and Engineering a-Structural Materials Properties Microstructure and Processing*, 772:138836, doi:10.1016/j.msea.2019.138836.
- [165] Wang L. Y., Gao Y. F., Li X. Y., Pu T. Z., Yin Y. K., 2020, Analytical prediction of subsurface microcrack damage depth in diamond wire sawing silicon crystal, *Materials Science in Semiconductor Processing*, 112:105015, doi:10.1016/j.mssp.2020.105015.
- [166] Wang P. Z., Ge P. Q., Gao Y. F., Bi W. B., 2017, Prediction of sawing force for single-crystal silicon carbide with fixed abrasive diamond wire saw, *Materials Science in Semiconductor Processing*, 63:25–32, doi:10.1016/j.mssp.2017.01.014.
- [167] Wang P. Z., Wang B., Melkote S. N., 2020, Modeling and simulation of phase transformation and crack formation during scribing of mono-crystalline silicon, *International Journal of Mechanical Sciences*, 175:105527, doi:10.1016/j.ijmecsci.2020.105527.
- [168] Wang Y., Song L. X., Liu J. G., Wang R., Zhao B. C., 2021, Investigation on the sawing temperature in ultrasonic vibration assisted diamond wire sawing monocrystalline silicon, *Materials Science in Semiconductor Processing*, 135:106070, doi:10.1016/j.mssp.2021.106070.
- [169] Wang Yan, Zhao Bocheng, Huang Shengju, Qian Zhaofeng, 2021, Study on the subsurface damage depth of monocrystalline silicon in ultrasonic vibration assisted diamond wire sawing, *Engineering Fracture Mechanics*, 258:108077, doi:https://doi.org/10.1016/j.engfracmech.2021.108077.
- [170] Wei L., Kuo P. K., Thomas R. L., Anthony T. R., Banholzer W. F., 1993, Thermal conductivity of isotopically modified single crystal diamond, *Phys Rev Lett*, 70(24):3764–3767, doi:10.1103/PhysRevLett.70.3764.
- [171] Williams J. A., 1996, Analytical models of scratch hardness, *Tribology International*, 29(8):675–694, doi:10.1016/0301-679x(96)00014-X.
- [172] Wu H. Melkote S. N., 2012, Effect of crystallographic orientation on ductile scribing of crystalline silicon: Role of phase transformation and

- slip, *Materials Science and Engineering a-Structural Materials Properties Microstructure and Processing*, 549:200–205, doi:10.1016/j.msea.2012.04.034.
- [173] Wu H. Melkote S. N., 2012, Study of Ductile-to-Brittle Transition in Single Grit Diamond Scribing of Silicon: Application to Wire Sawing of Silicon Wafers, *Journal of Engineering Materials and Technology-Transactions of the Asme*, 134(4):041011–041011–8, doi:10.1115/1.4006177.
- [174] Wu Q., Liu Z. D., Shen L. D., Yue W. D., Zhang B., 2017, Test research on wire deflection detection of a diamond wire saw, *International Journal of Advanced Manufacturing Technology*, 91(1-4):1347–1354, doi:10.1007/s00170-016-9787-6.
- [175] Wyen C., Jaeger D., Wegener K., 2013, Influence of cutting edge radius on surface integrity and burr formation in milling titanium, *International Journal of Advanced Manufacturing Technology*, 67(1):589–599, doi:10.1007/s00170-012-4507-3.
- [176] Xiao G. B., Ren M. J., To S., 2018, A Study of Mechanics in Brittle-Ductile Cutting Mode Transition, *Micromachines*, 9(2):49, doi:10.3390/mi9020049.
- [177] Xiao H. P., Wang H. R., Yu N., Liang R. G., Tong Z., Chen Z., Wang J. H., 2019, Evaluation of fixed abrasive diamond wire sawing induced subsurface damage of solar silicon wafers, *Journal of Materials Processing Technology*, 273, doi:10.1016/j.jmatprotec.2019.116267.
- [178] Yan J., Asami T., Kuriyagawa T., 2008, Nondestructive measurement of machining-induced amorphous layers in single-crystal silicon by laser micro-Raman spectroscopy, *Precision Engineering-Journal of the International Societies for Precision Engineering and Nanotechnology*, 32(3):186–195, doi:10.1016/j.precisioneng.2007.08.006.
- [179] Yang F. C., Li J. C. M., Kao I., 1999, Interaction Between Wire and Ingot in Wiresaw Slicing, In Sahay C., Sammakia B., Kao I., Baldswin D., editors, *IMECE: Electronics Manufacturing Issues*, volume 104, pages 3–8, 1999.
- [180] Yang J. T., Banerjee S., Wu J. N., Myung Y., Rezvanian O., Banerjee P., 2016, Phase and stress evolution in diamond microparticles during diamond-coated wire sawing of Si ingots, *International Journal of Advanced Manufacturing Technology*, 82(9-12):1675–1682, doi:10.1007/s00170-015-7446-y.

- [181] Yang M., Li C. H., Zhang Y. B., Jia D. Z., Zhang X. P., Hou Y. L., Li R. Z., Wang J., 2017, Maximum undeformed equivalent chip thickness for ductile-brittle transition of zirconia ceramics under different lubrication conditions, *International Journal of Machine Tools and Manufacture*, 122:55–65, doi:10.1016/j.ijmachtools.2017.06.003.
- [182] Yin Y., Gao Y., Li X., Pu T., Wang L., 2020, Study on cutting PV polysilicon with a new type of diamond abrasives-helix-distribution saw wire based on controlling the subsurface microcrack damage depth, *The International Journal of Advanced Manufacturing Technology*, 110(9):2389–2406, doi:10.1007/s00170-020-06019-w.
- [183] Yin Y. K., Gao Y. F., Li X. Y., Pu T. Z., Wang L. Y., 2020, Experimental study on slicing photovoltaic polycrystalline silicon with diamond wire saw, *Materials Science in Semiconductor Processing*, 106, doi:10.1016/j.mssp.2019.104779.
- [184] Yin Y. K., Gao Y. F., Wang L. Y., Zhang L., Pu T. Z., 2021, Analysis of crack-free surface generation of photovoltaic polysilicon wafer cut by diamond wire saw, *Solar Energy*, 216:245–258, doi:10.1016/j.solener.2021.01.009.
- [185] Yoder M., 1990, *Diamond: Potential and Status*, book section 1, pages 1–16. NATO ASI Series B: Physics. Plenum, New York, doi:10.1007/978-1-4684-5967-8.
- [186] Yoffe E. H., 1982, Elastic Stress-Fields Caused by Indenting Brittle Materials, *Philosophical Magazine a-Physics of Condensed Matter Structure Defects and Mechanical Properties*, 46(4):617–628, doi:10.1080/01418618208236917.
- [187] Yokohata T., Kato K., Miyamoto T., Kaneko R., 1998, Load-dependency of friction coefficient between silicon-oxides and diamond under ultra-low contact load, *Journal of Tribology-Transactions of the Asme*, 120(3):503–509, doi:10.1115/1.2834579.
- [188] Yu X. G., Wang P., Li X. Q., Yang D. R., 2012, Thin Czochralski silicon solar cells based on diamond wire sawing technology, *Solar Energy Materials and Solar Cells*, 98:337–342, doi:10.1016/j.solmat.2011.11.028.
- [189] Zarudi I. Zhang L. C., 1999, Structure changes in mono-crystalline silicon subjected to indentation - experimental findings, *Tribology International*, 32(12):701–712, doi:10.1016/S0301-679x(99)00103-6.

- [190] Zhang C., Zhu H. T., Jiang Z. L., Huang C. Z., Wang J., 2020, Removal mechanism and surface quality of crystal semiconductor materials in scratching tests with Berkovich indenter, *Materials Science in Semiconductor Processing*, 105:104746, doi:10.1016/j.mssp.2019.104746.
- [191] Zhao Y. X., Buehler F., Sites J. R., Spain I. L., 1986, New Metastable Phases of Silicon, *Solid State Communications*, 59(10):679–682, doi:10.1016/0038-1098(86)90372-8.
- [192] Zong W. J., Sun T., Li D., Cheng K., Liang Y. C., 2008, XPS analysis of the groove wearing marks on flank face of diamond tool in nanometric cutting of silicon wafer, *International Journal of Machine Tools and Manufacture*, 48(15):1678–1687, doi:10.1016/j.ijmachtools.2008.06.008.

Curriculum Vitae

Stefan Süssmaier

Date of Birth: February 10, 1989

Nationality: German

Education

06/2016 - 05/2023 Doctoral Studies, Department of Mechanical and Process Engineering, ETH Zürich

04/2014 - 04/2016 Production Engineering (M.Sc.), RWTH Aachen University

10/2008 - 03/2014 Mechanical Engineering and Business Administration (B.Sc.), RWTH Aachen University

08/2011 - 06/2012 Industrial Engineering (ERASMUS programme), INSA de Lyon

Professional Experience

from 06/2016 Scientific Assistant, Institute of Machine Tools and Manufacturing (IWF), Zurich, Switzerland

08/2015 - 01/2016 Manufacturing Engineer, Rolls-Royce Deutschland Ltd. & Co. KG, Oberursel, Germany

08/2011 - 06/2012 Auxiliary Research Assistant, Laboratory for Machine Tools and Production Engineering (WZL), Aachen, Germany

List of Publications

Süssmaier, S., Klippel, H., Kuffa, M., Wegener, K., 2023, Empirical Modelling of High-speed Scratch and Ploughing Hardness of Silicon with A Parameterisation for Different Indenter Shapes, to be submitted to *Tribology International*.

Süssmaier, S., Zhang, N., Kuffa, M., Wegener, K., 2023, Friction between Diamond and Si at Macroscopic Scale, to be submitted to *Wear*.

Podjanin, I., Avots, A., Süssmaier, S., Wegener, K., 2023, Application of an XGBoost Framework to Power Semiconductor Manufacturing: Prediction of Transfer Molding Force, to be submitted to *CIRP Journal of Manufacturing Science and Technology*.

Renggli, P., Wäfler, A., Weiss, L., Süssmaier, S., Glasder, M., Plüss, C., Di-ergardt, U., Köhnlein, M., Schmid, L., Josi, C., Schärli, M., Baumann, M., 2022, Learning Machine, Teaching Machine - Human-computer collaboration in a high precision environment: Reinforcement of performance through mutual human-AI learning, *5th International Conference on Intelligent Human Systems Integration: Integrating People and Intelligent Systems*

Klippel, H., Süssmaier, S., Kuffa, M., Wegener, K., 2022, Dry Cutting Experiments Database Ti6Al4V and Ck45, doi:10.48550/ARXIV.2209.04197

Klippel, H., Süssmaier, S., Röthlin, M., Afrasiabi, M., Pala, U., Wegener, K., 2021, Simulation of the ductile machining mode of silicon, *Int J Adv Manuf Technol*, 115(5-6), 1565-1578, doi:10.1007/s00170-021-07167-3

Pala, U., Süssmaier, S., Wegener, K., 2021, Grain flash temperatures in diamond wire sawing of silicon, *Int J Adv Manuf Technol*, 117(7-8), 2227-2236. doi:10.1007/s00170-021-07298-7

Seeholzer, L., Süssmaier, S., Kneubühler, F., Wegener, K. (2021). Experimental investigation of the machining characteristics in diamond wire sawing of unidirectional CFRP, *Int J Adv Manuf Technol*, doi:10.1007/s00170-021-07146-8

Pala, U., Süssmaier, S., Wegener, K., 2020, Schnelltest für die Eignung von Diamantdraht zum Wafering. In H.-W. Hoffmeister, B. Denkena (Eds.), *Jahrbuch Schleifen, Honen, Läppen und Polieren* 69,26-42, Essen: Vulkan Verlag.

Pala, U., Süssmaier, S., Kuster, F., Wegener, K., 2018, Experimental investigation of tool wear in electroplated diamond wire sawing of silicon, *8th CIRP Conference on High Performance Cutting (HPC 2018)*, 77, 371-374. doi:10.1016/j.procir.2018.09.038